Universidad de Oviedo

Departamento de Bioquímica y Biología Molecular

Biología Funcional y Molecular (Interdepartamental)

New biological mechanisms and intervention strategies in aging and cancer

Doctoral Thesis

Fernando García Osorio

October, 2015

RESUMEN DEL CONTENIDO DE TESIS DOCTORAL

1.- Título de la Tesis	
New biological mechanisms and intervention strategies in aging and cancer	Nuevos mecanismos biológicos y estrategias terapéuticas en envejecimiento y cáncer

2.- Autor	
Nombre: Fernando García Osorio	DNI/Pasaporte/NIE:
Programa de Doctorado: Biología Funcional y Molecular	
Órgano responsable: Interdepartamental	

RESUMEN (en español)

En esta Tesis Doctoral nos hemos centrado en el desarrollo de nuevos modelos animales para el estudio del envejecimiento y el cáncer. Paralelamente, hemos identificado nuevas alteraciones moleculares implicadas en el desarrollo de estos complejos procesos biológicos. Así, hemos generado una línea de ratones genéticamente modificados que portan la mutación p.G609G en el gen *LMNA*, causante del síndrome de Hutchinson-Gilford (HGPS). Estos ratones recapitulan fielmente las alteraciones genéticas y fenotípicas presentes en este síndrome, lo cual nos ha permitido desarrollar una estrategia terapéutica basada en la administración de oligonucleótidos antisentido y dirigida a bloquear el splicing aberrante en el gen *LMNA*, que es la alteración característica de HGPS. Además, hemos identificado alteraciones en los mecanismos de regulación epigenética y de comunicación intercelular en modelos animales de envejecimiento acelerado. El descubrimiento del papel central de NF-κB en el proceso de envejecimiento nos llevó a desarrollar distintas metodologías encaminadas a la detección y a la inhibición de esta vía en el envejecimiento. Por último, hemos caracterizado la función biológica del regulador de la proteostasis AIRAPL mediante la generación de ratones deficientes en el gen *Zfand2b*, que codifica esta proteína. Este estudio nos ha permitido descubrir una potente actividad supresora tumoral de AIRAPL en la transformación mieloide, a través de la regulación de los niveles del receptor del factor de crecimiento asociado a insulina (IGF1R).

RESUMEN (en Inglés)

Along this Doctoral Thesis work, we have developed new experimental animal models for the study of aging and cancer. We have also identified novel mechanistic alterations involved in these complex biological processes. Thus, we have generated a mutant mice strain carrying the characteristic mutation (p.G609G) in the *LMNA* gene, which causes Hutchinson-Gilford progeria syndrome (HGPS). These mice recapitulate both genetic and phenotypic alterations of this disease, which has allowed us to develop a therapy for HGPS based on the administration of antisense oligonucleotides to block the *LMNA* abnormal splicing. Moreover, we have identified new alterations in epigenetic regulation as well as in intercellular communication mechanisms in accelerated aging. The identification of the prominent role of NF-κB hyperactivation in the establishment

of the aged state has allowed us to develop diverse methodologies to monitor the activity of this pathway as well as to successfully inhibit its function during aging. Finally, we have characterized the biological role of the proteostasis regulator AIRAPL through the generation of mice deficient in the gene *Zfand2b*, which codifies this protein. This study has uncovered an important tumor suppressor activity of AIRAPL in myeloid transformation, through its ability to regulate the levels of insulin-related growth factor 1 receptor (IGF1R).

SR. DIRECTOR DE DEPARTAMENTO DE BIOQUÍMICA Y BIOLOGÍA MOLECULAR

Abbreviations

bp	base pair
cDNA	complementary deoxyribonucleic acid
DAPI	4´,6-diamidino-2-phenylindole
DMEM	Dulbecco´s Modified Eagle´s medium
DMSO	dimethyl sulfoxide
DNA	deoxyribonucleic acid
DTT	dithiothreitol
EDTA	ethylenediaminetetraacetic acid
ER	endoplasmic reticulum
ESC	embryonic stem cell
FBS	fetal bovine serum
FTIs	farnesyltransferase inhibitors
GEO	Gene Expression Omnibus
GSEA	Gene Set Enrichment Analysis
HRP	horseradish peroxidase
HGPS	Hutchinson-Gilford progeria syndrome
iPSCs	induced pluripotent stem cells
IVIS	*in vivo* imaging system
kb	kilobase
kDa	kilodalton
mRNA	messenger ribonucleic acid
NGPS	Néstor-Guillermo progeria syndrome
pA	polyadenylation signal

PBS	phosphate buffered saline
PCR	polymerase chain reaction
pQC	preemptive quality control
RNA	ribonucleic acid
RT-PCR	reverse transcriptase-PCR
qRT-PCR	quantitative reverse transcriptase-PCR
SA	splice acceptor
SD	splice donor
SEM	standard error of the mean
SDS	sodium dodecyl sulfate
TBE	Tris-borate EDTA
UPR	unfolded protein response
UPS	ubiquitin-proteasome system
VMSCs	vascular smooth muscle cells

Contents

Introduction

Aging is a biological phenomenon characterized by the progressive loss of physiological integrity, leading to impaired function and increased vulnerability to death [1, 2]. During decades, aging has been regarded as the consequence of a stochastic process caused by the accumulative effect of accidental events that deteriorate biological molecules [3, 4]. However, recent experimental evidences have demonstrated that aging is also driven by genetic programs, whose purpose is facilitating the evolutionary adaptation of the species [5, 6], therefore assuming that aging requires active signaling for its maintenance [7]. Genetic control of longevity became evident after the discovery of genetic pathways influencing lifespan in model organisms, from nematodes to mammals [8, 9]. Based on the complexity of the aging process, several questions have arisen regarding the physiological sources of aging-causing damage, the compensatory responses that try to re-establish homeostasis, the interconnection between cell autonomous and systemic alterations, and the intervention strategies to delay aging. In an attempt to identify and categorize the cellular and molecular foundations of aging, nine candidate aging hallmarks have been recently proposed [1]. Each of these hallmarks fulfills three criteria: (**1**) it should manifest during normal aging; (**2**) its experimental aggravation accelerates aging; and (**3**) its experimental amelioration retards the normal aging process, increasing healthspan.

Hallmarks of aging

The proposed nine hallmarks of aging are grouped in three categories: primary hallmarks, antagonistic hallmarks, and integrative hallmarks (Figure 1). The common characteristic of the primary hallmarks is that they show detrimental effects; this is the case of DNA damage, telomere loss, epigenetic drift, and defective proteostasis. In contrast to the primary hallmarks, antagonistic hallmarks, such as senescence, mitochondrial dysfunction or nutrient-sensing deregulation have opposite effects depending on their intensity. At low levels, they mediate beneficial effects, but at high levels, they become deleterious. These hallmarks can be viewed as being selected for protecting organism from damage or nutrient scarcity, but when they are exacerbated or chronic, they subvert their purpose and generate further damage. The last category is comprised of integrative hallmarks that compromise tissue homeostasis and function.

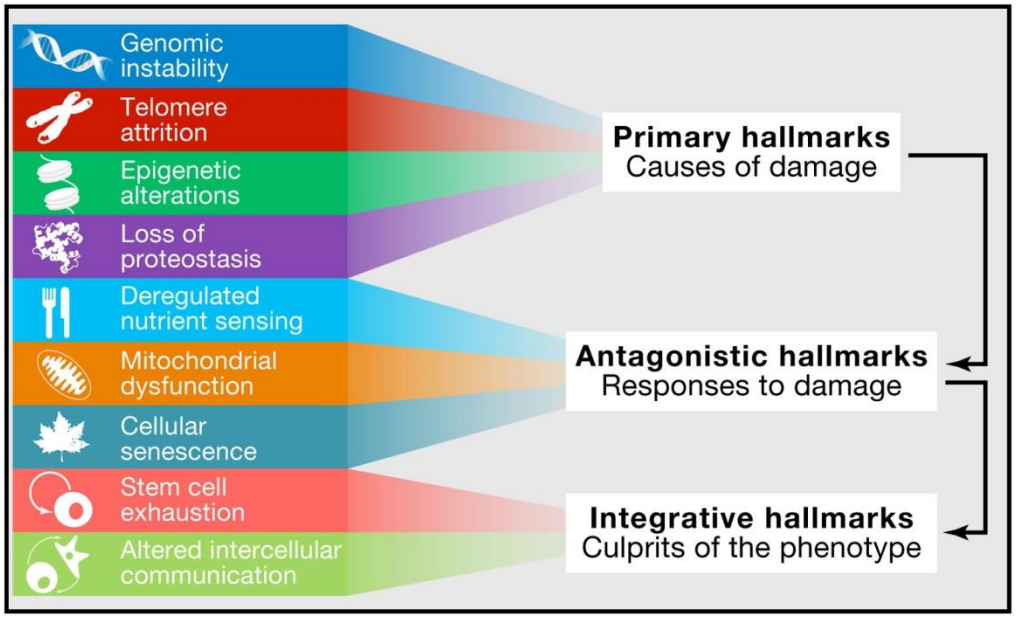

Figure 1. Hallmarks of aging. Adapted from López-Otín et al., *Cell* 153, 1194-1217 (2013)

Genomic instability

A common denominator of aging is the accumulation of genetic damage throughout lifetime. Moreover, numerous premature aging syndromes, such as Werner syndrome or Bloom syndrome, are caused by increased DNA damage accumulation. Genetic lesions arising from extrinsic and intrinsic sources are diverse and include point mutations, translocations, chromosomal gains and losses, or gene disruption by the integration of viruses or transposons [10]. In addition, defects in the nuclear architecture can cause genomic instability and result in premature aging syndromes [11]. Importantly, there is recent genetic evidence supporting that the enhancement in DNA repair machinery can extend longevity [12, 13].

Telomere attrition

Telomeres are particularly susceptible to age-related deterioration [14]. Most mammalian cells do not express the polymerase in charge of telomere replication, the enzyme telomerase; this leads to the progressive and cumulative loss of telomere sequences from chromosome ends. Telomere exhaustion explains the limited proliferative capacity of some *in vitro* cultured cells. Importantly, telomere shortening is observed during normal aging and

telomerase deficiency is associated with impaired tissue homeostasis [15, 16]. Moreover, recent evidences also indicate that experimental stimulation of telomerase expression can delay aging [17].

Epigenetic alterations

A large variety of epigenetic alterations affect cells and tissues throughout life [18]. Epigenetic alterations during aging include changes in DNA methylation patterns, posttranslational modifications of histones, and chromatin remodeling. The importance of the mechanisms involved in the generation and maintenance of epigenetic patterns is evidenced in the case of SIRT6, a NAD-dependent protein deacetylase, whose deficiency in mouse causes accelerated aging [19], whereas transgenic mice overexpressing SIRT6 have a longer lifespan. Other evidences of intervention strategies based on epigenetic alterations include the administration of pharmacological inhibitors of some epigenetic remodeling complexes extending lifespan of animal models of premature aging [20, 21], or activators of SIRT proteins to prevent some age-associated alterations [22].

Loss of proteostasis

Aging and some related disorders are linked to impaired protein homeostasis or proteostasis [23]. All cells take advantage of an array of quality control mechanisms to preserve the stability or functionality of their proteomes. Proteostasis involves mechanisms for the stabilization of correctly folded proteins as well as mechanisms for the degradation of proteins by the proteasome or the lysosome [24]. Many studies have demonstrated that proteostasis is altered with aging [25]. Deficiency in some chaperones or in other regulators of the ubiquitin-proteasome system causes accelerated aging in animal models [26], whereas overexpression of some chaperones or pharmacological stimulation of proteolytic systems reverses age-associated alterations and increases lifespan [27-30].

Deregulated nutrient sensing

Insulin and IGF-1 signaling (IIS) pathway is the most conserved aging-controlling pathway in evolution, and among its multiple targets are the FOXO family of transcription

factors and the mTOR complexes, which are also involved in aging [9, 31]. Collectively, current evidence supports that anabolic signaling accelerates aging and decreased nutrient signaling extends longevity [32]. Accordingly, genetic alterations that reduce the function of this pathway have been linked to longevity, demonstrating the impact of bioenergetics pathways in longevity. Consistent with this, dietary restriction (DR) increases lifespan or healthspan in all investigated eukaryote species. In mice, treatment with the mTOR inhibitor rapamycin also increases longevity [33].

Mitochondrial dysfunction

The efficacy of the respiratory chain tends to diminish with aging, therefore increasing electron leakage and reducing ATP generation [34]. The production of reactive oxygen species (ROS) is currently regarded as a stress-elicited survival signal, since its primary effect is the activation of a compensatory homeostatic response. As chronological age advances, ROS levels increase in an attempt to maintain survival. Beyond a certain threshold, ROS levels would eventually aggravate age-associated damage [35]. Moreover, dysfunctional mitochondria also contribute to aging as shown in mice deficient in DNA polymerase γ [36].

Cellular senescence

Cellular senescence can be defined as a stable arrest of the cell cycle coupled to defined phenotypic changes [37-39]. The accumulation of senescent cells in aged tissues has been described using direct and indirect markers such as senescence-associated β-galactosidase staining or DNA damage. Although the primary consequence of cellular senescence could be to prevent the propagation of damaged cells and to induce regeneration [40], the excessive accumulation of senescent cells may aggravate the damage and contribute to aging. In this sense, it has been reported that clearance of senescent cells in animal models of accelerated aging delays age-associated pathologies [41].

Stem cell exhaustion

The decline in the regenerative potential of tissues is an important feature of aging. Functional attrition of stem cells has been found in most of adult stem cell compartments [42,

43]. Stem cell exhaustion is the integrative consequence of multiple types of aging-associated damages and constitutes one of the culprits of tissue and organismal aging [44, 45]. In this regard, recent studies have suggested that stem cell rejuvenation has the potential to reverse aging phenotypes at the organism level [7].

Altered intercellular communication

Aging also involves changes at the level of intercellular communication, be it endocrine, neuroendocrine, or neuronal [46, 47]. Thus, neurohormonal signaling is deregulated in aging as inflammatory reactions increase [48], and the composition of pericellular and extracellular environment changes [49, 50]. In addition to these alterations, there are also examples of "contagious aging" in which senescent cells induce senescence in neighboring cells via cell contacts or through senescence-associated secretory phenotype [51]. Genetic, nutritional, or pharmacological approaches aimed at reverting altered intercellular communication have demonstrated their efficacy in several experimental models of chronological and accelerated aging [52]. Moreover, proof of principle exists for rejuvenation through blood systemic factors [53-55].

Cell-autonomous and systemic alterations in aging

Beyond cell-autonomous alterations, accumulating evidence indicates that aging-related changes in one tissue can lead to aging-specific deterioration of other tissues, explaining the interorgan coordination of the aging phenotype. Nevertheless, important questions remain to be answered, especially those related to the regulatory mechanisms that control and integrate the altered pathways, the specific contribution of cellular and systemic alterations to aging, and the intervention possibilities derived from them. In this regard, recent work has provided further support to the importance of cell-extrinsic pathways. Thus, parabiosis experiments have demonstrated that the decline in tissue homeostasis can be reverted by systemic factors from young animals [53, 55]. These findings also illustrate the difficulty of unraveling the mechanistic basis of some anti-aging interventions and underscore the interconnectedness between the different hallmarks of aging.

Rejuvenation strategies

The assumption that the aged state requires active maintenance has attracted special attention towards the identification of signals and regulatory mechanisms that sustain aging, as they may represent prominent targets of rejuvenation strategies. Despite aging appears to be inexorable, lifespan can be experimentally manipulated. Thus, both genetic and environmental interventions have been shown to extend lifespan in model organisms. However, extending lifespan is not equivalent to delaying aging. Interventions may prevent common causes of death, without changing the fundamental rate of organismal aging. Nevertheless, some of the discussed interventions appear to extend not only lifespan, but also healthspan. In this regard, it does appear that is possible to experimentally slow the rate of aging. Moreover, there are also clear examples in nature of aging arrest and even some species do not age at all [6], uncoupling the process of biological aging from chronological aging measured by the passage of time.

The reversal of the aging process occurs naturally with fertilization, erasing all age-associated marks. This reprogramming process that is central to reproduction has also been exploited in somatic cell nuclear transfer experiments [56]. Recently, advances in stem cell biology have begun to elucidate the events that follow cellular reprogramming. Specifically, these advances came with the development of induced pluripotent stem cells (iPSCs) [57]. Thus, although the process of generating iPSCs from aged donors is highly inefficient and a great percentage of the cells fail to attain the status of pluripotent stem cells, successful generation of bona-fide iPSCs from centenarian donors has been successfully achieved [58], further demonstrating the reversibility of the aged state. In both of these cases rejuvenation of adult cells is coupled to the reversal of the differentiated program. However, the ideal restoration of youthful properties to aged tissues would involve the resetting of the aging clock with no affectation of the differentiation program.

Actually, different experimental evidences have demonstrated the possibility of rejuvenation in adult organisms [59, 60]. Thus, heterochronic parabiosis experiments have shown that old tissues can be rejuvenated by exposure to young milieu [53]. Moreover, NF-κB inhibition could rejuvenate skin to a youthful state, demonstrating for the first time the existence of an active state of aging, in which signaling pathways positively maintains aging [48]. Another example of rejuvenation derives from the administration of mTOR inhibitors to

old mice, observing a notable extension of both healthspan and lifespan of the treated animals [33, 61]. In each case, old cells are induced to adopt a more youthful phenotype without losing differentiation. In this regard, epigenetic reprogramming of cells seems to be a common feature of rejuvenation strategies. Thus, it seems that the different strategies described above have an ultimate effect on the epigenome, and that pharmacological approaches based on epigenetic targets could also have a remarkable impact in both reprogramming and rejuvenation enhancement strategies [21].

Progeria as a paradigm of aging research

Over the last years, our knowledge of the molecular basis of aging has gained mechanistic insight from studies on progeroid syndromes in which features of human aging are manifested precociously or in an exacerbated form [62]. The vast majority of progeroid syndromes are a consequence of inefficient DNA repair mechanisms or defective nuclear envelope assembly, which ultimately lead to DNA damage accumulation and chromosome instability [63, 64]. Thus, mutations in the genes encoding lamin A or BAF (two essential components of the nuclear envelope) or in *Zmpste24* (encoding a metalloproteinase involved in the maturation of lamin A) are responsible for several human progeroid syndromes such as Hutchinson-Gilford progeria syndrome (HGPS), Néstor-Guillermo progeria syndrome (NGPS), atypical Werner syndrome, restrictive dermopathy, and mandibuloacral dysplasia, collectively known as progeroid laminopathies [65-71].

HGPS is a sporadic, autosomal dominant disease caused by a point mutation in *LMNA* gene [72, 73]. This gene encodes intermediate filament proteins lamin A and C, two prominent structural components of the nucleus of differentiated cells. HGPS patients present age-associated symptoms, including lack of subcutaneous fat, hair loss, joint contractures, progressive cardiovascular disease resembling atherosclerosis, and death due to heart attacks and stroke in childhood [65, 66]. Most of HGPS patients carry a heterozygous point mutation within exon 11 of the *LMNA* gene encoding lamin A (c.1824C>T; p.Gly608Gly). Lamin A is a core protein of the nuclear envelope that undergoes a complex maturation process, including the addition of a farnesyl group and a proteolytic processing event carried out by the metalloproteinase ZMPSTE24/FACE-1 [74]. The p.Gly608Gly mutation activates a cryptic splicing donor site that leads to the accumulation of a truncated form of prelamin A, called

LAΔ50 or progerin, which has an internal deletion of 50 amino acids encompassing the target sequence for cleavage by ZMPSTE24 (Figure 2). The accumulation of farnesylated progerin at the nuclear envelope leads to the functional and structural defects observed in the nucleus of affected patients. Progerin is not only detected in HGPS patients but also during normal aging, thereby adding a new level of interest to the study of the mechanisms that underlie progerin formation and accumulation in human cells and tissues [75].

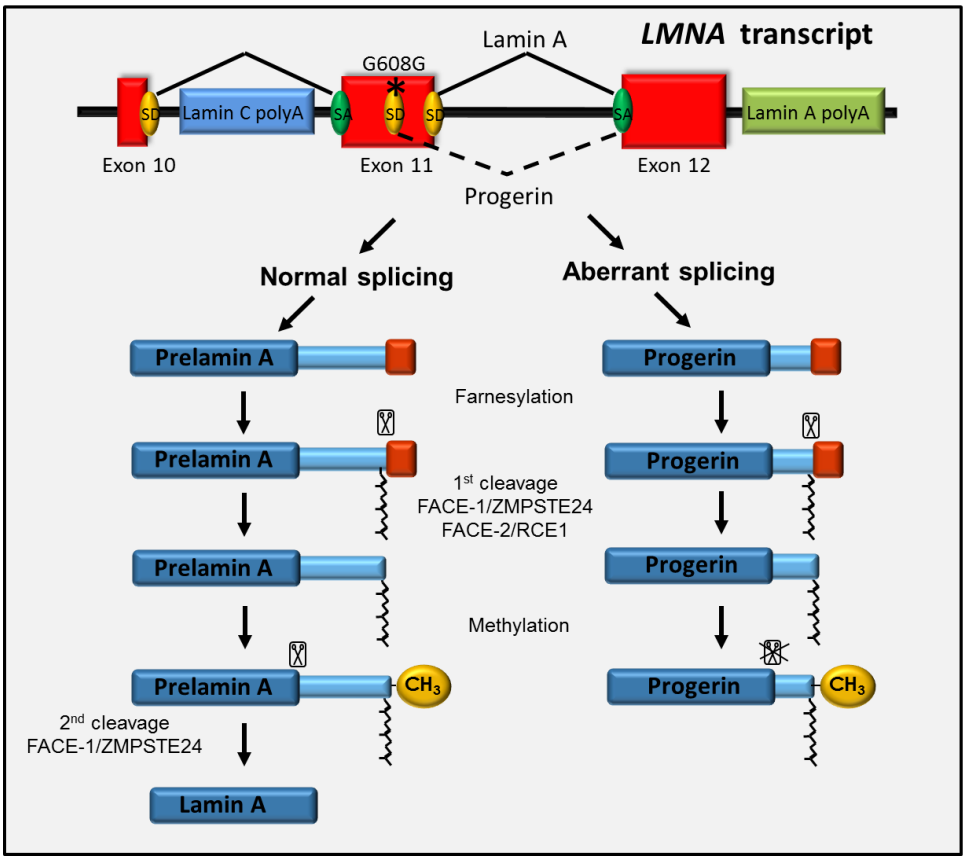

Figure 2. Posttranslational modifications of lamin A and progerin.

Elucidating the cascade of damaging events is a critical step in the understanding of any disease, and it is often crucial for identifying candidate drug targets. Cell from HGPS patients have numerous defects, and their study has become a powerful tool for both basic scientists and clinicians to ask questions about the role of major cellular processes in health and disease. The most prominent alteration in HGPS cells is related with nuclear morphology; progerin accumulation at nuclear envelope alters mechanical properties of the nucleus, and

consequently, patients' cells show profound structural alterations and increased stiffness compared with cells from healthy individuals. These alterations compromise homeostasis in tissues exposed to mechanical stress such as cardiovascular system, bones or joints, three tissues that exhibit some of the most prominent symptoms of HGPS.

The study of progeroid syndromes requires proper experimental models to investigate different alterations and test candidate drugs. In the case of HGPS, functional studies have been greatly benefited from the development of animal and cellular experimental models that have allowed the identification of regulatory and stress-response pathways involved in HGPS pathogenesis. Although several animal models of progeroid laminopathies have been generated over the past few years [74, 76-78], we focus next on *Zmpste24*-deficient mice, which have been widely used in HGPS studies and phenocopy most of the alterations present in HGPS.

Zmpste24-deficient mice

The use of genetically modified mice allowed identifying the zinc metalloproteinase ZMPSTE24 as the enzyme responsible for the final proteolytic step during lamin A maturation. Accordingly, *Zmpste24*-deficient mice accumulate farnesylated prelamin A at the nuclear envelope and phenocopy human HGPS, providing a valuable animal model for the study of this pathology [74]. The accumulation of immature prenylated forms of lamin A at the nuclear envelope produces severe alterations in nuclear architecture, leading to frequent nuclear blebbing and fragmentation. These alterations have been also linked to nuclear instability caused by inefficient recruitment of DNA repair factors [79]. In agreement with these findings, transcriptional profiling of *Zmpste24*-deficient mice revealed hyperactivation of p53 signaling [80]. Thus, p53 deficiency in *Zmpste24*-deficient mice extended their lifespan, demonstrating the causal effect of p53-mediated signaling in accelerated aging.

The fact that phenotype alterations in these progeroid mice are not completely rescued in p53-null background demonstrates a complex situation with multiple pathways contributing to their aged phenotype. Furthermore, alterations in lysosome-autophagy system and metabolism [81], as well as a severe dysfunction in the adult stem cell compartment of the skin [82], have also been reported in this animal model. More recently, *Zmpste24*-deficient

mice have also provided novel insights into the mechanisms that integrate different altered pathways, as well as about the specific contribution of cellular and systemic alterations to their progeroid phenotype (Figure 3).

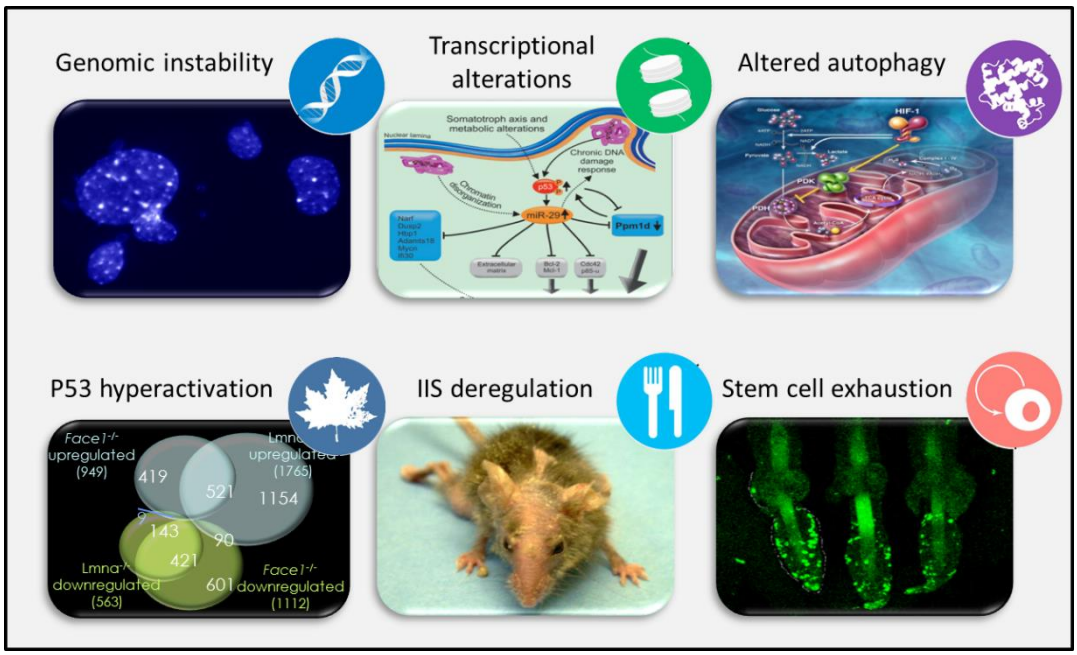

Figure 3. Aging-related alterations in *Zmpste24*-deficient mice

Important perturbations in genetic regulation have been reported in *Zmpste24*-deficient mice, unveiling a novel mechanism of stress-related cellular response upon genetic instability conditions. Thus, it has been described the role of the microRNA-29 family in the regulation of cell survival and proliferation in *Zmpste24*-deficient mice, through the modulation of the DNA-damage response in a p53-dependent way [83]. These studies have shown that miR-29 regulates important components of the DNA-damage response, such as p53, Chk1, Chk2, and ATM. Beyond cell autonomous alterations, important deregulation of nutrient sensing pathways is critically involved in accelerated aging, as illustrated by the fact that *Zmpste24*-deficient mice show a profound deregulation of the IIS pathway, with a progressive reduction in insulin-related growth factor 1 (IGF-1) levels [84]. Somatotroph alterations are responsible for important features of the progeroid phenotype, such as reduced growth rate and body size and, remarkably, the treatment with recombinant IGF-1 ameliorates some of the alterations of these mice [84].

Despite *Zmspte24*-deficient mice faithfully phenocopy HGPS alterations and have been successfully used for in vivo testing of anti-progeroid therapies, it is also noteworthy that neither *Zmspte24*-deficient mice nor other HGPS animal models initially generated reproduce the molecular situation that occur at the *LMNA* locus of these patients. This fact represents a serious limitation for both the study of splicing alterations in HGPS and the development of *in vivo* treatments with drugs that specifically modify *LMNA* splicing.

Therapeutic strategies in progeria

The development of therapeutic strategies for HGPS benefited from the extensive knowledge of lamin A function at the time of the discovery that *LMNA* mutations were the genetic cause of this pathology. First therapeutic approaches against HGPS have been based on the prevention of prelamin A farnesylation. Thus, several evidences supported that progerin toxicity depends to a great extent on its prenylation status and pointed to the use of farnesyltransferase inhibitors (FTIs) as a potential treatment for this condition [85]. However, work from our lab subsequently demonstrated that, in the absence of farnesyltransferase activity, prelamin A is alternatively geranylgeranylated, giving rise to an equally toxic form of prelamin A. Alternatively, the combination of statins and aminobisphosphonates, two drugs that block several steps of the farnesyl pyrophosphate and geranylgeranyl pyrophosphate biosynthetic pathway, efficiently blocked prelamin A prenylation and ameliorated age-associated alterations, extending lifespan of *Zmpste24*-deficient mice [86]. Currently, two clinical trials are being carried out based on the combination of statins and aminobisphosphonates, alone or in combination with a low dose of a farnesyltransferase inhibitor (NCT00731016 and NCT00916747) (Figure 4).

One promising avenue in progeria treatment is based on the identification of small molecules or antisense oligonucleotides aimed at blocking the aberrant splicing event characteristic of HGPS. Although successful proof of principle has been provided in fibroblasts from HGPS patients [87], the lack of a proper animal model has limited its preclinical evaluation. Similarly, recent advances in genome-editing technologies offer the possibility of repairing HGPS mutation *in vitro* or even *in vivo* using donor-templates and CRISPR-Cas9 or similar technologies [88, 89]. Although the alterations present in HGPS are consistent with stem cell dysfunction, cell replacement strategies face many challenges;

however targeting adult stem cell would be a critical feature of such therapies, as rejuvenated adult stem cell could show a major impact in most of the age-associated alterations. Moreover, it should be noted that cellular models of progeroid syndromes derived from iPSCs have demonstrated a great interest for studying progeria and for testing new therapeutic approaches [21, 90, 91].

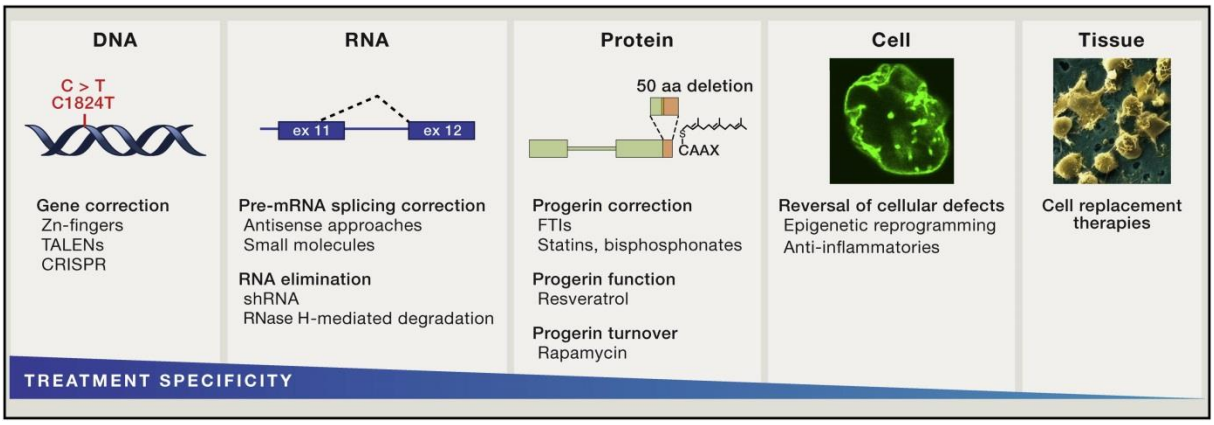

Figure 4. Spectrum of possible HGPS therapies. Adapted from Gordon et al., *Cell* 156:400-7 (2014)

Cancer and aging

Aging and cancer represent opposite manifestations of time persisting cellular damage [10]; while aging involves organism functional decline [1], cancer is generally associated with the uncontrolled increase of cellular fitness [92]. However, cancer and aging share common origins and mechanisms [93-95]. The time dependent accumulation of cellular damage is an important cause of aging. Concomitantly, cellular damage may occasionally provide aberrant advantages to certain cells, which can eventually lead to cancer. Thus, it has been established that DNA damage can trigger the development of cancer, accelerated aging, or both, depending on the type, amount, and location of the damage, the type of the cell sustaining the damage and its stage in the cell cycle, and the specific repair mechanisms. When the damage is not repaired, the outcome may be cancer or, if cell death or senescence occurs, protection against cancer with acceleration of aging process as a trade-off. Accordingly, the development of cancer and the process of aging can be delayed by reducing the load of DNA damage [96].

Although progeroid syndromes caused by defects in DNA repair machinery often present an increased susceptibility to cancer development, the paucity of reports on tumors in HGPS patients implies low susceptibility of their cells to malignant transformation, in contrast to the strong increase in tumor susceptibility during normal aging. This is even more surprising given the persistence of high levels of DNA damage in these progeroid cells [79]. Interestingly, recent studies using ZMPSTE24 mosaic mice have revealed that prelamin A accumulation prevents cancer invasion and results in a decrease in the incidence of infiltrating carcinomas, further supporting the suppressor activity of prelamin A and illustrating antagonistic properties of aging and cancer [97].

While the aged state implicates the activation of tumor suppressor pathways and the loss of replicative capacity, aging also represents the main cancer risk factor, reflecting such antagonistic pleiotropy. Aging in the hematopoietic system illustrates some of these effects, as it is characterized by functional impairment of this system [98, 99], but it is also frequently accompanied by the incidence of hematological malignancies [100, 101]. Myeloproliferative neoplasms (MPN) are chronic myeloid cancers associated with the elderly and characterized by the overproduction of mature blood cells arising from the transformation of hematopoietic stem cells (HSC) [102-104]. It has been largely assumed that the incidence of hematological malignancies with age is caused by alterations in the hematopoietic stem cell compartment [105-107].

Protein homeostasis in aging and cancer

Protein homeostasis is essential for a proper response to dynamic environments [26, 108]. Thus, proteostasis regulatory networks are present in all living beings and they have necessarily coevolved with the diversity of polypeptide sequences to enable the evolution of a wide variety of organisms by expanding the capacity of proteins to function in complex cellular environments, adding new levels of regulation and biological functions. Cellular proteostasis is maintained by a complex network which comprises pathways that control protein synthesis, folding, trafficking, aggregation, disaggregation, and degradation (Figure 5). The decreased ability of this proteostasis network to deal with cellular or environmental stress can trigger or exacerbate proteostasis-related diseases, having important implications in complex biological processes such as aging or cancer.

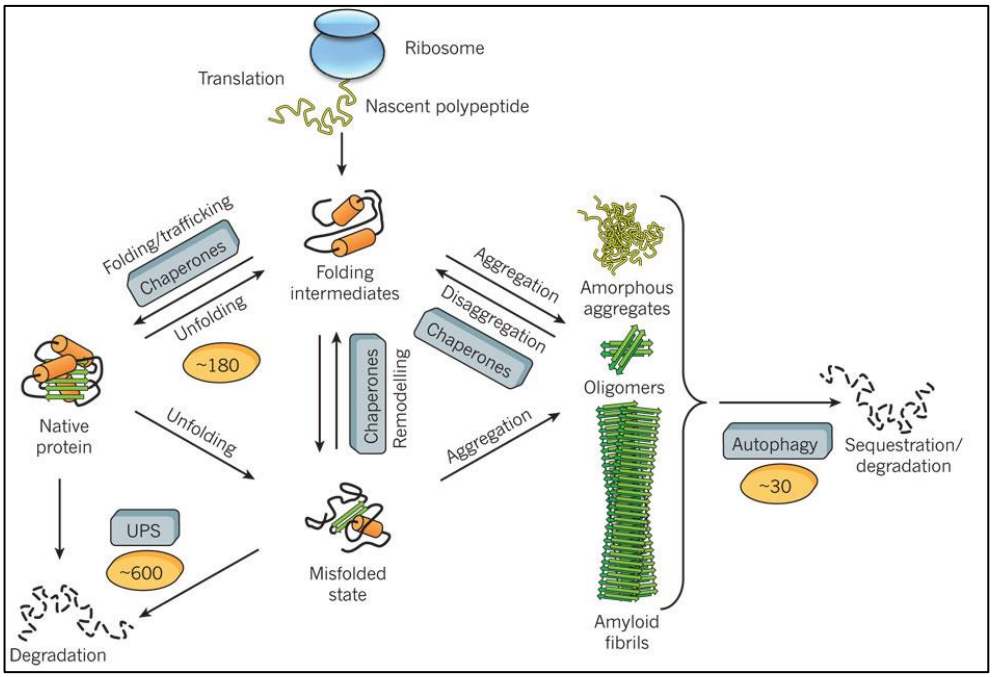

Figure 5. The proteostasis network. Adapted from Hartl et al., *Nature* 475:324-32 (2011)

The macromolecular complex of the proteostasis network includes over 1000 general and specialized chaperones, folding enzymes, and degradation and trafficking components, which influence not only folding but also compartmental distribution. Regulation of this network is accomplished by signaling pathways that directly regulate the concentration, distribution, and activities of its components. Initially, the folding function is facilitated by chaperones and related enzymes that promote folding and maintenance within the cell by minimizing misfolding and aggregation of nascent polypeptides. Although some of the chaperones are constitutively expressed in most cellular types, stress-inducible chaperones, such as HSP70, HSP90 and HSP40, are also critical to proteostasis challenges and are tightly regulated by stress-induced pathways [25].

Primary or secondary deficiencies in chaperones are associated with age-related pathologies, as many evidences have demonstrated the reduction of heat shock proteins during aging. Importantly, rejuvenation based approaches such as dietary restriction restore normal chaperone function in many cell types. Besides, some chaperones, such as HSP70, contribute to extend lifespan and healthspan in mammals and, conversely, deficiencies in HSP70-related chaperones, such as CHIP, lead to reduced longevity, further supporting the

causative role of chaperones as pivotal players in aging and age-intervention strategies [109, 110].

The endoplasmic reticulum (ER) is also a critical organelle in proteostasis regulation [111, 112], coordinating cellular functions that range from restoration of the structure of misfolded polypeptides to protein degradation, thus preventing the accumulation of damaged components and regulating the turnover of many cellular proteins [113]. The existence of regulatory mechanisms of protein quality control preserves the stability and functionality of the cellular proteome, including ER-associated degradation (ERAD) and unfolded protein response (UPR). Cells use stress sensors at ER and stress-inducible pathways to respond to a loss of proteostasis control. According to this function, different components of protein quality control machinery have been causally involved in cancer and aging, either affecting global regulation of ERAD, UPR, UPS and lysosome degradation pathways, or specifically controlling mediators of these processes [23, 25, 114-117].

Moreover, ubiquitin-proteasome (UPS) and autophagy-lysosome systems integrate the coordinated cellular machinery in charge of timely removal of misfolded and aggregated proteins. The ubiquitin-proteasome system (UPS) is the main proteolytic system involved in protein quality control. The two main components of this pathway, the ubiquitination machinery, responsible for substrate targeting, and the proteasome core, are not only involved in degradation of misfolded proteins but also regulate half-life of most protein cellular components. Structurally, the proteasome is a multicatalytic complex with a proteolytic core, known as the 20S proteasome, and several regulatory subunits (19S or 11S). The 26S proteasome, formed by the association of 20S proteasome to the 19S regulatory subunit has a prominent role in quality control. The components of the regulatory subunits are primarily chaperones, ATPases and enzymes that enhance or remove degradation tags. Degradation of most substrates requires the active involvement of regulatory complexes, which mediate substrate recognition, unfolding and often act as the driving force that opens the proteasome barrel and pushes substrates into its catalytic core.

Regulation of proteasome function often requires that proteins targeted for degradation are tagged by a covalent linkage of ubiquitin. Ubiquitination of the cargo protein is mediated by a group of enzymes that sequentially activate ubiquitin, present it to the substrate and catalyze the conjugation reaction. The activity of the proteasome is decreased with age in

main tissues. This could be due to changes in the expression of some components of the proteasome core complex, but also in accessory factors that regulate accession of some substrates directly or indirectly. In this regard, deficiencies in some of the components of this regulatory complex threaten the capacity of organisms to properly respond proteostasis challenges, shortening lifespan [26]. It has also been demonstrated that maintained UPS activity is required to attain maximal lifespan extension in long-lived mutants [114].

The autophagy-lysosome degradation pathway also plays an important role in protein homeostasis control. Thus, lysosomes are intracellular organelles involved in the degradation of intra- and extracellular components. In this regard, it has been demonstrated that autophagy is a stress-induced pathway essential for the maintenance of cellular homeostasis and energetic balance, and subtle alterations in this pathway render cells susceptible to numerous stressors and often precipitate them to death [118, 119]. Moreover, decreased autophagy activity with age has been described in different mammalian tissues. Incomplete degradation of proteins in lysosomes gives rise to the autofluorescent pigment lipofuscin, a marker of aging. Besides, lifespan extension mediated by genetic interventions often requires functional autophagy machinery.

The importance of proteostasis maintenance is illustrated by the fact that age-associated alterations have direct signaling connections to the proteostasis network. This is the representative case of IGF1R signaling; thus reduction of IGF1R results in HSF1 activation and upregulation of protective features of the proteostasis network. In this regard, reduction in IGF1R signaling during aging compensates aging-related collapse of proteostasis and conversely, IGF1R up-regulation induces proteostasis-related alterations [120].

Finally, although cancer research has mainly focused on genetic and epigenetic alterations in key oncogenes and tumor suppressors present in cancer cells, alterations in proteostasis regulation could also have a remarkable impact in several aspects of cell transformation and tumor progression. Thus, tumor cells trigger ER stress pathways as a consequence of different microenvironmental alterations such as hypoxia, nutrient deprivation and acidosis. These stress situations activate UPR, which acts as a selective factor to promote adaptation to stress and cell survival in cancer cells, increasing aggressiveness and resistance to chemotherapeutic agents. The importance of proteostasis mechanisms in cancer is also illustrated by the efficacy of therapeutic strategies that target several steps of the proteostasis

network. The unregulated cell division exhibited by cancer cells requires exceptionally high rates of protein synthesis and maintenance that are out of normal physiological balance. Thus, inhibition of some chaperones involved in stress conditions, such as HSP90, or proteasome inhibitors such as bortezomib, are effective as anticancer drugs, resulting in most cases in cell collapse and death.

Objectives

During decades, aging research has mainly focused on the study of cell-autonomous alterations as primary causes of aging process. However, recent evidences illustrate the functional relevance of systemic alterations in the establishment and maintenance of the aged state, involving new regulatory mechanisms and offering molecular targets for rejuvenation-based approaches. The study of non-cell autonomous alterations in aging often requires complex experimental systems that allow the manipulation of age-related primary and secondary hallmarks. In this regard, murine models of accelerated aging have not only provided a valuable model for studying human diseases and developing therapeutic strategies, but have also demonstrated their utility for aging research.

Aimed to generate new experimental models for aging research, we have focused on the generation of a genetically-engineered mouse model carrying the Hutchinson-Gilford progeria syndrome mutation, a model necessary to develop molecularly directed therapeutic strategies, as well as to identify novel cell and non-cell autonomous alterations involved in aging. In addition, we have developed a mouse model for the functional characterization of AIRAPL, a new proteostasis regulatory factor, with the purpose of studying the relative relevance of this process in aging.

The specific objectives of this Doctoral Thesis were:

- Generation of a knock-in mouse strain carrying the Hutchinson-Gilford progeria syndrome mutation to develop molecularly-driven therapeutic strategies.
- Characterization of epigenetic alterations in accelerated aging syndromes.
- Identification of the regulatory mechanisms that contribute to the establishment and maintenance of the aged state.
- Generation of *Zfand2b*-deficient mice to analyze the role of this protein in proteostasis control during aging.

Experimental procedures

Molecular Biology methods

Antibodies, reagents and plasmids

Antibodies specific for acK5H2b (12799, Cell Signaling), total H3 (ab45173, Abcam), lamin A/C (Manlac-1, generously provided by Prof. G. Morris; and sc-6215, Santa Cruz Biotechnology), GAPDH (MAB374, Millipore), α-tubulin (T6074, Sigma), β-actin (AC-40, Sigma), γH2AX (JBW301, Millipore), IκBα (4812, Cell Signaling), RelA (8242, Cell Signaling), NEMO (2685, Cell Signaling), ATM (2873, Cell Signaling), phospho-Ser1981-ATM (mouse: 200-301-400, Rockland Laboratories; human: 5883S, Cell Signaling), p52 (sc-7386, Santa Cruz Biotechnology), RelB (sc-48366, Santa Cruz Biotechnology), Ki-67 (DCS-Innovative Diagnostik-System KI681C01), AIRAPL (HPA035160, Atlas Antibodies), phospho-IGF1R (NB100-92555, Novus), IGF1R (9750, Cell Signaling; sc-713, Santa Cruz Biotechnology), HA (3F10, Roche), GFP (632592, Clontech), phospho-AKT (9275, Cell Signaling), AKT (9272, Cell Signaling), phospho-S6K (9430, Cell Signaling), S6K (2708, Cell Signaling), phospho-4EBP1 (9451, Cell Signaling), 4EBP1 (9452, Cell Signaling), phospho-ERK (9101, Cell Signaling), ERK (9102, Cell Signaling), phospho-JAK2 (3771, Cell Signaling), JAK2 (3229, Cell Signaling), phospho-STAT5 (9351, Cell Signaling), STAT5 (9310, Cell Signaling), phospho-PERK (3179, Cell Signaling), PERK (5683, Cell Signaling), IRE1α (3294, Cell Signaling), ATF6 (sc-22799, Santa Cruz Biotechnology), BiP (3177, Cell Signaling), calreticulin (22683, Abcam), myeloperoxidase (A0398, DAKO), CD3 (5690, Abcam), and VCP (2648, Cell Signaling), were used for western-blot, immunofluorescence and immunohistochemistry experiments. Mouse phospho receptor tyrosine kinase (RTK) array was purchased from R&D systems and used following the manufacturer's indications.

ATM inhibitor KU55933 was obtained from Calbiochem. 5-azacytidine, sodium salicylate, tunicamycin and MG-132 were obtained from Sigma. Endoporter and morpholinos for *in vitro* and *in vivo* studies were obtained from Gene Tools LLC. NVP-AEW541 was kindly provided by Novartis. ATM and NEMO siRNAs were purchased from Life Technologies. *Zfand2b* cDNA was amplified by PCR and either cloned into pcDNA3.1-HA, pEGFP-C1, or pCDH expression vectors. pBABE-bleo IGF1R was obtained from Addgene, and then, the IGF1R-encoding insert was subcloned into pEGFP-N1 or pCDH expression vectors. miR-125a locus was amplified by PCR from human genomic DNA and cloned into

pCDH. HA-ubiquitin plasmid was obtained from Addgene. The miR-125 sponge was kindly provided by Dr. G. Wulczyn [121], and then subcloned into pCDH lentiviral vector. IGF1R shRNAs were obtained from GE Dharmacon. Wild-type and V617F Jak2 plasmids were previously described [122].

Antisense oligonucleotides

The morpholino oligonucleotides used in this study were: MmEx10: 5'-GCTGCCACTCACACGGTGGTGATGG-3', MmEx11: 5'-G GATCCACCCACCTGGGCT CCCGCT-3') and negative control: 5'-CCTCTTACCTCAGTTACAATTTATA-3' for mouse cells and *in vivo* experiments. HsEx10: 5'-GCTACCACTCACGTGGTGGTGATGG-3' and HsEx11: 5'-GGGTCCACCCACCTGGGCTCCTGAG-3' were used for human cells (Gene Tools, LLC).

DNA genotyping

DNA was extracted from mouse tails following standard procedures. *Lmna-G609G* mice genotyping was performed with the following oligonucleotides: 5'-AAGGGGCTGGGA GGACAGAG-3', 5'-AGTAGAAGGTGGCGCGAAGG-3' and 5'-AGCATGCAATAGGGT GGAAGGA-3'. The PCR products consisted in fragments of 240 base pairs (bp) (G609G-allele), 340 bp (LCS allele) and 100 bp (wild-type allele). *Zfand2b*-deficient mice genotyping was performed with the following oligonucleotides: 5'-GTGAGCACTGGAGCTGGAAA-3'; 5'-GTGGGAAAGGGTTCGAAGTT-3' and 5'-CGCAAAGCTGCTACTCAGGT-3'. The PCR products consisted in fragments of 254 bp (ko-allele) and 150 bp (wild-type allele). Direct sequencing was performed using an ABI-Prism 3130XL automatic sequencer (Applied Biosystems, Foster City, California, USA).

Exome sequencing

Genomic DNA from bone marrow polymorphonuclear cells (200 ng) was sheared and used for the construction of a paired-end sequencing library as described in the protocol provided by Illumina. Enrichment of exonic sequences was then performed for each library using the SureSelectXT Mouse All Exon kit (Agilent) following the manufacturer's

instructions. Exon-enriched DNA was precipitated with magnetic beads coated with streptavidin (Invitrogen) and was washed and eluted. 18 additional cycles of amplification were then performed on the captured library. Enriched libraries were sequenced in two lanes of an Illumina Gene Analyzer II× sequencer, using the standard protocol. Data analysis and identification of sequence variants was performed using the Sidrón pipeline in a HD Genome One Research Edition station (DREAMgenics, Asturias, Spain) [123].

Analysis of DNA methylation

The methylation status of specific genomic DNA sequences was established by bisulfite genomic sequencing [124]. Following the bisulfite conversion reaction, the DNA sequence was amplified by PCR with primers specific for the bisulfite-converted DNA. The PCR product was cloned and at least 10 colonies per sequence were sequenced automatically to determine the methylation status of each sample. The percentage of methylation for each sample was calculated based on the number of clones that showed methylated or unmethylated cytosines. 5-methylcytosine (5mC) genomic content was determined by high-performance capillary electrophoresis (HPCE), as described [125]. Briefly, genomic DNA samples were boiled, treated with nuclease P1 (Sigma) for 16 h at 37 ºC, and with alkaline phosphatase (Sigma) for an additional 2 h at 37 ºC. After hydrolysis, total cytosine and 5mC content were measured by HPCE using a P/ACE MDQ system (Beckman-Coulter). Cytosine and methylcytosine were separated and quantified using the sodium dodecylsulfate (SDS) micelle system, based on size, charge, structure and hydrophobicity differences after application of specific voltages using a narrow-bore fused silica capillary tube. Relative 5mC content was expressed as a percentage of total cytosine content (methylated and non-methylated).

RNA preparation and quantitative RT-PCR

Cells or tissues were homogenized in TRIzol reagent (Life Technologies), and processed through alcohol precipitation. RNA pellets were then washed in cold 75% ethanol, and resuspended in nuclease free water (Ambion). The samples were quantified and evaluated for purity (260/280 nm ratio) with a NanoDrop ND-1000 spectrophotometer. cDNA was synthesized with 0.1 to 1 µg of total RNA with the ThermoScript RT-PCR system

(Invitrogen). Quantitative RT-PCR (qRT-PCR) was carried out in triplicate for each sample with 20 ng of cDNA, Power SYBR green PCR Master Mix, and 0.5 µL of the specific oligonucleotides for the gene of interest (Applied Biosystems). As an internal control for the amount of template cDNA used, gene expression was normalized to amounts obtained for the mouse Gapdh endogenous control. The following oligonucleotides were used for the amplification: Atm_fwd: 5'-GGAGACAGCTTGTGAAGGGCCG-3', Atm_rev: 5'-TGCAC CACTCGAGAACACCGC-3', Ikbkg_fwd: 5'-TGCCAACAGCAGATGGCTGAGG-3', Ikbkg_rev: 5'-GCTGTAGCACCTCCCGCTCAC-3', Zfand2b_fwd: 5'-AGGTCATCAGAC CAGCAGGGCA-3', Zfand2b_rev: 5'-GGTGTA GCTCTGCTTGGGGAGGAT-3'. Mouse progerin, human *ZFAND2B* and miR-125a-3p RNA levels were quantified with Taqman assays (Life Technologies), using β-actin, GAPDH or RNU6b as Taqman endogenous controls.

For detection of the aberrant splicing of *Lmna* gene the following oligonucleotides were used: Lmna-9F: 5'-GTGGAAGGCGCAGAACACCT-3', Lmna-12R: 5'- GTGAGGGG GGAGCAGGTG-3'), Lmna-7F: 5'-CCAGCCCTACCTCGCAGC-3' and Lmna-10R: 5'-GC GGCGGCTGCCACTCAC-3'. Gapdh was used as an endogenous control, Gapdh-F: 5'-GTGCAGTGCCAGCCTCGTCC-3' and Gapdh-R: 5'-GCCACTGCAAATGGCAGCCC-3'. Xbp1 splicing was analyzed by RT-PCR with the following oligonucleotides: mXbp1.3S: 5'-AAACAGAGTAGCAGCGCAGACTGC-3', mXBP1.12AS: 5'-TCCTTCTGGGTAGACCT CTGGGAG-3'. PCR products were then digested with PstI and run in agarose gels.

Transcriptional profiling

Total RNA was isolated using an RNeasy kit (Qiagen). Double-stranded cDNA was synthesized using the SuperScriptTM cDNA synthesis kit (Invitrogen). In vitro transcription was carried out with the Bioarray high yield RNA transcript labeling kit (Enzo Diagnostics). The biotin-labeled cRNA was purified, fragmented and hybridized to GeneChip Mouse Gene 1.0 ST Array (Affymetrix) or to Human Gene 2.0 ST (Affymetrix). Washing and scanning were performed using Fluidics Station 400 and GeneChip Scanner (Affymetrix). After scanning, raw data were processed with RMAExpress (http://RMAExpress.bmbolstad.com), using default settings or with Expression Console software (Affymetrix). Array data were

clustered using Cluster 3.0 software and the heat maps were created using TreeView 1.1.5 software (http://rana.lbl.gov/EisenSoftware. htm).

RNA sequencing

Transcriptional profiling of livers from *Zmpste24*-deficient and control mice was performed by RNA sequencing using a Solexa Illumina Platform. cDNA synthesis and sequencing was performed by The Centre for Applied Genomics, The Hospital for Sick Children, Toronto, Canada.

Western-blot analysis

Cultured cells were washed twice with 1× PBS and resuspended in RIPA buffer (10 mM Tris-Cl (pH 8.0), 1 mM EDTA, 1% Triton X-100, 0.1% sodium deoxycholate, 0.1% SDS, 140 mM NaCl) supplemented with protease and phosphatase inhibitors (Roche). Tissues were snap-frozen in liquid nitrogen. Frozen tissues (~50 mg in each sample) were homogenized in 300 µL of RIPA buffer with a Polytron homogenizer. Protein concentration was evaluated with the bicinchoninic acid technique (Pierce BCA Protein Assay Kit). Equal amounts of proteins were loaded onto SDS-polyacrylamide gels. After electrophoresis, gels were electrotransferred onto nitrocellulose membranes or Immobilon-FL polyvinylidene fluoride membranes (Millipore), blocked with 5% nonfat dry milk in TBS-T buffer [20 mM Tris (pH 7.4), 150 mM NaCl, and 0.05% Tween 20], and incubated overnight at 4 °C with the different primary antibodies. Finally, blots were incubated with 1:10,000 secondary antibody conjugated with horseradish peroxidase (HRP) (Jackson ImmunoResearch Laboratories) in 1.5% nonfat milk in TBS-T. Then, we washed and developed the immunoreactive bands with Immobilon Western chemiluminescent HRP substrate (Millipore).

Electrophoretic mobility shift assays

Nuclear extracts from cells were prepared as described previously [126]. For the preparation of nuclear extracts from tissues, a slightly modified protocol was used. Briefly, frozen tissues were homogenized in cold buffer A (10 mM Tris-HCl pH 8, 1.5 mM $MgCl_2$, 10 mM KCl, 1 mM DTT, protease inhibitor cocktail 2x) with a Potter homogenizer. After ice

incubation for 15 min, samples were pelleted by centrifugation and resuspended in cold buffer A containing 0.1% Triton X-100. After ice incubation, cells were pelleted, and nuclear pellets resuspended in cold buffer C (20 mM Tris-HCl pH 8, 25% glycerol (v/v), 0.4 M NaCl, 1.5 mM $MgCl_2$, 0.2 mM EDTA, 0.5 mM DTT, 2x protease inhibitor cocktail). Samples were vigorously rocked at 4 ºC for 15 min on a shaking platform. The nuclear extracts were finally centrifuged for 5 min in a microfuge at 4 °C and the supernatants were frozen in aliquots at -70 ºC. NF-κB and Oct-1 consensus oligonucleotides (Promega) were radiolabeled by T4 polynucleotide kinase (New England Biolabs) in presence of γ-32P-ATP. Labeled oligonucleotides were incubated with 15-20 µg of nuclear extracts in 1x binding buffer (4x glycerol, 20 mM Tris-HCl pH8, 60 mM NaCl, 5 mM $MgCl_2$, 1 mM DTT, protease inhibitor cocktail 1x) in the presence of poly-dI-dC. Complexes were run in nondenaturing, 6% acrylamide gels, and exposed to X-ray detector Fuji phosphorimager (Fujifilm Global).

Immunoprecipitation

AIRAPL co-immunoprecipitation experiments were performed in the HEK-293T cell line. To this end, cells were transfected with either pEGFP-Zfand2b plasmid or pEGFP empty vector and incubated with MG-132, 8 h prior to lysis. Cells were lysed with co-IP buffer (150 mM NaCl, 20 mM TrisHCl pH 7.4, 1% NP-40, 1 mM $MgCl_2$, 10% glycerol, and complete protease inhibitors 1x). Protein extracts were precleared for 2 h at 4 ºC with dynabeads (Life Technologies), and then incubated with anti-GFP-conjugated dynabeads for 1 h at 4 ºC. Beads were washed three times with lysis buffer, and bound proteins were released from beads by boiling in 2x Laemmli sample buffer. Immunoprecipitates and input samples were resolved by SDS-PAGE or subjected to protein digestion followed by nano-liquid chromatography coupled to mass spectrometry for protein identification and quantification by peptide counting [127]. For ubiquitination experiments, HEK-293T cells were transfected with HA-ubiquitin, pcDNA3.1-HA-Zfand2b and pEGFP-IGF1R plasmids, and total lysates were precipitated with anti-GFP antibody and immunostained with anti-HA antibody. For cycloheximide chase, assayed cells were incubated with 100 µg/mL cycloheximide (Sigma-Aldrich) during the indicated times.

Pulse-chase metabolic labeling

Forty-eight hours after transfection with pEGFP-IGF1R construct, HEK-293T cells were incubated in cysteine- and methionine-free DMEM containing 10% dialyzed FBS for 12 h. Then, ^{35}S-label (0.1 mCi/mL; EasyTag™ express35S Protein Labeling Mix; Pelkin Elmer) was added to the cells for 1 h. After labeling, cells were washed with chase medium (DMEM with 15 mg/L cold-methionine) and incubated in chase medium for the times indicated. Cells were then lysed in RIPA buffer, immunoprecipitated with anti-GFP antibody and resolved by SDS-PAGE. Nitrocellulose filters were exposed overnight and scanned using a Phosphorimager.

Quantification of histone acetylation

Histones were prepared in accordance with established protocols [128] and global acetylation at histones H2B and H4 was quantified as previously described [124]. Individual histone fractions were extracted from cell nuclei by acid treatment, and then purified by reverse-phase HPLC on a Jupiter C18 column (Phenomenex Inc.) with an acetonitrile gradient (20−60%) in 0.3% trifluoroacetic acid, using a high-performance liquid chromatography (HPLC) gradient system (Beckman-Coulter). This method separates molecules based on their hydrophobicity. Samples were lyophilized and then dissolved in 5 mM DTT in order to avoid oxidation. Acetylated histone derivatives were resolved by HPCE as described [124]. In brief, non-, mono-, di- and polyacetylated histone derivatives were resolved by HPCE. An uncoated fused silica capillary (Beckman-Coulter; 60.2 cm x 75 μm, effective length 50 cm) was used in a CE system (P/ACE MDQ, Beckman-Coulter) connected to a data-processing station (32 Karat Software, Beckman-Coulter). The running buffer was 100 mM phosphate buffer, pH 2.0 containing 0.02% (w/v) HPM-cellulose, and running conditions were 25 ºC with operating voltages of 12 kV. On-column absorbance was monitored at 214 nm. Before each run, the capillary system was conditioned by washing with 0.1 M NaOH (3 min), with 0.5 M H_2SO_4 (2 min) and equilibrated with running buffer (3 min). Samples were injected under pressure (0.3 psi, 3 sec). All samples were analyzed in duplicate and three measurements were made per replicate.

Nano-liquid chromatography and tandem mass spectrometry

The resulting H2B-derived tryptic peptides from control and mutant samples were on line injected onto a C18 reversed-phase micro-column (300 mm ID x 5 mm PepMapTM, LC Packings, Amsterdam, The Netherlands) to remove salts, and then analyzed in a continuous acetonitrile gradient consisting of 0-50% B in 45 min and 50-90% B in 1 min (B= 95% acetonitrile, 0.5% acetic acid in water) on a C18 reversed-phase nano-column (100 mm ID x 15 cm, Discovery® BIO Wide pore, Supelco, Bellafonte, PA). A flow-rate of 300 nl/min was used to elute peptides from the reversed-phase nano-column to a PicoTip™ emitter nano-spray needle (New Objective, Woburn, MA) for real-time ionization and peptide fragmentation on a 4000 Q-Trap LC/MS/MS system (Applied Biosystems /MDS Sciex, Concord, ON, Canada) equipped with a nanospray ion source (Protana). Nano-liquid chromatography was automatically performed on an advanced nano-gradient generator (Ultimate nano-HPLC, LC Packings) coupled to an autosampler (Famos, LC Packings). The needle voltage was set at 3000 V. Nitrogen was used as curtain (value of 15) and collision gas (set to high). For the analysis in the multiple reaction monitoring mode (MRM), Q1 was set on the multiply-charged parent ions at the indicated m/z values. Q3 was set on the marker filtering signal selected for each parent ion. Collision energy was set to 20. All chromatograms and MS/MS spectra were analyzed by the software packages Analyst 1.4.1 (Applied Biosystems).

ChIP-on-Chip assays

The chromatin immunoprecipitation assay was carried out as described [124] with anti-acK5H2b (Cell Signaling). DNA-protein interactions were fixed using formaldehyde as a crosslinking agent. Crosslinked protein/chromatin was fragmented by sonication into fragments of ~200-800 bp. Protein was then immunoprecipitated from the lysate using a specific antibody. After reversal of crosslinking, proteins were removed, DNA purified and used for ChIP-on-Chip assays. The ChIP on Chip assay was performed on the Agilent Mouse Promoter ChIP-on-chip microarrays with Designs IDs 014716 and 014717 containing probes covering 5.5 kb upstream and 2.5 kb downstream of the transcriptional start sites. Labelling was performed using a BioPrime Total Genomic Labelling System (Invitrogen) following manufacturer instructions. The hybridization was performed following Agilent manual

G4481-90010. The arrays were scanned on a G2565BA DNA microarray scanner (Agilent) and the images were quantified using Agilent Feature Extraction Software v9.5.3. Finally, Agilent ChIP Analytics v1.3.1 was used as analysis software using Whitehead model v1.0 as error model.

Cell Biology methods

Cell culture

We extracted mouse fibroblasts as previously described [80]. Human skin fibroblasts from control subjects (AG10803), patients with the HGPS p.Gly608Gly mutation (AG01972c) as well as dermal fibroblasts derived from young (GM05565, 3-year-old and GM00038, 9-year-old) and advanced age donors (AG04059, 96-year-old) were obtained from Coriell Cell repository. JM0097Y fibroblast cell line was obtained directly from a 97-year-old donor. HEK-293T, SET2 and HEL cell lines were purchased from ATCC or DSMZ cell repositories and maintained in culture following the provider's specifications. Transient transfections were performed using Lipofectamine reagent (Life Technologies). For lentiviral transduction, HEK-293T cells were transfected with pCDH-based vectors along with second generation lentiviral packaging plasmids. Viral particles were collected from supernatants, filtered through 0.45 μm PES filters and concentrated using Lenti-X concentrator reagent (Clontech).

For transfection with morpholinos, cells were plated at high density (80%) and the corresponding amount of each morpholino was added. After that, proper amount of endoporter reagent (Gene Tools, LLC) was added. Cells were retransfected 48 h later and the analyses were done 96 h after the first transfection. For transfection of small interference RNAs, we followed the manufacturer's instructions (Stealth siRNAs, Life Technologies). Briefly, cells were plated at low density (30-50%) and up to 150 pg of siRNA were added with 7.5 μL of lipofectamine RNAiMAX (Life Technologies). The same procedure was repeated after 4 h and analyses were performed 48 h after the first transfection. For pharmacological inhibition of ATM kinase activity, cells were incubated for 12 h in the presence of 10 μM KU55933 ATM inhibitor. MG-132 was used at a 2 μM concentration for the indicated times.

In vitro inhibitor assays

To assess anti-proliferative effects of NVP-AEW541, SET2 and HEL cell lines were cultured at 10,000 cells/200 μL with increasing inhibitor concentrations in triplicate. Proliferation was assessed at 48 h using Cell Titer 96 Non-Radioactive proliferation kit (Promega), and normalized to cell growth in media with an equivalent volume of DMSO. The concentration inhibiting proliferation by 50% (IC50) was determined with Graph Pad Prism 5.0. Ruxolitinib was obtained from Selleckchem.

Luciferase experiments

ZFAND2B 3'-UTR sequence was amplified by PCR and cloned into psiCHECK2 vector downstream the Renilla luciferase sequence. Luminescence determinations were performed using the firefly luciferase values as an endogenous control. miR-125a-3p miRNA precursor and inhibitor were purchased from Life Technologies.

CRISPR-Cas9 experiments

Genome editing experiments were performed as described previously [21]. In brief, for the generation of ZFAND2B-deficient HEK-293T cells, two different plasmids encoding CRISPR-Cas9 and ZFAND2B guide RNA (gRNA) were obtained from Sigma-Aldrich (5544: 5'-GACCTCGGCGCTCACTGTT CGG-3'; 5545: 5'- CTCCGAACACTGAGCGCCGAGG). gRNAs were selected to target ZFAND2B exon 1 in order to generate frameshift mutations that would cause premature termination of the open reading frame in this gene. CRISPR-Cas9 plasmids were transiently transduced into HEK-293T cells and clones were isolated by serial dilution. To analyze the resulting genomic DNA modifications induced by CRISPR-Cas9 activity, we amplified by PCR the targeted DNA region using external oligonucleotides. The forward oligonucleotide was modified to include 6-FAM fluorophore in its 5' position, which allowed the fragment analysis of resulting PCR products by capillary electrophoresis. Indels were also confirmed by DNA sequencing. Three HEK-293T cell clones carrying deleterious modifications and three wild-type clones were selected for the experiments to rule out potential off-target effects of Cas9.

Immunofluorescence analysis

Cells were fixed in 4% paraformaldehyde solution, rinsed in PBS and permeabilized with 0.5% Triton X-100. A different permeabilization step was needed for γH2AX staining with 0.1% sodium citrate and 0.1% Triton X-100 solution. Cells were incubated with primary antibodies diluted in PBS (added with 1% bovine serum albumin) 1-3 h at 25 ºC. After washes with PBS, slides were incubated with 1:500 Alexa 488-conjugated secondary antibody (Life Technologies) for 1 h at 25 °C. After the final washes, nuclei were counterstained with DAPI (Roche) and slides were mounted in Vectashield mounting medium (Vector). Microphotographs were recorded using an Axioplan-2 Zeiss fluorescent microscope (Zeiss) and images were captured with CCD camera (Fotometrics "SenSys"). 300 nuclei of progeroid and normal fibroblasts were counted for each experiment.

FACS analysis

All the antibodies used in the study were from Biolegend unless noted. The following monoclonal antibodies were used for HSC analysis: PE anti-mouse CD117 (105807), PerCP/Cy5.5 anti-mouse CD45 (103132), PE/Cy7 anti-mouse CD150 (115914), APC anti-mouse CD127 (135012), APC/Cy7 anti-mouse CD48 (103432), Brilliant Violet 421™ anti-mouse Ly-6A/E (Sca-1) (108127), FITC anti-mouse CD16/32 (101306), PE/Cy7 anti-mouse CD45.1 (110730), FITC anti-mouse CD45.2 (109806), Brilliant Violet 510™ anti-mouse/human CD45R/B220 (103247), Brilliant Violet 421™ anti-mouse CD3 (100227), anti-mouse CD34 (eBioscience, 11-0341-82), PE rat anti-mouse Ly-6G clone 1A8 (BD Pharmingen, 551461), APC rat anti-mouse Ly-6G and Ly-6C clone RB6-8C5 (BD Phamingen, 553129) and Lineage cocktail (BD PharMingen, 558074). FACS data were acquired using a FACScanto II flow cytometer (BD Biosciences) and analyzed using Infinicyt software (Cytognos, Santa Marta, Spain).

Animal model methods

Generation of *Lmna*^{G609G} mice

DNA fragments for the arms of the gene-targeting vector were generated by PCR of genomic DNA from 129 Ola ES cells. A 4.4-kb 5'-homology arm, spanning from exon 3 to

the middle of exon 10 was amplified and cloned in the 5'-polylinker of a modified PGKNeotpalox2 vector, where we had previously introduced the thymidine kinase selection gene. Next, we cloned the 5.6-kb 3'-homology arm, which spanned from exon 10 to the end of the gene, in the 3'-polylinker of PGKNeotpalox2. To this end, we amplified and cloned two subfragments. The first one, which spanned to the end of exon 11 was amplified using a reverse oligonucleotide containing the c.1827C>T mutation. The integrity of the vector was verified by DNA sequencing and restriction mapping. The targeting vector was linearized and electroporated into strain 129/Ola ES cells. To identify clones carrying the targeted *Lmna*^{LCS} allele, we performed Southern-blot analysis of HindIII and BspHI digested genomic DNA. The probes detected 9.8 and 10.5 kb fragments, respectively, in the recombinant allele. Mouse genotyping was performed by PCR of genomic DNA with the following oligonucleotides: 5'-AAGGGGCTGGGAGGACAGAG-3', 5'-AGTAGAAGGTGGCGCGAAGG-3' and 5'-AGCATGCAATAGGGTGGAAGGA-3'. The PCR fragment was 340 bp in the *Lmna*^{LCS} allele and 100 bp in the wild-type allele. Targeted 129/Ola ES cells were microinjected into C57BL/6 blastocysts to produce chimeric mice which were then crossed with C57BL/6 mice to generate heterozygous *Lmna*^{LCS} mice.

To generate mice carrying *Lmna*^{G609G} allele, *Lmna*^{LCS} mice were crossed with transgenic mice expressing constitutive CMV-Cre recombinase (Jackson Laboratory) and cassette excision was verified through PCR. The nomenclature for the description of sequence variants follows the HGVS guidelines at http://www.hgvs.org/mutnomen/. The reference sequences used for sequence variation description were: human *LMNA* NM_170707.2 and mouse *Lmna* NM_001002011.2.

Generation of *Zfand2b*-deficient mice

The gene-targeting vector for generation of *Zfand2b*-knock-out first allele was created through recombineering specific methodology as previously described [129, 130]. Briefly, a 12.7 Kb fragment of mouse genomic DNA including *Zfand2b* entire sequence was cloned into pL253 vector, that contains the thymidine kinase gene for ESC negative selection. A loxP sequence was inserted into the intron 1-2 of this gene along with a trapping element consisting in a splice acceptor sequence followed by a neomycin resistance gene, used for positive selection of ESCs. The trapping element was flanked by FRT sites. Then, a second

loxP site was inserted into the intron 8-9 of *Zfand2b* gene. Vector integrity was assessed by DNA sequencing and restriction mapping. The targeting vector was linearized and electroporated into the ES cell line AB2.2 from 129S5/SvEvBrd mice strain. ESCs clones were isolated after G418 and ganciclovir selection, and analyzed by Southern-blot for the identification of those clones that carried the targeted *Zfand2b*-ko first allele, using for this purpose XhoI-digested genomic DNA. The probes detected a 7.2 kb fragment in the recombinant allele. Two different clones of targeted AB2.2 ESCs were microinjected into C57BL/6 mouse blastocysts to produce chimeric mice that were then subsequently crossed with C57BL/6 mice to generate *Zfand2b*-heterozygous mice.

Mutant mice strains

Zmpste24-deficient mice were generated and genotyped as described previously [74]. *RelA*$^{+/-}$ mice were obtained from Jackson Laboratories. *Zmpste24*$^{+/-}$ and *RelA*$^{+/-}$ were crossed, and *Zmpste24*$^{+/-}$*RelA*$^{+/-}$ progeny were interbred to obtain *Zmspte24*$^{-/-}$*RelA*$^{+/-}$ mice. Conditional Jak2-V617F mice generation was previously described [131, 132]. *Igf1r*-haploinsufficient mice were kindly provided by Dr. M. Holzenberger [133].

Animal experiments

All the animal experiments were performed in accordance with the guidelines of the Committee for Animal Experimentation of the Universidad de Oviedo. For *in vivo* inhibition of DNA methylation, 5-azacitidine (2 mg/kg/day) in PBS was administrated intraperitoneally to mice every day for one week to 4 month-old *Zmpste24*-deficient mice and littermate controls. We administrated combined vivo-morpholinos (Gene Tools, LLC) MmEx10-MmEx11 at a concentration of 6 mg/Kg each one in a saline solution through tail vein injection twice a week. Control vivo-morpholino was administrated with the same routine at a concentration of 12 mg/Kg. Mice were treated for 12 weeks, starting at the age of 6 weeks. Neither vehicle alone nor control vivo-morpholinos treatments produced any apparent damage or stress in control mice. We administrated sodium salicylate (Sigma-Aldrich) (200 mg/kg/day) in PBS intraperitoneally to mice every day. Neither vehicle alone nor sodium salicylate treatment produced any apparent damage or stress responses in mice. For the experiments with Igf1r small molecule inhibitor, animals were administrated p.o. twice daily,

7 days/week with 50 mg/kg/day of NVP-AEW541, 10 mL/kg dissolved in 25 mM L(+)-tartaric acid. NVP-AEW541 was generously provided by Novartis. Tunicamycin (Sigma-Aldrich) was intraperitoneally injected into 8-week-old wild-type and *Zfand2b*-deficient mice at a dose of 1 μg/g body weight. Mice were euthanized 3 days after injection.

Blood analysis

For hematological determinations, blood was extracted directly from the mandibular sinus after anesthetizing mice with isoflurane. Blood samples were analyzed using Abacus junior vet equipment (Diatron Labs). In glucose determinations, animals were starved for 6 h to avoid any possible alteration in blood glucose levels due to food intake previous to measurements. Blood glucose was measured with an Accu-Chek glucometer (Roche Diagnostics) using blood from the tail vein. For other measured parameters, blood was extracted directly from the mandibular sinus after anesthetizing mice with isoflurane. To obtain plasma, blood was centrifuged immediately after collection at 3000 g and 4 ºC and the supernatant was collected and stored at -20 ºC until analysis. Plasma IGF-1 and CXCL1 concentration was determined using the R&D Systems Quantikine ELISA kit, whereas plasma GH concentration was measured using the Linco ELISA kit. For plasma insulin, leptin and adiponectin measurements, we used Millipore ELISA Kits. IL-6 and TNF-α concentrations were determined using eBioscience ELISA kits. All protocols were performed according to the manufacturer's instructions.

Heart analysis and blood pressure

Mice were anesthetized with 2.5% sevoflurane and a Vevo 2100 transthoracic echocardiograph equipped with a 30-MHz mouse ultrasound probe was used to assess left ventricular function and electrocardiographic parameters (PR and QRS intervals) using the VevoStrain™ software (Visual Sonic). Blood pressure and heart rate were measured using a noninvasive automated tail-cuff device (Visitech System BP2000, NC). Mice were trained on a daily basis for one week and then, measurements were taken on a weekly basis at the same time in the morning. For more accuracy the first 10 out of 20 measurements were discarded and mean values of individual mice were used for analysis.

Histological and immunohistochemistry analyses

Micro-CT analyses of bones were performed with a micro-CT Skyscan 1172 system (Skyscan). Forepaw strength of *Lmna*$^{G609G/G609G}$, *Lmna*$^{G609G/+}$ and *Lmna*$^{+/+}$ male mice was measured using a strain gauge sensor (Bioseb, France). For histology analysis, we fixed samples with 4% paraformaldehyde in PBS, processed the resulting preparations into serial paraffin sections, and stained each with hematoxylin and eosin (H&E). Formalin-fixed paraffin-embedded tissue sections were cut at 5 μm for immunohistochemical detection on a Discover automated immunostainer (Ventana Medical Systems). Deparaffinization and heat-induced antigen retrieval were performed directly on the stainer. Antigen retrieval procedures were as follows: retrieval performed with CC2 solution (Ventana) for 30 min at 95 ºC. Primary antibody incubation was performed for 1 h at 37 ºC. Finally, HRP-conjugated antibody (OmniMap anti-Rb HRP, Ventana) was applied for 16 min at 37 ºC. Staining was visualized by using ChromoMap DAB kit (Ventana). Cells were counterstained with hematoxylin and visualized by light microscopy. Quantitative analyses were performed according to the percentage of immunopositive cells per 0.5 mm. Blood smears were stained using May-Grünwald-Giemsa staining procedure. Reticulin fibers were revealed by silver staining according to the Gordon Sweet method. Histological analyses were performed in a blinded fashion.

Bone marrow transplantation

Recipient mice were treated with 25 mg/kg/day of busulfan (Sigma-Aldrich) for 4 days, followed by injection of 200 mg/kg of cyclophosphamide (Sigma-Aldrich). Twenty-four hours after last injection, bone marrow was collected from femurs and tibias of donor mice by flushing the cavity of freshly dissected bones with Hank's Balanced Salt Solution (HBSS). Cell suspension was filtered through 100 μm filters and counted. 2×106 cells were resuspended in HBSS and then injected in recipient animals via the jugular vein. Eight weeks later, the engraftment was evaluated by qRT-PCR and immunofluorescence analyses of peripheral blood from recipient mice. In competitive transplantation experiments, cell populations were distinguished through the Ly-5.1 marker. 2x10^6 cells from mutant or wild-type littermates were mixed with 2x10^6 cells from B6.SJL-PtprcaPepcb/BoyJ (Ly-5.1+) wild-type competitors and injected into mice recipients. Jak2-V617F transduction of bone marrow

cells and subsequent transplantation of progenitors was performed as described previously [134]. Briefly, donor mice were treated for 5 days with 5-fluorouracil (150 mg/kg, intraperitoneal injection). Bone marrow cells were harvested and cultured for 24 h in transplant medium (RPMI 10% FBS, 6 ng/mL IL-3, 10 ng/mL IL-6, and 10 ng/mL stem cell factor). Then, cells were treated by spin infection with Jak2-V617F viral supernatants centrifuged at 1800xg for 30 min, 24 h before and on the day of transplantation. Whole BM cells ($1x10^6$) were resuspended in HBSS and injected into the jugular vein of busulfan/cyclophosphamide-treated mice.

Hydrodynamic delivery of an NF-κB-luciferase gene reporter

A plasmid containing firefly luciferase gene under control of a minimal CMV promoter and tandem repeats of the NFκB transcriptional response element was injected by using the hydrodynamic technique previously described [135]. In brief, 10 μg/mL solution of the plasmid was prepared in sterile, Ringer's buffer at room temperature. Mice were anaesthetized and the lateral tail vein was accessed with a 21-gauge needle. Administration of the solution (1 mL/10 g) was performed without extravasation.

Lung-delivery of PEI/DNA complexes

The specific ratio of PEI/DNA was experimentally determined following the manufacturer's instructions. The best transfection results were obtained with an N/P ratio of 8 and 50 μg of DNA per mice, using a total amount of 8 μL of jetPEI^{TM} reagent. Complexes were injected through tail lateral vein.

Bioluminescent imaging and analysis

Mice were anaesthetized and injected intraperitoneally with 200 μL of D-luciferin solution (15 g/L in PBS, Melford Laboratories). Imaging was completed between 2 and 5 min after injection with a Xenogen IVIS system coupled to Living Image acquisition and analysis software (Xenogen). Photon flux was calculated for each mouse by using a rectangular region of interest. This value was scaled for each mouse to a comparable background value.

Represented values were recorded 7 days after injection to avoid any potential interference caused by experimental procedure-induced liver inflammation.

Caenorhabditis elegans experiments

Standard nematode growth medium and conditions were used for *C. elegans* growth and maintenance. The CB1370 [daf-2(e1370)III] and DH26 [fer-15(b26)] strains were obtained from the Caenorhabditis Genetics Center. Temperature sensitive fer-15 (fertility) mutation was used to prevent the production of offspring that would confound the evaluation of adult worms. The GM6 [fer-15(b26) II/ daf-2(e1370) II] strain was a kind gift of Dr. Manuel J. Muñoz Ruiz. All worm populations were synchronized with the alkaline hypochlorite treatment [136]. To perform RNA-mediated interference (RNAi) by feeding, nematode growth medium (NGM) plates were supplemented with 50 µg/mL ampicillin, 12.5 µg/mL tetracycline, and 1 mM IPTG. Plates were seeded with the corresponding RNAi clone, validated by PCR and/or sequencing, and dsRNA synthesis induced o/n at 37 ºC. aip-1 RNAi clone was obtained from the ORFeome library [137], while daf-16 RNAi clone was from the Ahringer library [138]. Worms were grown on regular NGM plates and transferred to RNAi plates at L4 stage. For N2 and daf-2(e1370) strains, plates were supplemented with 0.1 mg/mL fluorodeoxyuridine (FUDR) to prevent progeny growth and lifespan assays were conducted at 20 ºC. For fer-15(b26) and fer-15(b26)/daf-2(e1370) strains, experiments were performed at 25 ºC to avoid self-fertilization. At least 100 worms were used in each of the three experimental replicates. Animals were considered dead when no movement or pharyngeal pumping was observed after gentle touch in the head.

Human samples

Human MPN samples were collected from Hospital Universitario Central de Asturias (HUCA). The study was approved by the Ethical Committee of HUCA and all of the patients provided written informed consent. For *ZFAND2B* transcriptional analysis, 70 peripheral blood samples from MPN patients and 30 controls were analyzed. For AIRAPL immunohistochemistry analysis, 30 samples from MPN bone marrow biopsies and 10 controls were collected.

Statistical methods

Reproducibility of the experiments, statistical and bioinformatics analyses

All the experiments were performed at least in independent triplicates (unless noted otherwise) and statistical analyses were derived from these data. All comparisons between wild-type and knock-out animals were performed in animals from the same age. Experimental conditions were blinded randomized and no statistical method was used to predetermine sample size. Differences between groups were assayed using Microsoft Excel, SPSS and GraphPad Prism. In all cases, experimental data assumed t-test requirements (normal distribution and similar variance); in those cases where the assumption of the t-test was not valid, a non-parametric statistical method was used (for example, Wilcoxon signed-rank test). Significant differences were considered when *P<0.05 and **P<0.01. Error bars indicate the standard error of the mean, as indicated in figure legends. For computational prediction of miRNAs targeting *ZFAND2B*, a combination of the following software was used: TargetScan (http://www.targetscan.org) and miRanda (http://www.microrna.org).

Gene Set Enrichment Analysis (GSEA)

GSEA was performed as described in the original citation [139]. For data analysis, we used GSEA releases 2.06, 2.5 and 5 (http://www.broadinstitute.org/gsea/index.jsp). Weighted enrichment scores were calculated using gene expression lists ranked by signal-to-noise ratio. The maximum gene set size was set to 500 genes; the minimum gene set size was set to 20 genes; the number of permutations was set to 1000. Analyses were performed with a collection of gene sets from curated genes and canonical pathways (c2) and hallmark gene sets. Selected enriched pathways have a relaxed false discovery rate (FDR) ≤ 0.25 and $P \leq 0.01$.

Results

I. Cell autonomous and systemic alterations in accelerated aging

Aging research has been greatly benefited from the generation of animal models of accelerated aging syndromes, which faithfully recapitulate most of the alterations involved in this group of human diseases. In this regard, the characterization of *Zmpste24*-deficient mice as well as some other progeroid mouse models has unveiled a complex relationship of the cell autonomous and systemic alterations that underlie organismal aging. Furthermore, progeroid animal models have also allowed the preclinical testing of several therapeutic strategies. In order to provide an overview of these topics as a previous step to the experimental work carried out in this Doctoral Thesis, we have reviewed the development of *Zmpste24*-deficient mice as well as the main age-related alterations and therapeutic strategies described in this animal model.

Article 1: Fernando G. Osorio, Álvaro J. Obaya, Carlos López-Otín, and José M.P. Freije. "Accelerated ageing: from mechanism to therapy through animal models".

Transgenic Research. 2009 Feb; 18(1):7-15.

Personal contribution to this work

I contributed to the compilation of the information, preparation of the figures and writing of the manuscript under the supervision of Dr. José M.P. Freije.

Article 2: Fernando G. Osorio, Alejandro P. Ugalde, Guillermo Mariño, Xose S. Puente, José M.P. Freije, and Carlos López-Otín. "Cell autonomous and systemic factors in progeria development".

Biochemical Society Transactions. 2011 Dec; 39(6):1710-4.

Personal contribution to this work

I was responsible for the compilation of the information, preparation of the figures and writing of the manuscript under the supervision of Dr. Carlos López-Otín.

Transgenic Res (2009) 18:7–15
DOI 10.1007/s11248-008-9226-z

PERSPECTIVE

Accelerated ageing: from mechanism to therapy through animal models

Fernando G. Osorio · Álvaro J. Obaya · Carlos López-Otín · José M. P. Freije

Received: 17 October 2008 / Accepted: 27 October 2008 / Published online: 18 November 2008

Abstract Ageing research benefits from the study of accelerated ageing syndromes such as Hutchinson-Gilford progeria syndrome (HGPS), characterized by the early appearance of symptoms normally associated with advanced age. Most HGPS cases are caused by a mutation in the gene *LMNA*, which leads to the synthesis of a truncated precursor of lamin A known as progerin that lacks the target sequence for the metallopotease FACE-1/ZMPSTE24 and remains constitutively farnesylated. The use of Face-1/Zmpste24-deficient mice allowed us to demonstrate that accumulation of farnesylated prelamin A causes severe abnormalities of the nuclear envelope, hyper-activation of p53 signalling, cellular senescence, stem cell dysfunction and the development of a progeroid phenotype. The reduction of prenylated prelamin A levels in genetically modified mice leads to a complete reversal of the progeroid phenotype, suggesting that inhibition of protein farnesylation could represent a therapeutic option for the treatment of progeria. However, we found that both prelamin A and its truncated form progerin can undergo either farnesylation or geranylgeranylation, revealing the need of targeting both activities for an efficient treatment of HGPS. Using *Face-1/Zmpste24*-deficient mice as model, we found that a combination of statins and aminobisphosphonates inhibits both types of modifications of prelamin A and progerin, improves the ageing-like symptoms of these mice and extends substantially their longevity, opening a new therapeutic possibility for human progeroid syndromes associated with nuclear-envelope defects. We discuss here the use of this and other animal models to investigate the molecular mechanisms underlying accelerated ageing and to test strategies for its treatment.

Keywords Proteases · Tumor suppression · Cancer · Isoprenylation · Alternative splicing · Stem cell

F. G. Osorio · C. López-Otín · J. M. P. Freije (✉)
Departamento de Bioquímica y Biología Molecular, Facultad de Medicina, Instituto Universitario de Oncología, Universidad de Oviedo, 33006 Oviedo, Spain
e-mail: jmpf@uniovi.es

Á. J. Obaya
Departamento de Biología Funcional (Fisiología), Facultad de Medicina, Instituto Universitario de Oncología, Universidad de Oviedo, 33006 Oviedo, Spain

Introduction

Ageing, the progressive and irreversible loss of physiological integrity, is an extremely complex process whose molecular basis remain incompletely understood (Kirkwood 2005). Several human

illnesses, known as segmental progeroid syndromes, are characterized by the early development of multiple biological alterations normally associated with advanced age. Even though these rare and dramatic conditions only partially recapitulate normal ageing, their study has the potential of rendering valuable information on the molecular mechanisms implicated in the ageing process (Ramirez et al. 2007). Moreover, the development of animal models that phenocopy these syndromes can provide experimental systems useful to investigate the basis of particular pathologies associated with ageing (atherosclerosis, osteoporosis, osteoarthritis, cancer) and to perform preclinical testing of therapeutic strategies against these alterations.

Most human syndromes of accelerated ageing are caused by one of two major mechanisms: defects in DNA repair systems and alterations in the nuclear lamina. The best understood progeroid syndrome due to a DNA repair defect is Werner syndrome (WS), also known as progeria of the adult. WS patients show a wide array of symptoms of premature ageing, which emerge at puberty and include early growth stop, bilateral cataracts, grey hair, scleroderma-like skin changes, subcutaneous calcification, arteriosclerosis, diabetes mellitus, a prematurely aged facies and a high incidence of cancer. Most WS do not live past 50 years (Cox and Faragher 2007). Typical cases of WS are caused by null mutations in *WRN*, a gene coding for a protein of the RecQ family with helicase and exonuclease activities that plays important roles in homology-dependent recombination repair and telomere maintenance (Yu et al. 1996). A Wrn-knockout mouse model recapitulates the alterations observed in WS patients at the molecular and cellular levels but, strikingly, Wrn deficiency does not causes an accelerated ageing phenotype in mice (Lombard et al. 2000). In contrast, progeroid symptoms closely recapitulating WS develop in double-mutant mice lacking both Wrn and telomerase activity, revealing the critical role of Wrn in telomere biology and its relevance for the progeroid phenotypes caused by WRN deficiency (Chang et al. 2004; Multani and Chang 2007). These findings indicate that mice and humans may show different sensitivity to progeroid-causing alterations, and these differences have to be carefully taken in consideration to interpret results derived from the use of murine models.

Hutchinson-Gilford progeria syndrome (HGPS), also known as progeria of childhood, is the best known accelerated ageing syndrome caused by defects of the nuclear envelope. HGPS is characterized by shortened lifespan, growth impairment, sclerotic skin, early hair loss, aged-facies, decreased joint mobility and cardiovascular problems (Hennekam 2006; Merideth et al. 2008; Pereira et al. 2008). Most HGPS cases are caused by a silent mutation in the *LMNA* gene, which encodes two components of the nuclear envelope, the lamins A and C. Lamin A is synthesized as a precursor known as prelamin A, which undergoes a series of post-translational modifications including farnesylation, proteolytic removal of the C-terminal tripeptide, carboxyl methylation of the prenylated cysteine residue and finally, the excision of the 15-residue farnesylated peptide. The mutation present in HGPS patients activates a cryptic splicing site, and leads to the synthesis of a prelamin A isoform known as progerin or LAΔ50, which lacks a 50-residue long fragment containing the target sequence for the final proteolytic step and consequently remains constitutively farnesylated (De Sandre-Giovannoli et al. 2003; Eriksson et al. 2003).

The use of genetically modified mice allowed us to identify the zinc metalloprotease FACE-1 (also known as ZMPSTE24) as the enzyme responsible for the final proteolytic step during lamin A post-translational maturation (Pendas et al. 2002). Accordingly, *Face-1/Zmpste24*-deficient mice accumulate farnesylated prelamin A at the nuclear envelope and phenocopy human HGPS, providing a valuable animal model for the study of this pathology (Pendas et al. 2002; Bergo et al. 2002; Cadinanos et al. 2005; de Carlos et al. 2008). Using transcriptional profiling on tissues from this knockout model, we found that hyperactivation of p53 signalling plays a key role in the accelerated ageing phenotype, which is partially reversed by p53 deficiency (Varela et al. 2005). Moreover, the use of genetic approaches revealed that lowering the prelamin A levels results in a total rescue of this mouse model from the accelerated ageing condition (Varela et al. 2005; Fong et al. 2004; 2006b). Based on this information, we have performed preclinical studies to test anti-progeria pharmacological approaches aimed to prevent the accumulation of prenylated prelamin A isoforms (Varela et al. 2008).

Transgenic Res (2009) 18:7–15

Zmpste24-deficient mice as a model of accelerated ageing

The zinc metalloprotease FACE-1/ZMPSTE24 is an integral membrane protein highly conserved throughout evolution that shows widespread expression in mammalian tissues (Freije et al. 1999; Tam et al. 1998; Kumagai et al. 1999; Cadinanos et al. 2003). To investigate the biological roles of this enzyme, we used gene targeting to generate *Zmpste24*$^{-/-}$ mice (Pendas et al. 2002). *Zmpste24*-deficient mice are apparently normal at birth, but they show a striking accumulation of prelamin A at the nuclear envelope, which leads to frequent nuclear abnormalities at the cellular level. In turn, these molecular and cellular alterations lead to the development of severe age-related abnormalities at the organismal level, including loss of subcutaneous fat, reduced mobility due to skeletal and muscular defects, hair loss and metabolic alterations (Pendas et al. 2002; Bergo et al. 2002).

The subsequent identification of progerin as the molecular cause of HGPS (De Sandre-Giovannoli et al. 2003; Eriksson et al. 2003) revealed that a proteolytic defect explains the resemblance of the phenotype shown by *Zmpste24*-deficient mice to the clinical features characteristic of HGPS. Thus, whereas in *Zmpste24*$^{-/-}$ mice prenylated prelamin A accumulates due to the absence of the protease responsible for removing the C-terminal peptide that contains the prenyl-cysteine residue, the accumulation of progerin in HGPS is a consequence of the loss of the Zmpste24 target site in this prelamin A truncated isoform (Fig. 1). In addition, mutations in *ZMPSTE24* have also been found in several human progeroid syndromes, such as mandibuloacral dysplasia (MAD) and restrictive dermopathy (RD) (Agarwal et al. 2003; Navarro et al. 2005; Shackleton et al. 2005; Sander et al. 2008), providing additional support to the relevance of *Zmpste24*$^{-/-}$ mice as a model for studying accelerated ageing. Interestingly, accumulation of prenylated progerin has also been associated with normal ageing, a finding that expands considerably the interest of *Zmpste24*-deficient mice and other related animal models of progeria (Scaffidi and Misteli 2006).

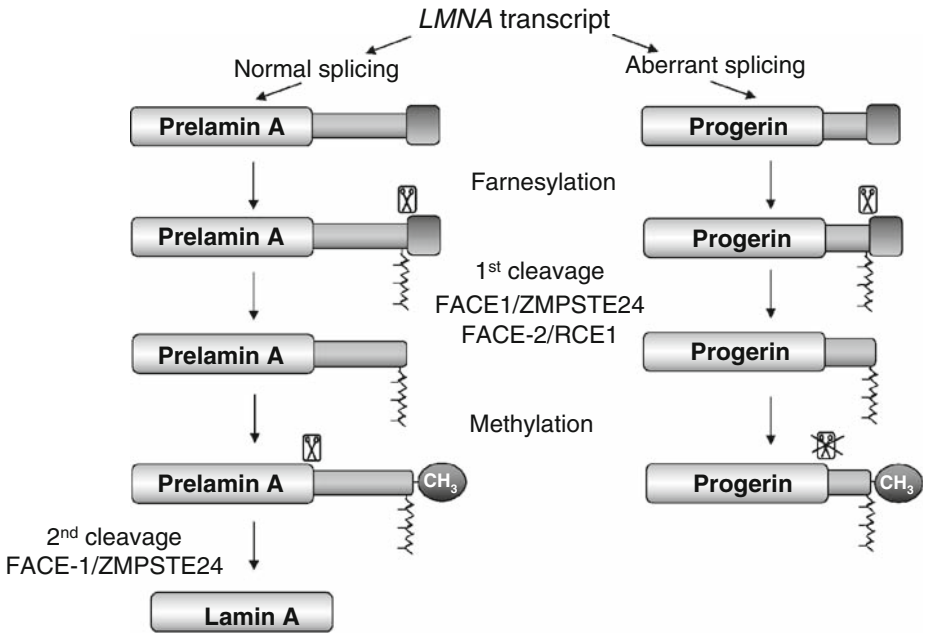

Fig. 1 Lamin A and progerin processing. In *Face-1/Zmpste24*-deficient mice, the absence of this metalloprotease causes the accumulation of farnesylated prelamin A. In HGPS cells, a C–T transition in the *LMNA* gene introduces a cryptic splicing site, leading to the synthesis of an alternatively spliced mRNA that encodes progerin, a truncated prelamin A variant that lacks the Face-1/Zmpste24 target sequence and remains constitutively farnesylated

Transcriptional and biochemical alterations in *Zmpste24*$^{-/-}$ progeroid mice

The accumulation of immature prenylated lamin forms (prelamin A and progerin) at the nuclear envelope produces severe alterations in its architecture, leading to frequent nuclear blebbing and fragmentation (Pendas et al. 2002). These alterations in nuclear architecture induced by prelamin A and progerin have also been linked to a defective recruitment of DNA repair factors and increased genomic instability (Liu et al. 2005). In agreement with these findings, transcriptional profiling of tissues from *Zmpste24*-deficient mice revealed a clear up-regulation of p53 target genes, which becomes more pronounced as the progeroid phenotype of these animals becomes more dramatic (Varela et al. 2005). Upregulation of p53 pathway seems to underlie the reduced proliferative capacity of adult *Zmpste24*-deficient fibroblasts and play a causal role in the accelerated ageing phenotype associated to prelamin A accumulation, as p53 deficiency results in a delay of the accelerated ageing process shown by *Zmpste24*$^{-/-}$ mice (Varela et al. 2005). The results derived from the use of this animal model are, at least partially, translatable to human as p53 activation has been detected in cells from RD and HGPS patients (Liu et al. 2006). Moreover, it has been reported that targeting progerin accumulation reverts overexpression of p53 targets in aged individuals (Scaffidi and Misteli 2006).

The persistence of ageing-related alterations in *Zmpste24*-deficient mice lacking p53 reveals that additional molecular mechanisms are involved in the phenotype developed by these mice. Some of these additional alterations seem to be part of a metabolic pro-survival strategy turned into a pro-ageing mechanism due to its chronic activation. This is the case of autophagy, the major lysosomal pathway for the turnover of cytoplasmic components. In contrast to the known decline of autophagy that results in the accumulation of damaged macromolecules during physiological ageing, progeroid mouse models exhibit a pronounced activation of autophagic proteolysis (Marino et al. 2008; Marino and Lopez-Otin 2008). Remarkably, we found that this alteration is also shared by other progeroid models which show alterations in DNA repair systems. Increased autophagy in *Zmpste24*-deficient mice is caused by a reduced activity of mTOR, which, in turn, is linked to activation of LKB1-AMPK signalling, transcriptional changes in key genes for lipid and glucose metabolism regulation, hypoglycemia and other alterations in serum factors such as leptin, insulin and adiponectin (Marino et al. 2008). These signalling alterations and their associated metabolic changes have been related to situations prolonging lifespan, such as calorie restriction (Vijg and Campisi 2008), and could be part of a response triggered by the nuclear abnormalities present in *Zmpste24*-deficient animals. However, the chronic activation of this pro-survival strategy can result in a pro-ageing effect that contributes to the progeroid phenotype of these mice (Marino et al. 2008). The apparently paradoxical activation of pro-longevity mechanisms in *Zmpste24*-deficient progeroid mice confers this animal model a special interest as a tool for investigating the potential undesirable effects of nutritional and pharmacological anti-ageing interventions and to develop complementary treatments to mitigate them.

Altered stem-cell biology in *Zmpste24*-deficient mice

The molecular alterations discussed in the previous paragraphs could have a special relevance on the accelerated ageing of *Zmpste24*-deficient organs and tissues if these alterations affect the stem cells responsible for their regenerative capacity. Physiological ageing has been associated with changes in the number and functionality of somatic stem cells (Campisi 2005; Rando 2006). Thus, the availability of *Zmpste24*-deficient mice allowed us to test the hypothesis that stem cell dysfunction could be similarly involved in accelerated ageing conditions. Using in vivo labelling, we observed a significant increase in the number of *Zmpste24*-deficient epidermal stem cells, accompanied by a reduction in their proliferative potential and an increase in apoptosis in their supporting cells (Espada et al. 2008). These abnormalities are associated with defects in signalling pathways such as Wnt-β-catenin, implicated in the functional regulation of epidermal stem cells, and microphtalmia transcription factor (Mitf), a master regulator of melanocyte stem cells (Espada et al. 2008). Remarkably, an independent but highly complementary study demonstrated in vitro that progerin interferes with the biology of human mesenchymal

Transgenic Res (2009) 18:7–15

stem cells (hMSCs) (Scaffidi and Misteli 2008), revealing that the stem cell dysfunction identified in the *Zmpste24*-deficient animal model also plays a role in human progeria. Taken together, these results suggest that the progeroid model of Zmpste24 protease deficiency could be used for in vivo testing of cell-based anti-progeroid therapies.

Zmpste24-deficient mice as a model for developing therapies against accelerated ageing

To investigate the role of unprocessed prelamin A in accelerated ageing, we designed a breeding program aimed at developing *Zmpste24*-deficient mice with reduced levels of prelamin A. This approach revealed that *Zmpste24*$^{-/-}$*Lmna*$^{+/-}$ mice show significantly reduced prelamin A levels and do not develop progeroid symptoms, demonstrating the role of prelamin A accumulation as the primary cause of the progeroid phenotype associated to *Zmpste24* deficiency (Varela et al. 2005; Fong et al. 2004). Parallel studies carried out using HGPS fibroblasts showed that accumulation of progerin plays an equivalent causal role in the cellular phenotype developed by these cells (Scaffidi and Misteli 2005). Moreover, these studies pointed to the reduction of progerin levels as an appropriate target to develop therapeutic approaches against HGPS. Surprisingly, genetic ablation of farnesyltransferase after birth does not lead to an accelerated ageing phenotype in mice, even though prenylation of prelamin A is a required step for its subsequent proteolytic processing (Mijimolle et al. 2005). This observation suggested that the toxicity of lamin A precursors depends on their prenylation status and pointed to the use of farnesyltransferase inhibitors (FTIs) as a potential treatment for these conditions (Cadinanos et al. 2005). Thus, several studies revealed that FTI treatment was capable of improving the nuclear abnormalities in several cellular models of progeria (Glynn and Glover 2005; Mallampalli et al. 2005; Yang et al. 2005; Toth et al. 2005; Capell et al. 2005).

Some in vivo benefit was also described in *Zmpste24*-deficient mice (Fong et al. 2006a), although further studies revealed that this treatment only produced a marginal (5%) reduction in prelamin A processing (Young et al. 2006). This low effectiveness at the molecular level could be explained by an alternative prenylation of prelamin A by geranylgeranyltransferase type I under FTI treatment (Fig. 2), as reported for other prenylated proteins such as K-Ras (Whyte et al. 1997). To address this question, we tested the effect of FTIs, alone or in combination with geranylgeranyltransferase inhibitors (GGTIs), on prelamin A processing in human cells. This approach revealed a synergistic action of FTIs and GGTIs, suggesting that prelamin A can be geranylgeranylated in the setting of farnesyltransferase inhibition (Varela et al. 2008). Furthermore, the use of mass

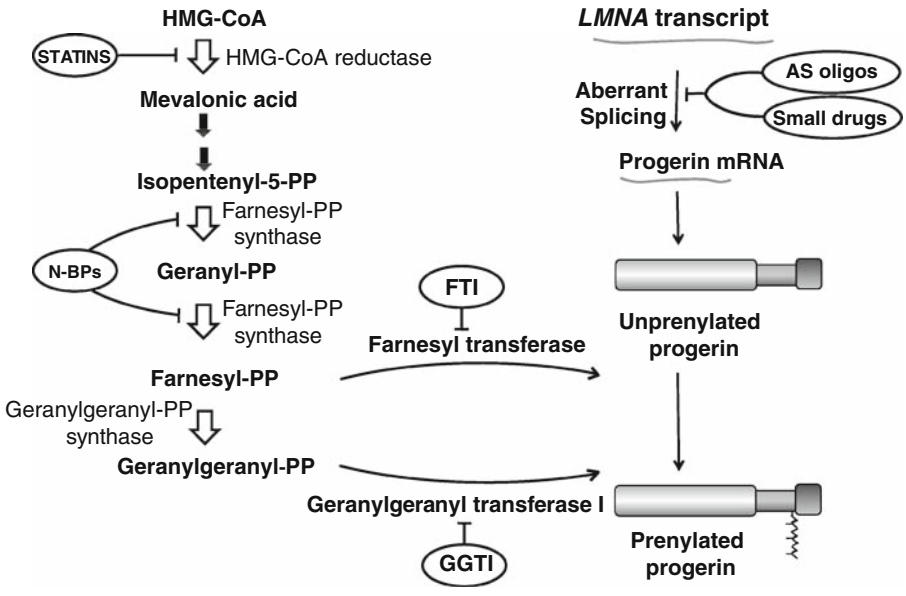

Fig. 2 Therapeutic options to prevent the accumulation of prenylated progerin. The possibilities discussed include compounds acting on the mevalonate pathway such as statins, and aminobisphosphonates (N-BPs), farnesyltransferase inhibitors (FTI), geranylgeranyltransferase inhibitors (GGTI), and agents designed to block the alternative splicing event that leads to progerin synthesis such as small drugs or specific antisense oligonucleotides (AS oligos)

spectrometry analysis of prelamin A derived from FTI-treated *Zmpste24*-deficient fibroblasts and progerin derived from HGPS cells provided direct evidence that these proteins are alternatively geranylgeranylated when farnesylation is inhibited, which could explain the low efficiency of FTIs in ameliorating the phenotypes of progeroid mouse models. In agreement with these findings, a combination of statins and aminobisphosphonates blocking several steps of the farnesyl pyrophosphate and geranylgeranyl pyrophosphate biosynthetic pathway, efficiently inhibited both farnesylation and geranylgeranylation of progerin and prelamin A and improved the ageing-like phenotypes of *Zmpste24*-deficient animals (Varela et al. 2008). Based on these results, a clinical trial to test this combination of drugs for the treatment of progeria has been recently approved.

Additional animal models for studying progeroid laminopathies

As discussed above, *Zmpste24*-deficient mice have constituted a crucial tool to explore the mechanisms underlying progeroid laminopathies and to design therapeutic approaches for their treatment, whereas other related animal models have confirmed or extended these findings. Thus, the so-called "lamin C only" mice, carrying a *Lmna* allele which fails to undergo the lamin A-specific splicing, have revealed that lamin A is dispensable in mice (Fong et al. 2006b). These studies have also provided additional evidence of the causative role of prelamin A accumulation in the progeroid phenotype of *Zmpste24*-deficient animals, thereby supporting the conclusions raised by using $Lmna^{+/-}$ animals (Varela et al. 2005). Similarly, knock-in mice carrying a "progerin-only" *Lmna* allele phenocopy many of the abnormalities present in *Zmpste24*-deficient animals, and show a modest amelioration upon FTI treatment (Yang et al. 2005; 2006; 2008b). Even though a knock-in mouse expressing the same mutant protein present in HGPS patients would be expected to be the ideal model for this disease, the reported "progerin-only" mice present some problems. First, the maintenance of the model has to rely on chimeras due to the fertility problems of the mice heterozygous for this mutation, making very difficult to generate enough animals to reach statistical significance in any study. Second, the expression levels of progerin and the ratio progerin/normal lamins A/C are different to those observed in HGPS patients. Third, the genomic sequences involved in the alternative splicing responsible for HGPS are absent in the "progerin-only" allele, precluding the use of this model to test therapeutic approaches such as specific oligonucleotides or small drugs designed to target this pathogenic splicing event (Fig. 2) (Scaffidi and Misteli 2005).

Remarkably, the recent information derived from two new *Lmna* knock-in models has validated important aspects of previous work with *Zmpste24*-deficient mice. Thus, Yang et al. have reported that mice with a *Lmna* allele encoding a non-prenylatable progerin (nHG) show substantially milder abnormalities and an extended longevity as compared to mice with a prenylatable "progerin-only" allele (Yang et al. 2008a). The amelioration observed in these mice is comparable to that obtained in *Zmpste24*-deficient animals treated with a combination of statins and aminobisphosphonates capable of blocking efficiently prelamin A prenylation (Varela et al. 2008). Moreover, this study has revealed that accumulation of non-prenylated progerin also causes accelerated ageing symptoms, suggesting that therapeutic approaches based on blocking progerin prenylation may require complementary interventions to reach a complete efficacy (Yang et al. 2008a). Finally, Davies et al., have described a *Lmna* knock-in allele encoding a geranylgeranylated progerin that also causes a progeroid phenotype, providing a formal demonstration of the toxicity of this alternatively modified protein (Davies et al. 2008), and supporting the conclusions derived from mass spectrometry analysis of FTI-treated *Zmpste24*-deficient and HGPS cells (Varela et al. 2008).

Besides the knock-in mice discussed above, several transgenic models of progeria have also been developed. Thus, Varga et al. (2006) have developed a transgenic mouse strain carrying a 164-kb bacterial artificial chromosome containing an LMNA allele with the HGPS point mutation. These transgenic mice suffer important vascular alterations, which constitute the most common cause of death for HGPS patients, but they do not show any other progeroid phenotype, limiting their utility as a model of accelerated ageing. The epidermal alterations characteristic of progeroid laminopathies have prompted other authors to develop transgenic models expressing progerin in keratinocytes. Thus, mice expressing FLAG-tagged human

progerin under the control of a keratin 14 promoter have abnormal morphology of keratinocyte nuclei, but they do not show any skin pathology (Wang et al. 2008). In contrast, doxycycline-regulated transgenic mice (tet-off) expressing human progerin under a keratin 5 promoter develop dental and skin alterations which are reversed upon suppression of the transgene expression (Sagelius et al. 2008a; b). The reasons for the apparent discrepancies between these two works are currently unclear, and can be related to subtle differences in the spatio-temporal pattern of expression of the transgene in both systems.

Future models and perspectives

As discussed above, several knock-out, knock-in and transgenic animal models have been used to investigate the role of alterations in the prelamin A post-translational maturation in accelerated ageing and to develop therapeutic strategies against progeroid symptoms. All these models have provided valuable information on the biological relevance of prelamin A maturation. However, important questions remain to be answered, concerning aspects such as the relative contribution to the progeroid phenotype of cell-autonomous versus systemic alterations. The investigation of this important aspect will be facilitated by the use of inducible systems, similar to the tet-off system used to direct progerin expression to keratinocytes, but designed to express prelamin A or progerin in other organs and tissues with a decisive role in the clinical manifestations of accelerated and physiological ageing. New animal models are also required to test in vivo anti-progeria therapies, since none of the currently available mice are appropriate to test approaches such as those targeting the alternative splicing responsible for progerin production. Lmna knock-in mice carrying an allele with the complete genomic sequence involved in this splicing event will probably be the ideal model to investigate this type of interventions. Finally, animal models will predictably play a key role as tools for investigating not only the implications of the Zmpste24/lamin A system in accelerated and physiological ageing, but also in other important processes such as cancer. In this regard, recent work illustrates the relevance of this system in cancer and supports its interest as target of anti-cancer therapies (Willis et al. 2008), an aspect that will be the subject of future studies based on the use of currently available and newly developed animal models. In summary, the use of genetically modified mice has allowed investigating the molecular mechanisms underlying progeroid laminopathies and has lead, in a very short period of time, to clinical trials for testing rationally designed treatments against these dramatic diseases. Nevertheless, important aspects remain unsolved that will require further investigations based on currently available and newly developed animal models.

Acknowledgments We thank I. Varela, X.S. Puente, J. Cadiñanos and G. Velasco for helpful comments and advice. This work was supported by grants from Ministerio de Educación y Ciencia-Spain, Fundación "La Caixa", Fundación "M. Botín", and the European Union (FP6 CancerDegradome and FP7 Microenvimet). The Instituto Universitario de Oncología is supported by Obra Social Cajastur-Asturias.

References

Agarwal AK, Fryns JP, Auchus RJ, Garg A (2003) Zinc metalloproteinase, ZMPSTE24, is mutated in mandibuloacral dysplasia. Hum Mol Genet 12:1995–2001. doi:10.1093/hmg/ddg213

Bergo MO, Gavino B, Ross J, Schmidt WK, Hong C, Kendall LV, Mohr A, Meta M, Genant H, Jiang Y, Wisner ER, Van Bruggen N, Carano RA, Michaelis S, Griffey SM, Young SG (2002) Zmpste24 deficiency in mice causes spontaneous bone fractures, muscle weakness, and a prelamin A processing defect. Proc Natl Acad Sci USA 99:13049–13054. doi:10.1073/pnas.192460799

Cadinanos J, Schmidt WK, Fueyo A, Varela I, Lopez-Otin C, Freije JM (2003) Identification, functional expression and enzymic analysis of two distinct CaaX proteases from *Caenorhabditis elegans*. Biochem J 370:1047–1054. doi:10.1042/BJ20021514

Cadinanos J, Varela I, Lopez-Otin C, Freije JM (2005) From immature lamin to premature aging: molecular pathways and therapeutic opportunities. Cell Cycle 4:1732–1735

Campisi J (2005) Senescent cells, tumor suppression, and organismal aging: good citizens, bad neighbors. Cell 120:513–522. doi:10.1016/j.cell.2005.02.003

Capell BC, Erdos MR, Madigan JP, Fiordalisi JJ, Varga R, Conneely KN, Gordon LB, Der CJ, Cox AD, Collins FS (2005) Inhibiting farnesylation of progerin prevents the characteristic nuclear blebbing of Hutchinson-Gilford progeria syndrome. Proc Natl Acad Sci USA 102:12879–12884. doi:10.1073/pnas.0506001102

Chang S, Multani AS, Cabrera NG, Naylor ML, Laud P, Lombard D, Pathak S, Guarente L, DePinho RA (2004) Essential role of limiting telomeres in the pathogenesis of Werner syndrome. Nat Genet 36:877–882. doi:10.1038/ng1389

Cox LS, Faragher RG (2007) From old organisms to new molecules: integrative biology and therapeutic targets in

accelerated human ageing. Cell Mol Life Sci 64:2620–2641. doi:10.1007/s00018-007-7123-x

Davies BS, Yang SH, Farber E, Lee R, Buck SB, Andres DA, Peter Spielmann H, Agnew BJ, Tamanoi F, Fong LG, Young SG (2008) Increasing the length of progerin's isoprenyl anchor does not worsen bone disease or survival in mice with Hutchinson-Gilford progeria syndrome. J Lipid Res. doi:10.1194/jlr.M800424-JLR200

de Carlos F, Varela I, Germana A, Montalbano G, Freije J, Vega J, López-Otin C, Cobo J (2008) Microcephalia with mandibular and dental dysplasia in adult Zmpste24 deficient mice. J Anat 213:509–519. doi:10.1111/j.1469-7580.2008.00970.x

De Sandre-Giovannoli A, Bernard R, Cau P, Navarro C, Amiel J, Boccaccio I, Lyonnet S, Stewart CL, Munnich A, Le Merrer M, Levy N (2003) Lamin A truncation in Hutchinson-Gilford progeria. Science 300:2055. doi:10.1126/science.1084125

Eriksson M, Brown WT, Gordon LB, Glynn MW, Singer J, Scott L, Erdos MR, Robbins CM, Moses TY, Berglund P, Dutra A, Pak E, Durkin S, Csoka AB, Boehnke M, Glover TW, Collins FS (2003) Recurrent de novo point mutations in lamin A cause Hutchinson-Gilford progeria syndrome. Nature 423:293–298. doi:10.1038/nature01629

Espada J, Varela I, Flores I, Ugalde AP, Cadinanos J, Pendas AM, Stewart CL, Tryggvason K, Blasco MA, Freije JM, Lopez-Otin C (2008) Nuclear envelope defects cause stem cell dysfunction in premature-aging mice. J Cell Biol 181:27–35. doi:10.1083/jcb.200801096

Fong LG, Ng JK, Meta M, Cote N, Yang SH, Stewart CL, Sullivan T, Burghardt A, Majumdar S, Reue K, Bergo MO, Young SG (2004) Heterozygosity for Lmna deficiency eliminates the progeria-like phenotypes in Zmpste24-deficient mice. Proc Natl Acad Sci USA 101:18111–18116. doi:10.1073/pnas.0408558102

Fong LG, Frost D, Meta M, Qiao X, Yang SH, Coffinier C, Young SG (2006a) A protein farnesyltransferase inhibitor ameliorates disease in a mouse model of progeria. Science 311:1621–1623. doi:10.1126/science.1124875

Fong LG, Ng JK, Lammerding J, Vickers TA, Meta M, Cote N, Gavino B, Qiao X, Chang SY, Young SR, Yang SH, Stewart CL, Lee RT, Bennett CF, Bergo MO, Young SG (2006b) Prelamin A and lamin A appear to be dispensable in the nuclear lamina. J Clin Invest 116:743–752. doi:10.1172/JCI27125

Freije JM, Blay P, Pendas AM, Cadinanos J, Crespo P, Lopez-Otin C (1999) Identification and chromosomal location of two human genes encoding enzymes potentially involved in proteolytic maturation of farnesylated proteins. Genomics 58:270–280. doi:10.1006/geno.1999.5834

Glynn MW, Glover TW (2005) Incomplete processing of mutant lamin A in Hutchinson-Gilford progeria leads to nuclear abnormalities, which are reversed by farnesyltransferase inhibition. Hum Mol Genet 14:2959–2969. doi:10.1093/hmg/ddi326

Hennekam RC (2006) Hutchinson-Gilford progeria syndrome: review of the phenotype. Am J Med Genet A 140:2603–2624. doi:10.1002/ajmg.a.31346

Kirkwood TB (2005) Understanding the odd science of aging. Cell 120:437–447. doi:10.1016/j.cell.2005.01.027

Kumagai H, Kawamura Y, Yanagisawa K, Komano H (1999) Identification of a human cDNA encoding a novel protein structurally related to the yeast membrane-associated metalloprotease, Ste24p. Biochim Biophys Acta 1426:468–474

Liu B, Wang J, Chan KM, Tjia WM, Deng W, Guan X, Huang JD, Li KM, Chau PY, Chen DJ, Pei D, Pendas AM, Cadinanos J, Lopez-Otin C, Tse HF, Hutchison C, Chen J, Cao Y, Cheah KS, Tryggvason K, Zhou Z (2005) Genomic instability in laminopathy-based premature aging. Nat Med 11:780–785. doi:10.1038/nm1266

Liu Y, Rusinol A, Sinensky M, Wang Y, Zou Y (2006) DNA damage responses in progeroid syndromes arise from defective maturation of prelamin A. J Cell Sci 119:4644–4649. doi:10.1242/jcs.03263

Lombard DB, Beard C, Johnson B, Marciniak RA, Dausman J, Bronson R, Buhlmann JE, Lipman R, Curry R, Sharpe A, Jaenisch R, Guarente L (2000) Mutations in the WRN gene in mice accelerate mortality in a p53-null background. Mol Cell Biol 20:3286–3291. doi:10.1128/MCB.20.9.3286-3291.2000

Mallampalli MP, Huyer G, Bendale P, Gelb MH, Michaelis S (2005) Inhibiting farnesylation reverses the nuclear morphology defect in a HeLa cell model for Hutchinson-Gilford progeria syndrome. Proc Natl Acad Sci USA 102:14416–14421. doi:10.1073/pnas.0503712102

Marino G, Lopez-Otin C (2008) Autophagy and aging: new lessons from progeroid mice. Autophagy 4:807–809

Marino G, Ugalde AP, Salvador-Montoliu N, Varela I, Quiros PM, Cadinanos J, van der Pluijm I, Freije JM, Lopez-Otin C (2008) Premature aging in mice activates a systemic metabolic response involving autophagy induction. Hum Mol Genet 17:2196–2211. doi:10.1093/hmg/ddn120

Merideth MA, Gordon LB, Clauss S, Sachdev V, Smith AC, Perry MB, Brewer CC, Zalewski C, Kim HJ, Solomon B, Brooks BP, Gerber LH, Turner ML, Domingo DL, Hart TC, Graf J, Reynolds JC, Gropman A, Yanovski JA, Gerhard-Herman M, Collins FS, Nabel EG, Cannon RO 3rd, Gahl WA, Introne WJ (2008) Phenotype and course of Hutchinson-Gilford progeria syndrome. N Engl J Med 358:592–604. doi:10.1056/NEJMoa0706898

Mijimolle N, Velasco J, Dubus P, Guerra C, Weinbaum CA, Casey PJ, Campuzano V, Barbacid M (2005) Protein farnesyltransferase in embryogenesis, adult homeostasis, and tumor development. Cancer Cell 7:313–324. doi:10.1016/j.ccr.2005.03.004

Multani AS, Chang S (2007) WRN at telomeres: implications for aging and cancer. J Cell Sci 120:713–721. doi:10.1242/jcs.03397

Navarro CL, Cadinanos J, De Sandre-Giovannoli A, Bernard R, Courrier S, Boccaccio I, Boyer A, Kleijer WJ, Wagner A, Giuliano F, Beemer FA, Freije JM, Cau P, Hennekam RC, Lopez-Otin C, Badens C, Levy N (2005) Loss of ZMPSTE24 (FACE-1) causes autosomal recessive restrictive dermopathy and accumulation of lamin A precursors. Hum Mol Genet 14:1503–1513. doi:10.1093/hmg/ddi159

Pendas AM, Zhou Z, Cadinanos J, Freije JM, Wang J, Hultenby K, Astudillo A, Wernerson A, Rodriguez F, Tryggvason K, Lopez-Otin C (2002) Defective prelamin A processing and muscular and adipocyte alterations in

Zmpste24 metalloproteinase-deficient mice. Nat Genet 31:94–99

Pereira S, Bourgeois P, Navarro C, Esteves-Vieira V, Cau P, De Sandre-Giovannoli A, Levy N (2008) HGPS and related premature aging disorders: from genomic identification to the first therapeutic approaches. Mech Ageing Dev 129:449–459. doi:10.1016/j.mad.2008.04.003

Ramirez CL, Cadinanos J, Varela I, Freije JM, Lopez-Otin C (2007) Human progeroid syndromes, aging and cancer: new genetic and epigenetic insights into old questions. Cell Mol Life Sci 64:155–170. doi:10.1007/s00018-006-6349-3

Rando TA (2006) Stem cells, ageing and the quest for immortality. Nature 441:1080–1086. doi:10.1038/nature04958

Sagelius H, Rosengardten Y, Hanif M, Erdos MR, Rozell B, Collins FS, Eriksson M (2008a) Targeted transgenic expression of the mutation causing Hutchinson-Gilford progeria syndrome leads to proliferative and degenerative epidermal disease. J Cell Sci 121:969–978. doi:10.1242/jcs.022913

Sagelius H, Rosengardten Y, Schmidt E, Sonnabend C, Rozell B, Eriksson M (2008b) Reversible phenotype in a mouse model of Hutchinson-Gilford progeria syndrome. J Med Genet. doi:10.1136/jmg.2008.060772

Sander CS, Salman N, van Geel M, Broers JL, Al-Rahmani A, Chedid F, Hausser I, Oji V, Al Nuaimi K, Berger TG, Verstraeten VL (2008) A newly identified splice site mutation in ZMPSTE24 causes restrictive dermopathy in the middle East. Br J Dermatol 159:961–967. doi:10.1111/j.1365-2133.2008.08772.x

Scaffidi P, Misteli T (2005) Reversal of the cellular phenotype in the premature aging disease Hutchinson-Gilford progeria syndrome. Nat Med 11:440–445. doi:10.1038/nm1204

Scaffidi P, Misteli T (2006) Lamin A-dependent nuclear defects in human aging. Science 312:1059–1063. doi:10.1126/science.1127168

Scaffidi P, Misteli T (2008) Lamin A-dependent misregulation of adult stem cells associated with accelerated ageing. Nat Cell Biol 10:452–459. doi:10.1038/ncb1708

Shackleton S, Smallwood DT, Clayton P, Wilson LC, Agarwal AK, Garg A, Trembath RC (2005) Compound heterozygous ZMPSTE24 mutations reduce prelamin A processing and result in a severe progeroid phenotype. J Med Genet 42:e36. doi:10.1136/jmg.2004.029751

Tam A, Nouvet FJ, Fujimura-Kamada K, Slunt H, Sisodia SS, Michaelis S (1998) Dual roles for Ste24p in yeast a-factor maturation: NH2-terminal proteolysis and COOH-terminal CAAX processing. J Cell Biol 142:635–649. doi:10.1083/jcb.142.3.635

Toth JI, Yang SH, Qiao X, Beigneux AP, Gelb MH, Moulson CL, Miner JH, Young SG, Fong LG (2005) Blocking protein farnesyltransferase improves nuclear shape in fibroblasts from humans with progeroid syndromes. Proc Natl Acad Sci USA 102:12873–12878. doi:10.1073/pnas.0505767102

Varela I, Cadinanos J, Pendas AM, Gutierrez-Fernandez A, Folgueras AR, Sanchez LM, Zhou Z, Rodriguez FJ, Stewart CL, Vega JA, Tryggvason K, Freije JM, Lopez-Otin C (2005) Accelerated ageing in mice deficient in Zmpste24 protease is linked to p53 signalling activation. Nature 437:564–568. doi:10.1038/nature04019

Varela I, Pereira S, Ugalde AP, Navarro CL, Suarez MF, Cau P, Cadinanos J, Osorio FG, Foray N, Cobo J, de Carlos F, Levy N, Freije JM, Lopez-Otin C (2008) Combined treatment with statins and aminobisphosphonates extends longevity in a mouse model of human premature aging. Nat Med 14:767–772. doi:10.1038/nm1786

Varga R, Eriksson M, Erdos MR, Olive M, Harten I, Kolodgie F, Capell BC, Cheng J, Faddah D, Perkins S, Avallone H, San H, Qu X, Ganesh S, Gordon LB, Virmani R, Wight TN, Nabel EG, Collins FS (2006) Progressive vascular smooth muscle cell defects in a mouse model of Hutchinson-Gilford progeria syndrome. Proc Natl Acad Sci USA 103:3250–3255. doi:10.1073/pnas.0600012103

Vijg J, Campisi J (2008) Puzzles, promises and a cure for ageing. Nature 454:1065–1071. doi:10.1038/nature07216

Wang Y, Panteleyev AA, Owens DM, Djabali K, Stewart CL, Worman HJ (2008) Epidermal expression of the truncated prelamin A causing Hutchinson-Gilford progeria syndrome: effects on keratinocytes, hair and skin. Hum Mol Genet 17:2357–2369. doi:10.1093/hmg/ddn136

Whyte DB, Kirschmeier P, Hockenberry TN, Nunez-Oliva I, James L, Catino JJ, Bishop WR, Pai JK (1997) K- and N-Ras are geranylgeranylated in cells treated with farnesyl protein transferase inhibitors. J Biol Chem 272:14459–14464. doi:10.1074/jbc.272.22.14459

Willis ND, Cox TR, Rahman-Casans SF, Smits K, Przyborski SA, van den Brandt P, van Engeland M, Weijenberg M, Wilson RG, de Bruine A, Hutchison CJ (2008) Lamin A/C is a risk biomarker in colorectal cancer. PLoS ONE 3:e2988. doi:10.1371/journal.pone.0002988

Yang SH, Bergo MO, Toth JI, Qiao X, Hu Y, Sandoval S, Meta M, Bendale P, Gelb MH, Young SG, Fong LG (2005) Blocking protein farnesyltransferase improves nuclear blebbing in mouse fibroblasts with a targeted Hutchinson-Gilford progeria syndrome mutation. Proc Natl Acad Sci USA 102:10291–10296. doi:10.1073/pnas.0504641102

Yang SH, Meta M, Qiao X, Frost D, Bauch J, Coffinier C, Majumdar S, Bergo MO, Young SG, Fong LG (2006) A farnesyltransferase inhibitor improves disease phenotypes in mice with a Hutchinson-Gilford progeria syndrome mutation. J Clin Invest 116:2115–2121. doi:10.1172/JCI28968

Yang SH, Andres DA, Spielmann HP, Young SG, Fong LG (2008a) Progerin elicits disease phenotypes of progeria in mice whether or not it is farnesylated. J Clin Invest 118:3291–3300. doi:10.1172/JCI35876

Yang SH, Qiao X, Fong LG, Young SG (2008b) Treatment with a farnesyltransferase inhibitor improves survival in mice with a Hutchinson-Gilford progeria syndrome mutation. Biochim Biophys Acta 1781:36–39

Young SG, Meta M, Yang SH, Fong LG (2006) Prelamin A farnesylation and progeroid syndromes. J Biol Chem 281:39741–39745. doi:10.1074/jbc.R600033200

Yu CE, Oshima J, Fu YH, Wijsman EM, Hisama F, Alisch R, Matthews S, Nakura J, Miki T, Ouais S, Martin GM, Mulligan J, Schellenberg GD (1996) Positional cloning of the Werner's syndrome gene. Science 272:258–262. doi:10.1126/science.272.5259.258

1710 Biochemical Society Transactions (2011) Volume 39, part 6

Biochemical Society Transactions www.biochemsoctrans.org

Cell autonomous and systemic factors in progeria development

Fernando G. Osorio, Alejandro P. Ugalde, Guillermo Mariño, Xose S. Puente, José M.P. Freije and Carlos López-Otín[1]
Departamento de Bioquímica y Biología Molecular, Facultad de Medicina, Instituto Universitario de Oncología, Universidad de Oviedo, 33006-Oviedo, Spain

Abstract

Progeroid laminopathies are accelerated aging syndromes caused by defects in nuclear envelope proteins. Accordingly, mutations in the *LMNA* gene and functionally related genes have been described to cause HGPS (Hutchinson–Gilford progeria syndrome), MAD (mandibuloacral dysplasia) or RD (restrictive dermopathy). Functional studies with animal and cellular models of these syndromes have facilitated the identification of the molecular alterations and regulatory pathways involved in progeria development. We have recently described a novel regulatory pathway involving *miR-29* and p53 tumour suppressor which has provided valuable information on the molecular components orchestrating the response to nuclear damage stress. Furthermore, by using progeroid mice deficient in ZMPSTE24 (zinc metalloprotease STE24 homologue) involved in lamin A maturation, we have demonstrated that, besides these abnormal cellular responses to stress, dysregulation of the somatotropic axis is responsible for some of the alterations associated with progeria. Consistent with these observations, pharmacological restoration of the somatotroph axis in these mice delays the onset of their progeroid features, significantly extending their lifespan and supporting the importance of systemic alterations in progeria progression. Finally, we have very recently identified a novel progeroid syndrome with distinctive features from HGPS and MAD, which we have designated NGPS (Néstor–Guillermo progeria syndrome) (OMIM #614008). This disorder is caused by a mutation in *BANF1*, a gene encoding a protein with essential functions in the assembly of the nuclear envelope, further illustrating the importance of the nuclear lamina integrity for human health and providing additional support to the study of progeroid syndromes as a valuable source of information on human aging.

Introduction

The nuclear envelope is a complex structure that surrounds and protects the genome, playing essential roles in its regulation, organization and maintenance [1]. The nuclear envelope is composed of two membrane bilayers with nuclear pores that control traffic in and out the nucleus [2,3]. The nuclear face of the inner membrane is covered by the nuclear lamina, a protein network that provides scaffold for nuclear envelope proteins and chromatin [4]. In humans, three genes named *LMNA*, *LMNB1* and *LMNB2* encode nuclear lamins. Whereas the two B-type lamins are encoded by two independent genes, *LMNB1* and *LMNB2*, the *LMNA* gene encodes lamin A and lamin C proteins by alternative splicing. Mutations in A-type lamins, lamin B and several lamin-binding proteins (emerin, MAN1 and lamin B receptor) have been found mutated in different human diseases which are collectively known as laminopathies [5]. The range, diversity and tissue-specificity of laminopathy phenotypes are providing valuable clues about the cellular functions of lamins and lamin-related proteins.

Key words: alternative splicing, laminopathy, microRNA (miRNA), progeria, senescence, tumour suppressor.

Abbreviations used: BAF, barrier to autointegration factor 1; FACE1, farnesylated proteins-converting enzyme 1; GH, growth hormone; HGPS, Hutchinson–Gilford progeria syndrome; IGF-1, insulin-like growth factor 1; miRNA, microRNA; NGPS, Néstor–Guillermo progeria syndrome; rIGF-1, recombinant IGF-1; ZMPSTE24, zinc metalloprotease STE24 homologue.

[1]To whom correspondence should be addressed (email clo@uniovi.es).

Progeroid laminopathies are human syndromes of accelerated aging caused by defects in the nuclear lamina [6,7]. Among them, HGPS (Hutchinson–Gilford progeria syndrome) is the best known. Affected patients show growth impairment, lipodystrophy, dermal and bone abnormalities and cardiovascular alterations, leading to a shortened lifespan [8–10]. HGPS is caused in most cases by a *de novo* point mutation within exon 11 of the *LMNA* gene encoding lamin A (c.1824C>T; p.G608G) [11,12]. Lamin A undergoes a complex maturation process, including the addition of a farnesyl group and a proteolytic processing event carried out by the metalloprotease ZMPSTE24 (zinc metalloprotease STE24 homologue)/FACE1 (farnesylated proteins-converting enzyme 1) [13]. The G608G mutation activates a cryptic splicing donor site, leading to the accumulation of a truncated form of prelamin A, called LAΔ50 or progerin, which lacks a 50-residue-long fragment containing the target sequence for the final proteolytic step carried out by ZMPSTE24/FACE1. Consequently, this aberrant lamin A isoform remains constitutively farnesylated [14,15].

The use of cellular and murine models of progeroid laminopathies [14–19] has provided valuable information about the molecular alterations involved in progeria, such as the involvement of the p53 tumour suppressor [20], the altered biology of adult stem cells [21] or the presence of metabolic alterations [22,23]. These studies have allowed the

development of the first therapeutic approaches for patients with HGPS [24–28]. Currently, two clinical trials are being carried out based on a combination of statins and amino bisphosphonates, alone or complemented with a low dose of a farnesyltransferase inhibitor (http://clinicaltrials.gov; NCT00731016 and NCT00916747).

Although murine models of progeroid laminopathies have been essential for understanding the pathways and alterations that drive progeria development, important questions remain to be answered, especially those related to the regulatory mechanisms that control and integrate the altered pathways, the specific contribution of cellular and systemic alterations to the progeroid phenotype, as well as the specific function of each nuclear lamina component. In this regard, three recent reports from our laboratory have shed light on these points, highlighting the importance of nuclear envelope for human health [28–30].

An *miR-29*/p53 regulatory circuit involved in aging and chronic DNA damage response

A common feature of aging is the progressive accumulation of cellular damage. Several stressors have been proposed to contribute to this situation, such as oxidative reactions, telomere attrition or the decline of DNA repair and protein turnover systems [31,32]. Progeroid syndromes associated with lamin A alterations show genomic instability as a consequence of the nuclear envelope disruption [33]. This stress triggers a series of cellular and systemic events directed to the restoration of cellular and organismal homoeostasis, which are ultimately responsible for many of the alterations characteristic of these syndromes. In this regard, important changes in chromatin organization and transcriptional profiles have been described in murine models of HGPS [20,34], but little is known about the molecular components that orchestrate these changes.

Over the last decade, miRNAs (microRNAs) have emerged as a new and fundamental level of gene regulation. Each miRNA has the potential ability to repress the translation of hundreds of transcripts and their impact on a great number of cellular processes has been broadly proved. To explore the possible involvement of miRNAs in progeria development, we have performed a miRNA transcriptome analysis in the liver of *Zmpste24*-deficient mice [29]. Among the differentially expressed miRNAs, three of them (*miR-29a*, *miR-29b* and *miR-29c*), belonging to the *miR-29* family, are significantly up-regulated in tissues of *Zmpste24* progeroid-knockout mice.

Through a series of functional analysis, we have found that *miR-29* plays a pivotal role in the regulation of cell survival and proliferation through the modulation of the DNA damage response in a p53-dependent way. Thus the p53-mediated activation of the DNA damage response in *Zmpste24*-deficient cells [35] would trigger multiple effector pathways, including an increase in *miR-29* expression (Figure 1). Among the potential targets of

Figure 1. | **Cellular and systemic alterations involved in progeroid laminopathies**

The accumulation of farnesylated forms of prelamin A at the nuclear envelope causes severe alterations in nuclear dynamics, triggering an adaptive response aimed at preserving organism viability under compromising circumstances. At a cellular level, the p53 signalling pathway orchestrates a chronic DNA damage response that involves *miR-29* transcriptional activation. Thus *miR-29*-mediated repression of *Ppm1d* phosphatase reinforces this stress response, favouring a decrease in cellular proliferation rates accompanied by an increase in apoptosis and senescence. These processes result in the loss of tissue and organism homoeostasis. In parallel, a chronic stress response cause changes in the transcriptional profiles of several somatotroph axis key regulators, such as *Igfbp1* (IGF-binding protein 1), *Socs2* (suppressor of cytokine signalling 2), *miR-1* or *Igfals* (IGF-binding protein, acid-labile subunit). These alterations dramatically reduce the levels of circulating IGF-1, which, together with the increased production of GH at the pituitary gland, favours a systemic metabolic switch towards somatic maintenance at the expense of somatic growth.

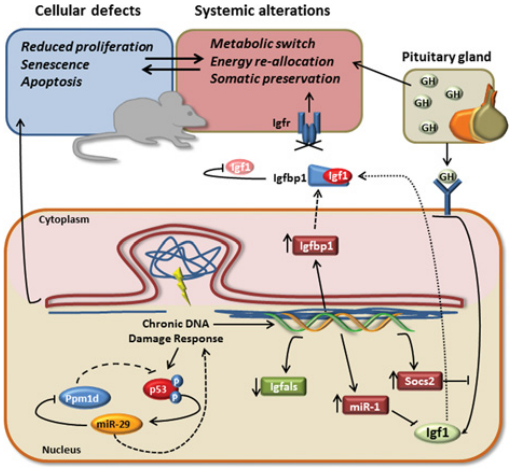

miR-29, Ppm1d/Wip1 phosphatase has been proposed as the key mediator for this effect. Ppm1d is a phosphatase that acts as a negative regulator of DNA damage response by dephosphorylating important components of this process such as p53, Chk1 (checkpoint kinase 1), Chk2 (checkpoint kinase 2), p38, γ-H2AX (phosphorylated histone H2AX) or ATM (ataxia telangiectasia mutated) [36,37]. Thus a decrease in Ppm1d levels mediated by *miR-29* would contribute to the activation of the DNA damage response. In agreement with these results, *miR-29* has been described as a tumour-suppressor miRNA in several human cancers. This tumour-suppressive function could be consistent with a pro-aging role for this miRNA, since a growing number of tumour-suppressor genes have been reported to be aging promoters, which could be illustrative examples of the antagonistic pleiotropy phenomenon [38].

Somatotroph suppression in *Zmpste24*-deficient mice

Although the dynamics of aging are far from being completely understood, our knowledge of the systemic factors involved in this process has considerably increased in recent years [39–41]. Somatotroph signalling has been identified as a major regulator of longevity from nematodes to humans [42]. Paradoxically, studies in different organisms have shown that the reduction of this signalling is a common feature of both long-lived model organisms and different progeroid mice [43,44].

In this sense, *Zmpste24*-deficient mice show a profound dysregulation of GH (growth hormone)/IGF-1 (insulin-like growth factor 1) balance, with a progressive reduction of blood IGF-1 levels, accompanied by a progressive increase in GH levels and a marked transcriptional alterations in key genes for somatotroph signalling [28] (Figure 1). Thus somatotroph alterations would be responsible for important features of progeroid phenotype such as reduced growth rate and body size. In this case, the observed alterations in somatotropic axis seem to constitute a detrimental phenomenon, rather than a successful adaptive strategy, as demonstrated by the fact that the treatment of *Zmpste24*-deficient mice with rIGF-1 (recombinant IGF-1) is able to ameliorate some of the progeroid features of these mice. rIGF-1-treated mice showed improved body weight, increased amounts of subcutaneous fat deposits, reduced degree of lordokyphosis and alopecia, and significantly extended longevity. Accordingly, rIGF-1 treatment could be a therapeutic approach to slow down disease progression in children with progeria [45].

Interestingly, many pathological features of GH resistance, also known as Laron syndrome, are characteristic of progeroid mice. Both *Zmpste24*$^{-/-}$ mice and patients with this syndrome show reduced muscle development, strength and endurance, as well as decreased bone mineral density, alopecia, skin atrophy and hypoglycaemia [14,22,46]. Some of these alterations could be consequence of an adaptive stress response aimed at preserving organism viability under compromising circumstances by reallocating resources from growth to somatic preservation. In *Zmpste24*-knockout mice, this systemic response could represent an attempt to reduce replication defects, chromosomal instability, nuclear envelope abnormalities and, finally, the risk of developing cancer by decreasing metabolic activity. This hypothesis is supported by the fact that patients with Laron syndrome or other somatotroph-related pathologies such as GH receptor deficiency exhibit a notable reduction in the incidence of malignancies [47,48].

NGPS, a new hereditary progeroid syndrome caused by *BANF1* mutation

The recent availability of high-throughput sequencing technologies has made it possible to address personal genome projects that could uncover the precise causes of human genetic diseases [49,50]. Thus exome sequencing of two unrelated patients that exhibit a progeroid syndrome without mutations in *LMNA* or *ZMPSTE24* has allowed the identification of a homozygous mutation in *BANF1* (c.34G>C; p.A12T), encoding BAF (barrier to autointegration factor 1), as the molecular abnormality responsible for this syndrome [30].

Affected patients of this disease, called NGPS (Néstor–Guillermo progeria syndrome) (OMIM #614008), partially phenocopy HGPS and MAD (mandibuloacral dysplasia), but also exhibit distinctive features, including the absence of cardiovascular alterations and metabolic anomalies, a very severe osteolysis and a relatively long lifespan of affected individuals [51]. NGPS can be considered as a chronic progeria because of its early onset but slow clinical course, which leads to a relatively long survival of patients.

BAF is a small protein (89 amino acids) highly conserved among metazoans [52,53]. BAF binds directly to double-stranded DNA, chromatin, nuclear lamina proteins (including lamin A and emerin), histones and transcription factors, these being required for higher-order organization of chromatin, nuclear envelope assembly, retrovirus infectivity and transcription of specific genes [54].

The A12T mutation in NGPS patients affects a highly conserved residue located at the surface of the protein, decreasing its stability. Skin fibroblasts from these patients show very low protein levels of BAF compared with control fibroblasts and exhibit profound nuclear abnormalities, including blebs and other aberrations associated with progeroid laminopathies. In fact, BAF reduction is correlated with mislocalization of emerin, which shows a predominant cytoplasmic localization in mutant cells. Taken together, these findings demonstrate the relevance of BAF in nuclear envelope dynamics, providing new insights about the relationship of nuclear envelope to aging.

Conclusions and perspectives

Over the last few years, the generation of experimental murine models of progeroid laminopathies has been crucial for a deeper understanding of the molecular basis of these diseases. This is the case for HGPS, where a fast progress has been made in the last 8 years since the identification of *LMNA* mutations to the first clinical trial in HGPS patients. However, new murine models that fully recapitulate all the disease phenotypes of HGPS [55] are necessary to boost the development of *in vivo* approaches directed to the correction of *LMNA* aberrant splicing [25]. Besides, several questions remain to be answered concerning important aspects such as the relative contribution to the progeroid phenotype of cell-autonomous compared with systemic alterations or the involvement of nuclear envelope dynamics during normal aging [56–58].

Funding

This work was supported by grants from Ministerio de Ciencia e Innovación-Spain, PCTI (Plan de Ciencia, Tecnología e Innovación del

Principado de Asturias)–FICYT (Fundación para el Fomento en Asturias de la Investigación Científica Aplicada y la Tecnología) Asturias, and the European Union Framework Programme 7 (MicroEnviMet). The Instituto Universitario de Oncología is supported by Obra Social Cajastur and Acción Transversal del Cáncer-RTICC (Red Tematica de Investigación Cooperativa en Cáncer). C.L-O. is an Investigator of the Botin Foundation.

References

1 Dechat, T., Pfleghaar, K., Sengupta, K., Shimi, T., Shumaker, D.K., Solimando, L. and Goldman, R.D. (2008) Nuclear lamins: major factors in the structural organization and function of the nucleus and chromatin. Genes Dev. **22**, 832–853

2 Mekhail, K. and Moazed, D. (2010) The nuclear envelope in genome organization, expression and stability. Nat. Rev. Mol. Cell Biol. **11**, 317–328

3 Fiserova, J. and Goldberg, M.W. (2010) Nucleocytoplasmic transport in yeast: a few roles for many actors. Biochem. Soc. Trans. **38**, 273–277

4 Gruenbaum, Y., Margalit, A., Goldman, R.D., Shumaker, D.K. and Wilson, K.L. (2005) The nuclear lamina comes of age. Nat. Rev. Mol. Cell Biol. **6**, 21–31

5 Worman, H.J., Ostlund, C. and Wang, Y. (2010) Diseases of the nuclear envelope. Cold Spring Harbor Perspect. Biol. **2**, a000760

6 Ramirez, C.L., Cadiñanos, J., Varela, I., Freije, J.M. and López-Otín, C. (2007) Human progeroid syndromes, aging and cancer: new genetic and epigenetic insights into old questions. Cell. Mol. Life Sci. **64**, 155–170

7 Burtner, C.R. and Kennedy, B.K. (2010) Progeria syndromes and ageing: what is the connection? Nat. Rev. Mol. Cell Biol. **11**, 567–578

8 Hennekam, R.C. (2006) Hutchinson–Gilford progeria syndrome: review of the phenotype. Am. J. Med. Genet. A **140**, 2603–2624

9 Merideth, M.A., Gordon, L.B., Clauss, S., Sachdev, V., Smith, A.C., Perry, M.B., Brewer, C.C., Zalewski, C., Kim, H.J., Solomon, B. et al. (2008) Phenotype and course of Hutchinson–Gilford progeria syndrome. N. Engl. J. Med. **358**, 592–604

10 Pereira, S., Bourgeois, P., Navarro, C., Esteves-Vieira, V., Cau, P., De Sandre-Giovannoli, A. and Lévy, N. (2008) HGPS and related premature aging disorders: from genomic identification to the first therapeutic approaches. Mech. Ageing Dev. **129**, 449–459

11 De Sandre-Giovannoli, A., Bernard, R., Cau, P., Navarro, C., Amiel, J., Boccaccio, I., Lyonnet, S., Stewart, C.L., Munnich, A., Le Merrer, M. and Lévy, N. (2003) Lamin A truncation in Hutchinson–Gilford progeria. Science **300**, 2055

12 Eriksson, M., Brown, W.T., Gordon, L.B., Glynn, M.W., Singer, J., Scott, L., Erdos, M.R., Robbins, C.M., Moses, T.Y., Berglund, P. et al. (2003) Recurrent *de novo* point mutations in lamin A cause Hutchinson–Gilford progeria syndrome. Nature **423**, 293–298

13 Freije, J.M., Blay, P., Pendás, A.M., Cadiñanos, J., Crespo, P. and López-Otín, C. (1999) Identification and chromosomal location of two human genes encoding enzymes potentially involved in proteolytic maturation of farnesylated proteins. Genomics **58**, 270–280

14 Pendás, A.M., Zhou, Z., Cadiñanos, J., Freije, J.M., Wang, J., Hultenby, K., Astudillo, A., Wernerson, A., Rodríguez, F., Tryggvason, K. and López-Otín, C. (2002) Defective prelamin A processing and muscular and adipocyte alterations in Zmpste24 metalloproteinase-deficient mice. Nat. Genet. **31**, 94–99

15 Bergo, M.O., Gavino, B., Ross, J., Schmidt, W.K., Hong, C., Kendall, L.V., Mohr, A., Meta, M., Genant, H., Jiang, Y. et al. (2002) Zmpste24 deficiency in mice causes spontaneous bone fractures, muscle weakness, and a prelamin A processing defect. Proc. Natl. Acad. Sci. U.S.A. **99**, 13049–13054

16 Yang, S.H., Bergo, M.O., Toth, J.I., Qiao, X., Hu, Y., Sandoval, S., Meta, M., Bendale, P., Gelb, M.H., Young, S.G. and Fong, L.G. (2005) Blocking protein farnesyltransferase improves nuclear blebbing in mouse fibroblasts with a targeted Hutchinson–Gilford progeria syndrome mutation. Proc. Natl. Acad. Sci. U.S.A. **102**, 10291–10296

17 Varga, R., Eriksson, M., Erdos, M.R., Olive, M., Harten, I., Kolodgie, F., Capell, B.C., Cheng, J., Faddah, D., Perkins, S. et al. (2006) Progressive vascular smooth muscle cell defects in a mouse model of Hutchinson–Gilford progeria syndrome. Proc. Natl. Acad. Sci. U.S.A. **103**, 3250–3255

18 Wang, Y., Panteleyev, A.A., Owens, D.M., Djabali, K., Stewart, C.L. and Worman, H.J. (2008) Epidermal expression of the truncated prelamin A causing Hutchinson–Gilford progeria syndrome: effects on keratinocytes, hair and skin. Hum. Mol. Genet. **17**, 2357–2369

19 Sagelius, H., Rosengardten, Y., Hanif, M., Erdos, M.R., Rozell, B., Collins, F.S. and Eriksson, M. (2008) Targeted transgenic expression of the mutation causing Hutchinson–Gilford progeria syndrome leads to proliferative and degenerative epidermal disease. J. Cell Sci. **121**, 969–978

20 Varela, I., Cadiñanos, J., Pendás, A.M., Gutiérrez-Fernández, A., Folgueras, A.R., Sánchez, L.M., Zhou, Z., Rodríguez, F.J., Stewart, C.L., Vega, J.A. et al. (2005) Accelerated ageing in mice deficient in Zmpste24 protease is linked to p53 signalling activation. Nature **437**, 564–568

21 Espada, J., Varela, I., Flores, I., Ugalde, A.P., Cadiñanos, J., Pendás, A.M., Stewart, C.L., Tryggvason, K., Blasco, M.A., Freije, J.M. and López-Otin, C. (2008) Nuclear envelope defects cause stem cell dysfunction in premature-aging mice. J. Cell Biol. **181**, 27–35

22 Marino, G., Ugalde, A.P., Salvador-Montoliu, N., Varela, I., Quirós, P.M., Cadiñanos, J., van der Pluijm, I., Freije, J.M. and López-Otin, C. (2008) Premature aging in mice activates a systemic metabolic response involving autophagy induction. Hum. Mol. Genet. **17**, 2196–2211

23 Worman, H.J., Fong, L.G., Muchir, A. and Young, S.G. (2009) Laminopathies and the long strange trip from basic cell biology to therapy. J. Clin. Invest. **119**, 1825–1836

24 Yang, S.H., Meta, M., Qiao, X., Frost, D., Bauch, J., Coffinier, C., Majumdar, S., Bergo, M.O., Young, S.G. and Fong, L.G. (2006) A farnesyltransferase inhibitor improves disease phenotypes in mice with a Hutchinson–Gilford progeria syndrome mutation. J. Clin. Invest. **116**, 2115–2121

25 Scaffidi, P. and Misteli, T. (2005) Reversal of the cellular phenotype in the premature aging disease Hutchinson–Gilford progeria syndrome. Nat. Med. **11**, 440–445

26 Varela, I., Pereira, S., Ugalde, A.P., Navarro, C.L., Suárez, M.F., Cau, P., Cadiñanos, J., Osorio, F.G., Foray, N., Cobo, J. et al. (2008) Combined treatment with statins and aminobisphosphonates extends longevity in a mouse model of human premature aging. Nat. Med. **14**, 767–772

27 Cao, K., Graziotto, J.J., Blair, C.D., Mazzulli, J.R., Erdos, M.R., Krainc, D. and Collins, F.S. (2011) Rapamycin reverses cellular phenotypes and enhances mutant protein clearance in Hutchinson–Gilford progeria syndrome cells. Sci. Transl. Med. **3**, 89ra58

28 Mariño, G., Ugalde, A.P., Fernández, A.F., Osorio, F.G., Fueyo, A., Freije, J.M. and López-Otín, C. (2010) Insulin-like growth factor 1 treatment extends longevity in a mouse model of human premature aging by restoring somatotroph axis function. Proc. Natl. Acad. Sci. U.S.A. **107**, 16268–16273

29 Ugalde, A.P., Ramsay, A.J., de la Rosa, J., Varela, I., Marino, G., Cadiñanos, J., Lu, J., Freije, J.M. and López-Otín, C. (2011) Aging and chronic DNA damage response activate a regulatory pathway involving miR-29 and p53. EMBO J. **30**, 2219–2232

30 Puente, X.S., Quesada, V., Osorio, F.G., Cabanillas, R., Cadiñanos, J., Fraile, J.M., Ordóñez, G.R., Puente, D.A., Gutiérrez-Fernández, A., Fanjul-Fernández, M. et al. (2011) Exome sequencing and functional analysis identifies *BANF1* mutation as the cause of a hereditary progeroid syndrome. Am. J. Hum. Genet. **88**, 650–656

31 Kirkwood, T.B. (2005) Understanding the odd science of aging. Cell **120**, 437–447

32 Kourtis, N. and Tavernarakis, N. (2011) Cellular stress response pathways and ageing: intricate molecular relationships. EMBO J. **30**, 2520–2531

33 Liu, B., Wang, J., Chan, K.M., Tjia, W.M., Deng, W., Guan, X., Huang, J.D., Li, K.M., Chau, P.Y., Chen, D.J. et al. (2005) Genomic instability in laminopathy-based premature aging. Nat. Med. **11**, 780–785

34 Osorio, F.G., Varela, I., Lara, E., Puente, X.S., Espada, J., Santoro, R., Freije, J.M., Fraga, M.F. and López-Otín, C. (2010) Nuclear envelope alterations generate an aging-like epigenetic pattern in mice deficient in Zmpste24 metalloprotease. Aging Cell **9**, 947–957

35 Cadiñanos, J., Varela, I., López-Otín, C. and Freije, J.M. (2005) From immature lamin to premature aging: molecular pathways and therapeutic opportunities. Cell Cycle **4**, 1732–1735

36 Lu, X., Nguyen, T.A., Moon, S.H., Darlington, Y., Sommer, M. and Donehower, L.A. (2008) The type 2C phosphatase Wip1: an oncogenic regulator of tumour suppressor and DNA damage response pathways. Cancer Metastasis Rev. **27**, 123–135

37 Cha, H., Lowe, J.M., Li, H., Lee, J.S., Belova, G.I., Bulavin, D.V. and Fornace, Jr, A.J. (2010) Wip1 directly dephosphorylates γ-H2AX and attenuates the DNA damage response. Cancer Res. **70**, 4112–4122

38 Campisi, J. (2005) Aging, tumour suppression and cancer: high wire-act! Mech. Ageing Dev. **126**, 51–58

39 Houtkooper, R.H., Williams, R.W. and Auwerx, J. (2010) Metabolic networks of longevity. Cell **142**, 9–14
40 Panowski, S.H. and Dillin, A. (2009) Signals of youth: endocrine regulation of aging in *Caenorhabditis elegans*. Trends Endocrinol. Metab. **20**, 259–264
41 Haigis, M.C. and Yankner, B.A. (2010) The aging stress response. Mol. Cell **40**, 333–344
42 Russell, S.J. and Kahn, C.R. (2007) Endocrine regulation of ageing. Nat. Rev. Mol. Cell Biol. **8**, 681–691
43 Niedernhofer, L.J., Garinis, G.A., Raams, A., Lalai, A.S., Robinson, A.R., Appeldoorn, E., Odijk, H., Oostendorp, R., Ahmad, A., van Leeuwen, W. et al. (2006) A new progeroid syndrome reveals that genotoxic stress suppresses the somatotroph axis. Nature **444**, 1038–1043
44 Hoeijmakers, J.H. (2009) DNA damage, aging, and cancer. N. Engl. J. Med. **361**, 1475–1485
45 Ugalde, A.P., Marino, G. and López-Otín, C. (2010) Rejuvenating somatotropic signaling: a therapeutical opportunity for premature aging? Aging **2**, 1017–1022
46 Laron, Z. (2004) Laron syndrome (primary growth hormone resistance or insensitivity): the personal experience 1958–2003. J. Clin. Endocrinol. Metab. **89**, 1031–1044
47 Steuerman, R., Shevah, O. and Laron, Z. (2011) Congenital IGF1 deficiency tends to confer protection against post-natal development of malignancies. Eur. J. Endocrinol. **164**, 485–489
48 Guevara-Aguirre, J., Balasubramanian, P., Guevara-Aguirre, M., Wei, M., Madia, F., Cheng, C.W., Hwang, D., Martin-Montalvo, A., Saavedra, J., Ingles, S. et al. (2011) Growth hormone receptor deficiency is associated with a major reduction in pro-aging signaling, cancer, and diabetes in humans. Sci. Transl. Med. **3**, 70ra13
49 Roach, J.C., Glusman, G., Smit, A.F., Huff, C.D., Hubley, R., Shannon, P.T., Rowen, L., Pant, K.P., Goodman, N., Bamshad, M. et al. (2010) Analysis of genetic inheritance in a family quartet by whole-genome sequencing. Science **328**, 636–639
50 Lupski, J.R., Reid, J.G., Gonzaga-Jauregui, C., Rio Deiros, D., Chen, D.C., Nazareth, L., Bainbridge, M., Dinh, H., Jing, C., Wheeler, D.A. et al. (2010) Whole-genome sequencing in a patient with Charcot–Marie–Tooth neuropathy. N. Engl. J. Med. **362**, 1181–1191
51 Cabanillas, R., Cadiñanos, J., Villameytide, J.A.F., Perez, M., Longo, J., Richard, J.M., Alvarez, R., Duran, N.S., Illan, R., Gonzalez, D.J. et al. (2011) Néstor–Guillermo progeria syndrome: a novel premature aging condition with early onset and chronic development caused by *BANF1* mutations. Am. J. Med. Genet. A **155**, 2617–2625
52 Segura-Totten, M. and Wilson, K.L. (2004) BAF: roles in chromatin, nuclear structure and retrovirus integration. Trends Cell Biol. **14**, 261–266
53 Margalit, A., Brachner, A., Gotzmann, J., Foisner, R. and Gruenbaum, Y. (2007) Barrier-to-autointegration factor: a BAFfling little protein. Trends Cell Biol. **17**, 202–208
54 Segura-Totten, M., Kowalski, A.K., Craigie, R. and Wilson, K.L. (2002) Barrier-to-autointegration factor: major roles in chromatin decondensation and nuclear assembly. J. Cell Biol. **158**, 475–485
55 Osorio, F.G., Obaya, A.J., López-Otín, C. and Freije, J.M. (2009) Accelerated ageing: from mechanism to therapy through animal models. Transgenic Res. **18**, 7–15
56 Scaffidi, P. and Misteli, T. (2006) Lamin A-dependent nuclear defects in human aging. Science **312**, 1059–1063
57 Ragnauth, C.D., Warren, D.T., Liu, Y., McNair, R., Tajsic, T., Figg, N., Shroff, R., Skepper, J. and Shanahan, C.M. (2010) Prelamin A acts to accelerate smooth muscle cell senescence and is a novel biomarker of human vascular aging. Circulation **121**, 2200–2210
58 Cao, K., Blair, C.D., Faddah, D.A., Kieckhaefer, J.E., Olive, M., Erdos, M.R., Nabel, E.G. and Collins, F.S. (2011) Progerin and telomere dysfunction collaborate to trigger cellular senescence in normal human fibroblasts. J. Clin. Invest. **121**, 2833–2844

Received 27 July 2011
doi:10.1042/BST20110677

II. Generation of a mutant mouse strain carrying the HGPS progeria mutation

Hutchinson-Gilford progeria syndrome (HGPS) is a paradigmatical human progeroid syndrome caused by alterations in the nuclear envelope structure. Most of HGPS patients carry a point mutation in *LMNA* gene (c.1824C>T; p.G608G) that activates a silent splice donor site, causing the accumulation of a truncated form of prelamin A called progerin. The accumulation of progerin has also been reported during normal aging, adding a new layer of interest to the study of this pathology, and therefore to the development of animal models that fully recapitulate the molecular alterations observed in these patients. In this work, we have generated a mutant mouse strain carrying the equivalent mutation in *Lmna* to that causing human HGPS (c.1827C>T; p.G609G). $Lmna^{G609G}$ mice fully recapitulate both molecular and phenotypic alterations presented in HGPS patients and allowed us to develop a new therapeutic approach based on the use of antisense oligonucleotides that specifically correct the aberrant splicing of the lamin A gene.

Article 3. Fernando G. Osorio, Claire L. Navarro, Juan Cadiñanos, Isabel C. López-Mejía, Pedro M. Quirós, Catherine Bartoli, José Rivera, Jamal Tazi, Gabriela Guzmán, Ignacio Varela, Danielle Depetris, Félix de Carlos, Juan Cobo, Vicente Andrés, Annachiara De Sandre-Giovannoli, José M. P. Freije, Nicolas Lévy and Carlos López-Otín. "Splicing-directed therapy in a new mouse model of human accelerated aging".

Science Translational Medicine. 2011 Oct 26; 3(106):106ra107.

Personal contribution to this work

I was responsible for most experiments shown in this work. I managed, genotyped and characterized $Lmna^{G609G}$ mice. Moreover, I performed subsequent *in vitro* and *in vivo* studies, including molecular, metabolic and histological analysis, as well as the experiments involving antisense oligonucleotides. Finally, I analyzed the data, prepared the figures and wrote the manuscript under the supervision of Dr. José M.P. Freije and Dr. Carlos López-Otín.

RESEARCH ARTICLE

HUTCHINSON-GILFORD PROGERIA

Splicing-Directed Therapy in a New Mouse Model of Human Accelerated Aging

Fernando G. Osorio,[1] Claire L. Navarro,[2] Juan Cadiñanos,[1]* Isabel C. López-Mejía,[3] Pedro M. Quirós,[1] Catherine Bartoli,[2] José Rivera,[4] Jamal Tazi,[3] Gabriela Guzmán,[5] Ignacio Varela,[1] Danielle Depetris,[2] Félix de Carlos,[6] Juan Cobo,[6] Vicente Andrés,[4] Annachiara De Sandre-Giovannoli,[2,7] José M. P. Freije,[1] Nicolas Lévy,[2,7] Carlos López-Otín[1†]

Hutchinson-Gilford progeria syndrome (HGPS) is caused by a point mutation in the *LMNA* gene that activates a cryptic donor splice site and yields a truncated form of prelamin A called progerin. Small amounts of progerin are also produced during normal aging. Studies with mouse models of HGPS have allowed the recent development of the first therapeutic approaches for this disease. However, none of these earlier works have addressed the aberrant and pathogenic *LMNA* splicing observed in HGPS patients because of the lack of an appropriate mouse model. Here, we report a genetically modified mouse strain that carries the HGPS mutation. These mice accumulate progerin, present histological and transcriptional alterations characteristic of progeroid models, and phenocopy the main clinical manifestations of human HGPS, including shortened life span and bone and cardiovascular aberrations. Using this animal model, we have developed an antisense morpholino–based therapy that prevents the pathogenic *Lmna* splicing, markedly reducing the accumulation of progerin and its associated nuclear defects. Treatment of mutant mice with these morpholinos led to a marked amelioration of their progeroid phenotype and substantially extended their life span, supporting the effectiveness of antisense oligonucleotide–based therapies for treating human diseases of accelerated aging.

INTRODUCTION

Progeroid laminopathies, including Hutchinson-Gilford progeria syndrome (HGPS), are human disorders of accelerated aging caused by defects in nuclear A–type lamins. The HGPS clinical phenotype is characterized by growth impairment, lipodystrophy (fat redistribution), dermal and bone abnormalities, and cardiovascular alterations, leading to shortened life span (*1*, *2*). Most HGPS patients carry a heterozygous point mutation within exon 11 of the *LMNA* gene encoding lamin A [a C-to-T transition in the *LMNA* coding region at nucleotide 1824 (c.1824C>T); no putative change in the protein sequence, because both encode a glycine at amino acid position 608 (p.Gly608Gly)] (*3*, *4*). Lamin A is a core component of the nuclear envelope that undergoes a complex maturation process, including the addition of a farnesyl group and a proteolytic processing event carried out by the metalloprotease ZMPSTE24/FACE1. The p.Gly608Gly mutation activates a cryptic splicing donor site that leads to the accumulation of a truncated form of prelamin A, called LAΔ50 or progerin, which has an internal deletion of 50 amino acids encompassing the target sequence for cleavage by ZMPSTE24. The accumulation of farnesylated progerin at the nuclear envelope leads to the functional and structural defects observed in the nucleus of affected patients (*5*, *6*). Progerin is not only detected in HGPS patients but also during normal aging, thereby adding a new level of interest to the study of the mechanisms that underlie progerin formation and accumulation in human cells and tissues (*7*, *8*).

Over the past few years, several mouse models of progeroid laminopathies have been generated (*9*–*14*), providing valuable information about the molecular alterations functionally involved in these diseases (*15*–*18*) and allowing the development of strategies to test anti-progeria therapeutic approaches (*19*–*22*). Although some of these models, especially *Zmpste24*-deficient mice (*9*, *10*), phenocopy most alterations present in HGPS, none of them reproduce the molecular situation that occurs at the *LMNA* locus of these patients. These differences have represented a serious limitation for both the study of splicing alterations in HGPS and the development of in vivo treatments with drugs that specifically modify *LMNA* splicing (*23*). Here, we describe the generation and characterization of a mouse model that carries the precise HGPS mutation. With this new model, we were able to test in vivo therapies aimed at targeting the abnormal *LMNA* splicing that occurs in both normal and pathological aging.

RESULTS

To generate a knock-in mouse strain carrying the HGPS mutation, we designed a strategy for replacement of the wild-type mouse *Lmna* gene with a mutant allele that carried the c.1827C>T;p.Gly609Gly mutation, which is equivalent to the HGPS c.1824C>T;p.Gly608Gly mutation in the human *LMNA* gene (Fig. 1A). In an attempt to avoid the breeding problems present in other mouse models that express progerin (*19*), we designed a conditional mutant allele with a *neomycin resistance* gene flanked by two loxP sites inserted in *Lmna* intron 10. This cassette was able to prevent the formation of prelamin A transcripts

[1]Departamento de Bioquímica y Biología Molecular, Facultad de Medicina, Instituto Universitario de Oncología, Universidad de Oviedo, 33006 Oviedo, Spain. [2]Université de la Méditerranée, Inserm UMR_S 910, Faculté de Médecine de Marseille, 13385 Marseille cedex 05, France. [3]Institut de Génétique Moléculaire, UMR 5535 CNRS, 34293 Montpellier cedex 5, France. [4]Departamento de Epidemiología, Aterotrombosis e Imagen, Centro Nacional de Investigaciones Cardiovasculares, 28029 Madrid, Spain. [5]Servicio de Cardiología, Hospital Universitario La Paz, 28046 Madrid, Spain. [6]Departamento de Cirugía y Especialidades Médico-Quirúrgicas and Instituto Asturiano de Odontología, Universidad de Oviedo, 33006 Oviedo, Spain. [7]AP-HM, Département de Génétique Médicale, Hôpital d'Enfants de la Timone, 13385 Marseille cedex 05, France.
*Present address: Instituto de Medicina Oncológica y Molecular de Asturias, Centro Médico de Asturias, 33193 Oviedo, Spain.
†To whom correspondence should be addressed. E-mail: clo@uniovi.es

RESEARCH ARTICLE

by blocking lamin A–specific splicing. Therefore, this allele, which we refer to as *Lmna*^{LCS} (Lamin C–Stop), directs only the expression of lamin C and allows study of the potential effects of lamin A deficiency (Fig. 1A). We generated *Lmna*$^{LCS/+}$ mice and crossed them with a *Cre*-deleter mouse strain to obtain germline removal of the *neomycin resistance* cassette (Fig. 1, A and B). As a result, we obtained offspring that carried the *Lmna*^{G609G} knock-in allele, which expressed lamin C, lamin A, and progerin (Fig. 1C).

To ensure the correct translation of the mutant allele, we analyzed protein extracts from cultures of mouse fibroblasts of each genotype by Western (immuno) blot with a specific antibody that recognizes lamin A/C (Fig. 1C). Genomic analysis of *Lmna* exon 11 confirmed the genotypes of *Lmna*$^{+/+}$, *Lmna*$^{G609G/+}$, and *Lmna*$^{G609G/G609G}$ mice (fig. S1). Likewise, semiquantitative transcriptional analysis and direct sequencing of RNA samples from several tissues confirmed that the aberrant *Lmna* splicing in *Lmna*^{G609G} mice was equivalent to the *LMNA* splicing error that occurs in HGPS patients (*3*, *4*) (fig. S1). Finally, several tissue samples from *Lmna*$^{+/+}$, *Lmna*$^{G609G/+}$, and *Lmna*$^{G609G/G609G}$ mice were analyzed further by Western blotting, which confirmed the expected lamin A/C and progerin expression patterns (fig. S2).

Homozygous mice for the conditional *Lmna*^{LCS} allele were indistinguishable from their wild-type littermates and did not show any detectable differences in growth or longevity up to 50 weeks of age (fig. S3), which is in agreement with previous reports on the dispensability of the lamin A isoform (*24*). Conversely, mice that carried the *Lmna*^{G609G} allele expressed lamin C, lamin A, and progerin, reproducing the same molecular situation as is present in HGPS patients. Homozygous mice with the c.1827C>T;p.Gly609Gly mutation were infertile but seemed healthy until 3 weeks of age. Subsequently, they showed a reduction in growth rates (Fig. 2A), with a progressive loss of weight (Fig. 2B) and the acquisition of an abnormal posture and a marked curvature of the spine (cervicothoracic lordokyphosis) (Fig. 2D). These multiple alterations finally resulted in premature death of these mutant mice, which have an average life span of 103 days (Fig. 2C) compared to more than 2 years for wild-type mice. Heterozygous *Lmna*$^{G609G/+}$ mice had normal weight, size, and fertility until about 8 months of age. At that point, the mice started to lose weight, exhibiting a process similar to that observed in homozygous mice and causing their premature death at an average of 242 days. Both heterozygous and homozygous mice that carried the c.1827C>T;p.Gly609Gly mutation showed profound nuclear abnormalities as a consequence of progerin accumulation (Fig. 2E).

As a starting point for phenotypic characterization of mice that carried the c.1827C>T;p.Gly609Gly mutation, we focused on *Lmna*$^{G609G/G609G}$ mice, which show a more pronounced and earlier progeroid phenotype than heterozygous *Lmna*$^{G609G/+}$ mice. The relatively milder phenotype of *Lmna*$^{G609G/+}$ mice, compared with *LMNA*$^{G608G/+}$ HGPS patients, is in agreement with previous observations that have evidenced a higher tolerance of mice compared to humans when it comes to accumulation of prelamin A forms. Thus, the complete absence of prelamin A processing as a result of full *ZMPSTE24* deficiency causes reduced fetal weight, premature delivery, and perinatal death in humans, whereas the same molecular alteration produces no overtly detectable phenotype in mice until 3 to 4 weeks after birth (*9*, *25*). Accordingly, homozygous *Lmna*$^{G609G/G609G}$ mice likely are a better model of HGPS than are *Lmna*$^{G609G/+}$ heterozygotes.

Lmna$^{G609G/G609G}$ mice of advanced age exhibited a generalized loss of the principal fat deposits. Microscopy analysis of the skin revealed loss of the subcutaneous fat layer and a general attrition of hair follicles (Fig. 2F). Senescence-associated β-galactosidase staining was increased in liver and kidney sections from 3-month-old *Lmna*$^{G609G/G609G}$ mice when compared with age-matched wild-type animals (Fig. 2F), reflecting a premature aging process in these animals.

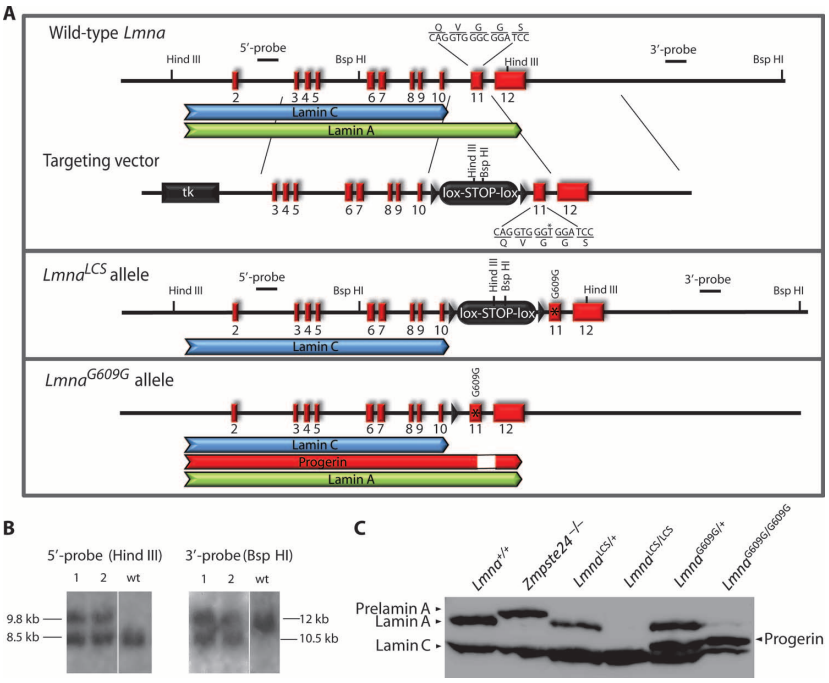

Fig. 1. Generation of knock-in *Lmna*^{G609G} mice. (**A**) Schematic representation of the wild-type *Lmna* locus, targeting vector, and targeted allele. Positions of restriction enzyme cleavage sites and probes used for Southern blot analysis are shown. (**B**) Southern (DNA) blot analysis of genomic DNA from two targeted *Lmna*^{LCS}-ES cell clones and wild-type ES. Probing of Hind III–digested DNA revealed fragments of 9.8 and 8.5 kb for mutant and wild-type (wt) alleles, respectively. Probing of Bsp HI–digested DNA revealed fragments of 12 and 10.5 kb for wt and mutant alleles, respectively. (**C**) Western (immuno) blot analysis of mouse adult fibroblasts obtained from the mice with the various genotypes used in the study. Lamin A, lamin C, prelamin A, and progerin were detected with a monoclonal antibody against lamin A/C (Manlac-1).

The size of most organs from homozygous mutant mice was proportional to their reduced body weight (fig. S4), but the main lymphoid organs, thymus and spleen, exhibited a marked involution relative to wild-type animals (Fig. 2F). Similar alterations are shown by other progeroid mouse models in association with defects in the immune system (*26*, *27*). Microcomputed tomography (μCT) analysis of tibias, skull, and vertebral column revealed profound bone alterations in $Lmna^{G609G/G609G}$ mice compared to wild-type mice. Thus, the tibias of mutant mice showed a reduction in bone density and cortical thickness as well as an increased porosity (Fig. 3A). Likewise, skulls showed a clear size reduction and smaller lower incisors, whereas vertebral column analysis confirmed a marked lordokyphosis in homozygous mutant mice (fig. S5, A and B). $Lmna^{G609G/G609G}$ mice also showed reduced grip strength (fig. S5C).

Moreover, mutant mice exhibited important cardiovascular alterations that could be related to their premature death and that also occur in HGPS patients as well as during normal aging (*28*). Because vascular smooth muscle cell (VSMC) depletion has been reported in another progeroid mouse model (*12*) and in some HGPS patients (*29*), we focused on the study of these cells. The number of VSMCs in the medial layer of the thoracic aorta was similar in wild-type and $Lmna^{G609G/G609G}$ mice (fig. S6A), but $Lmna^{G609G/G609G}$ mice displayed a significant loss of VSMCs in the aortic arch, a region that exhibits extensive branching and is subjected to high hemodynamic stress (Fig. 3B). Notably, the severity of this phenotype in one HGPS patient correlated with hemodynamic stress around the site of branching (*29*). Blood pressure appeared normal in $Lmna^{G609G/G609G}$ mutant mice (fig. S6B), but they progressively developed bradycardia between 9 and 15 weeks of age (Fig. 3B). Moreover, electrocardiographic (ECG) studies revealed prolonged QRS waves in $Lmna^{G609G/G609G}$ mice without changes in the PR interval (Fig. 3B) relative to wild-type mice, which indicates an alteration of heart ventricular depolarization. Finally, we assessed heart function by transthoracic echocardiography. Both M-mode and Simpson's method two-dimensional (2D) echocardiography of left ventricular function revealed no differences in systolic function (ejection fraction and fractional shortening) or diastolic

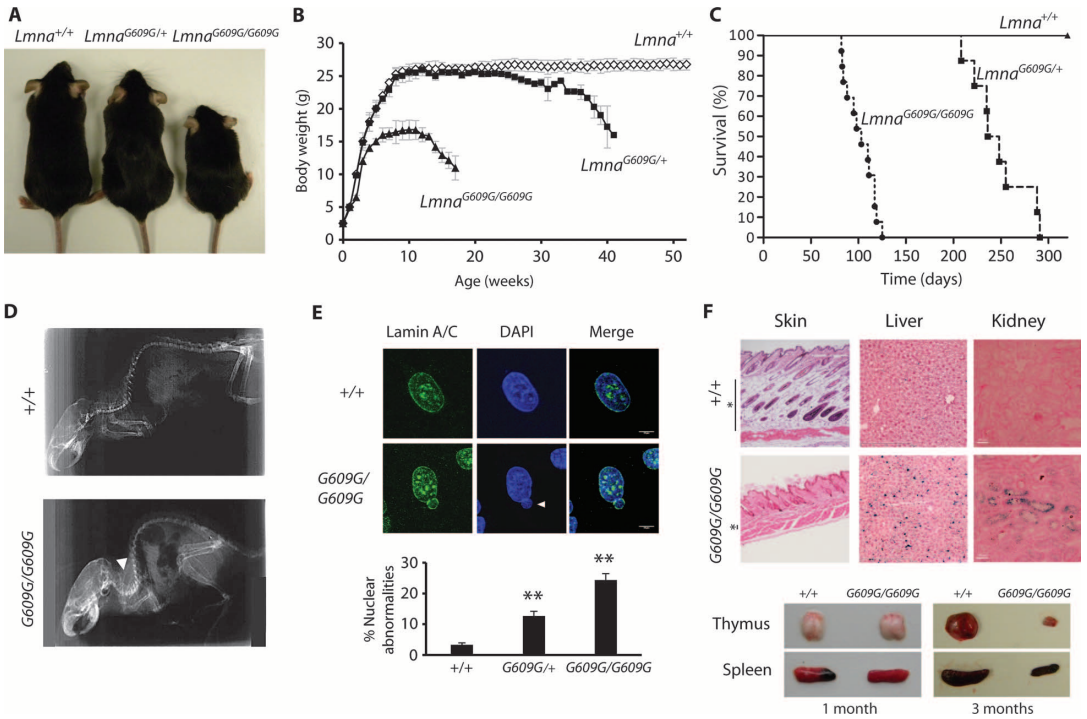

Fig. 2. Phenotypes of $Lmna^{G609G}$ mice. (**A**) Representative photographs of 3-month-old $Lmna^{+/+}$, $Lmna^{G609G/+}$, and $Lmna^{G609G/G609G}$ mice. (**B**) Cumulative plot of body weight versus age. Dots represent mean values, and error bars indicate SDs ($n > 10$ for each genotype) ($P < 0.01$ for all the comparisons, ANOVA test). (**C**) Kaplan-Meier survival plots for $Lmna^{G609G/G609G}$ ($n = 12$), $Lmna^{G609G/+}$ ($n = 8$), and $Lmna^{+/+}$ mice ($n = 15$) [$P < 0.01$ for all the comparisons, log-rank (Mantel-Cox) test]. (**D**) Radiograph of a 3-month-old $Lmna^{G609G/G609G}$ mouse compared with a wild-type littermate. (**E**) Nuclear envelope architecture analyzed in $Lmna^{G609G/G609G}$ and $Lmna^{+/+}$ fibroblasts with an anti–lamin A/C antibody and counterstained with DAPI (top panel). The white arrowhead indicates a representative example of membrane blebbing in an abnormal nucleus. The plot reflects the percentage of nuclei with abnormalities (nuclei with blebbing or irregular shape) in $Lmna^{+/+}$, $Lmna^{G609G/+}$, and $Lmna^{G609G/G609G}$ fibroblast cell lines. Error bars represent SDs. $^{**}P < 0.01$ (two-tailed Student's t test) compared to control (+/+) values (bottom panel). (**F**) H&E staining of skin from a 3-month-old $Lmna^{G609G/G609G}$ mouse compared with that of a wild-type littermate (asterisks indicate subcutaneous fat layer). Senescence-associated β-galactosidase activity in sections of liver and kidney from $Lmna^{G609G/G609G}$ and wild-type littermate (top panel). Representative photographs of thymus and spleen from $Lmna^{G609G/G609G}$ and wild-type littermates at 1 and 3 months of age (bottom panel).

RESEARCH ARTICLE

function (mitral valve inflow velocity E to A ratio) in *Lmna*$^{G609G/G609G}$ mutant versus wild-type mice (fig. S6C).

Lmna$^{G609G/G609G}$ mice also showed, relative to wild-type mice, altered circulating plasma concentrations of various hormones and other biochemical markers. For example, at 2 months of age, the *Lmna*$^{G609G/G609G}$ mutant mice showed a decrease in serum glucose concentrations, relative to wild-type mice, an alteration that worsened with age, leading to extreme hypoglycemia at 3 months of age (Fig. 3C). We also observed a decrease of serum glucose concentrations in heterozygous *Lmna*$^{G609G/+}$ mutant mice of advanced age (8 months), indicating

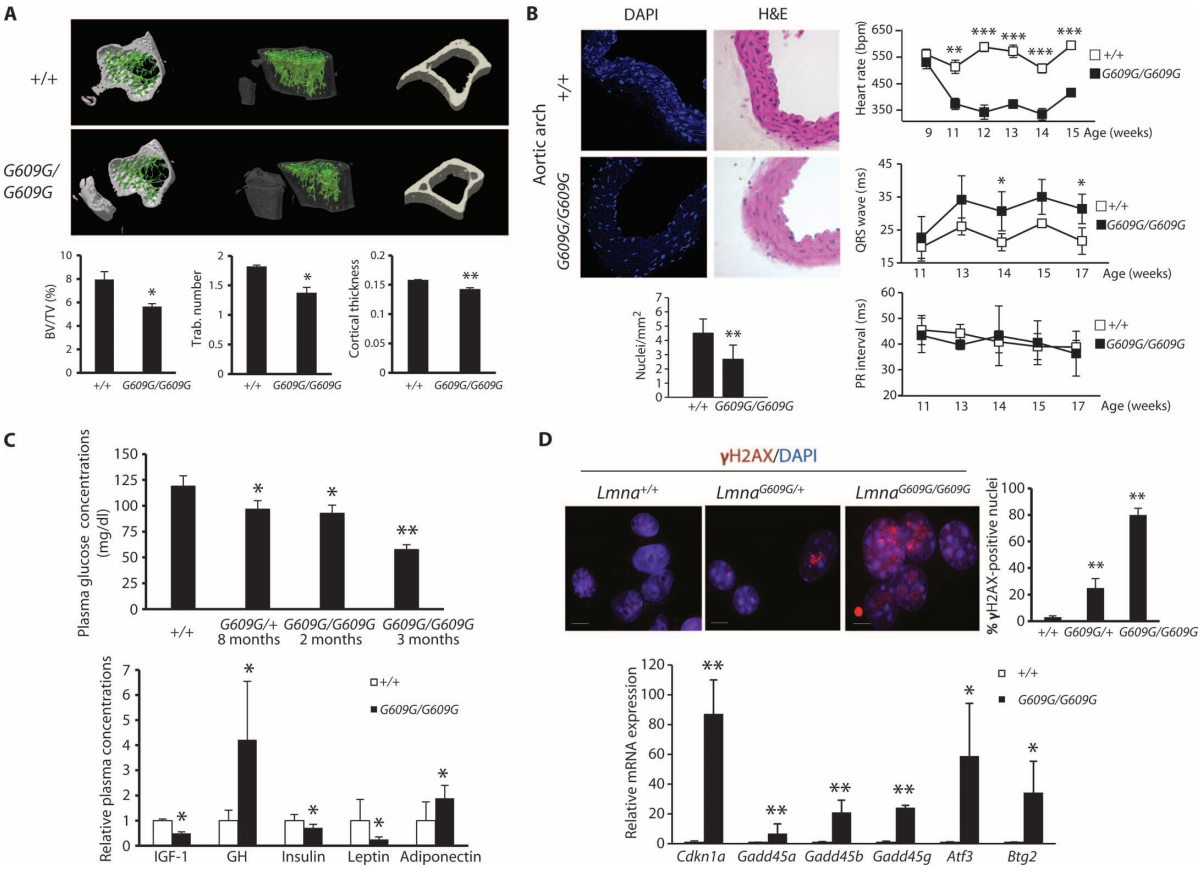

Fig. 3. Bone, cardiovascular, and biochemical alterations in *Lmna*$^{G609G/G609G}$ mice. (**A**) 3D image generated from μCT analysis of tibias from 3-month-old *Lmna*$^{G609G/G609G}$ and *Lmna*$^{+/+}$ mice (top panel). Bottom panel contains quantitative analysis of relative bone volumes [bone volume/tissue volume (BV/TV)], number of trabecules per millimeter, and cortical thickness in *Lmna*$^{G609G/G609G}$ (n = 4) and *Lmna*$^{+/+}$ (n = 4) mice. Mean values are represented, and error bars indicate SDs. *P < 0.05; **P < 0.01 (two-tailed Student's t test) compared to control (+/+) values. (**B**) Representative photographs showing VSMC depletion in the medial layer of the aortic arch (top left panel). Cross sections were stained with DAPI and H&E. Plot represents the average from 14 to 17 independent cross sections (bottom left panel). Right panels show the results of longitudinal studies to assess heart rate and ECG parameters (n = 4). Heart rate is represented as the number of beats per minute (bpm). Mean values are represented and error bars indicate SDs. *P < 0.05; **P < 0.01; ***P < 0.001 (two-tailed Student's t test) compared to control (+/+) values. (**C**) Blood glucose concentrations in *Lmna*$^{+/+}$ (n = 5), 8-month-old *Lmna*$^{G609G/+}$ (n = 4), and 2- (n = 6) and 3-month-old (n = 6) *Lmna*$^{G609G/G609G}$ mice, respectively (top panel). Mean values are represented and error bars indicate SDs. *P < 0.05; **P < 0.01 (two-tailed Student's t test) compared to control (+/+) values. Bottom panel shows comparisons of plasma concentrations of IGF-1, GH, insulin, leptin, and adiponectin between *Lmna*$^{G609G/G609G}$ (n = 4) and wild-type littermates (n = 4). Concentrations were normalized to the mean of control (+/+). Error bars indicate SDs. *P < 0.05 (two-tailed Student's t test) compared to control (+/+) values. (**D**) Indirect immunofluorescence staining of γH2AX in P5 skin fibroblasts issued from *Lmna*$^{+/+}$, *Lmna*$^{G609G/+}$, and *Lmna*$^{G609G/G609G}$ mice (top left panel). The number of enlarged nuclei that showed γH2AX foci staining for each cell line is reported on the graph. Three independent experiments were performed for each genotype. F = 4.05 (F, found variation of the group averages/expected variation of the group averages); mean values are represented and error bars indicate SDs. **P < 0.005 (ANOVA) compared to control (+/+) values. Contribution of the genotype to the variance: 32% (Cohen's d Ryan test) (top right panel). Transcriptional analysis by real-time quantitative PCR of p53 targets in 3-month-old *Lmna*$^{G609G/G609G}$ and *Lmna*$^{+/+}$ mice (bottom panel). mRNA levels were normalized to the mean of *Lmna*$^{+/+}$ liver mRNA. Error bars represent SDs. *P < 0.05; **P < 0.01; ***P < 0.001 (two-tailed Student's t test) compared to control (+/+) values.

that hypoglycemia might also contribute to the cardiovascular compromise and early death of mice that carried the c.1827C>T;p.Gly609Gly mutation. In addition, $Lmna^{G609G/G609G}$ mice showed decreased serum levels of insulin-like growth factor 1 (IGF-1), insulin, and leptin and increased levels of growth hormone (GH) and adiponectin relative to wild-type mice (Fig. 3C).

As a measure of genotoxic stress, we analyzed histone γH2AX levels—a marker for the amount of nuclear DNA double-strand breaks—in the nuclei of cultured fibroblasts from mice of the various genotypes (Fig. 3D). Most (81%) $Lmna^{G609G/G609G}$ fibroblasts at passage 5 (P5) contained large and abnormally shaped nuclei with foci that were highly stained with anti-γH2AX antibodies. Similar abnormal nuclei were identified in 24% of $Lmna^{G609G/+}$ fibroblasts and in 3% of $Lmna^{+/+}$ fibroblasts (Fig. 3D).

To elucidate the molecular pathways that underlie the phenotypic alterations described in $Lmna^{G609G/G609G}$ mice, we analyzed the transcription profiles of livers from $Lmna^{G609G/G609G}$ mutant mice and wild-type littermates using complementary DNA (cDNA) hybridization to DNA microarrays. A large number of genes showed reproducible changes in their expression levels in the mutant mice, consistent with the critical roles of nuclear lamins in chromatin structure and function (*30*) (table S1). From these data, gene set enrichment analysis (GSEA) was used for an unbiased identification of molecular pathways that were significantly altered in these mice (*31*). This analysis revealed a very strong correlation between the transcriptional alterations detected in these $Lmna^{G609G/G609G}$ and *Zmpste24*-deficient mice (*32*), supporting the existence of a common transcriptional signature in two different models of progeroid laminopathies.

Functionally, most of the pathways that were significantly enriched in $Lmna^{G609G/G609G}$ samples are associated with stress responses. Thus, the p53 tumor suppressor pathway (Fig. 3D) and the ATM (ataxia telangiectasia mutated)–related pathway are significantly up-regulated in $Lmna^{G609G/G609G}$ mice, probably as a consequence of unrepaired DNA damage caused by progerin accumulation (*33*). We previously hypothesized that these alterations, including chronic activation of the p53 pathway, are drivers of the senescent phenotype displayed by these mice (*32*). Moreover, the list of genes that were overexpressed in the $Lmna^{G609G/G609G}$ mutant mice relative to wild-type animals contains a significant number of components of the hypoxia response pathway mediated by induction of the HIF-1α (hypoxia-inducible factor 1α) transcription factor (fig. S7). This pathway recently was associated with metabolic changes in a mouse model of progeria and could be involved in the serum glucose alterations seen in these mice (*34*). Other pathways that were down-regulated in $Lmna^{G609G/G609G}$ mice are related to metabolic processes such as fatty acid metabolism, oxidative phosphorylation, and mitochondria biogenesis (figs. S7 and S8).

The marked similarities in the molecular alterations observed in $Lmna^{G609G}$ mice and HGPS patients prompted us to develop an in vivo therapeutic approach based on the use of morpholino antisense oligonucleotides (*35*). Morpholinos are small modified oligonucleotides that can block splicing events by preventing access of the splicing machinery to the splice sites (*36*). In contrast with other unmodified oligonucleotides, morpholinos are stable and do not induce ribonuclease (RNase) H–driven degradation of the morpholino-RNA heteroduplex. Previous in vitro studies have demonstrated how a 25-nucleotide morpholino that specifically binds the human c.1824C>T;p.Gly608Gly HGPS mutation in the altered *LMNA* transcript can restore normal *LMNA* splicing in fibroblasts from HGPS patients, correcting the main pathological alterations of these cells, including nuclear abnormalities and mislocalization of other nuclear envelope proteins (*23*). The lack of phenotypic alterations in mice homozygous for the $Lmna^{LCS}$ allele (fig. S3) prompted us to design a new approach based on modulation of *Lmna* splicing through interfering with the lamin A–specific splice donor site.

Thus, we designed a 25-nucleotide morpholino (MmEx10) that bound to the exon 10–lamin A splice donor site (Fig. 4A). In addition, using the same coordinates as were specified in the original human HGPS targeting experiments (*23*), we designed another 25-nucleotide morpholino that bound the c.1827C>T;p.Gly609Gly mutated sequence in the region of the *Lmna* transcript that corresponded to exon 11 (MmEx11), to test whether the combined administration of both morpholinos could be more effective at reducing progerin amounts than the separate administration of each individual oligonucleotide. In an initial attempt to evaluate the effects of these morpholinos on splicing of the $Lmna^{G609G}$ allele, we transfected the oligonucleotide reagents into a fibroblast cell line derived from a heterozygous mouse that carried the c.1827C>T;p.Gly609Gly mutation and found that both MmEx10 and MmEx11 morpholinos each reduced progerin amounts in a dose-dependent manner; MmEx10 was more effective than MmEx11 at reducing progerin concentrations when the morpholinos were administered separately (30% reduction in 10 μM MmEx11–treated cells when compared to untreated cells; 40% reduction in 10 μM MmEx10–treated cells when compared to untreated cells; $P < 0.01$). When the two reagents were administered to cells at the same time (at a final concentration of 40 μM), progerin amounts were reduced to undetectable levels (Fig. 4B). We obtained similar results after using the human equivalents of the morpholinos in an HGPS fibroblast cell line (Fig. 4B). We also observed that progerin reduction mediated by administration of morpholinos correlated with the correction of nuclear abnormalities in a cell line carrying the homozygous c.1827C>T;p.Gly609Gly mutation and in an HGPS fibroblast cell line (fig. S9). Thus, both independent administration of each morpholino and their combined administration were able to reduce, in a dose-dependent manner, the percentage of cells with nuclear abnormalities to wild-type levels (Fig. 4C).

On the basis of these in vitro studies, we next explored the effect of these antisense oligonucleotides on the progeroid phenotype of $Lmna^{G609G/G609G}$ mice. To this end, we chose a vivo-morpholino delivery approach. Vivo-morpholinos consist of a morpholino oligonucleotide with a covalent link to an octa-guanidine dendrimer that facilitates efficient delivery into most mouse tissues (*37*). To attempt to obtain a maximum in vivo reduction of progerin concentrations, we treated mice either with a control vivo-morpholino or with a combination of MmEx10-MmEx11 vivo-morpholinos. Mutant mice treated with MmEx10-11 showed significantly improved body weights, reduced degrees of lordokyphosis, and extended life spans (Fig. 4D). Thus, the mean survival of treated $Lmna^{G609G/G609G}$ mice was extended from 111 to 155 days, and the maximum survival from 119 to 190 days ($P < 0.001$; Fig. 4D). No significant differences were recorded in survival or body weight between untreated and control vivo-morpholino–treated $Lmna^{G609G/G609G}$ mice (Fig. 4D). To assess the direct effect of morpholino treatment, we carried out reverse transcription–polymerase chain reaction (RT-PCR) experiments and Western blot analyses on mice tissues, which demonstrated clear reductions in progerin mRNA and protein concentrations, respectively, in all tissues analyzed except

RESEARCH ARTICLE

skeletal muscle, in which we could detect only a slight reduction in progerin concentrations (Fig. 4E and figs. S10 and S11).

To evaluate the biological effect of morpholino treatment in the reversion of the phenotypical alterations displayed by *Lmna*$^{G609G/G609G}$ mice, we analyzed the abundance of several p53 targets in treated mice as a marker of the senescent phenotype, and remarkably found a more than fivefold reduction in *Cdkn1a*, *Gadd45g*, and *Atf3* mRNA levels in the liver of MmEx10-11–treated *Lmna*$^{G609G/G609G}$ mice in comparison with *Lmna*$^{G609G/G609G}$-untreated mice (fig. S12A). MmEx10-11–treated mice also showed significantly increased serum glucose concentrations compared with untreated *Lmna*$^{G609G/G609G}$ mice ($P < 0.01$, two-tailed Student's t test) (fig. S12B), a thicker subcutaneous fat layer, and reduced staining for senescence-associated β-galactosidase activity in kidney. Treated *Lmna*$^{G609G/G609G}$ mice also showed a reduced involution of thymus and spleen compared with untreated *Lmna*$^{G609G/G609G}$ mice (fig. S12C).

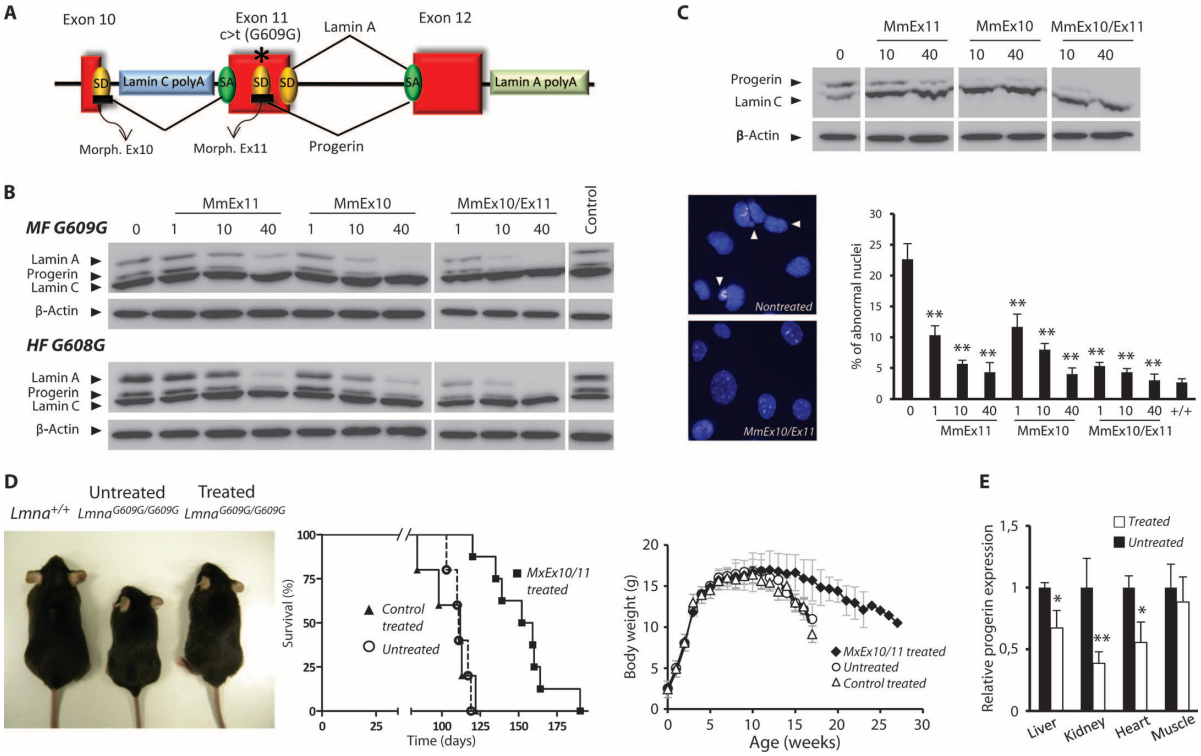

Fig. 4. Prevention of progeroid phenotypes upon treatment with antisense morpholino oligonucleotides. (**A**) Schematic representation of the morpholino-based strategy for *Lmna* splicing modulation. (**B**) Western (immuno) blot analysis of mouse *G609G/+* fibroblasts (MF) treated with varying concentrations of morpholinos MmEx10 and MmEx11 (top panel). AG01972c HGPS fibroblasts (HF) treated with varying concentrations of morpholinos HsEx10 and HsEx11 (bottom panel). Lamin A, lamin C, and progerin were detected with a monoclonal antibody against lamin A/C (Manlac-1). β-Actin was used as a loading control. As a specificity control, human morpholinos were used in mouse cells and mouse morpholinos were used in human cells at their maximum concentrations. (**C**) Nuclear envelope architecture analyzed in an *Lmna*$^{G609G/G609G}$ fibroblast cell line treated with varying concentrations (μM) of MmEx10 and MmEx11 morpholinos. Top panel shows Western blot analysis of lamin A/C in morpholino-treated cells. Bottom panel shows a quantitative analysis of nuclear abnormalities (right) and a representative photograph (left) of *Lmna*$^{G609G/G609G}$-untreated and morpholino-treated cells. White arrowheads indicate representative examples of abnormal nuclei. For each morpholino concentration, 300 nuclei were analyzed. Mean values are represented and error bars indicate SDs. $^{**}P < 0.01$ (two-tailed Student's t test) compared to values of untreated cells. (**D**) Representative photograph of a 3-month-old *Lmna*$^{+/+}$ mouse, a *Lmna*$^{G609G/G609G}$ mouse, and a *Lmna*$^{G609G/G609G}$ mouse treated with a combination of MmEx10-MmEx11 (6 mg/kg per day) (left panel). Kaplan-Meier survival plot (middle-left panel) showing a significant increase in life span in MmEx10-MmEx11–treated ($n = 8$) compared with untreated ($n = 5$) and control vivo-morpholino–treated *Lmna*$^{G609G/G609G}$ mice ($n = 5$) ($P < 0.01$ for the comparison between MmEx10-MmEx11–treated and nontreated *Lmna*$^{G609G/G609G}$ mice; $P < 0.01$ for the comparison between MmEx10-MmEx11 and control-treated *Lmna*$^{G609G/G609G}$ mice; log-rank/Mantel-Cox test). Middle-right panel shows a body weight versus age plot of untreated, control vivo-morpholino–treated, and MmEx10-MmEx11 vivo-morpholino–treated *Lmna*$^{G609G/G609G}$ mice. Mean values are represented and error bars indicate SDs ($P < 0.01$ for the comparison between MmEx10-MmEx11–treated and untreated *Lmna*$^{G609G/G609G}$ mice; $P < 0.01$ for the comparison between MmEx10-MmEx11–treated and control-treated *Lmna*$^{G609G/G609G}$ mice; ANOVA test). (**E**) qRT-PCR analysis of progerin mRNA in various tissues from MmEx10-11 vivo-morpholino–treated ($n = 3$) and untreated *Lmna*$^{G609G/G609G}$ ($n = 3$) mice. mRNA levels were normalized to the mean of untreated animals. Error bars indicate SDs. $^{*}P < 0.05$; $^{**}P < 0.01$ (two-tailed Student's t test).

DISCUSSION

We have previously provided preclinical proof of principle that the combined use of statins (pravastatin) and aminobisphosphonates (zoledronate) could ameliorate several HGPS parameters, including growth, bone density, and survival, by reducing progerin prenylation (*20*). On the basis of these findings, together with additional work from other groups (*19*), two clinical trials were designed and are ongoing in children affected with HGPS (ClinicalTrials.gov #NCT00731016 and #NCT00916747). These therapeutic approaches are aimed at reducing progerin toxicity by pharmacologically inhibiting its prenylation, whereas the one we propose in this study aims to lower the intracellular quantities of the mutant protein itself. The preclinical in vivo success of this approach in the $Lmna^{G609G}$ knock-in mouse model, which most closely mimics the genetics and pathophysiology of HGPS in patients, represents a fundamental proof of concept in the field of progeria therapeutics.

We have shown that $Lmna^{G609G}$ knock-in mice constitute a valuable model for the study of human accelerated aging syndromes because they recapitulate most of the described alterations associated with HGPS. The accumulation of progerin in $Lmna^{G609G/G609G}$ tissues is responsible for a progeroid syndrome characterized by a shortened life span, reduced body weight, and bone and cardiovascular abnormalities. The cardiovascular phenotype evident in the $Lmna^{G609G}$ mice resembles that of HGPS patients, as assessed by the loss of VSMCs and the alterations in ECG parameters. These similarities are a unique feature of this animal model when compared with previously available models of HGPS (*38*) and may facilitate further studies about the role of A-type lamins in cardiovascular pathophysiology during normal and pathological aging.

In addition, $Lmna^{G609G}$ knock-in mice may help to clarify the relevance of systemic factors as regulators of aging. Recent work has pinpointed metabolic alterations in several mouse progeria models (*15*, *21*, *27*, *39*). Accordingly, $Lmna^{G609G/G609G}$ animals also exhibited changes in several metabolic parameters, including blood insulin, leptin, and adiponectin concentrations, which are probably related to the altered glucose and lipid metabolism displayed by these mice. Likewise, $Lmna^{G609G/G609G}$ showed a marked dysregulation of the somatotroph axis, with a reduction and increase in blood levels of IGF-1 and GH, respectively, a situation that resembles a GH resistance condition known as Laron syndrome (*40*, *41*).

We have also demonstrated in this work that the combined administration of two antisense oligonucleotides that block the aberrant splicing in *Lmna* caused by the c.1827C>T;p.Gly609Gly mutation reduces progerin amounts in vivo. The fact that we could not observe a significant reduction of progerin levels in skeletal muscle could be the result of lower vivo-morpholino uptake in this tissue compared with liver or kidney, in which progerin expression was markedly downregulated. Notably, we have also shown that progerin reduction mediated by vivo-morpholino treatment significantly expands the life expectancy of $Lmna^{G609G/G609G}$ mice and ameliorates most phenotypical and molecular alterations in these animals relative to untreated mice, including a significant reduction in the expression of p53 target genes and a normalization of blood glucose levels.

Together, these findings provide an in vivo demonstration of the feasibility of ameliorating the characteristic alterations caused by progerin-linked premature aging through splicing modulation. Our results also suggest that these reagents might be tested in a future clinical trial for the treatment of HGPS. Setting up of therapeutic trials for rare diseases such as progeroid syndromes (*38*, *42*) is extremely challenging because of the lack of extensive clinical longitudinal studies with homogeneous evaluation parameters on cohorts of patients, which hinders the definition of homogeneous therapeutic outcome measures and endpoints. Also, multicentric trials are difficult to organize because of the very low number of patients within a single country, which hampers the strict application of identical protocols in various participating clinical investigation centers.

These difficulties have often prevented translation from established therapeutic proofs of principle to phase 1 and 2 clinical trials. However, the ongoing clinical trials in HGPS patients mentioned above have demonstrated the feasibility of designing and conducting a therapeutic trial for progeria and may serve as a basis for the design of a novel protocol that tests the oligonucleotides used in the present study. Furthermore, the development of this splicing-directed protocol for HGPS treatment may be facilitated by antisense oligonucleotide–based therapies that have already displayed preclinical efficacy in several other diseases (*43*) and are being currently tested in clinical trials for Duchenne muscular dystrophy (*44*).

MATERIALS AND METHODS

Gene targeting of *Lmna* gene

DNA fragments for the arms of the gene-targeting vector were generated by PCR of genomic DNA from 129/Ola embryonic stem (ES) cells. A 4.4-kb 5′-homology arm, spanning from exon 3 to the middle of exon 10, was amplified and cloned in the 5′-polylinker of a modified PGKNeotpalox2 vector into which we had previously introduced the *thymidine kinase* selection gene. Next, we cloned the 5.6-kb 3′-homology arm, which spanned from exon 10 to the end of the gene, in the 3′-polylinker of PGKNeotpalox2. To this end, we amplified and cloned two subfragments. The first one, which spanned to the end of exon 11, was amplified with a reverse oligonucleotide that contained the c.1827C>T mutation. Vector integrity was verified by DNA sequencing and restriction mapping. The targeting vector was linearized and electroporated into strain 129/Ola ES cells. To identify clones that carried the targeted $Lmna^{LCS}$ allele, we performed Southern (DNA) blot analysis of Hind III– and Bsp HI–digested genomic DNA. The probes detected 9.8- and 10.5-kb fragments, respectively, in the recombinant allele. Mouse genotyping was performed by PCR of genomic DNA with the following oligonucleotides: 5′-AAGGGGCTGGGAGGACAGAG-3′, 5′-AGTAGAAGGTGGCGCGAAGG-3′, and 5′-AGCATGCAATAGGGTGGAAGGA-3′. The PCR fragment consisted of 340 base pairs (bp) from the $Lmna^{LCS}$ allele and 100 bp from the wild-type allele. Targeted 129/Ola ES cells were microinjected into C57BL/6 mouse blastocysts to produce chimeric mice that were then crossed with C57BL/6 mice to generate heterozygous $Lmna^{LCS}$ mice. Electroporation of the targeting vector and microinjection of ES cells were performed in the facilities available at Centre D'Immunologie de Marseille-Luminy (Marseille-Luminy, France) under the supervision of B. Malissen. To generate mice that carry the $Lmna^{G609G}$ allele, we crossed $Lmna^{LCS}$ mice with transgenic mice that express constitutive cytomegalovirus Cre recombinase (Jackson Laboratory), and we verified cassette excision by PCR. The nomenclature for the description of sequence variants follows the Human Genome Variation Society guidelines given at http://www.hgvs.org/mutnomen/. The reference sequences used for

sequence variation description were as follows: human *LMNA* NM_170707.2 and mouse *Lmna* NM_001002011.2.

Animal experiments

We performed animal experiments in accordance with the guidelines of the Committee for Animal Experimentation of the Universidad de Oviedo and the Regional Ethics Committee for Animal Experimentation (Provence Committee). μCT analyses of bones were performed with a μCT Skyscan 1172 system (Skyscan). Forepaw strength of $Lmna^{G609G/G609G}$, $Lmna^{G609G/+}$, and $Lmna^{+/+}$ male mice was measured with a strain gauge sensor (Bioseb). We administrated combined vivo-morpholinos (Gene Tools, LLC) MmEx10-MmEx11 at a concentration of 6 mg/kg each in phosphate-buffered saline (PBS) through tail vein injection twice per week. Control vivo-morpholino was administrated according to the same routine at a concentration of 12 mg/kg in PBS. Mice were treated for 12 weeks, starting at the age of 6 weeks. Treatment with vehicle alone or control vivo-morpholinos did not produce any apparent damage or stress in control mice. For histology analysis, we fixed samples with 4% paraformaldehyde in PBS, processed the resulting preparations into serial paraffin sections, and stained each with either 4′,6-diamidino-2-phenylindole (DAPI) or hematoxylin and eosin (H&E).

Genomic and transcriptional characterization

DNA was extracted from mouse tails following standard procedures. Genotyping was performed with the following primers: DNA-Mm-Lmna forward, 5′-GGTTCCCACTGCAGCGGCTC-3′ (exon 11), and DNA-Mm-Lmna reverse, 5′-GGACCCCACTCCCTTGGGCT-3′ (intron 11). Direct sequencing was performed with an ABI Prism 3130XL automatic sequencer (Applied Biosystems). Total RNA was extracted with PureLink RNA Mini Kit (Invitrogen) and treated with deoxyribonuclease (Invitrogen). Total RNA (500 ng) was retrotranscribed with the high-capacity reverse transcription kit (Applied Biosystems). PCR primers that encompassed exon 11 were used for both amplification and sequencing: Mm-Lmna 10 forward, 5′-AGAGCTCCTCCATCACCACCGT-3′, and Mm-Lmna 12 reverse, 5′-TGCCTGGCAGGTCCCAGATT-3′.

Morpholino sequences

The morpholino oligonucleotides used in this study were as follows: MmEx10 (5′-GCTGCCACTCACACGGTGGTGATGG-3′), MmEx11 (5′-GGATCCACCCACCTGGGCTCCCGCT-3′), and a negative control (5′-CCTCTTACCTCAGTTACAATTTATA-3′) for mouse cells and in vivo experiments, and HsEx10 (5′-GCTACCACTCACGTGGTGGTGATGG-3′) and HsEx11 (5′-GGGTCCACCCACCTGGGCTCCTGAG-3′) for human cell experiments (Gene Tools, LLC).

Cell culture

We extracted mouse fibroblasts from 8-week-old ears as previously described (*32*). Human skin fibroblasts from control subjects (AG10803) and patients who carried the HGPS p.Gly608Gly mutation (AG01972c) were obtained from the Coriell Cell Repository. We maintained all cultures in Dulbecco's modified Eagle's medium (Gibco) supplemented with 10% fetal bovine serum (Gibco) and 1% antibiotic-antimycotic (Gibco). For transfection of the morpholinos, we followed the manufacturer's instructions (Gene Tools, LLC). Briefly, cells were plated at a high density (80%), and varying amounts of each morpholino were added to the cell cultures. Next, we added *endoporter* reagent at a final concentration of 6 μM (Gene Tools, LLC). Cells were retransfected 48 hours later following the same routine. Western (immuno) blot and inmunofluorescence analyses were performed 96 hours after the first transfection of the morpholinos. Analyses in primary mouse fibroblasts were performed at P5 and in HGPS human fibroblasts at passage 16.

Western (immuno) blot analysis

Cultured cells were washed twice with 1× PBS and resuspended in 2× Laemmli buffer. Tissues were snap-frozen in liquid nitrogen. Frozen tissues (~50 mg in each sample) were homogenized in 300 μl of 100 mM tris-HCl (pH 7.4), 2% SDS, and 50 mM EDTA with a Polytron homogenizer. Protein concentration was evaluated with the bicinchoninic acid technique (Pierce BCA Protein Assay Kit). Equal amounts of proteins were loaded onto 8% SDS-polyacrylamide gels. After electrophoresis, gels were electrotransferred onto nitrocellulose membranes or Immobilon-FL polyvinylidene fluoride membranes (Millipore), blocked with 5% nonfat dry milk in TBS-T buffer [20 mM tris (pH 7.4), 150 mM NaCl, and 0.05% Tween 20] or in Odyssey Blocking Buffer diluted 1:1 in PBS for 1 hour at room temperature, and incubated overnight at 4°C or 1 hour at room temperature with various primary antibodies: 1:500 monoclonal anti–lamin A/C (Manlac-1, provided by G. Morris), 1:1000 goat polyclonal anti–lamin A/C (sc-20681 and sc-6215, Santa Cruz Biotechnology), 1:40,000 monoclonal anti–glyceraldehyde-3-phosphate dehydrogenase (GAPDH) (MAB374, Millipore), 1:10,000 anti–α-tubulin (T6074, Sigma), or 1:10,000 anti–β-actin (AC-40, Sigma). Finally, blots were incubated with 1:10,000 goat anti-mouse horseradish peroxidase (HRP) (Jackson ImmunoResearch Laboratories) in 1.5% nonfat milk in TBS-T or 1:15,000 IR-Dye 800–conjugated secondary donkey anti-goat and anti-mouse antibodies in Odyssey blocking buffer. Then, we washed and developed the immunoreactive bands with Immobilon Western chemiluminescent HRP substrate (Millipore). For IR-Dye 800 detection, an Odyssey Infrared Imaging System (LI-COR Biosciences) was used.

Immunofluorescence analysis

Cells were fixed in 4% paraformaldehyde solution, rinsed in PBS, and permeabilized with 0.5% Triton X-100. A different permeabilization step was needed for γH2AX staining, which was performed with a 0.1% sodium citrate and 0.1% Triton X-100 solution. The antibodies used were anti–lamin A/C (Manlac-1, 1:50) or anti-γH2AX (Millipore, 1:300). Cells were incubated with primary antibodies diluted in PBS (supplemented with 1% bovine serum albumin) for 1 to 3 hours at 25°C. After washes with PBS, slides were incubated with 1:100 rhodamine-conjugated donkey anti-mouse secondary antibody (Jackson ImmunoResearch Laboratories) for 1 hour at 25°C. After the final washes, nuclei were counterstained with DAPI (Roche), and slides were mounted in Vectashield mounting medium (Vector). Microphotographs were recorded with an Axioplan-2 Zeiss fluorescent microscope (Zeiss), and images were captured with a charge-coupled device camera (Photometrics SenSys). The nuclei of progeroid and normal fibroblasts were then counted (n = 300 for each experiment).

RNA preparation and quantitative RT-PCR

Collected tissue was immediately homogenized in TRIzol reagent (Invitrogen) and processed through alcohol precipitation. RNA pellets were then washed in cold 75% ethanol and resuspended in nuclease-free water (Ambion), and the samples were quantified and evaluated

for purity (260-nm/280-nm ratio) with a NanoDrop ND-1000 spectrophotometer. cDNA was synthesized with 1 to 4 μg of total RNA with the ThermoScript RT-PCR system (Invitrogen). For detection of aberrant splicing of the *Lmna* gene, the following oligonucleotides were used: Lmna-9F (5′-GTGGAAGGCGCAGAACACCT-3′) and Lmna-12R (5′-GTGAGGGGGGAGCAGGTG-3′). The oligonucleotides used for specific amplification of the lamin C–encoding mRNA transcript were Lmna-7F (5′-CCAGCCCTACCTCGCAGC-3′) and Lmna-10R (5′-GCGGCGGCTGCCACTCAC-3′) (*23*). Mouse *Gapdh* mRNA was used as an endogenous control, and the corresponding cDNA was amplified with the following primers: Gapdh-F (5′-GTGCAGTGCCAGCCTCGTCC-3′) and Gapdh-R (5′-GCCACTGCAAATGGCAGCCC-3′). Quantitative RT-PCR (qRT-PCR) was carried out in triplicate for each sample with 20 ng of cDNA, TaqMan Universal PCR Master Mix, and 1 μl of the specific TaqMan custom gene expression assay solution for the gene of interest (Applied Biosystems). For the mouse progerin qRT-PCR experiments, the following oligonucleotides and probe were used: MmProgerin_fwd (5′-TGAGTACAACCTGCGCTCAC-3′), MmProgerin_rev (5′-TGGCAGGTCCCAGATTACAT-3′), and MmProgerin_probe (5′-CGGGAGCCCAGAGCTCCCAGAA-3′). As an internal control for the amount of template cDNA used, gene expression was normalized to amounts obtained for the mouse *Gapdh* endogenous control.

Heart analysis and blood pressure

We anesthetized mice with 2.5% sevoflurane and used a Vevo 2100 transthoracic echocardiograph equipped with a 30-MHz mouse ultrasound probe to assess left ventricular function and ECG parameters (PR and QRS intervals) with the VevoStrain software (Visual Sonic). Blood pressure and heart rate were measured with a noninvasive automated tail-cuff device (Visitech System BP2000). Mice were trained on a daily basis for 1 week, and then measurements were taken on a weekly basis at the same time in the morning. For more accuracy, the first 10 of 20 measurements were discarded, and mean values of the last 10 measurements for individual mice were used for analysis.

Blood and plasma parameters

Animals were starved for 6 hours before measurement to avoid any possible alteration in blood glucose concentrations as a result of food intake. Blood glucose was measured with an Accu-Chek glucometer (Roche Diagnostics) using blood from the tail vein. For other measured parameters, blood was extracted directly from the mandibular sinus after anesthetizing mice with isoflurane. To obtain plasma, we centrifuged blood immediately after collection at 3000*g* at 4°C, and we collected the supernatant and stored it at −20°C until analysis. Plasma IGF-1 concentrations were determined with the Quantikine ELISA (enzyme-linked immunosorbent assay) kit (R&D Systems), whereas plasma GH concentrations were measured with the Linco ELISA kit. For plasma insulin, leptin, and adiponectin measurements, we used Millipore ELISA Kits. All protocols were performed according to the manufacturer's instructions.

Transcriptional profiling

Total RNA was isolated with an RNeasy kit (Qiagen). Double-stranded cDNA was synthesized with the SuperScript cDNA synthesis kit (Invitrogen). In vitro transcription was carried out with the Bioarray high-yield RNA transcript labeling kit (Enzo Diagnostics). The biotin-labeled complementary RNA (cRNA) was purified, fragmented, and hybridized to a GeneChip Mouse Gene 1.0 ST Array (Affymetrix). Washing and scanning were performed with a Fluidics Station 400 and GeneChip Scanner (Affymetrix). After scanning, raw data were processed with the RMAExpress program (http://RMAExpress.bmbolstad.com) using default settings.

Gene set enrichment analysis

GSEA was performed as described in the original citation (*31*). For data analysis, we used GSEA release 2.06 and MSigDB release 2.5 (http://www.broadinstitute.org/gsea/index.jsp). Weighted enrichment scores were calculated with gene expression lists ranked by signal-to-noise ratio. The maximum gene set size was set to 500 genes; the minimum gene set size was set to 20 genes; the number of permutations was set to 1000. Analyses were performed with a collection of gene sets from curated genes and canonical pathways. Selected enriched pathways had a relaxed false discovery rate of ≤0.25 and $P \leq 0.01$.

Statistical analysis

We performed statistical analysis of the differences between mouse cohorts or treated and untreated cells with a two-tailed Student's *t* test. In experiments with more than two groups, differences were analyzed by multifactorial one-way analysis of variance (ANOVA). We performed statistical analysis on the differences between positive nuclei in indirect immunofluorescence experiments with ANOVA and Cohen's *d* Ryan test. The analysis of covariance (ANCOVA) with the body mass as the covariate was used to analyze the grip strength test results. We used Microsoft Excel or GraphPad Prism software for calculations and expressed the results as the means ± SDs.

SUPPLEMENTARY MATERIAL

www.sciencetranslationalmedicine.org/cgi/content/full/3/106/106ra107/DC1

Fig. S1. Genomic sequencing of *Lmna* exon 11 in $Lmna^{+/+}$, $Lmna^{G609G/+}$, and $Lmna^{G609G/G609G}$ mice.

Fig. S2. Western (immuno) blot analysis of human control fibroblasts (AG10803), human HGPS fibroblasts (AG01972c), and tissues from $Lmna^{+/+}$, $Lmna^{G609G/+}$, and $Lmna^{G609G/G609G}$ mice.

Fig. S3. Phenotypic characterization of $Lmna^{LCS/LCS}$ mice.

Fig. S4. Organ size evaluation in 3-month-old $Lmna^{G609G/G609G}$ versus $Lmna^{+/+}$ mice.

Fig. S5. μCT analysis of bone alterations in $Lmna^{G609G/G609G}$ mice.

Fig. S6. Cardiovascular phenotype of $Lmna^{G609G/G609G}$ mice.

Fig. S7. Enrichment score plots from GSEA-extracted representative pathways containing genes enriched in $Lmna^{G609G/G609G}$ mice samples.

Fig. S8. Enrichment score plots of GSEA-extracted representative pathways containing genes enriched in $Lmna^{+/+}$ mice samples.

Fig. S9. Nuclear envelope architecture analyzed in an HGPS fibroblast cell line (AG01972c) treated with HsEx10 and HsEx11 morpholinos.

Fig. S10. RT-PCR analysis in tissues from $Lmna^{+/+}$, untreated $Lmna^{G609G/G609G}$, and MmEx10-11–treated $Lmna^{G609G/G609G}$ and $Lmna^{G609G/+}$ mice.

Fig. S11. Western (immuno) blot analysis of lamin A/C in tissues from treated and untreated $Lmna^{G609G/G609G}$ mice.

Fig. S12. Phenotypic characterization of MmEx10-11–treated $Lmna^{G609G/G609G}$ mice.

Table S1. Affymetrix Mouse Gene 1.0 ST probes showing the greatest increase or decrease ($P < 0.005$) in liver from $Lmna^{G609G/G609G}$ mutant mice.

REFERENCES AND NOTES

1. R. C. Hennekam, Hutchinson–Gilford progeria syndrome: Review of the phenotype. *Am. J. Med. Genet. A* **140**, 2603–2624 (2006).
2. M. A. Merideth, L. B. Gordon, S. Clauss, V. Sachdev, A. C. Smith, M. B. Perry, C. C. Brewer, C. Zalewski, H. J. Kim, B. Solomon, B. P. Brooks, L. H. Gerber, M. L. Turner, D. L. Domingo, T. C. Hart, J. Graf, J. C. Reynolds, A. Gropman, J. A. Yanovski, M. Gerhard-Herman, F. S. Collins, E. G. Nabel, R. O. Cannon III, W. A. Gahl, W. J. Introne, Phenotype and course of Hutchinson–Gilford progeria syndrome. *N. Engl. J. Med.* **358**, 592–604 (2008).

3. A. De Sandre-Giovannoli, R. Bernard, P. Cau, C. Navarro, J. Amiel, I. Boccaccio, S. Lyonnet, C. L. Stewart, A. Munnich, M. Le Merrer, N. Lévy, Lamin a truncation in Hutchinson-Gilford progeria. *Science* **300**, 2055 (2003).
4. M. Eriksson, W. T. Brown, L. B. Gordon, M. W. Glynn, J. Singer, L. Scott, M. R. Erdos, C. M. Robbins, T. Y. Moses, P. Berglund, A. Dutra, E. Pak, S. Durkin, A. B. Csoka, M. Boehnke, T. W. Glover, F. S. Collins, Recurrent de novo point mutations in lamin A cause Hutchinson–Gilford progeria syndrome. *Nature* **423**, 293–298 (2003).
5. H. J. Worman, R. Foisner, The nuclear envelope from basic biology to therapy. *Biochem. Soc. Trans.* **38**, 253–256 (2010).
6. Y. Gruenbaum, A. Margalit, R. D. Goldman, D. K. Shumaker, K. L. Wilson, The nuclear lamina comes of age. *Nat. Rev. Mol. Cell Biol.* **6**, 21–31 (2005).
7. P. Scaffidi, T. Misteli, Lamin A-dependent nuclear defects in human aging. *Science* **312**, 1059–1063 (2006).
8. C. R. Burtner, B. K. Kennedy, Progeria syndromes and ageing: What is the connection? *Nat. Rev. Mol. Cell Biol.* **11**, 567–578 (2010).
9. A. M. Pendás, Z. Zhou, J. Cadiñanos, J. M. Freije, J. Wang, K. Hultenby, A. Astudillo, A. Wernerson, F. Rodríguez, K. Tryggvason, C. López-Otín, Defective prelamin A processing and muscular and adipocyte alterations in Zmpste24 metalloproteinase–deficient mice. *Nat. Genet.* **31**, 94–99 (2002).
10. M. O. Bergo, B. Gavino, J. Ross, W. K. Schmidt, C. Hong, L. V. Kendall, A. Mohr, M. Meta, H. Genant, Y. Jiang, E. R. Wisner, N. Van Bruggen, R. A. Carano, S. Michaelis, S. M. Griffey, S. G. Young, *Zmpste24* deficiency in mice causes spontaneous bone fractures, muscle weakness, and a prelamin A processing defect. *Proc. Natl. Acad. Sci. U.S.A.* **99**, 13049–13054 (2002).
11. S. H. Yang, M. O. Bergo, J. I. Toth, X. Qiao, Y. Hu, S. Sandoval, M. Meta, P. Bendale, M. H. Gelb, S. G. Young, L. G. Fong, Blocking protein farnesyltransferase improves nuclear blebbing in mouse fibroblasts with a targeted Hutchinson–Gilford progeria syndrome mutation. *Proc. Natl. Acad. Sci. U.S.A.* **102**, 10291–10296 (2005).
12. R. Varga, M. Eriksson, M. R. Erdos, M. Olive, I. Harten, F. Kolodgie, B. C. Capell, J. Cheng, D. Faddah, S. Perkins, H. Avallone, H. San, X. Qu, S. Ganesh, L. B. Gordon, R. Virmani, T. N. Wight, E. G. Nabel, F. S. Collins, Progressive vascular smooth muscle cell defects in a mouse model of Hutchinson–Gilford progeria syndrome. *Proc. Natl. Acad. Sci. U.S.A.* **103**, 3250–3255 (2006).
13. Y. Wang, A. A. Panteleyev, D. M. Owens, K. Djabali, C. L. Stewart, H. J. Worman, Epidermal expression of the truncated prelamin A causing Hutchinson–Gilford progeria syndrome: Effects on keratinocytes, hair and skin. *Hum. Mol. Genet.* **17**, 2357–2369 (2008).
14. H. Sagelius, Y. Rosengardten, M. Hanif, M. R. Erdos, B. Rozell, F. S. Collins, M. Eriksson, Targeted transgenic expression of the mutation causing Hutchinson–Gilford progeria syndrome leads to proliferative and degenerative epidermal disease. *J. Cell Sci.* **121**, 969–978 (2008).
15. G. Mariño, A. P. Ugalde, N. Salvador-Montoliu, I. Varela, P. M. Quirós, J. Cadiñanos, I. van der Pluijm, J. M. Freije, C. López-Otín, Premature aging in mice activates a systemic metabolic response involving autophagy induction. *Hum. Mol. Genet.* **17**, 2196–2211 (2008).
16. J. Espada, I. Varela, I. Flores, A. P. Ugalde, J. Cadiñanos, A. M. Pendás, C. L. Stewart, K. Tryggvason, M. A. Blasco, J. M. Freije, C. López-Otín, Nuclear envelope defects cause stem cell dysfunction in premature-aging mice. *J. Cell Biol.* **181**, 27–35 (2008).
17. H. J. Worman, L. G. Fong, A. Muchir, S. G. Young, Laminopathies and the long strange trip from basic cell biology to therapy. *J. Clin. Invest.* **119**, 1825–1836 (2009).
18. F. G. Osorio, I. Varela, E. Lara, X. S. Puente, J. Espada, R. Santoro, J. M. Freije, M. F. Fraga, C. López-Otín, Nuclear envelope alterations generate an aging-like epigenetic pattern in mice deficient in Zmpste24 metalloprotease. *Aging Cell* **9**, 947–957 (2010).
19. S. H. Yang, M. Meta, X. Qiao, D. Frost, J. Bauch, C. Coffinier, S. Majumdar, M. O. Bergo, S. G. Young, L. G. Fong, A farnesyltransferase inhibitor improves disease phenotypes in mice with a Hutchinson-Gilford progeria syndrome mutation. *J. Clin. Invest.* **116**, 2115–2121 (2006).
20. I. Varela, S. Pereira, A. P. Ugalde, C. L. Navarro, M. F. Suárez, P. Cau, J. Cadiñanos, F. G. Osorio, N. Foray, J. Cobo, F. de Carlos, N. Lévy, J. M. Freije, C. López-Otín, Combined treatment with statins and aminobisphosphonates extends longevity in a mouse model of human premature aging. *Nat. Med.* **14**, 767–772 (2008).
21. G. Mariño, A. P. Ugalde, A. F. Fernández, F. G. Osorio, A. Fueyo, J. M. Freije, C. López-Otín, Insulin-like growth factor 1 treatment extends longevity in a mouse model of human premature aging by restoring somatotroph axis function. *Proc. Natl. Acad. Sci. U.S.A.* **107**, 16268–16273 (2010).
22. K. Cao, J. J. Graziotto, C. D. Blair, J. R. Mazzulli, M. R. Erdos, D. Krainc, F. S. Collins, Rapamycin reverses cellular phenotypes and enhances mutant protein clearance in Hutchinson-Gilford progeria syndrome cells. *Sci. Transl. Med.* **3**, 89ra58 (2011).
23. P. Scaffidi, T. Misteli, Reversal of the cellular phenotype in the premature aging disease Hutchinson-Gilford progeria syndrome. *Nat. Med.* **11**, 440–445 (2005).
24. L. G. Fong, J. K. Ng, J. Lammerding, T. A. Vickers, M. Meta, N. Coté, B. Gavino, X. Qiao, S. Y. Chang, S. R. Young, S. H. Yang, C. L. Stewart, R. T. Lee, C. F. Bennett, M. O. Bergo, S. G. Young, Prelamin A and lamin A appear to be dispensable in the nuclear lamina. *J. Clin. Invest.* **116**, 743–752 (2006).
25. C. L. Navarro, J. Cadiñanos, A. De Sandre-Giovannoli, R. Bernard, S. Courrier, I. Boccaccio, A. Boyer, W. J. Kleijer, A. Wagner, F. Giuliano, F. A. Beemer, J. M. Freije, P. Cau, R. C. Hennekam, C. López-Otín, C. Badens, N. Lévy, Loss of ZMPSTE24 (FACE-1) causes autosomal recessive restrictive dermopathy and accumulation of lamin A precursors. *Hum. Mol. Genet.* **14**, 1503–1513 (2005).
26. J. S. Hale, R. L. Frock, S. A. Mamman, P. J. Fink, B. K. Kennedy, Cell-extrinsic defective lymphocyte development in *Lmna*$^{-/-}$ mice. *PLoS One* **5**, e10127 (2010).
27. R. Mostoslavsky, K. F. Chua, D. B. Lombard, W. W. Pang, M. R. Fischer, L. Gellon, P. Liu, G. Mostoslavsky, S. Franco, M. M. Murphy, K. D. Mills, P. Patel, J. T. Hsu, A. L. Hong, E. Ford, H. L. Cheng, C. Kennedy, N. Nunez, R. Bronson, D. Frendewey, W. Auerbach, D. Valenzuela, M. Karow, M. O. Hottiger, S. Hursting, J. C. Barrett, L. Guarente, R. Mulligan, B. Demple, G. D. Yancopoulos, F. W. Alt, Genomic instability and aging-like phenotype in the absence of mammalian SIRT6. *Cell* **124**, 315–329 (2006).
28. M. Olive, I. Harten, R. Mitchell, J. K. Beers, K. Djabali, K. Cao, M. R. Erdos, C. Blair, B. Funke, L. Smoot, M. Gerhard-Herman, J. T. Machan, R. Kutys, R. Virmani, F. S. Collins, T. N. Wight, E. G. Nabel, L. B. Gordon, Cardiovascular pathology in Hutchinson-Gilford progeria: Correlation with the vascular pathology of aging. *Arterioscler. Thromb. Vasc. Biol.* **30**, 2301–2309 (2010).
29. W. E. Stehbens, B. Delahunt, T. Shozawa, E. Gilbert-Barness, Smooth muscle cell depletion and collagen types in progeric arteries. *Cardiovasc. Pathol.* **10**, 133–136 (2001).
30. T. Dechat, K. Pfleghaar, K. Sengupta, T. Shimi, D. K. Shumaker, L. Solimando, R. D. Goldman, Nuclear lamins: Major factors in the structural organization and function of the nucleus and chromatin. *Genes Dev.* **22**, 832–853 (2008).
31. A. Subramanian, P. Tamayo, V. K. Mootha, S. Mukherjee, B. L. Ebert, M. A. Gillette, A. Paulovich, S. L. Pomeroy, T. R. Golub, E. S. Lander, J. P. Mesirov, Gene set enrichment analysis: A knowledge-based approach for interpreting genome-wide expression profiles. *Proc. Natl. Acad. Sci. U.S.A.* **102**, 15545–15550 (2005).
32. I. Varela, J. Cadiñanos, A. M. Pendás, A. Gutiérrez-Fernández, A. R. Folgueras, L. M. Sánchez, Z. Zhou, F. J. Rodríguez, C. L. Stewart, J. A. Vega, K. Tryggvason, J. M. Freije, C. López-Otín, Accelerated ageing in mice deficient in Zmpste24 protease is linked to p53 signalling activation. *Nature* **437**, 564–568 (2005).
33. B. Liu, J. Wang, K. M. Chan, W. M. Tjia, W. Deng, X. Guan, J. D. Huang, K. M. Li, P. Y. Chau, D. J. Chen, D. Pei, A. M. Pendas, J. Cadiñanos, C. López-Otín, H. F. Tse, C. Hutchison, J. Chen, Y. Cao, K. S. Cheah, K. Tryggvason, Z. Zhou, Genomic instability in laminopathy-based premature aging. *Nat. Med.* **11**, 780–785 (2005).
34. L. Zhong, A. D'Urso, D. Toiber, C. Sebastian, R. E. Henry, D. D. Vadysirisack, A. Guimaraes, B. Marinelli, J. D. Wikstrom, T. Nir, C. B. Clish, B. Vaitheesvaran, O. Iliopoulos, I. Kurland, Y. Dor, R. Weissleder, O. S. Shirihai, L. W. Ellisen, J. M. Espinosa, R. Mostoslavsky, The histone deacetylase Sirt6 regulates glucose homeostasis via Hif1α. *Cell* **140**, 280–293 (2010).
35. J. Summerton, Morpholino antisense oligomers: The case for an RNase H-independent structural type. *Biochim. Biophys. Acta* **1489**, 141–158 (1999).
36. M. K. Parra, S. Gee, N. Mohandas, J. G. Conboy, Efficient in vivo manipulation of alternative pre-mRNA splicing events using antisense morpholinos in mice. *J. Biol. Chem.* **286**, 6033–6039 (2011).
37. P. A. Morcos, Y. Li, S. Jiang, Vivo-Morpholinos: A non-peptide transporter delivers Morpholinos into a wide array of mouse tissues. *Biotechniques* **45**, 613–614 (2008).
38. F. G. Osorio, A. J. Obaya, C. López-Otín, J. M. Freije, Accelerated ageing: From mechanism to therapy through animal models. *Transgenic Res.* **18**, 7–15 (2009).
39. L. J. Niedernhofer, G. A. Garinis, A. Raams, A. S. Lalai, A. R. Robinson, E. Appeldoorn, H. Odijk, R. Oostendorp, A. Ahmad, W. van Leeuwen, A. F. Theil, W. Vermeulen, G. T. van der Horst, P. Meinecke, W. J. Kleijer, J. Vijg, N. G. Jaspers, J. H. Hoeijmakers, A new progeroid syndrome reveals that genotoxic stress suppresses the somatotroph axis. *Nature* **444**, 1038–1043 (2006).
40. Z. Laron, Laron syndrome (primary growth hormone resistance or insensitivity): The personal experience 1958–2003. *J. Clin. Endocrinol. Metab.* **89**, 1031–1044 (2004).
41. A. P. Ugalde, G. Mariño, C. López-Otín, Rejuvenating somatotropic signaling: A therapeutical opportunity for premature aging? *Aging* **2**, 1017–1022 (2010).
42. X. S. Puente, V. Quesada, F. G. Osorio, R. Cabanillas, J. Cadiñanos, J. M. Fraile, G. R. Ordóñez, D. A. Puente, A. Gutiérrez-Fernández, M. Fanjul-Fernández, N. Lévy, J. M. Freije, C. López-Otín, Exome sequencing and functional analysis identifies *BANF1* mutation as the cause of a hereditary progeroid syndrome. *Am. J. Hum. Genet.* **88**, 650–656 (2011).
43. S. M. Hammond, M. J. Wood, Genetic therapies for RNA mis-splicing diseases. *Trends Genet.* **27**, 196–205 (2011).
44. S. Cirak, V. Arechavala-Gomeza, M. Guglieri, L. Feng, S. Torelli, K. Anthony, S. Abbs, M. E. Garralda, J. Bourke, D. J. Wells, G. Dickson, M. J. Wood, S. D. Wilton, V. Straub, R. Kole, S. B. Shrewsbury, C. Sewry, J. E. Morgan, K. Bushby, F. Muntoni, Exon skipping and dystrophin restoration in patients with Duchenne muscular dystrophy after systemic phosphorodiamidate morpholino oligomer treatment: An open-label, phase 2, dose-escalation study. *Lancet* **378**, 595–605 (2011).

RESEARCH ARTICLE

45. **Acknowledgments:** We thank G. Velasco, A. Fueyo, A. Ramsay, J. Valcárcel, M. S. Fernández, P. Roubertoux, M. G. Mattei, C. Tardieu, P. Cau, P. Roll, M. J. Andrés-Manzano, J. M. González, B. Malissen, and L. J. Jiménez-Borreguero for their support and assistance. **Funding:** This work was supported by grants from Ministerio de Ciencia e Innovación-Spain, PCTI-FICYT Asturias, European Union (FP7 MicroEnviMet), Botín Foundation, Red de Investigación en Enfermedades Cardiovasculares (RECAVA), Institut National de la Santé et de la Recherche Médicale, Agence Nationale de la Recherche, and Association Française contre les Myopathies. The Instituto Universitario de Oncología is supported by Obra Social Cajastur and Acción Transversal del Cáncer-Red Temática de Investigación Cooperativa en Cáncer (RTICC). **Author contributions:** F.G.O., C.L.N., I.C.L.-M., C.B., A.D.S.-G., and J.T. carried out animal experiments. J. Cadiñanos and J.M.P.F. designed and generated the targeting vector. F.G.O., P.M.Q., I.V., C.L.N., and D.D. performed molecular biology and cell culture–based studies. J.R., G.G., and V.A. carried out cardiovascular analyses. F.d.C. and J. Cobo conducted μCT analysis. C.L.-O., J.M.P.F., and N.L. were responsible for designing and supervising the project. C.L.-O., F.G.O., J.M.P.F., and N.L. wrote the manuscript. **Competing interests:** The authors declare that they have no competing interests. **Accession numbers:** RNA expression data are available at the Gene Expression Omnibus repository (accession number GSE32609).

Submitted 30 June 2011
Accepted 20 September 2011
Published 26 October 2011
10.1126/scitranslmed.3002847

Citation: F. G. Osorio, C. L. Navarro, J. Cadiñanos, I. C. López-Mejía, P. M. Quirós, C. Bartoli, J. Rivera, J. Tazi, G. Guzmán, I. Varela, D. Depetris, F. de Carlos, J. Cobo, V. Andrés, A. De Sandre-Giovannoli, J. M. P. Freije, N. Lévy, C. López-Otín, Splicing-directed therapy in a new mouse model of human accelerated aging. *Sci. Transl. Med.* **3**, 106ra107 (2011).

III. Characterization of epigenetic alterations in accelerated aging

Epigenetic alterations constitute a critical hallmark of aging. Thus, epigenetic regulation is essential not only for the establishment but also for the maintenance of biological states, and consequently it shows a prominent role in the aging process. In this work, we focused on the study of the epigenetic alterations shown by *Zmpste24*-deficient mice, identifying age-associated alterations in methylation status as well as in posttranslational modifications of histones H2B and H4. Moreover, we found that these alterations are associated with important transcriptional changes occurring in this animal model in cell cycle regulation and in metabolic pathways. Finally, we demonstrated the reversibility of epigenetic alterations through pharmacological intervention, providing proof-of-principle about epigenetic-based therapies in aging.

Article 4. Fernando G. Osorio*, Ignacio Varela*, Ester Lara, Xose S. Puente, Jesús Espada, Raffaella Santoro, José M. P. Freije, Mario F. Fraga and Carlos López-Otín. "Nuclear envelope alterations generate an aging-like epigenetic pattern in mice deficient in Zmpste24 metalloprotease".

*Contributed equally to this work.

Aging Cell. 2010 Dec; 9(6):947-57.

Personal contribution to this work

I contributed with Dr. Ignacio Varela to the different *in vitro* and *in vivo* studies included in this article. Similarly, I participated in the discussion of the experiments, analysis of the data, preparation of the figures and writing of the manuscript under the supervision of Dr. José M.P. Freije and Dr. Carlos López-Otín.

Aging Cell (2010) pp1–11 Doi: 10.1111/j.1474-9726.2010.00621.x

Nuclear envelope alterations generate an aging-like epigenetic pattern in mice deficient in Zmpste24 metalloprotease

Fernando G. Osorio,[1] Ignacio Varela,[1] Ester Lara,[2] Xose S. Puente,[1] Jesús Espada,[3] Raffaella Santoro,[4] José M. P. Freije,[1] Mario F. Fraga[5] and Carlos López-Otín[1]

[1]Departamento de Bioquímica y Biología Molecular and [2]Unidad de Epigenética, Instituto Universitario de Oncología, Universidad de Oviedo, 33006-Oviedo, Spain
[3]Instituto de Investigaciones Biomédicas ''Alberto Sols'', Consejo Superior de Investigaciones Científicas-Universidad Autónoma de Madrid, 28029-Madrid, Spain
[4]Institute of Veterinary Biochemistry and Molecular Biology, University of Zürich, Winterthurerstrasse 190, Zürich 8057, Switzerland
[5]Centro Nacional de Biotecnología, Consejo Superior de Investigaciones Científicas-Universidad Autónoma de Madrid, 28029-Madrid, Spain

Summary

Mutations in the nuclear envelope protein lamin A or in its processing protease ZMPSTE24 cause human accelerated aging syndromes, including Hutchinson–Gilford progeria syndrome. Similarly, *Zmpste24*-deficient mice accumulate unprocessed prelamin A and develop multiple progeroid symptoms, thus representing a valuable animal model for the study of these syndromes. *Zmpste24*-deficient mice also show marked transcriptional alterations associated with chromatin disorganization, but the molecular links between both processes are unknown. We report herein that *Zmpste24*-deficient mice show a hypermethylation of rDNA that reduces the transcription of ribosomal genes, being this reduction reversible upon treatment with DNA methyltransferase inhibitors. This alteration has been previously described during physiological aging in rodents, suggesting its potential role in the development of the progeroid phenotypes. We also show that *Zmpste24*-deficient mice present global hypoacetylation of histones H2B and H4. By using a combination of RNA sequencing and chromatin immunoprecipitation assays, we demonstrate that these histone modifications are associated with changes in the expression of several genes involved in the control of cell proliferation and metabolic processes, which may contribute to the plethora of progeroid symptoms exhibited by *Zmpste24*-deficient mice. The identification of these altered genes may help to clarify the molecular mechanisms underlying aging and progeroid syndromes as well as to define new targets for the treatment of these dramatic diseases.

Key words: aging; histone acetylation; lamina; methylation; progeria; proteolysis.

Introduction

Hutchinson–Gilford progeria syndrome (HGPS) is an accelerated aging process characterized by short stature, low body weight, early hair loss, lack of subcutaneous fat, scleroderma, decreased joint mobility, osteolysis, atherosclerosis, and premature death (Hennekam, 2006; Merideth *et al.*, 2008). Hutchinson–Gilford progeria syndrome belongs to an array of human disorders collectively known as laminopathies, caused by defects in components of the nuclear lamina and including Emery-Dreifuss muscular dystrophy, limb-girdle muscular dystrophy, dilated cardiomyopathy, Charcot-Marie-Tooth disease, Dunningan-type familial partial lipodystrophy, and mandibuloacral dysplasia (Navarro *et al.*, 2006; Ramirez *et al.*, 2007). Around 80% of patients with HGPS have the same de novo silent point mutation (G608G: GGC->GGT) in exon 11 of *LMNA* gene that encodes lamins A and C. This mutation activates a cryptic donor splice site, eliminating 150 bp of exon 11 and generating a truncated lamin A isoform known as progerin/LAdelta50 (De Sandre-Giovannoli *et al.*, 2003; Eriksson *et al.*, 2003).

Lamin A post-translational processing includes prenylation, cleavage of the C-terminal tripeptide, methylation of the prenylated C-terminal cysteine residue, and finally, the proteolytic removal of the C-terminal prenylated peptide by the metalloproteinase FACE-1/ZMPSTE24 (Pendas *et al.*, 2002). The target sequence of this last proteolytic event is included in the region deleted in progerin, and consequently progerin undergoes normally the initial steps of lamin A maturation but the prenylated peptide cannot be excised. Thus, the HGPS mutation causes the accumulation of permanently prenylated progerin, which leads to structural alterations in the nuclear envelope and its associated chromatin (De Sandre-Giovannoli *et al.*, 2003; Eriksson *et al.*, 2003). Similarly, disruption of the

Correspondence
Carlos López-Otín, Departamento de Bioquímica y Biología Molecular, Facultad de Medicina, Universidad de Oviedo, 33006-Oviedo, Spain. Tel.: +34 985104201; fax: +34 985103564; e-mail: clo@uniovi.es Or Mario F. Fraga, Centro Nacional de Biotecnología, CSIC, Universidad Autónoma, 28029-Madrid, Spain. Tel.: +34 985109475; fax: +34 985109495; e-mail: mffraga@cnb.csic.es
FGO and IV have contributed equally to this work.

Accepted for publication *5 August 2010*

murine *Zmpste24* gene prevents the cleavage of the lamin A prenylated peptide, leading to the accumulation of farnesylated prelamin A in the nuclear envelope. Prelamin accumulation in *Zmpste24*-deficient mice causes nuclear architecture abnormalities, shortened lifespan, and a progeroid phenotype that recapitulates most HGPS symptoms (Bergo *et al.*, 2002; Pendas *et al.*, 2002). Consequently, *Zmpste24*-deficient mice constitute a valuable animal model to study the mechanisms underlying the development of progeroid syndromes and to investigate possible therapeutic approaches for these pathologies. The transcriptional profiles of *Zmpste24*-deficient tissues and HGPS cells have been investigated, leading to the identification of signaling alterations that could be implicated in the onset of the progeroid phenotypes (Csoka *et al.*, 2004; Varela *et al.*, 2005; Osorio *et al.*, 2009). Significantly, the production of progerin, accompanied by some of these transcriptional alterations, has been detected in the context of physiological aging (Scaffidi & Misteli, 2006). These findings support the use of progeroid animal models such as *Zmpste24*-deficient mice to investigate the molecular mechanisms underlying the manifestations of normal and pathological aging. Nevertheless, despite the intense research in this field, little is known about the link between the alterations in nuclear structure and dynamics and the transcriptional deregulation detected in laminopathies. As nuclear structure is essential for a correct epigenetic pattern and because anomalous epigenetic signaling could be an important determinant of cellular senescence and organism aging (Issa, 2003; Sinclair & Oberdoerffer, 2009; Gravina & Vijg, 2010), we hypothesized that epigenetic alterations could be involved in the development of HGPS symptoms. In agreement with this hypothesis, changes in the methylation pattern of histone H3 have been recently described in HGPS cells but the relevance of these changes remains largely unknown (Scaffidi & Misteli, 2005; Shumaker *et al.*, 2006; Dechat *et al.*, 2008).

In the present work, we describe that the abnormalities in nuclear structure and dynamics caused by *Zmpste24*-deficiency lead to the accumulation of characteristic epigenetic marks such as rDNA hypermethylation and histone hypoacetylation. Based on these findings, together with the observation that similar abnormalities also occur during physiological aging, we propose that chromatin disorganization generates a characteristic aging-like epigenetic pattern which contributes to the transcriptional deregulation associated with both normal and accelerated aging.

Results

Zmpste24-deficiency causes hypermethylation of ribosomal DNA

DNA methylation and histone post-translational modifications are the most widely analyzed epigenetic changes. The relationship between DNA methylation and aging is complex. Early studies suggested the occurrence of a global decrease in DNA methylation associated with physiological aging (Wilson & Jones, 1983). By contrast, other works have revealed that an overall decrease in DNA methylation is not a common feature of mammalian aging, and changes in this regard are circumscribed to a specific subset of genes (Tawa *et al.*, 1992; Tra *et al.*, 2002; Fuke *et al.*, 2004). Further studies have even shown that several loci in CpG islands gain methylation with age (Christensen *et al.*, 2009; Maegawa *et al.*, 2010). To evaluate the putative occurrence of DNA-methylation alterations in *Zmpste24*$^{-/-}$ progeroid mice, we first analyzed by high-performance capillary electrophoresis (HPCE) the global 5-methylcytosine (5mC) content in liver samples from these mutant mice. As shown in Fig. 1a, we did not observe significant differences in global methylation between *Zmpste24*$^{-/-}$ and control mice. Likewise, we failed to find significant methylation differences in subtelomeric regions or in major satellites located in pericentromeric regions of DNA from *Zmpste24*$^{-/-}$ mice when compared with wild-type animals (Fig. 1b).

To test the possibility that specific alterations in the methylation status of certain DNA loci rather than global changes in DNA methylation, could be linked to the premature aging of *Zmpste24*$^{-/-}$ mice, we investigated the methylation pattern of their ribosomal RNA-encoding genomic regions (rDNA), as several works have shown that alterations in rDNA methylation occur in aging (Johnson *et al.*, 1998; Olson & Dundr, 2005). Ribosomal RNA is synthesized as a 45S pre-rRNA, which is subsequently processed into 18S, 5.8S, 28S, and 5S mature rRNAs. Interestingly, and as can be seen in Fig. 2, bisulfite sequencing analysis revealed a significant trend to hypermethylation of the rDNA units of *Zmpste24*$^{-/-}$ mice, especially in internal regions such as the 28S 5′-region. Remarkably, two CpG sites located at positions -133 and -144 in the Upstream Control Element (UCE) of the rDNA promoter are hypermethylated in *Zmpste24*-deficient animals (Fig. 2). Methylation of these two CpGs is sufficient to inhibit the formation of the Pol I pre-initiation complex, thus blocking rDNA transcription (Chen & Pikaard, 1997; Santoro *et al.*, 2002). Consistent with these results, qRT–PCR experiments revealed a significant reduction in 45S pre-rRNA in *Zmpste24*-deficient animals, which was reverted upon azacitidine treatment (Fig. 3a), providing additional support to the causal role of promoter hypermethylation in this alteration. We next used chromatin immunoprecipitation to examine the amounts of rDNA-associated RNA polymerase I. As shown in Fig. 3b, while the levels of polymerase bound to the promoter region are similar among wild-type and mutant animals, *Zmpste24*$^{-/-}$ mice show a 3-fold reduction in the levels of elongating RNA polymerase I associated with the rDNA coding regions. Collectively, these results indicate that *Zmpste24* deficiency causes a severe dysfunction of rRNA gene activity, which could be implicated in the premature cellular senescence and accelerated aging phenotype observed in these mice (Varela *et al.*, 2005). In agreement with this possibility, rDNA hypermethylation has been reported to occur during physiological aging in rats (Oakes *et al.*, 2003), and a decrease in the rRNA gene activity with age has also been observed in humans (Thomas & Mukherjee, 1996).

Loss of acetylated forms of nucleosome histones in *Zmpste24*$^{-/-}$ mice

Chromatin conformation and transcriptional control are influenced not only by promoter methylation but also by histone post-translational modifications, most notably site-specific methylation and acetylation/deacetylation of histone tails (Shahbazian & Grunstein, 2007). Interestingly, genes potentially involved in the progeroid phenotype of *Zmpste24*-deficient mice, such as p21WAF1 and INK4/ARF, have been described to be regulated by histone acetylation (Archer *et al.*, 1998; Matheu *et al.*, 2005). Consequently, we decided to investigate the modification status of histones in *Zmpste24*-deficient mice. As a first approach to this aim, we used HPCE to analyze H2B and H4 acetylation status. As can be seen in Fig. 4a, *Zmpste24*-deficient mice show a loss of about 15% of global acetylation in histone H4, produced by a reduction in all its monoacetylated, diacetylated, and triacetylated forms. Likewise, and similar to the case of histone H4, *Zmpste24*-deficient mice show an important decrease (about 50%) in global acetylation of histone H2B (Fig. 4b). This decrease mainly derives from a significant loss (about 80%) of the monoacetylated form of H2B. To determine the residue that could be target of this specific loss of acetylation, we carried out mass spectrometry analysis on this fraction. As can be seen in Fig. 5a, we observed a clear decrease in the relative abundance of a peptide corresponding to the first 12 amino acids of the protein which contain one acetyl group at lysine 5, indicating that the loss of H2B monoacetylation occurs mostly at this residue. This conclusion was further confirmed by Western blot analysis with an antibody that specifically recognizes this modification (Fig. 5b). This analysis also showed that this decrease in histone acetylation is not restricted to the liver. As can be seen in Fig. 5b, the same alteration was also present in other tissues from *Zmpste24*-deficient mice.

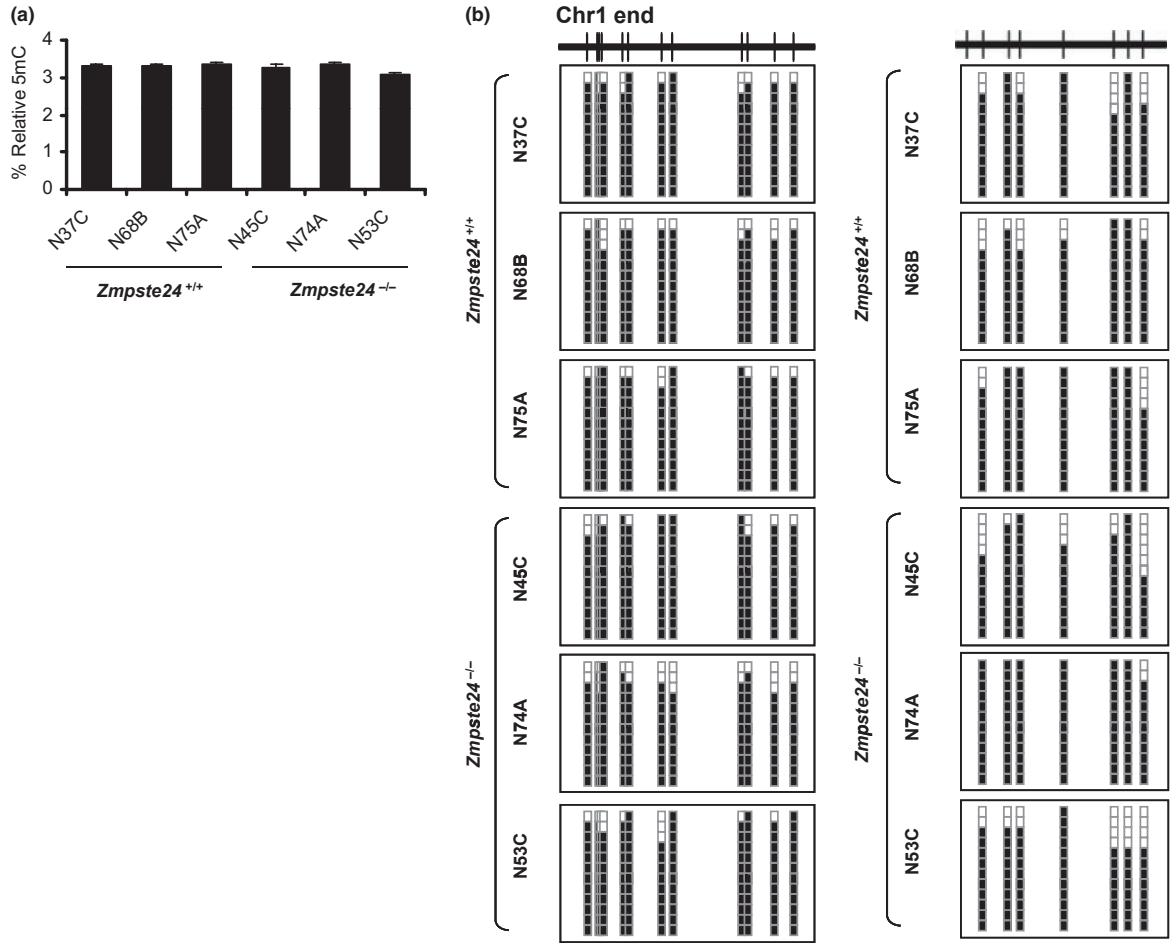

Fig. 1 Global DNA methylation analysis in *Zmpste24*$^{-/-}$ mice. (a) Global 5-methyl-cytosine content analyzed by high-performance capillary electrophoresis (HPCE) in liver samples from representative wild-type (N37C, N68B, and N75A) and *Zmpste24*-deficient mice (N45C, N74A, and N53C). (b) Analysis of the DNA methylation status by bisulfite sequencing of multiple clones (see Experimental procedures) of subtelomeric repeats (left) and major satellites (right) in liver samples from the same control and *Zmpste24*$^{-/-}$ mice as in (a). Distribution of CpG sites within the amplified DNA is shown by vertical bars on and horizontal bar over each panel. Three mice per genotype and 12 clones per mouse were analyzed. Methylated and unmethylated CpG positions are shown as black and white squares, respectively.

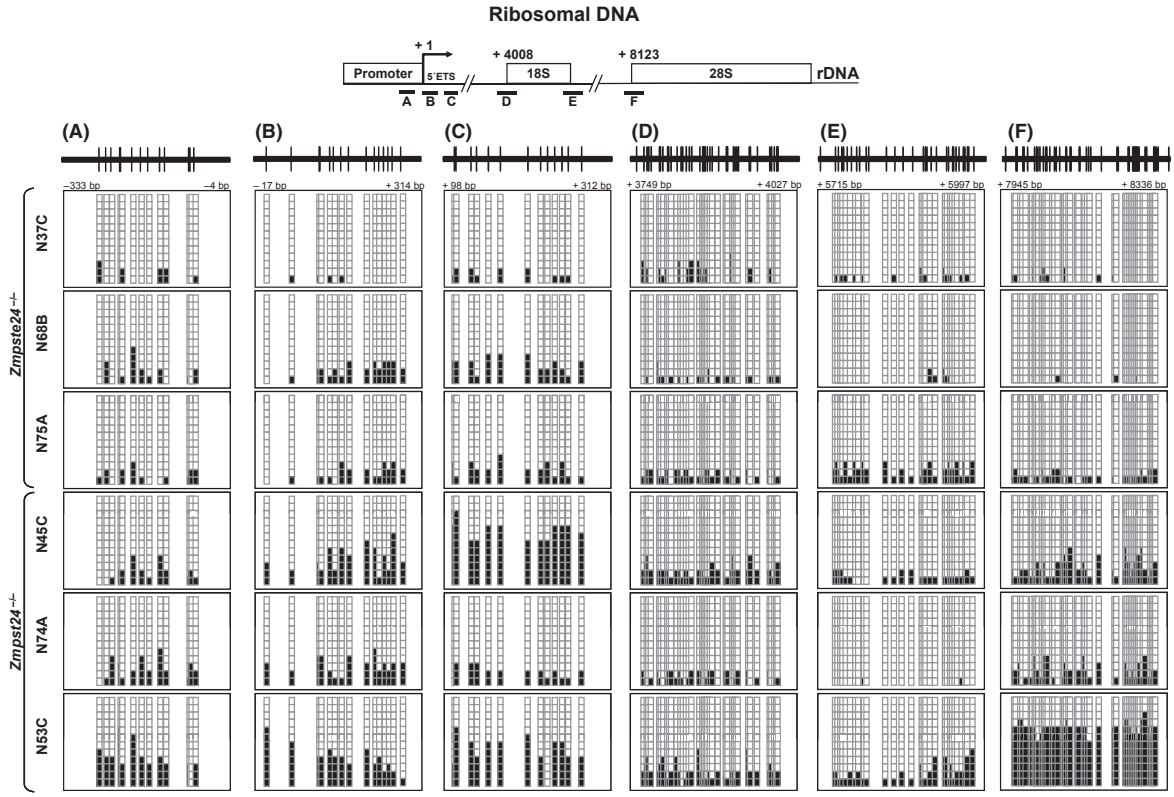

Fig. 2 rDNA methylation analysis in *Zmpste24*$^{-/-}$ mice. Analysis of DNA methylation at ribosomic DNA using bisulfite sequencing of multiple clones in liver DNA samples from *Zmpste24*-deficient mice (N45C, N74A and N53C) and control littermates (N37C, N68B and N75A). Scheme showing the rRNA gene (top), depicting the six regions subjected to methylation analysis (AF); these correspond to the proximal promoter (A-C), and the ends of 18S (D-E) and 28S (F) regions. Three mice per genotype and twelve clones per mouse were analyzed. Methylated and unmethylated CpG positions are represented as black and white squares, respectively.

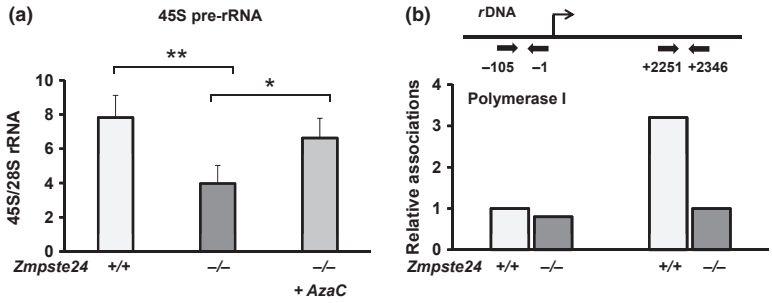

Fig. 3 Transcriptional activity of the rRNA gene in *Zmpste24*$^{-/-}$ mice. (a) qRT–PCR quantification of the precursor rRNA transcript in liver samples from wild-type, *Zmpste24*-deficient animals, and azacitidine-treated *Zmpste24*-deficient mice (AzaC) relative to the levels of 28S rRNA. (b) RNA polymerase I association with the rDNA promoter and internal regions indicated at the top, as determined by chromatin immunoprecipitation of liver samples from *Zmpste24*$^{-/-}$ mice and control littermates. A schematic map of the rRNA gene is included at the top, indicating the position of the two analyzed regions. **P* < 0.05. Error bars represent SEM.

Acetyl-H2B-mediated differential gene regulation in *Zmpste24*$^{-/-}$ mice

The reduction of acetylated forms of nucleosome histones is associated with a stronger association of these nucleosomes with the DNA, which generates a more compacted or silent chromatin state. We hypothesized that the decrease of histone acetylation observed in *Zmpste24*$^{-/-}$ mice could produce both a general decrease in the transcriptional activity of their cells and a deregulation of the expression of specific genes implicated in the generation of the senescence phenotype observed in these animals. Consequently, we performed two independent ChIP-

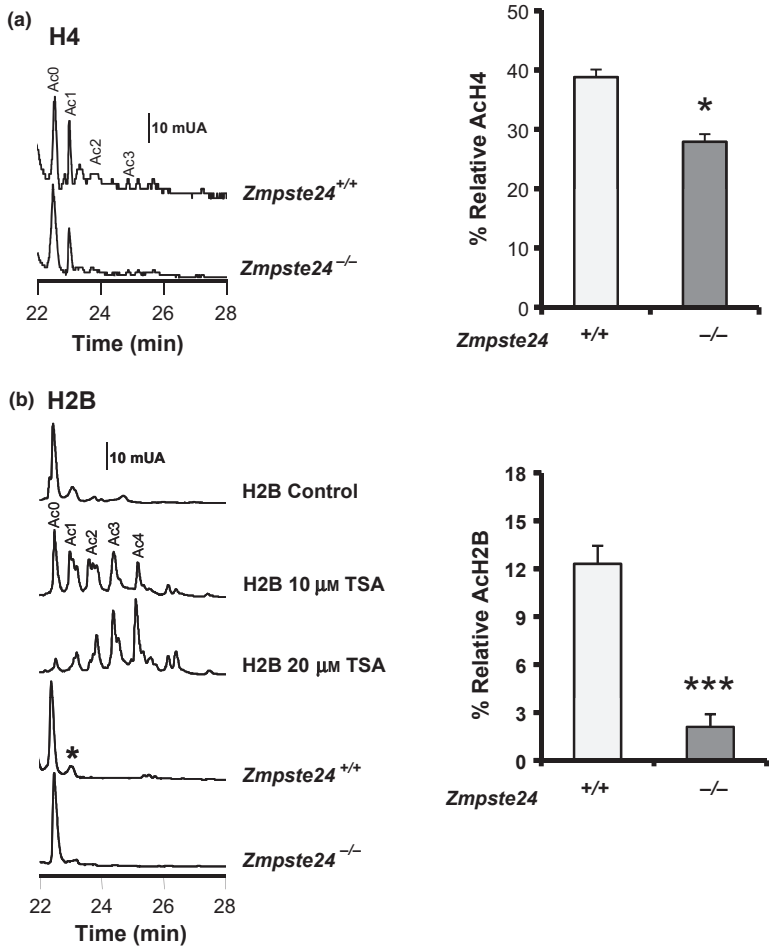

Fig. 4 Histones H4 and H2B acetylation status in *Zmpste24*$^{-/-}$ mice. (a) High-performance capillary electrophoresis (HPCE) analysis of histone H4 post-translational modifications. Representative electropherograms show peaks corresponding to the nonacetylated (Ac0), mono- (Ac1), di- (Ac2), and triacetylated (Ac3) forms of histone H4 in liver samples from wild-type (WT) and *Zmpste24*-deficient mice (left). Relative levels of acetylated histone H4 in two WT and three mutant mice (right). (b) HPCE analysis of histone H2B post-translational modifications. Representative electropherograms corresponding to liver samples from WT and *Zmpste24*-deficient mice are shown, along with samples from HL60 cells treated with the indicated concentrations of the histone deacetylase inhibitor trichostatin A (TSA) (left). Electropherograms of samples treated with TSA show mono-, di-, tri-, and tetra-acetylated forms of histone H2B. Relative levels of acetylated histone H2B in three WT and three mutant mice (right) are shown. *$P < 0.05$; ***$P < 0.001$. Error bars represent SEM.

on-Chip experiments to determine specific genomic regions of association of acetyl-H2B in both *Zmpste24*$^{-/-}$ and control mice. In the first experiment, we compared samples from a *Zmpste24*$^{-/-}$ mice with a control littermate, while for the second experiment we used pools of genomic DNA obtained from three wild-type and three mutant animals, respectively. A complete list of all the probes that showed recurrent differences in enrichment between *Zmpste24*-deficient and control samples can be found in Tables S2 and S3 (Supporting information). Additionally, and to determine if the putative differences in association of acetyl-H2B to specific genomic regions of control and mutant mice could modulate the expression of specific genes, we performed transcriptional profiling on liver samples from a *Zmpste24*$^{-/-}$ mouse and a littermate control. For this purpose, we isolated total liver RNA and used it for expression analysis by ultra-deep RNA sequencing using an Illumina platform (Wilhelm *et al.*, 2008).

A list of key genes that were found recurrently enriched in the samples belonging to control mice compared to *Zmpste24*$^{-/-}$ mice and which also showed a reduced expression in *Zmpste24*-mutant samples is shown in Table 1. Additional validation of these results was performed by qRT–PCR, as shown in Fig. S1 (Supporting information). Interestingly, one of these genes is *Bcl6*, a known inhibitor of the senescence process mediated by p53 (Shvarts *et al.*, 2002). The transcriptional down-regulation of this gene can play a key role in the accelerated senescence phenotype triggered by the activation of p53 observed in *Zmpste24*-deficient mice. We also observed transcriptional down-regulation associated with a decrease in the levels of acetyl-H2B in several genes involved in fatty acid metabolism (*Sec14p*,

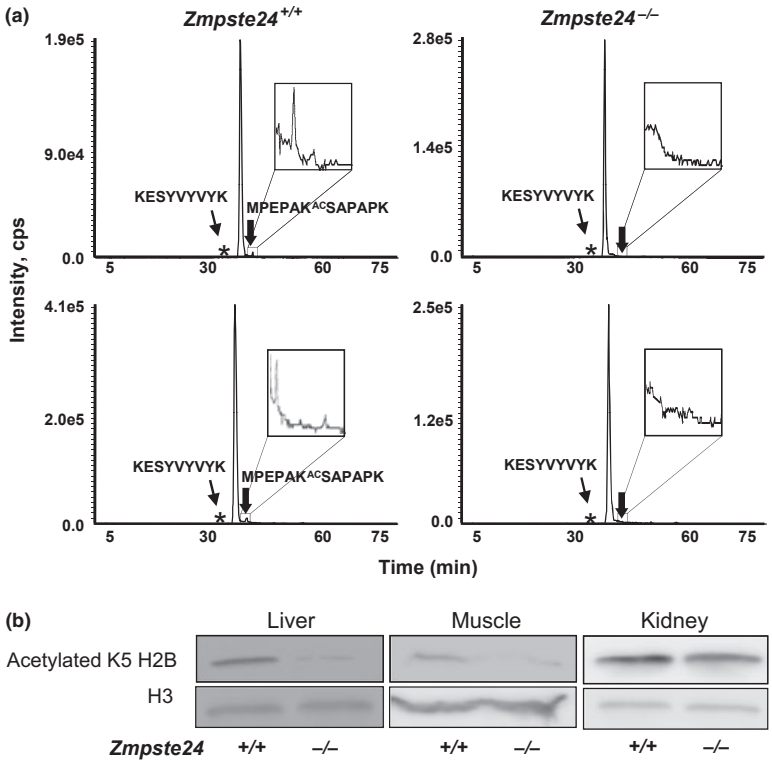

Fig. 5 H2B acetylation in lysine 5 in *Zmpste24*$^{-/-}$ mice. (a) Mass spectrometry identification of the histone H2B residue differentially acetylated in wild-type vs. *Zmpste24*$^{-/-}$ mice. Identification of the peptide MPEPACK^{AC}SAPAPK indicates the presence of acetylated histone H2B at lysine 5 in control samples (left); this peptide is not detected in *Zmpste24*$^{-/-}$ mice (right). Control peptide is shown (*). (b) Western blot analysis of histone H2B acetylation in control and *Zmpste24*-deficient. Histone H3 was used as a loading control.

Table 1 Genes recurrently enriched in either *Zmpste24*$^{+/+}$ (upper half) or *Zmpste24*$^{-/-}$ (lower half) samples that also show changes in expression levels

	ChIP on chip Analysis		*Expression Analysis*	
Gene	Enrichment	*P*-value	*Zmpste24*$^{-/-}$	*Zmpste24*$^{+/+}$
Elovl3	2.399	0.011	0.38	335.02
Cmah	2.188	0.012	0.28	1.82
Ifi47	2.117	0.003	1.94	5.17
6430527G18Rik	2.100	0.011	1.02	2.37
Sec14l2	2.044	0.009	20.69	88.66
Bcl6	1.895	0.002	3.56	6.87
Apoc1	1.689	0.006	2639.22	6902.38
Ppp1r3b	1.622	0.005	3.27	21.41
Cyp2b10	3.579	0.026	70.84	0.11
Fmo2	3.293	0.014	1.75	0.23
Apcs	3.278	0.007	803.57	71.87
Htatip2	2.775	0.009	31.87	5.11
Cyp4a14	2.684	0.019	65.31	5.02
Fgl1	2.554	0.009	1007.95	119.41
Agxt2l1	2.162	0.012	114.41	6.16
Orm1	2.111	0.007	4201.28	528.02

The enrichment value refers to the ratio between the enrichment ratios obtained in *Zmpste24*-deficient and control samples. Control vs. *Zmpste24*$^{-/-}$ in the upper half and *Zmpste24*$^{-/-}$ vs. control in the lower half.

Elovl3, and *Apoc1*) and glycogen metabolism (*Ppp1r3b* and *Cmah*). These alterations may contribute to the lipodystrophy phenotype and the altered metabolic response previously described in *Zmpste24*$^{-/-}$ mice (Pendas *et al.*, 2002; Marino *et al.*, 2008).

In addition to this general decrease in acetylation of the histone H2B, we could also observe specific enrichment of acetyl-H2B in several genes from *Zmpste24*-deficient samples. Some of them are also transcriptionally up-regulated in these progeroid mice. Remarkably, among these genes we have found *Apcs* (Table S3, Supporting information) that has been reported to control chromatin degradation and could be involved in the chromatin abnormalities observed in *Zmpste24*$^{-/-}$ cells (Bickerstaff *et al.*, 1999; Varela *et al.*, 2005). Additionally, we have also found acetyl-H2B-related up-regulation of known proliferation inhibitors such as *Agxt2l1* and *Htatip2* that could contribute to the senescence phenotype. Finally, several genes involved in liver inflammation and detoxification were identified (*Cyp2b10*, *Cyp4a14*, *Orm1*, *Fmo2*, and *Fgl1*). The up-regulation of these genes could indicate that the liver from *Zmpste24*-deficient mice is subjected to a kind of cellular stress that triggers an adaptive metabolic response involving the activation of inflammation and detoxification mechanisms in these progeroid mice.

Discussion

Hutchinson–Gilford progeria syndrome is a premature aging disease characterized by a rapid progression of symptoms such as hair loss, growth retardation, lack of subcutaneous fat, aged-looking skin, osteoporosis, and arteriosclerosis. Patients with HGPS usually die at around 13 years and there is no specific treatment for them (Navarro *et al.*, 2006). Accordingly, analysis of the molecular pathways implicated in the development of this disease has been necessary for developing therapeutic approaches for these patients (Espada *et al.*, 2008; Varela *et al.*, 2008). In this scenario, *Zmpste24*-deficient mice, which also accumulate a farnesylated lamin A precursor, have become an excellent tool for the molecular study of progeria. The use of these mice has allowed to demonstrate that the accumulation of farnesylated prelamin A causes alterations in nuclear structure and chromatin organization, which in turn activate DNA damage sensor pathways that finally lead to the development of the progeroid phenotypes characteristic of *Zmpste24*-mutant mice (Liu *et al.*, 2005; Varela *et al.*, 2005). Nevertheless, the molecular links between the chromatin disorganization and the transcriptional alterations present in these progeroid mice remain unknown. In this work, we report the presence of epigenetic alterations in *Zmpste24*-deficient mice which are related to those observed in physiologically aged mice. We also propose that these epigenetic abnormalities may be implicated in the development of the progeroid phenotype.

Previous studies have reported a significant decrease in global DNA methylation with aging (Wilson & Jones, 1983; Richardson, 2003; Fuke *et al.*, 2004). By contrast, this trend was not observed in our progeroid animal model, in which the total methylcytosine content did not differ significantly from that of control mice. These differences between methylation changes in physiological and accelerated aging could derive from the fact that the loss of global DNA methylation during physiological aging mainly results of the passive demethylation of heterochromatic DNA, because of a progressive loss of efficacy of DNA methyltransferase 1 (Dnmt1) or to the erroneous targeting of this enzyme by other cofactors (Casillas *et al.*, 2003). The shortened lifespan of *Zmpste24*-deficient mice, which develop an evident progeroid phenotype before the decline in Dnmt1 activity occurs, could contribute to explain the absence of global DNA demethylation in this animal model of accelerated aging. Nevertheless, it is remarkable that, in accordance with our observations in this progeroid animal model, a number of works have reported that an aging-associated decline in total methylcytosine content is not a common finding in mammalian tissues (Tawa *et al.*, 1992; Tra *et al.*, 2002; Fuke *et al.*, 2004). Furthermore, very recent studies have demonstrated that several loci present in CpG islands gain methylation with age (Christensen *et al.*, 2009; Maegawa *et al.*, 2010), pointing to the need of detailed analysis of specific genes in specific tissues before raising definitive conclusions about the relevance of methylation changes during normal and pathological aging.

Consistent with this possibility, and in contrast to the absence of alterations in global methylation, we observed a marked hypermethylation of the rDNA loci in *Zmpste24*$^{-/-}$ progeroid mice. This epigenetic mark has been previously described in physiological aging but its precise relevance in this process is largely unknown (Oakes *et al.*, 2003). Our observation that rDNA hypermethylation also occurs in the context of accelerated aging suggests that it could be functionally involved in the development of age-associated phenotypes and consequently it could provide a potential target of anti-progeroid therapies. We hypothesize that down-regulation of rDNA transcription resulting from promoter hypermethylation plays a crucial role in the cellular senescence phenotype observed in both accelerated and physiological aging. Supporting this proposal, it has been described that rDNA hypermethylation is associated with progression-free survival in ovarian and endometrial cancer (Powell *et al.*, 2002; Chan *et al.*, 2005).

In relation to histone modifications, we describe herein that *Zmpste24*-deficient mice present hypoacetylation of histones H2B and H4, which in the case of H2B mostly occurs in the monoacetylated form modified at lysine 5. Although the significance of this loss of acetylation is still unclear, the general trend to a loss of histone acetylation suggests a switch of chromatin structure to a close, inactive conformation, characteristic of quiescent or senescent cellular states, which could contribute to the cellular phenotype observed in these mice. Alternatively, histone modifications can promote specific promoter methylation and regulate DNA transcription even in the absence of methylation, as described in the case of *CDKN1A* locus (Archer *et al.*, 1998; Richon *et al.*, 2004). Finally, we have found a direct correlation between loss of acetylated forms of histone H2B and transcriptional down-regulation of several genes involved in the control of proliferation/senescence such as *Bcl6*, *Apcs*, or *Htatip2*, which can contribute to the senescence phenotype observed in the context of *Zmpste24* deficiency (Varela *et al.*, 2005, 2008). Additionally, the expression of other genes involved in fatty acid and glycogen metabolism is also altered and can contribute to the systemic defects described in *Zmpste24*$^{-/-}$ mice (Marino *et al.*, 2008). Also in this regard, we must emphasize that other histone modifications distinct from loss of H2B and H4 acetylation can also contribute to the multiple alterations observed in the *Zmpste24*$^{-/-}$ progeroid mice and further studies will be required to clarify this question. Nevertheless, the identification of a series of genes with marked expression changes associated with specific histone modifications in tissues from *Zmpste24*$^{-/-}$ mice may help to further clarify the molecular mechanisms underlying aging and progeroid syndromes and to define new targets for the treatment of these devastating diseases.

Experimental procedures

Animals

Face1/Zmpste24-deficient mice were generated and genotyped as described (Pendas *et al.*, 2002). For *in vivo* inhibition of DNA

methylation, 5-azacitidine (2 mg Kg^{-1} day^{-1}) in PBS was administrated intraperitoneally to mice every day for 1 week. Four month-old *Face1/Zmpste24*-deficient mice and littermate controls were sacrificed by cervical dislocation, and their livers were extracted and stored at –80°C until further use. All the procedures were carried out following the guidelines of the animal facility of the Universidad de Oviedo.

Analysis of sequence-specific DNA methylation

The methylation status of specific genomic DNA sequences was established by bisulfite genomic sequencing (Fraga *et al.*, 2005). Following the bisulfite conversion reaction, the DNA sequence was amplified by PCR with primers specific for the bisulfite-converted DNA. The PCR product was cloned and at least ten colonies per sequence were sequenced automatically to determine the methylation status of each sample. The percentage of methylation for each sample was calculated based on the number of clones that showed methylated or unmethylated cytosines. Primer sequences are available as Table S1 (Supporting information).

Quantification of global DNA methylation

5-Methylcytosine (5mC) genomic content was determined by HPCE, as described (Fraga *et al.*, 2002). Briefly, genomic DNA samples were boiled, treated with nuclease P1 (Sigma, St. Quentin Fallavier, France) for 16 h at 37°C and with alkaline phosphatase (Sigma, St. Quentin Fallavier, France) for an additional 2 h at 37°C. After hydrolysis, total cytosine and 5mC content were measured by HPCE using a P/ACE MDQ system (Beckman-Coulter, Beckman-Coulter, Fullerton, CA, USA). Cytosine and methylcytosine were separated and quantified using the sodium dodecylsulfate (SDS) micelle system, based on size, charge, structure, and hydrophobicity differences after the application of specific voltages using a narrow-bore fused silica capillary tube. Relative 5mC content was expressed as a percentage of total cytosine content (methylated and nonmethylated).

Quantification of histone acetylation

Histones were prepared in accordance with established protocols (Turner & Fellows, 1989) and global acetylation at histones H2B and H4 was quantified as previously described (Fraga *et al.*, 2005). Individual histone fractions were extracted from cell nuclei by acid treatment, and then purified by reverse-phase high performance liquid chromatography (HPLC) on a Jupiter C18 column (Phenomenex Inc., Torrance, CA, USA) with an acetonitrile gradient (20–60%) in 0.3% trifluoroacetic acid, using a HPLC gradient system (Beckman-Coulter). This method separates molecules based on their hydrophobicity. Samples were lyophilized and then dissolved in 5 mM DTT to avoid oxidation. Acetylated histone derivatives were resolved by HPCE as described (Fraga *et al.*, 2005). In brief, nonacetylated, mono-, di- and polyacetylated histone derivatives were resolved by HPCE. An uncoated fused silica capillary (60.2 cm × 75 μm, effective length 50 cm; Beckman-Coulter) was used in a CE system (P/ACE MDQ; Beckman-Coulter) connected to a data-processing station (32 Karat Software; Beckman-Coulter). The running buffer was 100 mM phosphate buffer, pH 2.0 containing 0.02% (w/v) HPM-cellulose, and running conditions were 25°C with operating voltages of 12 kV. On-column absorbance was monitored at 214 nm. Before each run, the capillary system was conditioned by washing with 0.1 M NaOH (3 min), with 0.5 M H_2SO_4 (2 min), and equilibrated with running buffer (3 min). Samples were injected under pressure (0.3 psi, 3 s). All samples were analyzed in duplicate and three measurements were made per replicate.

Nano-liquid chromatography and tandem mass spectrometry

The resulting H2B-derived tryptic peptides from control and mutant samples were on line injected onto a C18 reversed-phase micro-column (300 mm ID × 5 mm PepMapTM; LC Packings, Amsterdam, The Netherlands) to remove salts, and then analyzed in a continuous acetonitrile gradient consisting of 0–50% B in 45 min and 50–90% B in 1 min (B = 95% acetonitrile, 0.5% acetic acid in water) on a C18 reversed-phase nano-column (100 mm ID × 15 cm, Discovery®; BIO Wide pore, Supelco, Bellafonte, PA, USA). A flow-rate of 300 nL min^{-1} was used to elute peptides from the reversed-phase nano-column to a PicoTip™ emitter nano-spray needle (New Objective, Woburn, MA, USA) for real-time ionization and peptide fragmentation on a 4000 Q-Trap LC/MS/MS system (Applied Biosystems/MDS Sciex, Concord, ON, Canada) equipped with a nanospray ion source (Protana, Ontario, Canada). Nano-liquid chromatography was automatically performed on an advanced nano-gradient generator (Ultimate nano-HPLC; LC Packings) coupled to an autosampler (Famos; LC Packings). The needle voltage was set at 3000 V. Nitrogen was used as curtain (value of 15) and collision gas (set to high). For the analysis, in the multiple reaction monitoring mode (MRM), Q1 was set on the multiply charged parent ions at the indicated *m/z* values. Q3 was set on the marker filtering signal selected for each parent ion. Collision energy was set to 20. All chromatograms and MS/MS spectra were analyzed by the software packages Analyst 1.4.1 (Applied Biosystems).

ChIP-on-Chip and data analysis

The chromatin immunoprecipitation assay was carried out as described (Fraga *et al.*, 2005) with anti-acK5H2b (Cell Signaling). DNA-protein interactions were fixed using formaldehyde as a crosslinking agent. Crosslinked protein/chromatin was fragmented by sonication into fragments of ~200–800 bp. Protein was then immunoprecipitated from the lysate using a specific antibody. After reversal of crosslinking, proteins were removed, DNA purified and used for ChIP-on-Chip assays. The ChIP on Chip assay was performed on the Agilent Mouse Promoter ChIP-on-chip microarrays with Designs IDs 014716 and 014717

containing probes covering 5.5 kb upstream and 2.5 kb downstream of the transcriptional start sites. Labeling was performed using a BioPrime Total Genomic Labelling System (Invitrogen, Carlsbad, CA, USA) following manufacturer instructions. The hybridization was performed following Agilent manual G4481-90010. The arrays were scanned on a G2565BA DNA microarray scanner (Agilent) and the images were quantified using Agilent Feature Extraction Software v9.5.3. Finally, Agilent ChIP Analytics v1.3.1 was used as analysis software using Whitehead model v1.0 as error model.

RNA sequencing

Transcriptional profiling of livers from *Zmpste24*-deficient and control mice was performed by RNA sequencing. Briefly, total RNA was used for cDNA synthesis and sequenced at The Centre for Applied Genomics, The Hospital for Sick Children, Toronto, Canada, using a GAII instrument following the manufacturer instructions (Illumina). Reads were mapped to the mouse reference genome (mm9) using TopHat and Bowtie (Trapnell *et al.*, 2009), and gene expression was computed using Cufflinks (Trapnell *et al.*, 2010) and mouse gene models from Ensembl v56. Relative expression was expressed as RPKM values (Reads Per Kilobase of transcript per Million mapped reads).

Western blotting

Mice tissues were immediately frozen in liquid nitrogen after extraction and were homogenized in a 20 mM Tris buffer pH 7.4, containing 150 mM NaCl, 1% Triton X-100, 10 mM EDTA, and Complete® protease inhibitor cocktail (Roche Applied Science, Indianapolis, IN, USA). Once homogenized, tissue extracts were centrifuged at 12 000 *g* at 4°C and supernatants were collected. The protein concentration of the supernatant was evaluated by bicinchoninic acid technique (BCA protein assay kit; Pierce Biotechnology, Rockford, IL, USA); 25 μg of protein sample was loaded on 13% SDS-polyacrylamide gels. After electrophoresis, gels were electrotransferred onto nitrocellulose filters, and then the filters were blocked with 5% nonfat dried milk in PBT (phosphate-buffered saline with 0.05% Tween 20) and incubated with anti-acK5H2b (Cell Signaling) and anti-H3 (Abcam) antibodies in 5% BSA in PBT. After three washes with PBT, filters were incubated with the corresponding secondary antibody at 1:10000 dilution in 1.5% milk in PBT and developed with Immobilon Western Chemiluminescent HRP substrate (Millipore).

Acknowledgments

We thank Dr. G. Mariño and Dr. T. Bernal for helpful comments, Dr. I. Grummt for providing reagents, and F. Rodríguez, S. Álvarez, M. Fernández, and D. Álvarez for excellent technical assistance. This work has been supported by grants from Ministerio de Ciencia e Innovación-Spain, Fundación ''M. Botín'', and European Union (FP7 MicroEnviMet). The Instituto Universitario de Oncología is supported by Obra Social Cajastur and Acción Transversal del Cáncer-RTICC.

Author contributions

FGO, IV, EL, JE, and RS carried out the experimental work, FGO, IV, JMPF, and CLO wrote the paper, IV, XSP, MFF, JMPF, and CLO designed the study and were involved in the analysis and interpretation of the data.

References

Archer SY, Meng S, Shei A, Hodin RA (1998) p21(WAF1) is required for butyrate-mediated growth inhibition of human colon cancer cells. *Proc. Natl. Acad. Sci. U.S.A.* **95**, 6791–6796.

Bergo MO, Gavino B, Ross J, Schmidt WK, Hong C, Kendall LV, Mohr A, Meta M, Genant H, Jiang Y, Wisner ER, Van Bruggen N, Carano RA, Michaelis S, Griffey SM, Young SG (2002) Zmpste24 deficiency in mice causes spontaneous bone fractures, muscle weakness, and a prelamin A processing defect. *Proc. Natl. Acad. Sci. U.S.A* **99**, 13049–13054.

Bickerstaff MC, Botto M, Hutchinson WL, Herbert J, Tennent GA, Bybee A, Mitchell DA, Cook HT, Butler PJ, Walport MJ, Pepys MB (1999) Serum amyloid P component controls chromatin degradation and prevents antinuclear autoimmunity. *Nat. Med.* **5**, 694–697.

Casillas MA Jr, Lopatina N, Andrews LG, Tollefsbol TO (2003) Transcriptional control of the DNA methyltransferases is altered in aging and neoplastically-transformed human fibroblasts. *Mol. Cell. Biochem.* **252**, 33–43.

Chan MW, Wei SH, Wen P, Wang Z, Matei DE, Liu JC, Liyanarachchi S, Brown R, Nephew KP, Yan PS, Huang TH (2005) Hypermethylation of 18S and 28S ribosomal DNAs predicts progression-free survival in patients with ovarian cancer. *Clin. Cancer Res.* **11**, 7376–7383.

Chen ZJ, Pikaard CS (1997) Epigenetic silencing of RNA polymerase I transcription: a role for DNA methylation and histone modification in nucleolar dominance. *Genes Dev.* **11**, 2124–2136.

Christensen BC, Houseman EA, Marsit CJ, Zheng S, Wrensch MR, Wiemels JL, Nelson HH, Karagas MR, Padbury JF, Bueno R, Sugarbaker DJ, Yeh RF, Wiencke JK, Kelsey KT (2009) Aging and environmental exposures alter tissue-specific DNA methylation dependent upon CpG island context. *PLoS Genet.* **5**, e1000602.

Csoka AB, English SB, Simkevich CP, Ginzinger DG, Butte AJ, Schatten GP, Rothman FG, Sedivy JM (2004) Genome-scale expression profiling of Hutchinson-Gilford progeria syndrome reveals widespread transcriptional misregulation leading to mesodermal/mesenchymal defects and accelerated atherosclerosis. *Aging Cell* **3**, 235–243.

De Sandre-Giovannoli A, Bernard R, Cau P, Navarro C, Amiel J, Boccaccio I, Lyonnet S, Stewart CL, Munnich A, Le Merrer M, Levy N (2003) Lamin a truncation in Hutchinson-Gilford progeria. *Science* **300**, 2055.

Dechat T, Pfleghaar K, Sengupta K, Shimi T, Shumaker DK, Solimando L, Goldman RD (2008) Nuclear lamins: major factors in the structural organization and function of the nucleus and chromatin. *Genes Dev.* **22**, 832–853.

Eriksson M, Brown WT, Gordon LB, Glynn MW, Singer J, Scott L, Erdos MR, Robbins CM, Moses TY, Berglund P, Dutra A, Pak E, Durkin S, Csoka AB, Boehnke M, Glover TW, Collins FS (2003) Recurrent de novo point mutations in lamin A cause Hutchinson-Gilford progeria syndrome. *Nature* **423**, 293–298.

Espada J, Varela I, Flores I, Ugalde AP, Cadinanos J, Pendas AM, Stewart CL, Tryggvason K, Blasco MA, Freije JM, Lopez-Otin C (2008) Nuclear envelope defects cause stem cell dysfunction in premature-aging mice. *J. Cell Biol.* **181**, 27–35.

Fraga MF, Uriol E, Borja Diego L, Berdasco M, Esteller M, Canal MJ, Rodriguez R (2002) High-performance capillary electrophoretic method for the quantification of 5-methyl 2′-deoxycytidine in genomic DNA: application to plant, animal and human cancer tissues. *Electrophoresis* **23**, 1677–1681.

Fraga MF, Ballestar E, Villar-Garea A, Boix-Chornet M, Espada J, Schotta G, Bonaldi T, Haydon C, Ropero S, Petrie K, Iyer NG, Perez-Rosado A, Calvo E, Lopez JA, Cano A, Calasanz MJ, Colomer D, Piris MA, Ahn N, Imhof A, Caldas C, Jenuwein T, Esteller M (2005) Loss of acetylation at Lys16 and trimethylation at Lys20 of histone H4 is a common hallmark of human cancer. *Nat. Genet.* **37**, 391–400.

Fuke C, Shimabukuro M, Petronis A, Sugimoto J, Oda T, Miura K, Miyazaki T, Ogura C, Okazaki Y, Jinno Y (2004) Age related changes in 5-methylcytosine content in human peripheral leukocytes and placentas: an HPLC-based study. *Ann. Hum. Genet.* **68**, 196–204.

Gravina S, Vijg J (2010) Epigenetic factors in aging and longevity. *Pflugers Arch.* **459**, 247–258.

Hennekam RC (2006) Hutchinson-Gilford progeria syndrome: review of the phenotype. *Am. J. Med. Genet. A* **140**, 2603–2624.

Issa JP (2003) Age-related epigenetic changes and the immune system. *Clin. Immunol.* **109**, 103–108.

Johnson FB, Marciniak RA, Guarente L (1998) Telomeres, the nucleolus and aging. *Curr. Opin. Cell Biol.* **10**, 332–338.

Liu B, Wang J, Chan KM, Tjia WM, Deng W, Guan X, Huang JD, Li KM, Chau PY, Chen DJ, Pei D, Pendas AM, Cadinanos J, Lopez-Otin C, Tse HF, Hutchison C, Chen J, Cao Y, Cheah KS, Tryggvason K, Zhou Z (2005) Genomic instability in laminopathy-based premature aging. *Nat. Med.* **11**, 780–785.

Maegawa S, Hinkal G, Kim HS, Shen L, Zhang L, Zhang J, Zhang N, Liang S, Donehower LA, Issa JP (2010) Widespread and tissue specific age-related DNA methylation changes in mice. *Genome Res.* **20**, 332–340.

Marino G, Ugalde AP, Salvador-Montoliu N, Varela I, Quiros PM, Cadinanos J, van der Pluijm I, Freije JM, Lopez-Otin C (2008) Premature aging in mice activates a systemic metabolic response involving autophagy induction. *Hum. Mol. Genet.* **17**, 2196–2211.

Matheu A, Klatt P, Serrano M (2005) Regulation of the INK4a/ARF locus by histone deacetylase inhibitors. *J. Biol. Chem.* **280**, 42433–42441.

Merideth MA, Gordon LB, Clauss S, Sachdev V, Smith AC, Perry MB, Brewer CC, Zalewski C, Kim HJ, Solomon B, Brooks BP, Gerber LH, Turner ML, Domingo DL, Hart TC, Graf J, Reynolds JC, Gropman A, Yanovski JA, Gerhard-Herman M, Collins FS, Nabel EG, Cannon III RO, Gahl WA, Introne WJ (2008) Phenotype and course of Hutchinson-Gilford progeria syndrome. *N. Engl. J. Med.* **358**, 592–604.

Navarro CL, Cau P, Levy N (2006) Molecular bases of progeroid syndromes. *Hum. Mol. Genet.* **15** (Spec No. 2), R151–R161.

Oakes CC, Smiraglia DJ, Plass C, Trasler JM, Robaire B (2003) Aging results in hypermethylation of ribosomal DNA in sperm and liver of male rats. *Proc. Natl. Acad. Sci. U.S.A* **100**, 1775–1780.

Olson MO, Dundr M (2005) The moving parts of the nucleolus. *Histochem. Cell Biol.* **123**, 203–216.

Osorio FG, Obaya AJ, Lopez-Otin C, Freije JM (2009) Accelerated ageing: from mechanism to therapy through animal models. *Transgenic Res.* **18**, 7–15.

Pendas AM, Zhou Z, Cadinanos J, Freije JM, Wang J, Hultenby K, Astudillo A, Wernerson A, Rodriguez F, Tryggvason K, Lopez-Otin C (2002) Defective prelamin A processing and muscular and adipocyte alterations in Zmpste24 metalloproteinase-deficient mice. *Nat. Genet.* **31**, 94–99.

Powell MA, Mutch DG, Rader JS, Herzog TJ, Huang TH, Goodfellow PJ (2002) Ribosomal DNA methylation in patients with endometrial carcinoma: an independent prognostic marker. *Cancer* **94**, 2941–2952.

Ramirez CL, Cadinanos J, Varela I, Freije JM, Lopez-Otin C (2007) Human progeroid syndromes, aging and cancer: new genetic and epigenetic insights into old questions. *Cell. Mol. Life Sci.* **64**, 155–170.

Richardson B (2003) Impact of aging on DNA methylation. *Ageing Res. Rev.* **2**, 245–261.

Richon VM, Zhou X, Secrist JP, Cordon-Cardo C, Kelly WK, Drobnjak M, Marks PA (2004) Histone deacetylase inhibitors: assays to assess effectiveness *in vitro* and *in vivo*. *Methods Enzymol.* **376**, 199–205.

Santoro R, Li J, Grummt I (2002) The nucleolar remodeling complex NoRC mediates heterochromatin formation and silencing of ribosomal gene transcription. *Nat. Genet.* **32**, 393–396.

Scaffidi P, Misteli T (2005) Reversal of the cellular phenotype in the premature aging disease Hutchinson-Gilford progeria syndrome. *Nat. Med.* **11**, 440–445.

Scaffidi P, Misteli T (2006) Lamin A-dependent nuclear defects in human aging. *Science* **312**, 1059–1063.

Shahbazian MD, Grunstein M (2007) Functions of site-specific histone acetylation and deacetylation. *Annu. Rev. Biochem.* **76**, 75–100.

Shumaker DK, Dechat T, Kohlmaier A, Adam SA, Bozovsky MR, Erdos MR, Eriksson M, Goldman AE, Khuon S, Collins FS, Jenuwein T, Goldman RD (2006) Mutant nuclear lamin A leads to progressive alterations of epigenetic control in premature aging. *Proc. Natl. Acad. Sci. U.S.A* **103**, 8703–8708.

Shvarts A, Brummelkamp TR, Scheeren F, Koh E, Daley GQ, Spits H, Bernards R (2002) A senescence rescue screen identifies BCL6 as an inhibitor of anti-proliferative p19(ARF)-p53 signaling. *Genes Dev.* **16**, 681–686.

Sinclair DA, Oberdoerffer P (2009) The ageing epigenome: damaged beyond repair? *Ageing Res. Rev.* **8**, 189–198.

Tawa R, Ueno S, Yamamoto K, Yamamoto Y, Sagisaka K, Katakura R, Kayama T, Yoshimoto T, Sakurai H, Ono T (1992) Methylated cytosine level in human liver DNA does not decline in aging process. *Mech. Ageing Dev.* **62**, 255–261.

Thomas S, Mukherjee AB (1996) A longitudinal study of human age-related ribosomal RNA gene activity as detected by silver-stained NORs. *Mech. Ageing Dev.* **92**, 101–109.

Tra J, Kondo T, Lu Q, Kuick R, Hanash S, Richardson B (2002) Infrequent occurrence of age-dependent changes in CpG island methylation as detected by restriction landmark genome scanning. *Mech. Ageing Dev.* **123**, 1487–1503.

Trapnell C, Pachter L, Salzberg SL (2009) TopHat: discovering splice junctions with RNA-Seq. *Bioinformatics* **25**, 1105–1111.

Trapnell C, Williams BA, Pertea G, Mortazavi A, Kwan G, van Baren MJ, Salzberg SL, Wold BJ, Pachter L (2010) Transcript assembly and quantification by RNA-Seq reveals unannotated transcripts and isoform switching during cell differentiation. *Nat. Biotechnol.* **28**, 511–515.

Turner BM, Fellows G (1989) Specific antibodies reveal ordered and cell-cycle-related use of histone-H4 acetylation sites in mammalian cells. *Eur. J. Biochem.* **179**, 131–139.

Varela I, Cadinanos J, Pendas AM, Gutierrez-Fernandez A, Folgueras AR, Sanchez LM, Zhou Z, Rodriguez FJ, Stewart CL, Vega JA, Tryggvason K, Freije JM, Lopez-Otin C (2005) Accelerated ageing in mice deficient in Zmpste24 protease is linked to p53 signalling activation. *Nature* **437**, 564–568.

Varela I, Pereira S, Ugalde AP, Navarro CL, Suarez MF, Cau P, Cadinanos J, Osorio FG, Foray N, Cobo J, de Carlos F, Levy N, Freije JM, Lopez-Otin C (2008) Combined treatment with statins and aminobisphosphonates extends longevity in a mouse model of human premature aging. *Nat. Med.* **14**, 767–772.

Wilhelm BT, Marguerat S, Watt S, Schubert F, Wood V, Goodhead I, Penkett CJ, Rogers J, Bahler J (2008) Dynamic repertoire of a eukaryotic transcriptome surveyed at single-nucleotide resolution. *Nature* **453**, 1239–1243.

Wilson VL, Jones PA (1983) DNA methylation decreases in aging but not in immortal cells. *Science* **220**, 1055–1057.

Supporting Information

Additional supporting information may be found in the online version of this article:

Fig. S1 Differential expression of genes associated with acetylated histone H2B in *Zmpste24*-deficient and control mice. RNA levels corresponding to a selection of genes found to be differentially expressed by ultra-deep RNA sequencing were studied by qRT–PCR with specific Taqman probes. (a) Genes up-regulated in control mice. (b) Genes down-regulated in *Zmpste24*-deficient mice. $*P < 0.05$; $**P < 0.01$; $***P < 0.001$. Error bars represent SEM.

Table S1 Oligonucleotides used to amplify bisulfite-modified DNA.

Table S2 Genes recurrently enriched in $Zmpste24^{+/+}$ samples.

Table S3 Genes recurrently enriched in $Zmpste24^{-/-}$ samples.

As a service to our authors and readers, this journal provides supporting information supplied by the authors. Such materials are peer-reviewed and may be re-organized for online delivery, but are not copy-edited or typeset. Technical support issues arising from supporting information (other than missing files) should be addressed to the authors.

IV. Identification of NF-κB signaling as a critical mediator of the aging process

Alterations in cell communication have been causally involved in aging. However, the precise nature of the molecular signals that integrate cell-based and systemic alterations in aging has been largely unknown. In this work, through molecular characterization of two different animal models of accelerated aging, we have uncovered the role of NF-κB signaling as a critical mediator of this function. Thus, NF-κB is hyperactivated as a consequence of nuclear envelope alterations, which induces the secretion of several pro-inflammatory cytokines and causes a systemic inflammation, affecting distant cells and finally leading to homeostasis collapse. Finally, NF-κB inhibition prevented age-associated alterations as well as extended longevity, further illustrating the importance of this mechanism in aging.

Article 5. Fernando G. Osorio, Clea Bárcena, Clara Soria-Valles, Andrew J. Ramsay, Félix de Carlos, Juan Cobo, Antonio Fueyo, José M. P. Freije and Carlos López-Otín. "Nuclear lamina defects cause ATM-dependent NF-κB activation and link accelerated aging to a systemic inflammatory response".

Genes & Development. 2012 Oct 15; 26(20):2311-24.

Personal contribution to this work

I was responsible for most experiments shown in this work. I generated, managed, genotyped and characterized *Zmpste24-RelA* double mutant mice. Likewise, I performed subsequent *in vitro* and *in vivo* studies, including molecular and histological analysis, as well as the different pharmacological approaches performed along the article. Finally, I analyzed the data, prepared the figures and wrote de manuscript under the supervision of Dr. José M.P. Freije and Dr. Carlos López-Otín.

Nuclear lamina defects cause ATM-dependent NF-κB activation and link accelerated aging to a systemic inflammatory response

Fernando G. Osorio,[1] Clea Bárcena,[1] Clara Soria-Valles,[1] Andrew J. Ramsay,[1] Félix de Carlos,[2] Juan Cobo,[2] Antonio Fueyo,[3] José M.P. Freije,[1,4] and Carlos López-Otín[1,4]

[1]Departamento de Bioquímica y Biología Molecular, Facultad de Medicina, Instituto Universitario de Oncología, Universidad de Oviedo, 33006-Oviedo, Spain; [2]Departamento de Cirugía y Especialidades Médico-Quirúrgicas, Instituto Asturiano de Odontología, Universidad de Oviedo, 33006-Oviedo, Spain; [3]Área de Fisiología, Departamento de Biología Funcional, Facultad de Medicina, Instituto Universitario de Oncología, Universidad de Oviedo, 33006-Oviedo, Spain

Alterations in the architecture and dynamics of the nuclear lamina have a causal role in normal and accelerated aging through both cell-autonomous and systemic mechanisms. However, the precise nature of the molecular cues involved in this process remains incompletely defined. Here we report that the accumulation of prelamin A isoforms at the nuclear lamina triggers an ATM- and NEMO-dependent signaling pathway that leads to NF-κB activation and secretion of high levels of proinflammatory cytokines in two different mouse models of accelerated aging (*Zmpste24*$^{-/-}$ and *Lmna*$^{G609G/G609G}$ mice). Causal involvement of NF-κB in accelerated aging was demonstrated by the fact that both genetic and pharmacological inhibition of NF-κB signaling prevents age-associated features in these animal models, significantly extending their longevity. Our findings provide in vivo proof of principle for the feasibility of pharmacological modulation of the NF-κB pathway to slow down the progression of physiological and pathological aging.

[*Keywords*: nuclear envelope; longevity; progeroid laminopathies]

Supplemental material is available for this article.

Received June 5, 2012; revised version accepted September 4, 2012.

Aging is associated with the progressive and irreversible loss of tissue homeostasis. Several stressors have been related to this process, including DNA damage, telomere attrition, or accumulation of damaged macromolecules (Kirkwood 2005; Vijg and Campisi 2008). An exaggerated accumulation of cellular damage or the inefficient ability to respond to stress causes progeroid syndromes, characterized by a precocious manifestation of several features related to human aging (Burtner and Kennedy 2010). Most progeroid syndromes are caused by defective DNA repair mechanisms or by alterations in the nuclear lamina (Ramirez et al. 2007; Hoeijmakers 2009). The nuclear lamina is a complex structure that surrounds and protects the nuclear content, playing important roles in genome regulation, organization, and maintenance (Dechat et al. 2008). Covering the inner face of the nuclear membrane, the nuclear lamina forms a protein network that provides a scaffold for nuclear envelope proteins and chromatin (Gruenbaum et al. 2005; Mekhail and Moazed 2010).

Alterations in the nuclear lamina affect nuclear structure and DNA integrity, leading to defects in DNA replication and repair processes and inducing the accumulation of different types of DNA damage (Worman and Foisner 2010). Thus, several mutations in lamins and lamin-binding proteins have been associated with a subgroup of progeroid syndromes known collectively as progeroid laminopathies (Worman et al. 2010). Among them, Hutchinson-Gilford progeria syndrome (HGPS) is one of the most comprehensively studied. HGPS patients show growth impairment, lipodystrophy, dermal and bone abnormalities, and cardiovascular alterations, leading to a dramatically shortened life span (Hennekam 2006; Merideth et al. 2008). HGPS is primarily caused by a de novo silent mutation within exon 11 of the *LMNA* gene encoding lamin A (c.1824C>T; p.Gly608Gly) (De Sandre-Giovannoli et al. 2003; Eriksson et al. 2003).

Lamin A, a core component of the nuclear lamina, undergoes a complex maturation process, including

[4]**Corresponding authors**
E-mail clo@uniovi.es
E-mail jmpf@uniovi.es
Article published online ahead of print. Article and publication date are online at http://www.genesdev.org/cgi/doi/10.1101/gad.197954.112.

farnesylation, carboxyl methylation, and proteolytic processing by the metalloproteinase ZMPSTE24/FACE-1. The HGPS mutation c.1824C>T activates a cryptic splice donor site, leading to a truncated form of prelamin A, called LAΔ50 or progerin, which lacks a 50-residue-long fragment containing the cleavage site for ZMPSTE24. Accordingly, *Zmpste24*$^{-/-}$ mice show a premature aging phenotype that phenocopies human HGPS (Bergo et al. 2002; Pendas et al. 2002; Osorio et al. 2011a). In all cases, the accumulation of farnesylated forms of prelamin A in the nuclear envelope leads to the nuclear abnormalities and functional defects characteristic of cells from HGPS patients and *Zmpste24*$^{-/-}$ mice. Interestingly, progerin accumulation is also detected during normal aging, thereby adding a new level of interest to the study of the mechanisms that underlie progerin formation and accumulation (Scaffidi and Misteli 2006).

NF-κB transcription factors form a cytoplasmic sensor system responding to not only pathogen attack, but also a variety of external and internal danger signals, such as oxidative stress, hypoxia, and genotoxic stress (Perkins 2007; Hayden and Ghosh 2008). NF-κB active transcription factors are composed of dimeric combinations of members of the Rel family. In mammals, five different Rel family members have been identified: RelA (p65), RelB, c-Rel, NF-κB1 (p50 and its precursor, p105), and NF-κB2 (p52 and its precursor, p100), which can form heterodimers or homodimers (Hayden and Ghosh 2012). Many known stimuli that activate NF-κB require signaling through the conserved IKK complex, consisting of at least two catalytic subunits, IKKα and IKKβ, and a regulatory subunit known as NEMO (also known as IKKγ). Activation of the NF-κB signaling pathway is one of the cellular responses evoked to maintain homeostasis after DNA damage (Janssens and Tschopp 2006). As part of the DNA damage response (DDR), activation of the kinase ataxia telangiectasia mutated (ATM) triggers a signaling pathway involving NEMO to directly link DNA damage events in the nucleus with the cytoplasmic activation of NF-κB (Miyamoto 2011). Thus, upon DNA damage, NEMO undergoes a sequence of post-translational modifications that includes sumoylation, ATM-mediated phosphorylation, and ubiquitylation (Huang et al. 2003; Wu et al. 2006). NEMO trafficking between the cytoplasm and nucleus is a consequence of these modifications and finally results in the activation of the IKK complex and the nuclear translocation of NF-κB active dimers (McCool and Miyamoto 2012).

NF-κB hyperactivation has been related to the aging process (Adler et al. 2007). In addition, aberrant NF-κB activation is well documented in numerous age-associated diseases, including neurodegeneration, osteoporosis, diabetes, sarcopenia, immunosenescence, or atherosclerosis (Tak and Firestein 2001; Le Saux et al. 2012). Given the links between accelerated aging, chronic DDRs, and NF-κB activation (Salminen et al. 2008; Ugalde et al. 2011a; Tilstra et al. 2012), we hypothesized that structural abnormalities in the nuclear envelope could activate the NF-κB pathway. Accordingly, we used two different progeroid mouse models to test this hypothesis and formulate potential therapeutic intervention strategies. Here we report that accumulation of prelamin A or progerin in the nuclear envelope of progeroid mice triggers a signaling pathway involving ATM and NEMO proteins to activate NF-κB. We also demonstrate that NF-κB-driven inflammation is responsible for the development of several important features of progeroid phenotypes. Notably, inhibition of the NF-κB pathway using genetic or pharmacological strategies was able to prevent these alterations, demonstrating the causal involvement of this inflammatory pathway in the pathogenesis of accelerated aging.

Results

Zmpste24-deficient mice show NF-κB hyperactivation

Zmpste24-deficient mice accumulate farnesylated prelamin A at the nuclear envelope and develop a progeroid syndrome that phenocopies most features of HGPS, including growth impairment, lipodystrophy, dermal and bone abnormalities, and shortened life span (Bergo et al. 2002; Pendas et al. 2002). Previous studies in *Zmpste24*$^{-/-}$ mice have revealed that prelamin A accumulation induces cellular senescence as well as important changes in nuclear dynamics (Varela et al. 2005; Osorio et al. 2010). On the other hand, NF-κB activation during aging has been reported in human and mouse tissues as well as in cells from HGPS patients (Adler et al. 2007; Kawahara et al. 2009; Tilstra et al. 2011).

To evaluate the activity of NF-κB in *Zmpste24*-deficient mice, we first analyzed the transcriptional profile of liver tissues from *Zmpste24*$^{-/-}$ and wild-type littermates. By using the gene set enrichment analysis (GSEA) algorithm, we identified a strong positive correlation between the transcriptional changes in tissues from mutant mice and a gene set composed of genes whose promoters contain the recognition sequence for NF-κB transcription factors (Fig. 1A; Supplemental Fig. 1). Next, we analyzed NF-κB activation in vivo in these progeroid mice using a gene reporter-based assay (Fig. 1B; Supplemental Fig. 2). To this end, we hydrodynamically delivered a plasmid vector encoding the firefly luciferase gene under the control of an NF-κB response element in *Zmpste24*$^{-/-}$ and wild-type animals. This approach allowed us to quantify NF-κB activation in vivo by measuring the bioluminescence image obtained from these mice. Remarkably, the bioluminescence signal of *Zmpste24*-deficient mice was >10-fold higher as compared with age-matched control animals (Fig. 1B). NF-κB hyperactivation was further confirmed by NF-κB electrophoretic mobility shift assay (EMSA) using nuclear extracts from livers of *Zmpste24*$^{-/-}$ and control mice (Fig. 1C). Accordingly, reduced levels of the NF-κB inhibitor IκBα were also reproducibly observed in *Zmpste24*-deficient samples (Fig. 1C).

We next examined NF-κB activation in other tissues previously reported to be affected during the development of progeria in *Zmpste24*$^{-/-}$ mice (Pendas et al. 2002; Varela et al. 2005). Thus, EMSA analysis of the thymus, spleen, kidney, and heart revealed an increase of >2.5-fold in NF-κB activity in *Zmpste24*$^{-/-}$ tissues as compared

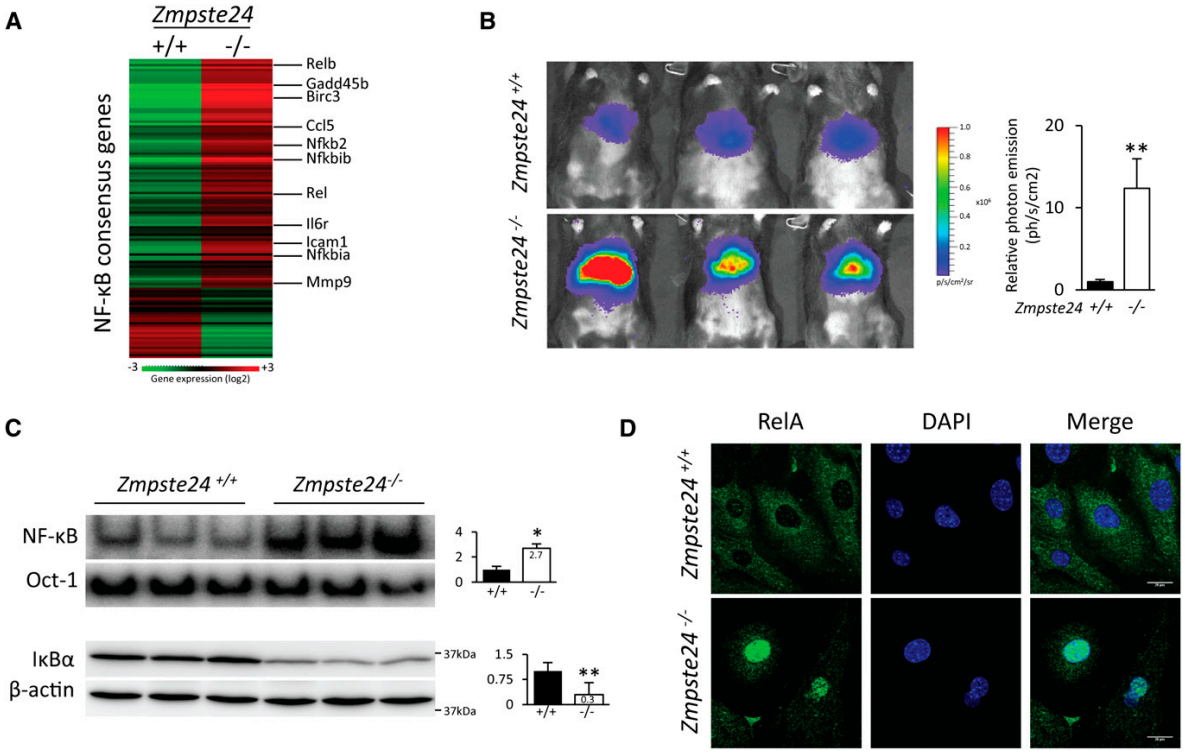

Figure 1. NF-κB hyperactivation in *Zmpste24*-deficient mice. (*A*) NF-κB target gene induction in *Zmpste24*-deficient mice. Heat map represents gene expression analysis (in *Zmpste24*$^{-/-}$ and wild-type livers) of genes that contain the consensus binding site for the NF-κB transcription factor, displayed as Log2 transformed expression signals. (*B*) Hydrodynamic delivery of NF-κB–luciferase gene reporter in the livers of 3-mo-old *Zmpste24*$^{-/-}$ mice (n = 10) and age-matched control littermates (n = 10). The bioluminescence image was recorded as the photon flux per second and square centimeter, and three representative mice from each genotype are shown. Relative mean values are represented, and error bars indicate SEM. $P < 0.01$, two-tailed Student's t-test. See also Supplemental Figure 2. (*C*) NF-κB EMSA of livers from 3-mo-old *Zmpste24*$^{-/-}$ mice (n = 3) and wild-type littermates (n = 3). Nuclear extracts were analyzed by using ^{32}P-labeled NF-κB and Oct-1 probes. Western blot of IκBα was performed using total liver extracts. β-Actin was used as loading control. Signals were quantified, and plots represent relative mean values ± SEM. (*) $P < 0.05$; (**) $P < 0.01$, two-tailed Student's t-test. (*D*) Representative image of immunofluorescence analysis using a RelA-specific antibody in fibroblasts from *Zmpste24*-deficient and wild-type mice. Bar, 20 μm.

with wild-type tissues (Supplemental Fig. 3). In agreement with this preferential nuclear localization of NF-κB in progeroid cells, immunofluorescence analysis revealed nuclear accumulation of RelA in *Zmpste24*$^{-/-}$ fibroblasts (Fig. 1D). Together, these data demonstrate that NF-κB is constitutively hyperactive in *Zmpste24*-deficient mouse tissues.

ATM and NEMO cooperate to induce NF-κB activation upon prelamin A accumulation

Prelamin A accumulation at the nuclear envelope causes genomic instability and activates several DNA repair mechanisms that configure an integrated DDR (Liu et al. 2005; Ugalde et al. 2011b). ATM kinase has a central role in coordinating the cellular response to DNA damage (Lavin 2008; Bensimon et al. 2011) and is essential for nuclear activation of NF-κB (Wu et al. 2006). To gain insight into the putative relevance of this molecular pathway in the hyperactivation of NF-κB in tissues from *Zmpste24*-deficient mice, we first analyzed the status of ATM in these progeroid mice. As shown in Figure 2A, Western blot analysis of phospho-Ser1981-ATM revealed a 1.5-fold increase in the levels of active ATM in *Zmpste24*$^{-/-}$ mice as compared with wild-type animals.

As NEMO accumulation in the nucleus has been reported during DDR activation, we next prepared whole-cell and nuclear protein extracts from *Zmpste24*-deficient and control mice and analyzed NEMO levels by Western blot. This approach revealed that the nuclear levels of NEMO were higher in *Zmpste24*$^{-/-}$ mice (Fig. 2A). Immunofluorescence analysis of NEMO in mouse fibroblasts further confirmed this result (Fig. 2B). We next tested whether NF-κB activation was dependent on ATM activation. To this end, we chemically inhibited ATM and ablated ATM by using siRNAs (Supplemental Fig. 4) in fibroblasts derived from *Zmpste24*-deficient mice. Both ATM chemical inhibition and siRNA knockdown were

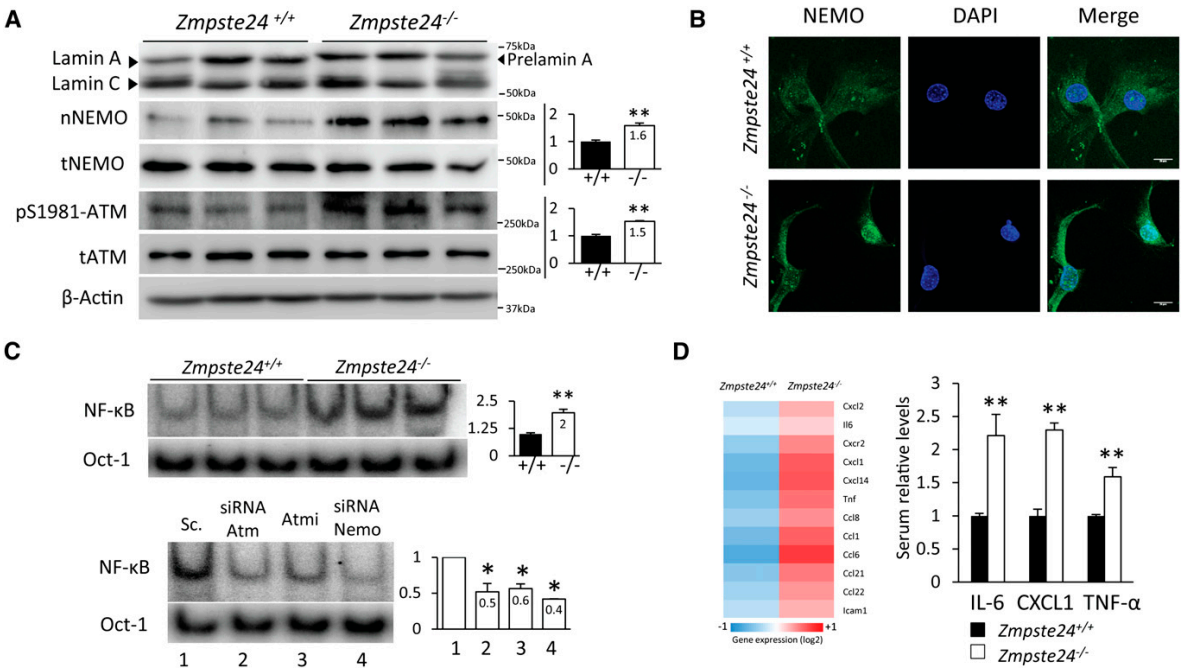

Figure 2. A signaling pathway involving ATM and NEMO activates NF-κB in *Zmpste24*-deficient mice. (*A*) ATM activation and nuclear translocation of NEMO in *Zmpste24*$^{-/-}$ cells. Western blot of NEMO protein was performed in nuclear extracts from livers of 3-mo-old *Zmpste24*$^{-/-}$ mice ($n = 3$) and wild-type littermates ($n = 3$). Total NEMO, ATM, and pSer1981-ATM levels were analyzed in total extracts of the same animals. β-Actin was used as loading control. Signals were quantified and are represented as relative mean values ± SEM. (*) $P < 0.05$; (**) $P < 0.01$, two-tailed Student's *t*-test. (*B*) Nuclear staining of NEMO protein in fibroblasts from *Zmpste24*-deficient mice supports nuclear translocation upon prelamin A-induced nuclear stress. Representative images are shown. Bar, 10 μm. (*C*) ATM and NEMO siRNA transfection experiments demonstrate causal involvement of these proteins in NF-κB activation. (*Top* panel) Nuclear extracts from *Zmpste24*$^{-/-}$ and *Zmpste24*$^{+/+}$ fibroblasts were analyzed by EMSA using ^{32}P-labeled NF-κB and Oct-1 probes. (*Bottom* panel) siRNA transfection analysis by EMSA as well as ATM inhibitor KU55933 incubations were performed in three independent *Zmpste24*$^{-/-}$ fibroblast cell lines, and the image shows a representative example. Signals were quantified and are represented as relative mean values ± SEM. (*) $P < 0.05$; (**) $P < 0.01$, two-tailed Student's *t*-test. See also Supplemental Figure 4. (*D*, *left* panel) Transcriptional analysis of SASP-related genes in *Zmpste24*$^{-/-}$ and wild-type livers. The *right* panel shows serum determinations of IL-6, CXCL1, and TNF-α in 3-mo-old *Zmpste24*$^{-/-}$ ($n = 5$) and *Zmpste24*$^{+/+}$ mice ($n = 5$). Plot represents relative mean values ± SEM. (*) $P < 0.05$; (**) $P < 0.01$, two-tailed Student's *t*-test.

able to reduce the nuclear presence of NF-κB dimers to levels comparable with those of wild-type fibroblasts (Fig. 2C). Moreover, and consistent with the proposed role of NEMO in nuclear NF-κB activation, NEMO siRNA also abrogated NF-κB activation (Fig. 2C).

The secretory phenotype of senescent cells contributes to the establishment of chronic inflammation in Zmpste24-deficient mice

Senescent cells secrete a plethora of interleukins, inflammatory cytokines, and growth factors that can affect surrounding cells, ultimately developing a secretory phenotype of senescent cells (SASP) (Kuilman and Peeper 2009; Coppe et al. 2010; Freund et al. 2010). Accordingly, we analyzed the transcriptional profile of SASP-associated genes in livers from *Zmpste24*-deficient mice and found a >1.5-fold up-regulation of several cytokine-encoding genes, such as *Il6*, *Cxcl1*, *Cxcl2*, *Ccl8*, and *Tnf* (Fig. 2D). Likewise, genes encoding different receptors and adhesion molecules, such as *Cxcr2* or *Icam1*, were also found altered in these mutant animals. Moreover, serum levels of IL-6, CXCL1, and TNF-α were increased in *Zmpste24*-deficient mice (Fig. 2D). These three cytokines are important mediators of inflammatory processes and have been related to aging and DDR (Kuilman and Peeper 2009; Biton and Ashkenazi 2011).

Together, these results provide experimental evidence that prelamin A accumulation induces NF-κB activation by an ATM- and NEMO-dependent pathway. Nuclear activation of NF-κB contributes to the establishment of a secretory phenotype that could give rise to a systemic inflammatory situation.

RelA heterozygosity extends longevity and prevents the development of progeroid features in Zmpste24$^{-/-}$ *mice*

To test the specific contribution of NF-κB activation to the progeroid phenotype shown by *Zmpste24*-deficient

mice, we used a previously described method of NF-κB genetic reduction (Kawahara et al. 2009; Tilstra et al. 2012) based on the use of *RelA*-haploinsufficient mice ($RelA^{+/-}$). RelA is a component of NF-κB pathway with essential developmental functions (Hayden and Ghosh 2004). Thus, $RelA^{-/-}$ mice present embryonic lethality, but $RelA^{+/-}$ mice are viable and apparently normal despite having reduced NF-κB activity (Beg et al. 1995). We crossed $Zmpste24^{+/-}$ mice with *RelA*-haploinsufficient mice to create double-mutant $Zmpste24^{+/-}RelA^{+/-}$ animals, which were then inbred to obtain *Zmpste24* knockout mice with different dosages of RelA. As expected, we did not obtain any $RelA^{-/-}$ mice, as they were embryonic-lethal, and $Zmpste24^{-/-}RelA^{+/+}$ animals resulting from these crosses exhibited a phenotype identical to that of $Zmpste24^{-/-}$ mice (Pendas et al. 2002). However, $Zmpste24^{-/-}RelA^{+/-}$ showed improved body weights (Fig. 3A,B) and extended life spans as compared with $Zmpste24^{-/-}RelA^{+/+}$ animals (Fig. 3C). Significantly, the mean survival of $Zmpste24^{-/-}RelA^{+/-}$ mice was extended from 118 to 146 d, and the maximum survival was extended from 147 to 174 d ($P < 0.05$) (Fig. 3C). Notably, increased life span in *RelA*-haploinsufficient mice correlated to a reduction in NF-κB activity in vivo, as assessed by hydrodynamic delivery of the NF-κB luciferase reporter. Thus, $Zmpste24^{-/-}RelA^{+/-}$ mice have lower bioluminescence signals as compared with $Zmpste24^{-/-}RelA^{+/+}$, reaching levels similar to wild-type animals (Fig. 3D). Furthermore, NF-κB EMSA and Western blot experiments confirmed that *RelA* haploinsufficiency reduces the amount of nuclear RelA dimers (Fig. 3E; Supplemental Fig. 5) without affecting the levels of other NF-κB active members, such as p52 or RelB (Supplemental Fig. 5). Remarkably, no differences were found in nuclear levels of NEMO protein between $Zmpste24^{-/-}RelA^{+/-}$ and $Zmpste24^{-/-}RelA^{+/+}$ animals, supporting the fact that NEMO translocation is an upstream event not affected by *RelA* haploinsufficiency.

The accumulation of farnesylated forms of prelamin A has been associated with profound dermal alterations, including loss of hypodermal adipocytes, decreased proliferation of keratinocytes, structural aberrations in hair follicles, and functional defects in stem cells present in this tissue (Espada et al. 2008; Sagelius et al. 2008; Wang et al. 2008). Notably, $Zmpste24^{-/-}RelA^{+/-}$ mice showed a complete recovery in most of the skin phenotypes

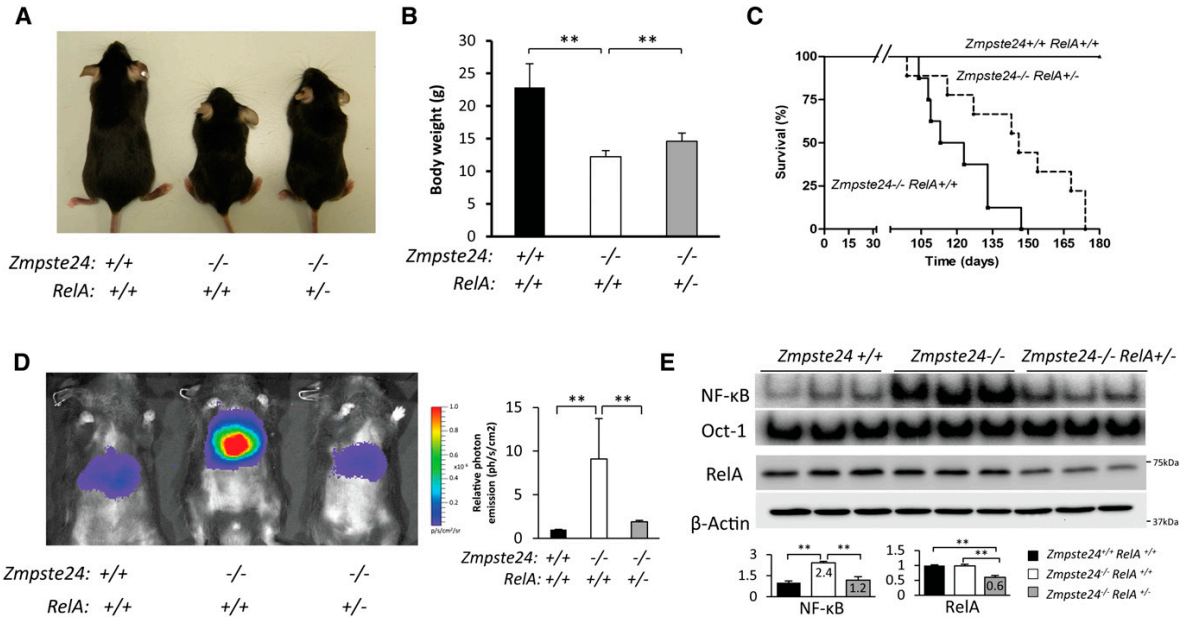

Figure 3. *RelA* haploinsufficiency extends longevity of *Zmpste24*-deficient mice by reducing NF-κB activity. (*A*) Representative photograph of 3-mo-old wild-type, $Zmpste24^{-/-}RelA^{+/+}$, and $Zmpste24^{-/-}RelA^{+/-}$ littermates. (*B*) $Zmpste24^{-/-}RelA^{+/-}$ mice ($n = 8$) showed improved body weight as compared with $Zmpste24^{-/-}RelA^{+/+}$ mice ($n = 7$). $P < 0.01$, two-tailed Student's *t*-test. Plot represents mean values ± SEM. (*C*) Kaplan-Meier survival plot showing the increase in life span of $Zmpste24^{-/-}RelA^{+/-}$ mice ($n = 8$) as compared with $Zmpste24^{-/-}RelA^{+/+}$ littermates ($n = 7$). $P < 0.05$, log-rank/Mantel-Cox test. (*D*) Reduced NF-κB activity in vivo in $Zmpste24^{-/-}RelA^{+/-}$ animals. Hydrodynamic delivery of the NF-κB–luciferase gene reporter in the livers of 3-mo-old wild-type ($n = 5$), $Zmpste24^{-/-}RelA^{+/+}$ ($n = 5$) and $Zmpste24^{-/-}RelA^{+/-}$ ($n = 5$) mice. The bioluminescence image was recorded as the photon flux per second and square centimeter, and representative mice of each genotype are shown. Relative mean values are shown, and error bars indicate SEM. $P < 0.01$ $Zmpste24^{-/-}RelA^{+/+}$ as compared with wild-type or $Zmpste24^{-/-}RelA^{+/-}$ animals, two-tailed Student's *t*-test). (*E*) NF-κB and Oct-1 EMSA of 3-mo-old wild-type ($n = 3$), $Zmpste24^{-/-}RelA^{+/+}$ ($n = 3$), and $Zmpste24^{-/-}RelA^{+/-}$ ($n = 3$) livers. Western blot shows reduced levels of RelA in haploinsufficient $RelA^{+/-}$ animals. β-Actin was used as loading control. Signals were quantified and are represented as relative mean values ± SEM. $P < 0.01$, two-tailed Student's *t*-test.

studied, which are also present in normal aging. Thus, NF-κB blockade in the skin of *Zmpste24*-deficient mice increased cell proliferation, as indicated by increased expression of the proliferation marker Ki-67 (Fig. 4A). Additionally, *Zmpste24*$^{-/-}$*RelA*$^{+/-}$ showed a normal subcutaneous fat layer and well-structured hair follicles (Fig. 4A).

NF-κB activity is also essential for a normal activity of the immune system, as demonstrated by the fact that mutations in several NF-κB genes, including NEMO, cause immunodeficiency syndromes (Li and Verma 2002). In this regard, we observed that *Zmpste24*-deficient mice show marked histological alterations in the spleen and thymus, two of the most important lymphoid organs. Thus, *Zmpste24*-deficient mice exhibit reduced spleen size and cellularity as well as abnormal lymphoid follicles, which present an expansion of the mantle, disrupting the germinal centers (Fig. 4B). Notably, the thymus from *Zmpste24*$^{-/-}$ mice shows an involution process characterized by a reduction in tissue mass and thymic cellularity, loss of tissue structure, and abnormal architecture (Fig. 4B). *Zmpste24*$^{-/-}$*RelA*$^{+/-}$ mice display a notable improvement in both tissues. The spleen exhibits normal lymphoid follicles, whereas the thymus has recovered normal tissue mass, cellularity, and architecture, demonstrating the direct implication of NF-κB activation in the lymphoid alterations characteristic of *Zmpste24*-deficient mice.

We also studied bone architecture in order to explore the potential involvement of NF-κB activation in the bone abnormalities described in *Zmpste24*-deficient mice

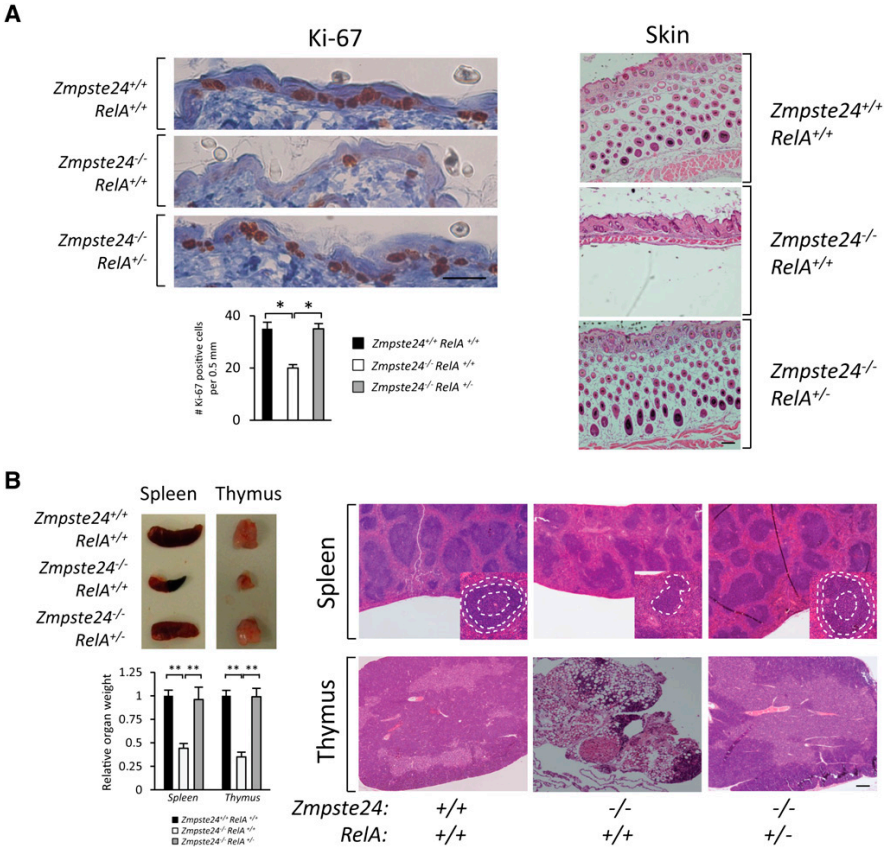

Figure 4. *RelA* heterozygosis prevents important progeroid features of *Zmpste24*$^{-/-}$ mice. (*A*) Reversal of skin alterations by NF-κB blockade. (*Left* panel) Ki-67 immunohistochemistry of 3-mo-old wild-type ($n = 3$), *Zmpste24*$^{-/-}$*RelA*$^{+/+}$ ($n = 3$), and *Zmpste24*$^{-/-}$*RelA*$^{+/-}$ ($n = 3$) mice. Representative photographs are shown. Plot represents average number of Ki-67-positive cells ±SEM. $P < 0.01$, two-tailed Student's *t*-test. Bar, 30 μm. The *right* panel shows full recovery of the subcutaneous fat layer in 3-mo-old *Zmpste24*$^{-/-}$*RelA*$^{+/-}$ mice as compared with *Zmpste24*$^{-/-}$*RelA*$^{+/+}$ littermates. Representative hematoxylin-eosin (H&E) staining micrographs are shown. Bar, 100 μm. (*B*) Thymus and spleen involution in *Zmpste24*-deficient mice is prevented in the *RelA*$^{+/-}$ background. (*Top left* panel) Representative photographs of spleen and thymus from 3-mo-old wild-type ($n = 3$), *Zmpste24*$^{-/-}$*RelA*$^{+/+}$ ($n = 3$), and *Zmpste24*$^{-/-}$*RelA*$^{+/-}$ ($n = 3$) mice are shown. (*Bottom left* panel) Relative weight values of thymus and spleen are represented ±SEM. $P < 0.01$, two-tailed Student's *t*-test. The *right* panel shows representative micrographs from spleen and thymus tissues of wild-type, *Zmpste24*$^{-/-}$*RelA*$^{+/+}$, and *Zmpste24*$^{-/-}$*RelA*$^{+/-}$ animals. Spleen details show representative lymphoid follicles; different regions are circled by dotted white lines (germinal center and mantle and marginal zones). Note that the *Zmpste24*$^{-/-}$*RelA*$^{+/+}$ thymus shows a notable tissue involution where lymphoid tissue has been mostly replaced by adipose tissue. Bar, 100 μm.

(de Carlos et al. 2008). To this end, microcomputed tomography (μCT) analyses were performed on tibias from *Zmpste24*$^{-/-}$*RelA*$^{+/-}$ and *Zmpste24*$^{-/-}$*RelA*$^{+/+}$ mice. No differences were found between the two groups in the trabecular region, and only a slight improvement was found in the cortical region of bones from *Zmpste24*$^{-/-}$*RelA*$^{+/-}$ as compared with *Zmpste24*$^{-/-}$*RelA*$^{+/+}$ mice (Supplemental Fig. 6). These experiments demonstrate that NF-κB hyperactivation contributes to reducing the life span of progeroid mice and is responsible for some important features of the progeroid phenotype. Moreover, the phenotypic improvement of progeroid mice upon genetic reduction of NF-κB supports the feasibility of developing pharmacological strategies aimed at inhibiting this pathway to treat progeria.

Sodium salicylate treatment efficiently prevents NF-κB activation and its associated alterations in Zmpste24-deficient mice

Having shown that genetic inhibition of NF-κB extends longevity in *Zmspte24*-deficient mice, we asked whether the same biological effect could be achieved by using a pharmacological strategy. To this end, we chose sodium salicylate, a nonsteroidal anti-inflammatory drug that at high doses is able to efficiently inhibit the IKK complex and has been satisfactorily used to reduce NF-κB activation in animal models of muscular dystrophy (Cai et al. 2004). Thus, we treated *Zmpste-24*-deficient mice with sodium salicylate (200 mg/kg per day), and both treated and control mice were weighted and observed during their lifetimes. Salicylate-treated *Zmpste24*$^{-/-}$ mice showed improved body weights (Fig. 5A,B) and extended life spans as compared with nontreated *Zmpste24*-deficient mice (Fig. 5C). Thus, the mean survival of salicylate-treated *Zmpste24*$^{-/-}$ mice was extended from 123 to 148 d, and the maximum survival was extended from 151 to 243 d ($P < 0.01$) (Fig. 5C).

NF-κB EMSA analysis of livers from treated and untreated mice demonstrated the targeted effect of salicylate on NF-κB activation (Fig. 5D), as treated mice showed decreased amounts of RelA dimers in the nucleus as well as reduced degradation of the NF-κB inhibitor IκBα (Fig. 5D). Salicylate-treated *Zmpste24*$^{-/-}$ mice showed

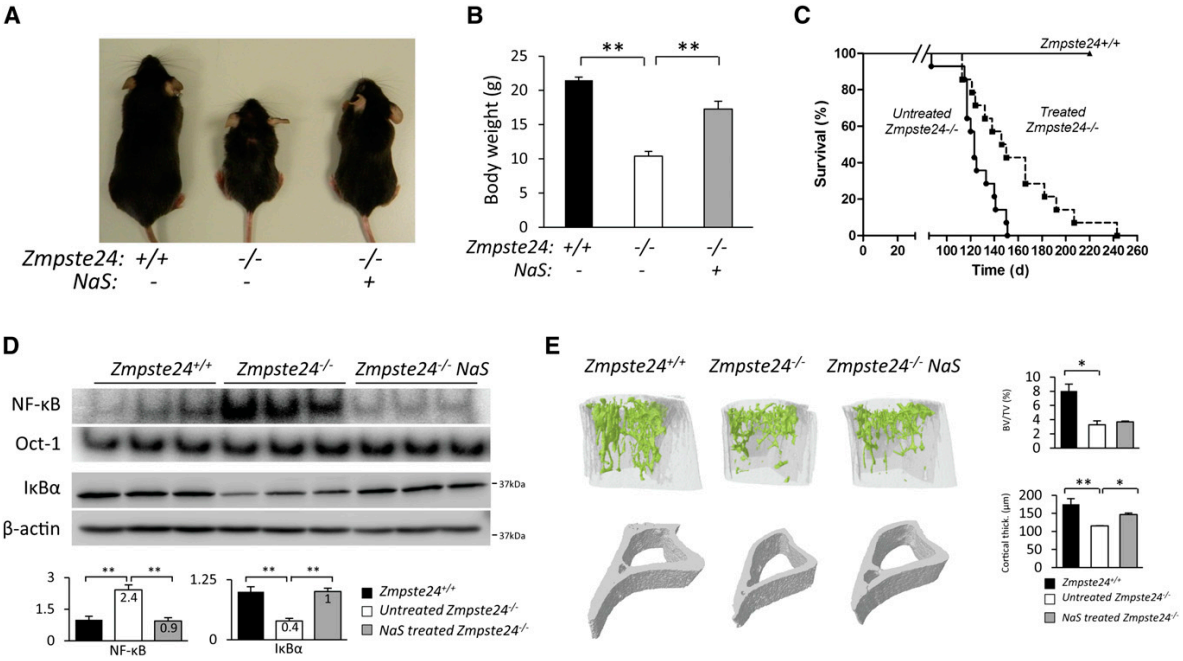

Figure 5. Sodium salicylate treatment extends longevity and prevents progeroid features of *Zmpste24*-deficient mice. (*A*) Representative photographs of 3-mo-old *Zmpste24*$^{+/+}$, untreated, and salicylate-treated *Zmpste24*-deficient mice. (*B*) Sodium salicylate-treated *Zmpste24*$^{-/-}$ mice ($n = 12$) showed improved body weight as compared with untreated *Zmpste24*$^{-/-}$ mice ($n = 12$). Plot represents weight mean values ± SEM. $P < 0.01$, two-tailed Student's *t*-test. (*C*) Kaplan-Meier survival plot showing the increase in life span of salicylate-treated *Zmpste24*$^{-/-}$ mice ($n = 12$) as compared with untreated *Zmpste24*$^{-/-}$ littermates ($n = 12$). $P < 0.01$, log-rank/Mantel-Cox test. (*D*) Liver NF-κB and Oct-1 EMSA analysis demonstrates effective NF-κB inhibition in salicylate-treated *Zmpste24*-deficient mice. Western blot of IκBα was performed in total liver extracts. β-Actin was used as loading control. Signals were quantified and are represented as relative mean values ± SEM. $P < 0.01$, two-tailed Student's *t*-test. (*E*, *left* panel) Representative three-dimensional image generated from μCT analysis of tibias from 3-mo-old *Zmpste24*$^{+/+}$ ($n = 3$), untreated ($n = 3$), and treated *Zmpste24*$^{-/-}$ ($n = 3$) littermates. The *right* panel contains a quantitative analysis of relative bone volumes (bone volume/tissue volume [BV/TV]) and cortical thickness. Mean values are represented, and error bars indicate SEM. $P < 0.05$ as compared treated and untreated *Zmpste24*-deficient mice, two-tailed Student's *t*-test.

an increase in cell proliferation, subcutaneous fat layer thickness, and normal hair follicles in the skin (Supplemental Fig. 7). Moreover, this treatment also prevented thymic and spleen involution, with these organs having a size similar to wild-type organs (Supplemental Fig. 8). Notably, bone architecture analysis revealed no significant changes in the trabecular region upon salicylate treatment. However, treated *Zmpste24*-deficient mice showed significantly improved cortical regions (Fig. 5E). This effect of salicylate treatment may derive from the known inhibitory effect of this compound on the synthesis of prostaglandins involved in bone homeostasis (Ricciotti and FitzGerald 2011). In summary, these data demonstrate that salicylate treatment is effective at inhibiting NF-κB activation in vivo and at significantly extending the longevity of progeroid *Zmpste24*-deficient mice.

NF-κB is hyperactivated in Lmna$^{G609G/G609G}$ mice

We recently generated a knock-in mouse strain carrying the most frequent HGPS mutation (*Lmna* c.1827C>T; p.Gly609Gly) (Osorio et al. 2011a). *Lmna$^{G609G/G609G}$* mice accumulate progerin and phenocopy the main clinical manifestations of HGPS, being a valuable model for the study of progeroid syndromes as well as for the preclinical evaluation of approaches aimed at preventing the pathological features of this condition. Comparison of transcriptional profiles from *Lmna$^{G609G/G609G}$* and *Lmna$^{+/+}$* mouse livers using GSEA showed a significant correlation between transcriptional alterations detected and the gene set that contains NF-κB-regulated genes (Supplemental Fig. 9). Next, we analyzed the NF-κB activation status in *Lmna$^{G609G/G609G}$* mice. Hydrodynamic delivery of the NF-κB luciferase reporter showed that mutant mice have an eightfold increase in bioluminescent signal (Fig. 6A) as compared with control littermates, indicating that these mutant mice present an activation of the NF-κB pathway similar to that observed in *Zmpste24*-deficient animals. These results were also confirmed by NF-κB EMSA experiments and IκBα Western blot analysis using nuclear extracts from control and mutant liver samples (Fig. 6B).

The nuclear accumulation of progerin activates ATM kinase, as revealed by the increased amounts of phospho-Ser1981-ATM present in *Lmna$^{G609G/G609G}$* samples (Fig. 6B). Consequently, NEMO accumulation in the nucleus supports the view that both prelamin A and progerin activate NF-κB through the same molecular mechanism. Serum levels of IL-6, CXCL1, and TNF-α were also increased in *Lmna$^{G609G/G609G}$* mice (Fig. 6C), which is in agreement with the systemic inflammation condition described above for *Zmpste24*-deficient mice and could be responsible for the similar immunological alterations found in *Lmna$^{G609G/G609G}$* mice (Supplemental Fig. 10).

To explore the possible occurrence of these alterations in human progeria, we first performed an EMSA analysis on HGPS fibroblasts. This study revealed a twofold increase in NF-κB activity in progeria cells (Supplemental Fig. 11A). HGPS cells also showed increased levels of phospho-Ser1981-ATM and nuclear NEMO, suggesting that NF-κB activation in these human progeria cells results from the same mechanism as in the animal models described above. To gain insight into the potential relevance of this phenomenon during normal human aging, we analyzed NF-κB activation in fibroblasts from aged healthy donors. As shown in Supplemental Figure 11B, cells from advanced age donors showed a fivefold increase in NF-κB activity as compared with fibroblasts obtained from young donors. In addition, aged fibroblasts showed increased ATM activation and nuclear NEMO translocation (Supplemental Fig. 11B), supporting that ATM- and NEMO-dependent NF-κB activation could be at least in part responsible for the increased inflammation observed during normal aging (Adler et al. 2007).

Pharmacological inhibition of NF-κB extends longevity in the Lmna$^{G609G/G609G}$ model of HGPS

Currently, *Lmna$^{G609G/G609G}$* mice represent the best animal model available for the preclinical testing of therapeutic approaches for both HGPS and the age-associated pathologies derived from progerin accumulation in normal aging. Thus, aiming to provide preclinical proof of concept of the feasibility of using nonsteroidal anti-inflammatory drugs to prevent the pathological consequences of progerin accumulation, we decided to extend the salicylate treatment results to the *Lmna$^{G609G/G609G}$* mouse strain. To this end, we treated *Lmna$^{G609G/G609G}$* mice with sodium salicylate (200 mg/kg per day) and found that salicylate-treated animals showed improved body weight as well an extended life span as compared with untreated mice (Fig. 6D–F). Moreover, the mean survival of salicylate-treated mice was extended from 107 to 152 d, and the maximum survival was extended from 114 to 180 d ($P < 0.01$).

Together, these results demonstrate that hyperactivation of the NF-κB pathway plays an important role in the development of aging-associated pathologies derived from the accumulation of abnormal lamin A precursors at the nuclear lamina. Moreover, these data provide evidence of the feasibility of developing anti-aging strategies based on the use of anti-inflammatory compounds.

Discussion

Over recent years, mechanistic studies on human aging have gained new insights from the elucidation of the molecular defects underlying the development of accelerated aging syndromes. These complex and dramatic diseases result from the combined action of both cell-autonomous and systemic alterations (Marino et al. 2008; Osorio et al. 2011b). Thus, nuclear envelope defects causative of progeroid laminopathies lead to perturbations in cellular pathways, including p53-dependent cell senescence, deregulation of the somatotroph axis, and changes in metabolic master regulators (Lammerding et al. 2004; Varela et al. 2005; Scaffidi and Misteli 2008; Marino et al. 2010). Moreover, secretion of signaling molecules by affected cells could be a major contributor to progeria development, as secreted molecules can act on distant organs, leading to an amplifying cascade of aged signals.

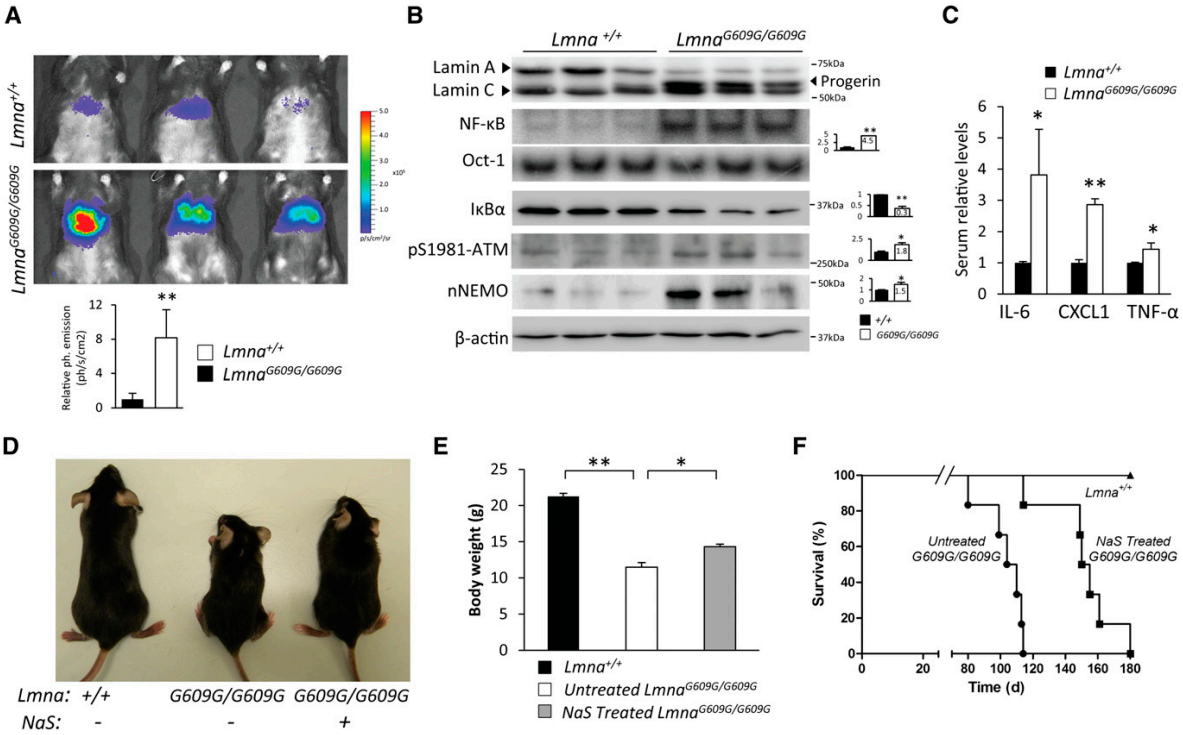

Figure 6. Salicylate treatment reduces NF-κB hyperactivation and extends longevity in *Lmna*$^{G609G/G609G}$ mice. (*A*) *Lmna*$^{G609G/G609G}$ mice show an increased NF-κB activation, as demonstrated by hydrodynamic delivery of NF-κB-luciferase gene reporter in the livers of *Lmna*$^{+/+}$ ($n = 5$) and *Lmna*$^{G609G/G609G}$ ($n = 5$) mice. The bioluminescence image was recorded as the photon flux per second and square centimeter, and three representative mice from each genotype are shown. Plot represents relative mean values, and error bars indicate SEM. $P < 0.01$, two-tailed Student's *t*-test. (*B*) NF-κB activation in *Lmna*$^{G609G/G609G}$ mouse livers. Western blot of lamin A/C isoforms showing progerin accumulation in mutant mice. NF-κB and Oct-1 were analyzed by EMSA. Western blots of lamin A/C, IκBα, pS1981-ATM, and β-actin were performed in whole-liver extracts. NEMO Western blot was performed in nuclear extracts. Signals were quantified and are represented as relative mean values ± SEM. (*) $P < 0.05$; (**) $P < 0.01$, two-tailed Student's *t*-test. (*C*) Serum determinations of IL-6, CXCL1, and TNF-α in 3-mo-old *Lmna*$^{+/+}$ ($n = 5$) and *Lmna*$^{G609G/G609G}$ ($n = 5$) mice. Plot represents relative mean values ± SEM. (*) $P < 0.05$; (**) $P < 0.01$, two-tailed Student's *t*-test. (*D*) Representative photographs of 3-mo-old *Lmna*$^{+/+}$, untreated, and sodium salicylate-treated *Lmna*$^{G609G/G609G}$ mice. (*E*) Sodium salicylate-treated *Lmna*$^{G609G/G609G}$ mice ($n = 6$) showed improved body weight as compared with untreated *Lmna*$^{G609G/G609G}$ mice ($n = 6$). Plot represents weight mean values ± SEM. $P < 0.01$, two-tailed Student's *t*-test. (*F*) Kaplan-Meier survival plot showing a significant increase in the life span of salicylate-treated *Lmna*$^{G609G/G609G}$ mice ($n = 6$) as compared with *Lmna*$^{G609G/G609G}$ littermates ($n = 6$). $P < 0.01$, log-rank/Mantel-Cox test.

However, little is known about the nature of systemic factors involved in aging or aging-like processes as well as the mechanisms connecting nuclear defects to perturbations in such systemic factors. Here, we present an ATM-dependent NF-κB activation pathway that links nuclear lamina defects to systemic inflammation. We also demonstrate in vivo the causal role for this pathway in the emergence of age-associated pathologies and illustrate the feasibility of targeting this signaling cascade for the treatment of premature aging symptoms.

By using two different mouse models of progeroid laminopathy (*Zmpste24*-deficient and *Lmna*^{G609G} mice), we showed that accumulation of prelamin A/progerin at the nuclear lamina activates the NF-κB pathway in an ATM- and NEMO-dependent manner, illustrating that alterations in the nuclear architecture generate stress signals that activate important DNA damage sensors. In this context, ATM and NEMO act coordinately to activate NF-κB, as demonstrated by the finding that their respective inhibition prevents prelamin A-induced NF-κB activation. Consistent with the observed activation of NF-κB signaling in *Zmpste24*$^{-/-}$ and *Lmna*$^{G609G/G609G}$ progeroid mice, several cytokines and adhesion molecules are strongly up-regulated in cells and tissues from these mice, likely contributing to the initiation and maintenance of an inflammatory response. Among the plethora of proinflammatory cytokines secreted by senescent cells, we propose that IL-6, CXCL1, and TNF-α may have essential roles in progeria development by nonautonomous stimulation of surrounding cells through the activation of their cognate cell surface receptors and signal transduction pathways (Coppe et al. 2010; Freund et al. 2010). Thus, systemically increased levels of cytokines amplify the inflammatory stimuli and are implicated

in the establishment of a feed-forward signaling process (Biton and Ashkenazi 2011). Since senescent cells are potentially time-persisting, the continued production of cytokines and the subsequent NF-κB activation lead to an increased inflammation in progeroid mice that contributes to age-related wasting and dramatically shortens organismal life span (Fig. 7).

According to our results, NF-κB could be regarded as a major regulator of accelerated aging, as demonstrated by the fact that NF-κB blockade significantly increases life span in both *Zmpste24*$^{-/-}$ and *Lmna*$^{G609G/G609G}$ progeroid mice. Furthermore, the NF-κB blockade strategies used in this study have allowed us to provide new molecular insights into the involvement of NF-κB in dermal and immunological homeostasis. The primary manifestations of accelerated aging in skin affect cell proliferation, hair follicles, and the subcutaneous fat layer (Sur et al. 2008). NF-κB blockade was able to prevent these alterations, demonstrating a causal role of NF-κB deregulation in age-associated defects in skin homeostasis. A similar situation has been shown in lymphoid organs, which is of special interest, as thymic involution is considered one of the leading regulators of aging (Aw and Palmer 2011). The reduction in tissue mass and cellularity and the loss of tissue structure leads to a decline in naive T-cell output as well as to the occurrence of changes in the peripheral T-cell compartment that contribute to the clinical signs of immunosenescence (Hale et al. 2010). Consistent with these observations, we demonstrated in this study that NF-κB hyperactivation and the systemic inflammation derived therefrom drive thymus and spleen involution and that NF-κB inhibition is able to prevent these age-related alterations.

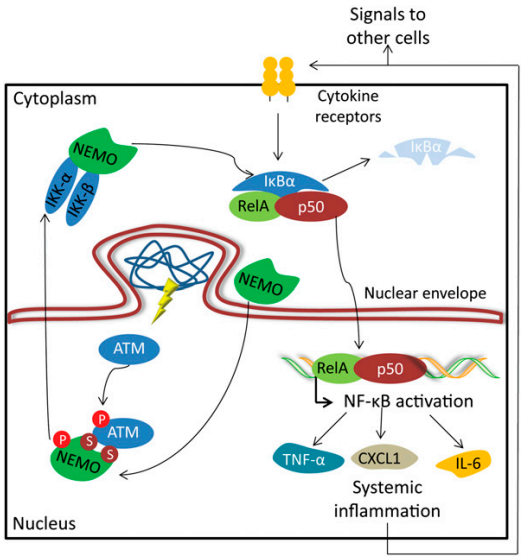

Figure 7. A model depicting ATM- and NEMO-mediated NF-κB activation upon accumulation of prelamin A isoforms. Nuclear envelope alterations caused by the accumulation of prelamin A isoforms trigger a nuclear stress pathway involving ATM and NEMO proteins. As a consequence of prelamin A/progerin accumulation, ATM is activated, and NEMO is translocated into the nucleus. NEMO phosphorylation by ATM induces their translocation out of the nucleus to activate the cytoplasmic IKK complex. Subsequent NF-κB activation triggers an inflammatory-associated transcriptional program that leads to the secretion of IL-6, CXCL1, and TNF-α. Increased levels of senescence-associated cytokines cause systemic inflammation by acting over distant cells and tissues. Systemic inflammation amplifies a cascade of aged signals, critically affecting tissue homeostasis and finally reducing the life span of progeroid mice.

Although the biological significance of NF-κB activation during aging is not completely clear, the findings reported herein, together with the fact that other models of normal and accelerated aging show increased levels of NF-κB activity (Kawahara et al. 2009; Rodier et al. 2009), support the idea that inflammation is a major regulator of the aging process. The mechanism by which NF-κB signaling is activated with age also remains largely unexplored, but our data indicate that the nuclear envelope abnormalities occurring in both normal and premature aging (Scaffidi and Misteli 2006) may contribute, at least in part, to the activation of this inflammatory pathway. The primary function of NF-κB activation in response to nuclear envelope defects could be to protect damaged cells against apoptosis (Wang et al. 1999; Salminen et al. 2011). Since a proper clearance of senescent cells by the immune system seems to be crucial for homeostasis maintenance in aging and cancer (Baker et al. 2011; Kang et al. 2011), both NF-κB hyperactivation and the subsequent age-related immunological decline could be compromising an appropriate response against age-accumulated senescent cells.

The results of the present work also suggest that the use of nonsteroidal anti-inflammatory drugs, alone or in combination with statins and aminobisphophonates (Varela et al. 2008), could be useful for the treatment of accelerated aging-associated alterations occurring during the course of progeroid laminopathies (Hennekam 2006; Merideth et al. 2008; Puente et al. 2011). Moreover, pharmacological modulation of the NF-κB pathway also could be of interest for slowing down the progression of physiological aging (Rando and Chang 2012). The identification of NF-κB signaling activation in mouse models with accelerated aging also provides further in vivo support for the provocative proposal that the maintenance of the aged state requires an active signaling program and that age-linked phenotypes can be substantially reversed by intervention on the activity of individual genes (Adler et al. 2007; Freije and Lopez-Otin 2012; Rando and Chang 2012). Accordingly, we suggest that the progeroid mice used in this study may represent a valuable tool for further exploration of this proposal due to their faithful recapitulation of the biological dysfunctions normally associated with advanced age. Likewise, we propose that these progeroid mice are an essential tool for the development of putative rejuvenation strategies aimed at controlling the inflammatory responses driven by NF-κB signaling that occur during both normal and pathological aging.

Materials and methods

Antibodies and reagents

Antibodies specific for lamin A/C (sc-6215, Santa Cruz Biotechnology), IκBα (4812, Cell Signaling), RelA (8242, Cell Signaling), NEMO (2685, Cell Signaling), ATM (2873, Cell Signaling), phospho-Ser1981-ATM (mouse: 200-301-400, Rockland Laboratories; human: 5883S, Cell Signaling), p52 (sc-7386, Santa Cruz Biotechnology), RelB (sc-48366, Santa Cruz Biotechnology), Ki-67 (KI681C01, DCS-Innovative Diagnostik-Systeme), α-tubulin (T6074, Sigma), and β-actin (AC-40, Sigma) were used in this study for Western blot, immunofluorescence, and immunohistochemistry experiments. The ATM inhibitor KU55933 was obtained from Calbiochem.

Mice

We generated and genotyped *Zmpste24*$^{-/-}$ and *Lmna*^{G609G} mice as previously described (Pendas et al. 2002; Osorio et al. 2011a). *RelA*$^{+/-}$ mice were obtained from Jackson Laboratories. *Zmpste24*$^{+/-}$ and *RelA*$^{+/-}$ were crossed, and *Zmpste24*$^{+/-}$*RelA*$^{+/-}$ progeny were interbred to obtain *Zmspte24*$^{-/-}$*RelA*$^{+/-}$ mice. We administrated sodium salicylate (200 mg/kg per day; Sigma-Aldrich) in PBS intraperitoneally to mice every day. Neither vehicle alone nor sodium salicylate treatment produced any apparent damage or stress responses in mice. We performed μCT analysis of tibias with a μCT SkyScan 1172 system (SkyScan). For histology analysis, we fixed samples with 4% paraformaldehyde in PBS, processed the resulting preparations into serial paraffin sections, and stained each with hematoxylin and eosin (H&E). All of the animal experiments were performed in accordance with the guidelines of the Committee for Animal Experimentation of the Universidad de Oviedo.

Hydrodynamic delivery of an NF-κB–luciferase gene reporter

A plasmid containing a firefly luciferase gene under the control of a minimal CMV promoter and tandem repeats of the NFκB transcriptional response element was injected by using the hydrodynamic technique previously described (Herweijer and Wolff 2007). In brief, 10 μg/mL solution of the plasmid was prepared in sterile Ringer's buffer at room temperature. Mice were anaesthetized, and the lateral tail vein was accessed with a 21-gauge needle. Administration of the solution (1 mL/10 g) was performed without extravasation.

Bioluminescent imaging and analysis

Mice were anaesthetized and injected intraperitoneally with 200 μL of D-luciferin solution (15 g/L in PBS; Melford Laboratories). Imaging was completed between 2 and 5 min after injection with a Xenogen IVIS system coupled to Living Image acquisition and analysis software (Xenogen). Photon flux was calculated for each mouse by using a rectangular region of interest. This value was scaled for each mouse to a comparable background value. Represented values were recorded 7 d after injection to avoid any potential interference caused by experimental procedure-induced liver inflammation.

Cell culture and siRNA delivery

We extracted mouse fibroblasts from 15-wk-old ears as previously described (Varela et al. 2005). We maintained cultures in Dulbecco's modified Eagle's medium (Gibco) supplemented with 10% fetal bovine serum (Gibco) and 1% antibiotic antimycotic (Gibco). Studies with primary mouse fibroblasts were performed at postnatal day 3 (P3). HGPS (AG01972) and control fibroblasts (AG10803) were obtained from Coriell Cell repository. Dermal fibroblasts derived from young (GM05565, 3-yr-old; and GM00038, 9-yr-old) and advanced age donors (AG04059, 96-yr-old) were obtained from Coriell Cell repository, except the JM0097Y cell line that was obtained directly from a 97-yr-old donor. For transfection of siRNAs, we followed the manufacturer's instructions (Stealth siRNAs, Life Technologies). Briefly, cells were plated at low density (30%–50%), and up to 150 pg of siRNA was added with 7.5 μL of Lipofectamine RNAiMAX (Life Technologies). The same procedure was repeated after 4 h, and analyses were performed 48 h after the first transfection. For pharmacological inhibition of ATM kinase activity, cells were incubated for 12 h in the presence of 10 μM KU55933 ATM inhibitor.

EMSA

Nuclear extracts from cells were prepared as described previously (Schreiber et al. 1989). For the preparation of nuclear extracts from tissues, a slightly modified protocol was used. Briefly, frozen tissues were homogenized in cold buffer A (10 mM Tris-HCl at pH 8, 1.5 mM $MgCl_2$, 10 mM KCl, 1 mM DTT, 2× protease inhibitor cocktail) with a Potter homogenizer. After incubation on ice for 15 min, samples were pelleted by centrifugation and resuspended in cold buffer A containing 0.1% Triton X-100. After incubation on ice, cells were pelleted, and nuclear pellets were resuspended in cold buffer C (20 mM Tris-HCl at pH 8, 25% glycerol [v/v], 0.4 M NaCl, 1.5 mM $MgCl_2$, 0.2 mM EDTA, 0.5 mM DTT, 2× protease inhibitor cocktail). Samples were vigorously rocked for 15 min at 4°C on a shaking platform. The nuclear extracts were finally centrifuged for 5 min in a microfuge at 4°C, and the supernatants were frozen in aliquots at −70°C. NF-κB and Oct-1 consensus oligonucleotides (Promega) were radiolabeled by T4 polynucleotide kinase (New England Biolabs) in the presence of γ-^{32}P-ATP. Labeled oligonucleotides were incubated with 15–20 μg of nuclear extracts in 1× binding buffer (4× glycerol, 20 mM Tris-HCl at pH 8, 60 mM NaCl, 5 mM $MgCl_2$, 1 mM DTT, 1× protease inhibitor cocktail) in the presence of poly-dI–dC. Complexes were run in nondenaturing, 6% acrylamide gels, and exposed to X-ray detector Fuji PhosphorImager (Fujifilm Global).

Western blot analysis

Cultured cells were washed twice with 1× PBS and resuspended in 100 mM Tris-HCl (pH 7.4), 2% SDS, and 50 mM EDTA. Tissues were snap-frozen in liquid nitrogen. Frozen tissues (~50 mg in each sample) were homogenized in 300 μL of 100 mM Tris-HCl (pH 7.4), 2% SDS, and 50 mM EDTA with a Polytron homogenizer. Protein concentration was evaluated with the bicinchoninic acid technique (Pierce BCA protein assay kit). Equal amounts of proteins were loaded onto SDS–polyacrylamide gels. After electrophoresis, gels were electrotransferred onto nitrocellulose membranes or Immobilon-FL polyvinylidene fluoride membranes (Millipore), blocked with 5% nonfat dry milk in TBS-T buffer (20 mM Tris at pH 7.4, 150 mM NaCl, 0.05% Tween 20), and incubated overnight at 4°C with the different primary antibodies. Finally, blots were incubated with 1:10,000 secondary antibody conjugated with horseradish peroxidase (HRP) (Jackson ImmunoResearch Laboratories) in 1.5% nonfat milk in TBS-T. Then, we washed and developed the immunoreactive bands with Immobilon Western chemiluminescent HRP substrate (Millipore).

Immunohistochemistry and immunofluorescence analysis

Formalin-fixed paraffin-embedded tissue sections were cut at 5 μm for immunohistochemical detection of Ki67 on a Discover automated immunostainer (Ventana Medical Systems). Deparaffinization and heat-induced antigen retrieval were performed directly on the stainer. Antigen retrieval procedures were as follows: Retrieval was performed with CC2 solution (Ventana Medical Systems) for 30 min at 95°C. Primary antibody incubation was performed for 1 h at 37°C. Finally, HRP-conjugated antibody (OmniMap anti-Rb HRP, Ventana Medical Systems) was applied for 16 min at 37°C. Staining was visualized by using ChromoMap DAB kit (Ventana Medical Systems). Cells were counterstained with hematoxylin and visualized by light microscopy. Quantitative analyses were performed according to the percentage of immunopositive cells per 0.5 mm. For the immunofluorescence analysis, cells were fixed in 4% paraformaldehyde solution, rinsed in PBS, and permeabilized with 0.5% Triton X-100. Cells were incubated with primary antibodies diluted in 15% goat serum in 1× PBS for 1–3 h at room temperature. After washes with PBS, slides were incubated with 1:500 Alexa 488-conjugated secondary antibody (Life Technologies) for 1 h at 25°C. After the final washes, nuclei were counterstained with DAPI (Roche), and slides were mounted in VectaShield mounting medium (Vector Laboratories). Microphotographs were recorded with an Axioplan-2 Zeiss fluorescent microscope (Zeiss), and images were captured with a charge-coupled device camera (Photometrics SenSys).

RNA preparation and quantitative RT–PCR (qRT–PCR)

Cells were resuspended in TRIzol reagent (Life Technologies) and processed through alcohol precipitation. RNA pellets were then washed in cold 75% ethanol and resuspended in nuclease-free water (Ambion). The samples were quantified and evaluated for purity (260/280 nm ratio) with a NanoDrop ND-1000 spectrophotometer. cDNA was synthesized with 1–4 μg of total RNA with the ThermoScript RT–PCR system (Invitrogen). qRT–PCR was carried out in triplicate for each sample with 20 ng of cDNA, Power SYBR Green PCR Master Mix, and 0.5 μL of the specific oligonucleotides for the gene of interest (Applied Biosystems). As an internal control for the amount of template cDNA used, gene expression was normalized to amounts obtained for the mouse *Gapdh* endogenous control. The following oligonucleotides were used for mouse *Atm* and *Ikbkg* (Nemo) amplification: Atm_fwd (5′-GGAGACAGCTTGTGAAGGGCCG-3′), Atm_rev (5′-TGCACCACTCGAGAACACCGC-3′), Ikbkg_fwd (5′-TGCCAACAGCAGATGGCTGAGG-3′), and Ikbkg_rev (5′-GCTGTAGCACCTCCCGCTCAC-3′).

Blood and plasma parameters

Blood was extracted directly from the mandibular sinus after anesthetizing mice with isoflurane. Serum IL-6, CXCL1, and TNF-α concentrations were determined by ELISA (IL-6, reference 88-7064-22, eBioscience; CXCL1, reference MKC00B, R&D Systems; and TNF-α, reference 88-7324-22, eBioscience). All protocols were performed according to the manufacturer's instructions.

Transcriptional profiling

Zmpste24-deficient mouse liver transcriptional profiles as well as $Lmna^{G609G}$ profiles were previously reported (Varela et al. 2005; Osorio et al. 2011a). Array data were clustered using Cluster 3.0 software, and the heat maps were created using TreeView 1.1.5 software (http://rana.lbl.gov/EisenSoftware.htm).

GSEA

GSEA was performed as described in the original citation (Subramanian et al. 2005). For data analysis, we used GSEA release 2.06 and MSigDB release 2.5 (http://www.broadinstitute.org/gsea/index.jsp). Weighted enrichment scores were calculated with gene expression lists ranked by signal to noise ratio. The maximum gene set size was set to 500 genes, the minimum gene set size was set to 20 genes, and the number of permutations was set to 1000. Analyses were performed with a gene set composed of genes that contain, in the promoter regions [−2 kb, 2 kb] around the transcription start site, the motif GGGRATTTCC, which matches the consensus binding site for the NF-κB transcription factor. Selected enriched pathways had a relaxed false discovery rate of <0.25 and $P < 0.05$.

Statistical analysis

We performed statistical analysis of the differences between mouse cohorts or different conditions with a two-tailed Student's *t*-test. In experiments with more than two groups, differences were analyzed by multifactorial one-way analysis of variance (ANOVA), and for the comparison of different groups in Kaplan-Meier survival plots, we used a log-rank (Mantel-Cox) test. We used Microsoft Excel or GraphPad Prism software for calculations and expressed the results as the means ± SEM.

Acknowledgments

We thank Drs. G. Velasco, X.S. Puente, N. Lévy, M.S. Fernández, L. Boscá, O. Fernández-Capetillo, and J. Rivera for their support and assistance. This work was supported by grants from Ministerio de Ciencia e Innovación-Spain and European Union (FP7 MicroEnviMet). The Instituto Universitario de Oncología is supported by Obra Social Cajastur and Acción Transversal del Cáncer-RTICC. C.L.-O. is an Investigator of the Botin Foundation.

References

Adler AS, Sinha S, Kawahara TL, Zhang JY, Segal E, Chang HY. 2007. Motif module map reveals enforcement of aging by continual NF-κB activity. *Genes Dev* **21:** 3244–3257.

Aw D, Palmer DB. 2011. The origin and implication of thymic involution. *Aging Dis* **2:** 437–443.

Baker DJ, Wijshake T, Tchkonia T, LeBrasseur NK, Childs BG, van de Sluis B, Kirkland JL, van Deursen JM. 2011. Clearance of p16Ink4a-positive senescent cells delays ageing-associated disorders. *Nature* **479:** 232–236.

Beg AA, Sha WC, Bronson RT, Ghosh S, Baltimore D. 1995. Embryonic lethality and liver degeneration in mice lacking the RelA component of NF-κB. *Nature* **376:** 167–170.

Bensimon A, Aebersold R, Shiloh Y. 2011. Beyond ATM: The protein kinase landscape of the DNA damage response. *FEBS Lett* **585:** 1625–1639.

Bergo MO, Gavino B, Ross J, Schmidt WK, Hong C, Kendall LV, Mohr A, Meta M, Genant H, Jiang Y, et al. 2002. Zmpste24 deficiency in mice causes spontaneous bone fractures, muscle weakness, and a prelamin A processing defect. *Proc Natl Acad Sci* **99:** 13049–13054.

Biton S, Ashkenazi A. 2011. NEMO and RIP1 control cell fate in response to extensive DNA damage via TNF-α feedforward signaling. *Cell* **145:** 92–103.

Burtner CR, Kennedy BK. 2010. Progeria syndromes and ageing: What is the connection? *Nat Rev Mol Cell Biol* **11:** 567–578.

Cai D, Frantz JD, Tawa NE Jr, Melendez PA, Oh BC, Lidov HG, Hasselgren PO, Frontera WR, Lee J, Glass DJ, et al. 2004.

IKKβ/NF-κB activation causes severe muscle wasting in mice. *Cell* **119:** 285–298.

Coppe JP, Desprez PY, Krtolica A, Campisi J. 2010. The senescence-associated secretory phenotype: The dark side of tumor suppression. *Annu Rev Pathol* **5:** 99–118.

de Carlos F, Varela I, Germana A, Montalbano G, Freije JM, Vega JA, Lopez-Otin C, Cobo JM. 2008. Microcephalia with mandibular and dental dysplasia in adult Zmpste24-deficient mice. *J Anat* **213:** 509–519.

Dechat T, Pfleghaar K, Sengupta K, Shimi T, Shumaker DK, Solimando L, Goldman RD. 2008. Nuclear lamins: Major factors in the structural organization and function of the nucleus and chromatin. *Genes Dev* **22:** 832–853.

De Sandre-Giovannoli A, Bernard R, Cau P, Navarro C, Amiel J, Boccaccio I, Lyonnet S, Stewart CL, Munnich A, Le Merrer M, et al. 2003. Lamin a truncation in Hutchinson-Gilford progeria. *Science* **300:** 2055. doi: 10.1126/science.1084125.

Eriksson M, Brown WT, Gordon LB, Glynn MW, Singer J, Scott L, Erdos MR, Robbins CM, Moses TY, Berglund P, et al. 2003. Recurrent de novo point mutations in lamin A cause Hutchinson-Gilford progeria syndrome. *Nature* **423:** 293–298.

Espada J, Varela I, Flores I, Ugalde AP, Cadinanos J, Pendas AM, Stewart CL, Tryggvason K, Blasco MA, Freije JM, et al. 2008. Nuclear envelope defects cause stem cell dysfunction in premature-aging mice. *J Cell Biol* **181:** 27–35.

Freije JM, Lopez-Otin C. 2012. Reprogramming aging and progeria. *Curr Opin Cell Biol* doi: 10.1016/j.ceb.2012.08.009.

Freund A, Orjalo AV, Desprez PY, Campisi J. 2010. Inflammatory networks during cellular senescence: Causes and consequences. *Trends Mol Med* **16:** 238–246.

Gruenbaum Y, Margalit A, Goldman RD, Shumaker DK, Wilson KL. 2005. The nuclear lamina comes of age. *Nat Rev Mol Cell Biol* **6:** 21–31.

Hale JS, Frock RL, Mamman SA, Fink PJ, Kennedy BK. 2010. Cell-extrinsic defective lymphocyte development in Lmna$^{-/-}$ mice. *PLoS ONE* **5:** e10127. doi: 10.1371/journal.pone.0010127.

Hayden MS, Ghosh S. 2004. Signaling to NF-κB. *Genes Dev* **18:** 2195–2224.

Hayden MS, Ghosh S. 2008. Shared principles in NF-κB signaling. *Cell* **132:** 344–362.

Hayden MS, Ghosh S. 2012. NF-κB, the first quarter-century: Remarkable progress and outstanding questions. *Genes Dev* **26:** 203–234.

Hennekam RC. 2006. Hutchinson-Gilford progeria syndrome: Review of the phenotype. *Am J Med Genet A* **140:** 2603–2624.

Herweijer H, Wolff JA. 2007. Gene therapy progress and prospects: Hydrodynamic gene delivery. *Gene Ther* **14:** 99–107.

Hoeijmakers JH. 2009. DNA damage, aging, and cancer. *N Engl J Med* **361:** 1475–1485.

Huang TT, Wuerzberger-Davis SM, Wu ZH, Miyamoto S. 2003. Sequential modification of NEMO/IKKγ by SUMO-1 and ubiquitin mediates NF-κB activation by genotoxic stress. *Cell* **115:** 565–576.

Janssens S, Tschopp J. 2006. Signals from within: The DNA-damage-induced NF-κB response. *Cell Death Differ* **13:** 773–784.

Kang TW, Yevsa T, Woller N, Hoenicke L, Wuestefeld T, Dauch D, Hohmeyer A, Gereke M, Rudalska R, Potapova A, et al. 2011. Senescence surveillance of pre-malignant hepatocytes limits liver cancer development. *Nature* **479:** 547–551.

Kawahara TL, Michishita E, Adler AS, Damian M, Berber E, Lin M, McCord RA, Ongaigui KC, Boxer LD, Chang HY, et al. 2009. SIRT6 links histone H3 lysine 9 deacetylation to NF-κB-dependent gene expression and organismal life span. *Cell* **136:** 62–74.

Kirkwood TB. 2005. Understanding the odd science of aging. *Cell* **120:** 437–447.

Kuilman T, Peeper DS. 2009. Senescence-messaging secretome: SMS-ing cellular stress. *Nat Rev Cancer* **9:** 81–94.

Lammerding J, Schulze PC, Takahashi T, Kozlov S, Sullivan T, Kamm RD, Stewart CL, Lee RT. 2004. Lamin A/C deficiency causes defective nuclear mechanics and mechanotransduction. *J Clin Invest* **113:** 370–378.

Lavin MF. 2008. Ataxia-telangiectasia: From a rare disorder to a paradigm for cell signalling and cancer. *Nat Rev Mol Cell Biol* **9:** 759–769.

Le Saux S, Weyand CM, Goronzy JJ. 2012. Mechanisms of immunosenescence: Lessons from models of accelerated immune aging. *Ann N Y Acad Sci* **1247:** 69–82.

Li Q, Verma IM. 2002. NF-κB regulation in the immune system. *Nat Rev Immunol* **2:** 725–734.

Liu B, Wang J, Chan KM, Tjia WM, Deng W, Guan X, Huang JD, Li KM, Chau PY, Chen DJ, et al. 2005. Genomic instability in laminopathy-based premature aging. *Nat Med* **11:** 780–785.

Marino G, Ugalde AP, Salvador-Montoliu N, Varela I, Quiros PM, Cadinanos J, van der Pluijm I, Freije JM, Lopez-Otin C. 2008. Premature aging in mice activates a systemic metabolic response involving autophagy induction. *Hum Mol Genet* **17:** 2196–2211.

Marino G, Ugalde AP, Fernandez AF, Osorio FG, Fueyo A, Freije JM, Lopez-Otin C. 2010. Insulin-like growth factor 1 treatment extends longevity in a mouse model of human premature aging by restoring somatotroph axis function. *Proc Natl Acad Sci* **107:** 16268–16273.

McCool KW, Miyamoto S. 2012. DNA damage-dependent NF-κB activation: NEMO turns nuclear signaling inside out. *Immunol Rev* **246:** 311–326.

Mekhail K, Moazed D. 2010. The nuclear envelope in genome organization, expression and stability. *Nat Rev Mol Cell Biol* **11:** 317–328.

Merideth MA, Gordon LB, Clauss S, Sachdev V, Smith AC, Perry MB, Brewer CC, Zalewski C, Kim HJ, Solomon B, et al. 2008. Phenotype and course of Hutchinson-Gilford progeria syndrome. *N Engl J Med* **358:** 592–604.

Miyamoto S. 2011. Nuclear initiated NF-κB signaling: NEMO and ATM take center stage. *Cell Res* **21:** 116–130.

Osorio FG, Varela I, Lara E, Puente XS, Espada J, Santoro R, Freije JM, Fraga MF, Lopez-Otin C. 2010. Nuclear envelope alterations generate an aging-like epigenetic pattern in mice deficient in Zmpste24 metalloprotease. *Aging Cell* **9:** 947–957.

Osorio FG, Navarro CL, Cadinanos J, Lopez-Mejia IC, Quiros PM, Bartoli C, Rivera J, Tazi J, Guzman G, Varela I, et al. 2011a. Splicing-directed therapy in a new mouse model of human accelerated aging. *Sci Transl Med* **3:** 106ra107. doi: 10.1126/scitranslmed.3002847.

Osorio FG, Ugalde AP, Marino G, Puente XS, Freije JM, Lopez-Otin C. 2011b. Cell autonomous and systemic factors in progeria development. *Biochem Soc Trans* **39:** 1710–1714.

Pendas AM, Zhou Z, Cadinanos J, Freije JM, Wang J, Hultenby K, Astudillo A, Wernerson A, Rodriguez F, Tryggvason K, et al. 2002. Defective prelamin A processing and muscular and adipocyte alterations in Zmpste24 metalloproteinase-deficient mice. *Nat Genet* **31:** 94–99.

Perkins ND. 2007. Integrating cell-signalling pathways with NF-κB and IKK function. *Nat Rev Mol Cell Biol* **8:** 49–62.

Puente XS, Quesada V, Osorio FG, Cabanillas R, Cadinanos J, Fraile JM, Ordonez GR, Puente DA, Gutierrez-Fernandez A, Fanjul-Fernandez M, et al. 2011. Exome sequencing and

functional analysis identifies BANF1 mutation as the cause of a hereditary progeroid syndrome. *Am J Hum Genet* **88:** 650–656.
Ramirez CL, Cadinanos J, Varela I, Freije JM, Lopez-Otin C. 2007. Human progeroid syndromes, aging and cancer: New genetic and epigenetic insights into old questions. *Cell Mol Life Sci* **64:** 155–170.
Rando TA, Chang HY. 2012. Aging, rejuvenation, and epigenetic reprogramming: Resetting the aging clock. *Cell* **148:** 46–57.
Ricciotti E, FitzGerald GA. 2011. Prostaglandins and inflammation. *Arterioscler Thromb Vasc Biol* **31:** 986–1000.
Rodier F, Coppe JP, Patil CK, Hoeijmakers WA, Munoz DP, Raza SR, Freund A, Campeau E, Davalos AR, Campisi J. 2009. Persistent DNA damage signalling triggers senescence-associated inflammatory cytokine secretion. *Nat Cell Biol* **11:** 973–979.
Sagelius H, Rosengardten Y, Hanif M, Erdos MR, Rozell B, Collins FS, Eriksson M. 2008. Targeted transgenic expression of the mutation causing Hutchinson-Gilford progeria syndrome leads to proliferative and degenerative epidermal disease. *J Cell Sci* **121:** 969–978.
Salminen A, Suuronen T, Huuskonen J, Kaarniranta K. 2008. NEMO shuttle: A link between DNA damage and NF-κB activation in progeroid syndromes? *Biochem Biophys Res Commun* **367:** 715–718.
Salminen A, Ojala J, Kaarniranta K. 2011. Apoptosis and aging: Increased resistance to apoptosis enhances the aging process. *Cell Mol Life Sci* **68:** 1021–1031.
Scaffidi P, Misteli T. 2006. Lamin A-dependent nuclear defects in human aging. *Science* **312:** 1059–1063.
Scaffidi P, Misteli T. 2008. Lamin A-dependent misregulation of adult stem cells associated with accelerated ageing. *Nat Cell Biol* **10:** 452–459.
Schreiber E, Matthias P, Muller MM, Schaffner W. 1989. Rapid detection of octamer binding proteins with 'mini-extracts', prepared from a small number of cells. *Nucleic Acids Res* **17:** 6419. doi: 10.1093/nar/17.15.6419.
Subramanian A, Tamayo P, Mootha VK, Mukherjee S, Ebert BL, Gillette MA, Paulovich A, Pomeroy SL, Golub TR, Lander ES, et al. 2005. Gene set enrichment analysis: A knowledge-based approach for interpreting genome-wide expression profiles. *Proc Natl Acad Sci* **102:** 15545–15550.
Sur I, Ulvmar M, Toftgard R. 2008. The two-faced NF-κB in the skin. *Int Rev Immunol* **27:** 205–223.
Tak PP, Firestein GS. 2001. NF-κB: A key role in inflammatory diseases. *J Clin Invest* **107:** 7–11.
Tilstra JS, Clauson CL, Niedernhofer LJ, Robbins PD. 2011. NF-κB in aging and disease. *Aging Dis* **2:** 449–465.
Tilstra JS, Robinson AR, Wang J, Gregg SQ, Clauson CL, Reay DP, Nasto LA, St Croix CM, Usas A, Vo N, et al. 2012. NF-κB inhibition delays DNA damage-induced senescence and aging in mice. *J Clin Invest* **122:** 2601–2612.
Ugalde AP, Espanol Y, Lopez-Otin C. 2011a. Micromanaging aging with miRNAs: New messages from the nuclear envelope. *Nucleus* **2:** 549–555.
Ugalde AP, Ramsay AJ, de la Rosa J, Varela I, Marino G, Cadinanos J, Lu J, Freije JM, Lopez-Otin C. 2011b. Aging and chronic DNA damage response activate a regulatory pathway involving miR-29 and p53. *EMBO J* **30:** 2219–2232.
Varela I, Cadinanos J, Pendas AM, Gutierrez-Fernandez A, Folgueras AR, Sanchez LM, Zhou Z, Rodriguez FJ, Stewart CL, Vega JA, et al. 2005. Accelerated ageing in mice deficient in Zmpste24 protease is linked to p53 signalling activation. *Nature* **437:** 564–568.
Varela I, Pereira S, Ugalde AP, Navarro CL, Suarez MF, Cau P, Cadinanos J, Osorio FG, Foray N, Cobo J, et al. 2008. Combined treatment with statins and aminobisphosphonates extends longevity in a mouse model of human premature aging. *Nat Med* **14:** 767–772.
Vijg J, Campisi J. 2008. Puzzles, promises and a cure for ageing. *Nature* **454:** 1065–1071.
Wang CY, Cusack JC Jr, Liu R, Baldwin AS Jr. 1999. Control of inducible chemoresistance: Enhanced anti-tumor therapy through increased apoptosis by inhibition of NF-κB. *Nat Med* **5:** 412–417.
Wang Y, Panteleyev AA, Owens DM, Djabali K, Stewart CL, Worman HJ. 2008. Epidermal expression of the truncated prelamin A causing Hutchinson-Gilford progeria syndrome: Effects on keratinocytes, hair and skin. *Hum Mol Genet* **17:** 2357–2369.
Worman HJ, Foisner R. 2010. The nuclear envelope from basic biology to therapy. *Biochem Soc Trans* **38:** 253–256.
Worman HJ, Ostlund C, Wang Y. 2010. Diseases of the nuclear envelope. *Cold Spring Harb Perspect Biol* **2:** a000760. doi: 10.1101/cshperspect.a000760.
Wu ZH, Shi Y, Tibbetts RS, Miyamoto S. 2006. Molecular linkage between the kinase ATM and NF-κB signaling in response to genotoxic stimuli. *Science* **311:** 1141–1146.

V. Development of experimental methodologies to study NF-κB signaling in aging

Recent evidences have demonstrated the implication of NF-κB signaling in aging, uncovering a pivotal role of this pathway in the maintenance of the aged state. Thus, the possibility of inhibiting NF-κB constitutes a promising target for rejuvenation based approaches. In this regard, the development of new methodologies to monitor NF-κB signaling during aging also represents a critical point, as chronic inflammation detection often requires extremely sensitive methods. In these works, we have reviewed the existing evidences about NF-κB signaling in aging and developed a luciferase-based approach to monitor NF-κB activity in live animals.

Article 6. Fernando G. Osorio, Carlos López-Otín and José M. P. Freije. "Causative role of NF-κB signaling and inflammation in premature aging".

Aging (Albany NY). 2012 Nov; 4(11):726-7.

Personal contribution to this work

I was responsible for the compilation of the information, preparation of the figure and writing of the manuscript under the supervision of Dr. José M.P. Freije and Dr. Carlos López-Otín.

Article 7. Fernando G. Osorio, Jorge de la Rosa and José M. P. Freije. "Luminescence-based in vivo monitoring of NF-κB activity through a gene delivery approach".

Cell Communication & Signaling. 2013 Mar 21; 11(1):19.

Personal contribution to this work

I participated with Dr. José M.P. Freije in the discussion and development of the experimental methodology. Also, I prepared the manuscript under his supervision.

www.impactaging.com AGING, November 2012, Vol 4 N 11

Editorial

NF-κB in premature aging

Fernando G. Osorio, Carlos López-Otín and José M. P. Freije

During decades, aging has been regarded as the consequence of a stochastic process caused by the accumulative effect of damaged molecules. However, recent experimental evidences have extended this view and suggested that aging also requires active signaling programs for the maintenance of the aged state [1]. Beyond cell-autonomous alterations, age signals get systemic through changes in intercellular communication pathways [2]. The identification of the precise nature of these mechanisms and signals could provide valuable information, uncovering potential targets for rejuvenation-aimed approaches [3].

Aging research has greatly benefited from the study of progeroid syndromes, accelerated aging conditions caused by an excessive accumulation of cellular damage or by an inefficient response of the repair mechanisms. Progeroid laminopathies are accelerated aging syndromes caused by defects of the nuclear lamina. Among them, Hutchinson-Gilford Progeria Syndrome (HGPS) is one the most intensely studied. This syndrome is caused by a point mutation in the *LMNA* gene, leading to the accumulation of a truncated form of lamin A called progerin which induces important alterations in the cell nucleus. Interestingly, progerin accumulation has also been reported during normal aging, adding a new layer of interest to the study of this syndrome.

NF-κB transcription factors respond to a large variety of external and internal stress signals, having essential roles in development and tissue homeostasis maintenance. Through the study of two related mouse models of progeroid laminopathies (*Zmpste24*-deficient and $Lmna^{G609G}$ knock-in mice), we have recently found that aberrant activation of NF-κB is involved in the pathogenesis of accelerated aging syndromes, providing new insights into the mechanisms that allow the integration of cellular and systemic alterations in the aging process [4].

The *in vivo* monitoring of NF-κB activity by using a reporter-based assay revealed that this pathway was constitutively hyperactivated in progeroid mice. Further experiments allowed us to unveil the molecular pathway involved in this aberrant activation. Thus, in response to nuclear envelope alterations some important DNA damage sensors such as p53 or ATM were activated. In this context, we provide evidence that active ATM kinase cooperates with nuclear NEMO, an NF-κB regulatory subunit, resulting in the activation of NF-κB. We also found that, in response to NF-κB activation, several pro-inflammatory cytokines were significantly up-regulated. Among them, secretion of IL-6, CXCL-1 and TNF-α could have a causal role in the premature aging syndrome by establishing a chronic inflammatory situation through feed-forward regulatory signaling, affecting distant cells and tissues.

Aimed at dissecting the precise contribution of NF-κB hyperactivation to the progeroid phenotype, we used an anti-inflammatory genetic strategy based on crossing *Zmpste24*-deficient mice with *RelA* haploinsufficient mice [5]. Interestingly, double mutant $Zmpste24^{-/-}$ $RelA^{+/-}$ mice displayed a retardation in the aging process, showing an extended longevity as compared with $Zmpste24^{-/-}RelA^{+/+}$ mice. Furthermore, double mutant mice showed a remarkable recovery of skin and immunological alterations, which is consistent with the proposed relevance of NF-κB activity in tissue homeostasis maintenance. These results prompted us to test a pharmacological approach to target NF-κB activation in progeroid mice. Thus, sodium salicylate treatment of both $Zmpste24^{-/-}$ and $Lmna^{G609G/G609G}$ mice extended longevity and led to a significant prevention of skin and immune alterations, demonstrating the feasibility of targeting this pathway for slowing down the progression of accelerated aging.

Finally, our results indicate that these findings can be extended to normal aging, suggesting that a common accumulation of genetic damage and nuclear envelope alterations with age could be responsible, at least in part, of the abnormal NF-κB activity reported in tissues from advanced aged donors. The accumulation of senescent cells together with the decline in adult stem cell function is a primary cause of the compromise of tissue homeostasis during aging. The primary function of NF-κB activation in this context could be related to the prevention of apoptosis of damaged cells, so that

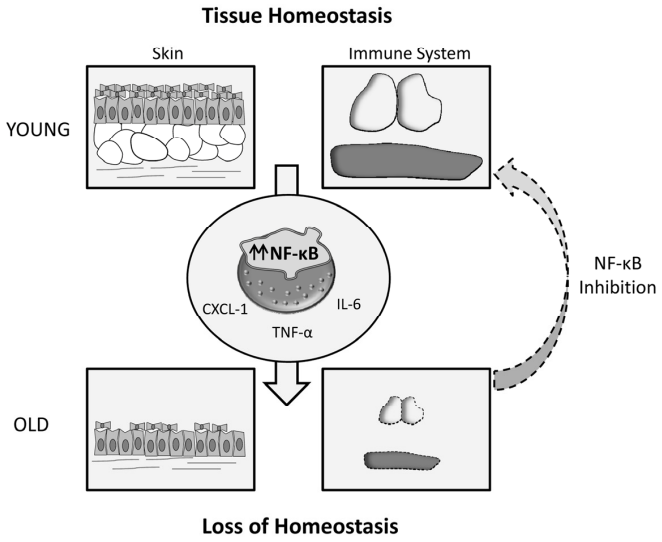

Figure 1. Exacerbated NF- κB signaling leads to age-related loss of tissue homeostasis, which takes place at an accelerated rate in progeroid syndromes. This phenomenon can be alleviated through NF- κB inhibition.

chronic activation of this pathway with the subsequent immunological decline could preclude a proper clearance of senescent and damaged cells. In this regard, a recent report has described the causal involvement of inflammatory pathways in the age-related decline in stem cell function [6].

Globally, the data discussed herein clarify three important aspects that define NF-κB role during aging. Thus, experimental data confirm that NF-κB signaling is active during normal aging [7], its hyperactivation is associated with the development of accelerated aging and its amelioration retards the aging process [4-5, 8]. These characteristics support the use of strategies aimed at controlling NF-κB related inflammation as putative rejuvenation strategies during both normal and pathological aging. Over the last years, aging research has composed a complex picture where both cell autonomous and systemic alterations cooperate for establishing the aged state in organisms. Rational design of new interventions aimed to slow down this process should act in a coordinate way, targeting pro-aging signals as well as altered cellular communication pathways for the effective prevention of aging-related disorders.

Fernando G. Osorio, Carlos López-Otín and José M. P. Freije

Departamento de Bioquímica y Biología Molecular, Facultad de Medicina, Instituto Universitario de Oncología, Universidad de Oviedo, 33006-Oviedo, Spain
Email: clo@uniovi.es; jmpf@uniovi.es

Received: 11/20/12; Published: 11/27/12

REFERENCES

1. Rando TA and Chang HY. Cell. 2012; 148: 46-57.
2. Osorio FG et al. Biochem Soc Trans. 2011; 39: 1710-1714.
3. Freije JM and Lopez-Otin C. Curr Opin Cell Biol. 2012: [Epub ahead of print] doi: 10.1016/j.ceb.2012.1008.1009.
4. Osorio FG et al. Genes Dev. 2012; 26: 2311-2324.
5. Kawahara TL et al. Cell. 2009; 136: 62-74.
6. Doles J et al. Genes Dev. 2012; 26: 2144-2153.
7. Adler AS et al. Genes Dev. 2007; 21: 3244-3257.
8. Tilstra JS et al. J Clin Invest. 2012; 122: 2601-2612.

Osorio et al. Cell Communication and Signaling 2013, 11:19
http://www.biosignaling.com/content/11/1/19

CELL COMMUNICATION & SIGNALING

METHODOLOGY Open Access

Luminescence-based *in vivo* monitoring of NF-κB activity through a gene delivery approach

Fernando G Osorio, Jorge de la Rosa and José MP Freije*

Abstract

Background: Monitoring activity of specific signaling pathways *in vivo* is challenging and requires highly sensitive methods to detect dynamic perturbations in whole organisms.

Results: *In vivo* gene delivery of a luciferase reporter followed by bioluminiscence imaging allows measuring NF-κB activity in mice liver and lungs.

Conclusions: This protocol allows a direct measure of NF-κB activity through quantification of bioluminescence signal, demonstrating its accuracy and sensitivity in different animal models and experimental conditions. Variants could be also applied for the analysis of NF-κB activity in different tissues or for studying other signaling pathways *in vivo*.

Background

Monitoring biological processes *in vivo* remains experimentally challenging. Visualization of biochemical perturbations in whole organisms requires highly sensitive methods that allow detection in a quantitative and reproducible manner [1-3]. Reporter gene approaches are based on the use of specific regulatory sequences attached to genes that confer organisms a property that could be easily detected and quantified, typically light or fluorescence emission [4]. Different luciferase and fluorescent proteins-based strategies have been developed for monitoring signaling pathways involved in cancer and aging [5-11].

Most of the available strategies rely on the generation of transgenic mice that stably express reporter genes. These mutant animals allow dynamic studies of complex processes, as the activity of the monitored signaling pathways could be recorded at different time points during lifetime. The main limitation of these approaches is that they imply the generation of transgenic strains, involving a long and expensive process that requires the use of a large number of experimentation animals. An alternative approach is described herein, based on the use of *in vivo* gene delivery strategies that potentially overcome previous limitations, allowing a fast and reliable quantification of the activity of signaling pathways in a wide variety of experimental models and physiological situations. Here we specifically describe a luciferase-based approach to measure *in vivo* NF-κB activity in different mice tissues.

NF-κB is involved in the response against a large variety of external and internal stress signals, having essential roles in inflammation, immune response, cell proliferation and protection against apoptosis [12-14]. Consequently with its key role in cellular stress response, NF-κB aberrant activation has been linked with several pathophysiological conditions including cancer and accelerated aging [15,16]. In this regard, it has been described that not only acute NF-κB activation is related with disease but also subtle changes in NF-κB activity that persist in time have important biological consequences, giving rise to chronic inflammatory conditions. The monitoring of these subtle changes in NF-κB activity has been especially challenging.

NF-κB luciferase reporter-based assay

NF-κB activation is most often monitored in cultured cells using a non-viral vector system that encodes firefly luciferase reporter gene under the control of a minimal cytomegalovirus (CMV) promoter and tandem repeats of the NF-κB transcriptional response element. The reporter gene will be only transcribed when NF-κB signaling pathway is active; otherwise Rel transcription factors are sequestered in the cytoplasm by an inhibitory complex. Inflammatory signals trigger NF-κB activation that involves nuclear

* Correspondence: jmpf@uniovi.es
Departamento de Bioquímica y Biología Molecular, Facultad de Medicina, Instituto Universitario de Oncología, Universidad de Oviedo, Oviedo 33006, Spain

translocation of the NF-κB transcription factors. The reporter gene will be transcribed, like endogenous NF-κB targets, proportionally to the magnitude of NF-κB activation and the time persistence of the induction signal. Monitoring bioluminescence emission by the tissues upon luciferin administration allows visualization of NF-κB activity *in vivo*.

In vivo gene delivery

Reporter-based strategies *in vivo* require using highly efficient methods of gene delivery that ensure the transfection of a high proportion of cells. For liver gene delivery, we have selected hydrodynamic transfection, a simple and efficient non-viral method that allows transfection of a naked DNA in a high proportion of the liver hepatocytes [17]. Rapid injection of a high-volume (10%, vol/weight) solution of the naked plasmid DNA through the tail vein generates a hydrodynamic pressure that expands liver endothelium resulting in DNA uptake by the hepatocytes [18,19]. Although the protocol is optimized for mice tissues, the technique could be modified for other animal models, even muscles of larger animals [20].

For lung delivery we have used DNA complexed with a polycation, polyethyleneimine (PEI). DNA-PEI complexes are efficiently internalized into the cells and the DNA is subsequently transported into the nucleus [21,22]. Systemic administration of DNA complexes results in gene delivery primarily to the lungs, reaching all the anatomical areas of this organ; this is an important advantage of this method as compared with others based on instillation, where only the proximal area is achieved [23].

Methods

Reagents

- Mice. We routinely use 6–20 week-old C57BL/6 mice, but we have also successfully used mice from other strains (129S1/SvImJ, BALB/c and CD1) as well as several genetically modified mouse models. All the animal experiments were performed with the aproval of the Committee for Animal Experimentation of the Universidad de Oviedo.
- NF-κB luciferase gene reporter (Qiagen, cat. no. CCS-013 L).
- In vivo jet-PEI™. Linear 22-kDa polyethylenimine (see reagent setup) (Polyplus transfection, cat. no. 201-10G).
- Autoclaved Ringer's solution (123 mM NaCl, 5 mM KCl and 1.5 mM $CaCl_2$).
- Autoclaved saline. 0.9% (wt/vol) sodium chloride.
- Anesthetic. Isoflurane (Abbott laboratories, cat. no. 571329.8).
- D-Luciferin firefly luciferase substrate, potassium salt (Melford laboratories, cat. no. L1350).
- *Escherichia coli* lipopolysaccharide (LPS) (Sigma, L2630).
- Sodium salicylate (Sigma, S3007).
- Endo-Free plasmid maxi kit (Qiagen, cat. no. 12362).

Equipment

- Xenogen or other *in vivo* luminescence imaging system (we have used Xenogen IVIS 100 series for the recording and data analysis).
- Isoflurane vaporizer.
- 27-G needle (BD microlance, cat. no. 300635).
- 2 mL. syringe (BD discardit, cat. no. 300928).
- 45–50°C waterbath and/or heat lamp.
- Shaver to remove mouse hair.
- Scale for weighing mice.

Reagent setup

Preparation of NF-κB luciferase reporter gene

Plasmids are purified by ion-exchange chromatography using EndoFree plasmid maxi kit following the manufacturer's instructions. It is very important that plasmids used for *in vivo* gene delivery be free of endotoxins.

Luciferin stock solution

Prepare a stock solution of luciferin (14.3 mg/mL) by dissolving 1 g substrate in 70 mL saline solution (0.9% sodium chloride). Filter the solution through a 0.22 μm sterile filter. Store reconstituted substrate in aliquots at −80°C. Use 0.2 mL per mice for intraperitoneal injection.

Preparation of PEI/DNA complexes

For an effective cell delivery of plasmid DNA, the overall ionic charge of the DNA complexes needs to be cationic. The amount of nitrogen (N) in the PEI and phosphate in the DNA (P) determines the charge of the complexes. In practice, the best transfection results are obtained with a N/P ratio of 5–10. For this specific purpose we have successfully used an N/P ratio of 8 and 50 μg of DNA per mice, using a total amount of 8 μL of jetPEI™ reagent. If using other mouse strains or targeting a different organ, a dose response should be carried out to determine the optimal PEI-DNA ratio. Calculate the amount of *in vivo*-jetPEI™ in each case as follows:

$$\mu L\ of\ in\ vivo - jetPEI^{TM} = \frac{(\mu g\ of\ DNA \times 3) \times N/P\ ratio}{150}$$

Equipment setup

General setup considerations

Prepare all the necessary material, warm up the water bath, turn on the vaporizer anesthesia machine, and

Osorio *et al. Cell Communication and Signaling* 2013, **11**:19
http://www.biosignaling.com/content/11/1/19

switch on the heat lamp, placing a cage under it for mice recovery after the procedure.

Procedure

Mice preparation (Timing 5 min)

1) Check the vaporizer system to ensure adequate amounts of supply gas (O_2) and isoflurane for duration of the procedure. Make sure system is set to flow to induction chamber. Turn on supply gas. Weigh mouse before this point.
2) Turn on flowmeter between 500–1000 mL/min and place animal in the induction chamber. Turn on vaporizer to 2-3%. Monitor animals until recumbent.
3) Switch system to flow to nosecone, remove animal from induction chamber and place in nosecone. Turn the vaporizer to 1.5-2%.

Preparation of DNA sample and hydrodynamic injection (Timing 15 min)

4) Calculate the volume required for hydrodynamic injection based on the weight of the mouse (10%, vol/weight). For example: a 15 g mouse will be injected with 1.5 mL of DNA solution. We normally use a 10 μg/mL DNA solution although this amount could be varied depending on the experimental requirements.
5) Dilute DNA in Ringer's solution and set a syringe according with the calculated volume.
6) Place the tail of the anesthetized mice in 45–50°C heated water for 30 s. This will make tail veins more easily visualized.
7) Mice have two lateral tail veins, both of which are superficial and could be used for the procedure. Place the tail with the lateral side up between your fingers. Inject the needle into the vein 2–3 cm from the tail tip. You can often see the needle into the vein.
8) Press with force the plunger of the syringe, trying to inject the entire volume in less than 10 s. When finished, remove the needle and apply light pressure to the injection site until the bleeding stops.
9) In general, a cohort of several mice could be injected one after the other, and up to 15–20 mice could be easily injected in a session.
10) The recovery phase could last up to an hour for full recovery; we recommend placing the injected mice under a heat lamp to avoid hypothermia.

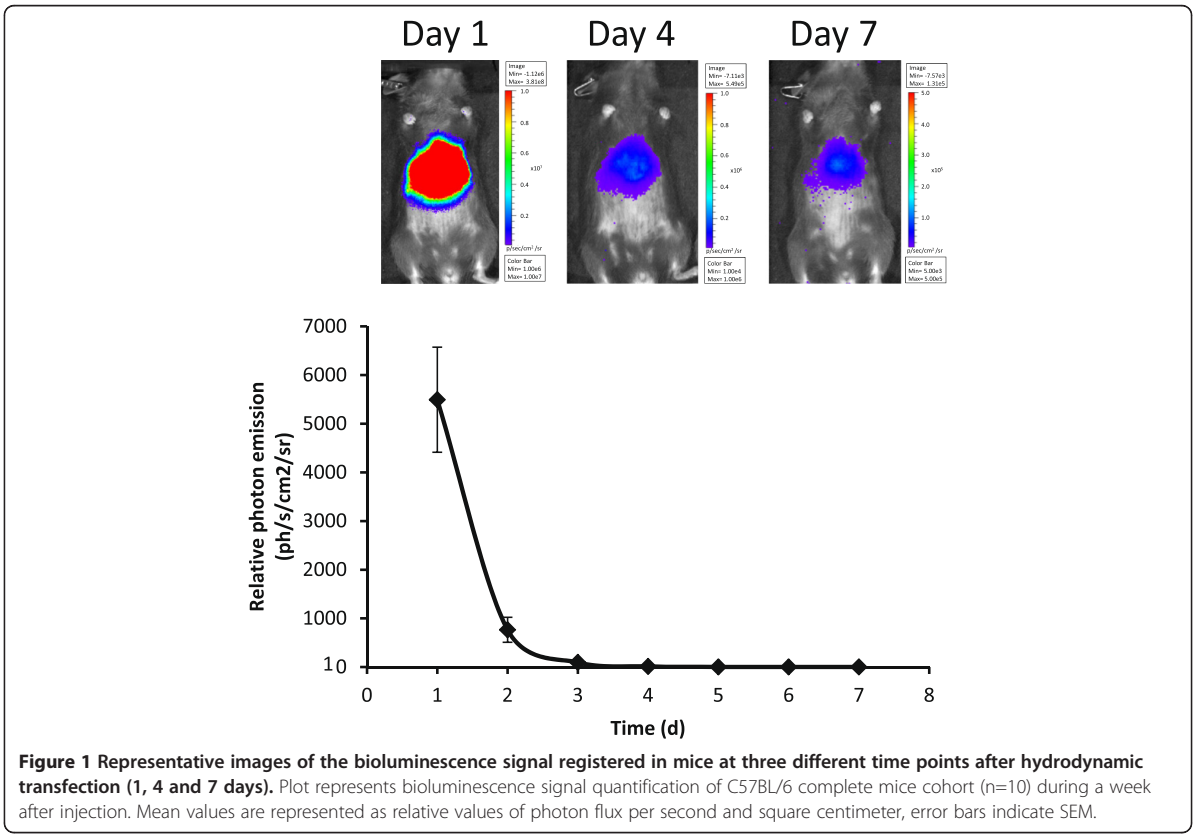

Figure 1 Representative images of the bioluminescence signal registered in mice at three different time points after hydrodynamic transfection (1, 4 and 7 days). Plot represents bioluminescence signal quantification of C57BL/6 complete mice cohort (n=10) during a week after injection. Mean values are represented as relative values of photon flux per second and square centimeter, error bars indicate SEM.

Osorio *et al. Cell Communication and Signaling* 2013, **11**:19
http://www.biosignaling.com/content/11/1/19

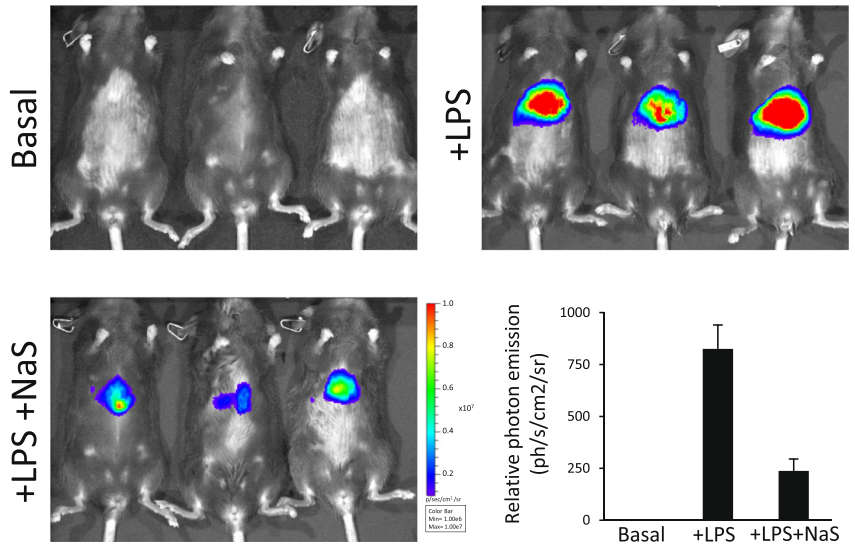

Figure 2 Constitutive and LPS-induced measure of liver NF-κB activity. Representative pictures are shown of three C57BL/6 mice before LPS administration and 24 hours after the injection, half of the cohort also received an injection of sodium salicylate (NaS). Plot represents relative mean bioluminescence values as photon flux per second and square centimeter, error bars indicate SEM.

Preparation of PEI/DNA complexes and injection into mice (Timing 15 min)

11) Dilute 50 μg of the plasmid in 100 μL of 5% glucose solution. Vortex gently. Dilute 8 μL of *in vivo*-jetPEI™ reagent in 100 μL of 5% glucose solution. Combined both and incubate the 200 μL final volume 15 min at room temperature (RT). From this point the complexes are stable for 2 hours at RT. Critical step, proceed immediately to the next point.
12) Proceed from step 3 and place the tail of the anesthetized mice under 45–50°C heated water for 30 s. Inject 0.2 mL PEI-complexed DNA into the lateral vein.
13) Place mice under the heat lamp for recovery.

In vivo bioluminescence imaging (Timing 30 min)

14) Anesthetize mice using isoflurane vaporizer coupled to the IVIS imaging system. Shave the ventral (for imaging of liver) or dorsal (for imaging of lungs) area of the mice. This is especially important for an adequate imaging of dark-coated mice such as C57BL/6.

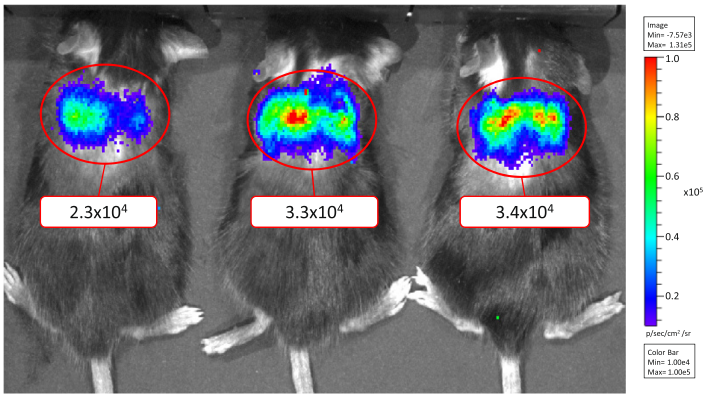

Figure 3 NF-κB basal activity in mouse lungs. Representative image of three C57BL/6 mice 24 hours after the injection of the PEI/DNA complexes.

15) Inject 0.2 mL luciferin i.p. and wait for 5 min. Imaging should be carried out between 5 and 30 min after luciferin injection. We usually perform imaging of several mice at the same time.
16) Image the mice according with the equipment instructions; we have good results with the Xenogen's IVIS Living image program selecting a medium binning and a variable exposure time depending on signal intensity. Avoid signal saturation in order to obtain a lineal signal.

Data analysis

17) Change image setting from counts to photons. Photons are absolute physical units that measure the light emission from the subject. The radiance unit of photons/sec/cm2/sr is the number of photons per second that leave a square centimeter of tissue and radiate into a solid angle of one steradian (sr). Measurements in units of radiance automatically take into account camera settings and allow comparing data obtained from different animals or from the same animal in different days.
18) For each mouse draw a measurement region of interest (ROI), and adjust the threshold value depending on the intensity of the signal. Obtain a background-corrected ROI measurement by subtracting an average background ROI from the measured ROI by using software computation options.
19) Critical step. We recommend measuring basal NF-κB activity starting at 72 hours after the plasmid injection, the reason is that hydrodynamic delivery procedure could induce a transient inflammatory response in the liver that interfere with the measurements (Figure 1). We have not seen this effect using PEI/DNA complexes.

Results and discussion

A cohort of C57BL/6 mice was hydrodynamically transfected with the NF-κB luciferase reporter (Figure 1). Bioluminescence signals were recorded each day during a week. According to the data shown, bioluminescence signal is especially high during the first 48 hours after the injection, rapidly diminishing thereafter and reaching stable values 72 hours after the injection. This phenomenon is due to a transient inflammatory response caused by the hydrodynamic procedure; for this reason, we recommend measuring NF-κB activity at least 72 hours after injection in order to prevent potential interference in the signal recorded.

A potential application of this method to study basal and acute induced activity of NF-κB in mice livers is described in the Figure 2. To this end, we first measured NF-κB basal activity in C57BL/6 mice and then we induced acute inflammation with *E. coli* lipopolysaccharide (LPS). Additionally, half of the mice injected with the LPS received a dose (200 mg/Kg) of sodium salicylate, a powerful inhibitor of NF-κB signaling. Quantification of the bioluminescence signals demonstrates the sensitivity and reproducibility of the method described.

The analysis of constitutive NF-κB activity in the lungs is showed in Figure 3. PEI/DNA complexes allow an efficient and highly-specific delivery of the NF-κB reporter to the lungs.

The method described herein has been successfully used for studying constitutive and acute-induced NF-κB signaling in mice tissues [12,24]. The use of this approach allowed us to demonstrate chronic activation of NF-κB in two different mouse models of accelerated aging and to monitor the response in these models to non-steroid anti-inflammatory drugs [12,16]. These results support the utility of this approach to study both chronic conditions as well as acute inflammatory responses.

Conclusions

The methodology described herein includes a step-by-step procedure for liver and lung gene delivery, recording of the bioluminescence signal and data analysis. Besides, we provide experimental validation of the protocol, demonstrating the sensitivity and reproducibility of the method.

The possibility of using viral vectors with different tissue tropisms for the reporter delivery potentially allows monitoring NF-κB in any tissue. Additionally, the same strategy may be applied for studying different signaling pathways, replacing the NF-κB response element with other regulatory sequences in the luciferase reporter system.

Competing interests

The authors declare that they have no competing interests.

Authors' contributions

JMPF designed the overall protocol and supervised the project. FGO and JR carried out the experiments. FGO and JMPF wrote the manuscript. All authors read and approved the final manuscript.

Acknowledgements

We thank Drs. C. López-Otín, G. Velasco and A. Fueyo for helpful comments and support. This work was supported by grants from Ministerio de Ciencia e Innovación-Spain and European Union (FP7 MicroEnviMet). JR is supported by a fellowship from Fundación María Cristina Masaveu Peterson. The Instituto Universitario de Oncología is supported by Obra Social Cajastur and Acción Transversal del Cáncer-RTICC.

Received: 19 February 2013 Accepted: 11 March 2013
Published: 21 March 2013

References

1. Badr CE, Tannous BA: **Bioluminescence imaging: progress and applications.** *Trends Biotechnol* 2011, **29**(12):624–633.
2. Tangney M, Francis KP: **In vivo optical imaging in gene & cell therapy.** *Curr Gene Ther* 2012, **12**(1):2–11.

3. Carlsen H, Moskaug JO, Fromm SH, Blomhoff R: **In vivo imaging of NF-kappa B activity.** *J Immunol* 2002, **168**(3):1441–1446.
4. Brogan J, Li F, Li W, He Z, Huang Q, Li CY: **Imaging molecular pathways: reporter genes.** *Radiat Res* 2012, **177**(4):508–513.
5. Uhrbom L, Nerio E, Holland EC: **Dissecting tumor maintenance requirements using bioluminescence imaging of cell proliferation in a mouse glioma model.** *Nat Med* 2004, **10**(11):1257–1260.
6. Zindy F, Williams RT, Baudino TA, Rehg JE, Skapek SX, Cleveland JL, Roussel MF, Sherr CJ: **Arf tumor suppressor promoter monitors latent oncogenic signals in vivo.** *Proc Natl Acad Sci U S A* 2003, **100**(26):15930–15935.
7. Goldman SJ, Chen E, Taylor R, Zhang S, Petrosky W, Reiss M, Jin S: **Use of the ODD-luciferase transgene for the non-invasive imaging of spontaneous tumors in mice.** *PLoS One* 2011, **6**(3):e18269.
8. Safran M, Kim WY, O'Connell F, Flippin L, Gunzler V, Horner JW, Depinho RA, Kaelin WG Jr: **Mouse model for noninvasive imaging of HIF prolyl hydroxylase activity: assessment of an oral agent that stimulates erythropoietin production.** *Proc Natl Acad Sci U S A* 2006, **103**(1):105–110.
9. Ohtani N, Imamura Y, Yamakoshi K, Hirota F, Nakayama R, Kubo Y, Ishimaru N, Takahashi A, Hirao A, Shimizu T, *et al*: **Visualizing the dynamics of p21 (Waf1/Cip1) cyclin-dependent kinase inhibitor expression in living animals.** *Proc Natl Acad Sci U S A* 2007, **104**(38):15034–15039.
10. Burd CE, Sorrentino JA, Clark KS, Darr DB, Krishnamurthy J, Deal AM, Bardeesy N, Castrillon DH, Beach DH, Sharpless NE: **Monitoring tumorigenesis and senescence in vivo with a p16(INK4a)-luciferase model.** *Cell* 2013, **152**(1–2):340–351.
11. O'Neill K, Lyons SK, Gallagher WM, Curran KM, Byrne AT: **Bioluminescent imaging: a critical tool in pre-clinical oncology research.** *J Pathol* 2010, **220**(3):317–327.
12. Osorio FG, Barcena C, Soria-Valles C, Ramsay AJ, de Carlos F, Cobo J, Fueyo A, Freije JM, Lopez-Otin C: **Nuclear lamina defects cause ATM-dependent NF-kappaB activation and link accelerated aging to a systemic inflammatory response.** *Genes Dev* 2012, **26**(20):2311–2324.
13. Hayden MS, Ghosh S: **NF-kappaB, the first quarter-century: remarkable progress and outstanding questions.** *Genes Dev* 2012, **26**(3):203–234.
14. Hayden MS, Ghosh S: **Shared principles in NF-kappaB signaling.** *Cell* 2008, **132**(3):344–362.
15. Tilstra JS, Clauson CL, Niedernhofer LJ, Robbins PD: **NF-kappaB in aging and disease.** *Aging Dis* 2011, **2**(6):449–465.
16. Osorio FG, Lopez-Otin C, Freije JM: **NF-kB in premature aging.** *Aging (Albany NY)* 2012, **4**(11):726–727.
17. Bell JB, Podetz-Pedersen KM, Aronovich EL, Belur LR, McIvor RS, Hackett PB: **Preferential delivery of the sleeping beauty transposon system to livers of mice by hydrodynamic injection.** *Nat Protoc* 2007, **2**(12):3153–3165.
18. Liu F, Song Y, Liu D: **Hydrodynamics-based transfection in animals by systemic administration of plasmid DNA.** *Gene Ther* 1999, **6**(7):1258–1266.
19. Zhang G, Budker V, Wolff JA: **High levels of foreign gene expression in hepatocytes after tail vein injections of naked plasmid DNA.** *Hum Gene Ther* 1999, **10**(10):1735–1737.
20. Herweijer H, Wolff JA: **Gene therapy progress and prospects: hydrodynamic gene delivery.** *Gene Ther* 2007, **14**(2):99–107.
21. Rudolph C, Lausier J, Naundorf S, Muller RH, Rosenecker J: **In vivo gene delivery to the lung using polyethylenimine and fractured polyamidoamine dendrimers.** *J Gene Med* 2000, **2**(4):269–278.
22. Goula D, Benoist C, Mantero S, Merlo G, Levi G, Demeneix BA: **Polyethylenimine-based intravenous delivery of transgenes to mouse lung.** *Gene Ther* 1998, **5**(9):1291–1295.
23. Belur LR, Podetz-Pedersen K, Frandsen J, McIvor RS: **Lung-directed gene therapy in mice using the nonviral Sleeping Beauty transposon system.** *Nat Protoc* 2007, **2**(12):3146–3152.
24. Hyoudou K, Nishikawa M, Kobayashi Y, Kuramoto Y, Yamashita F, Hashida M: **Analysis of in vivo nuclear factor-kappaB activation during liver inflammation in mice: prevention by catalase delivery.** *Mol Pharmacol* 2007, **71**(2):446–453.

doi:10.1186/1478-811X-11-19
Cite this article as: Osorio *et al.*: Luminescence-based *in vivo* monitoring of NF-κB activity through a gene delivery approach. *Cell Communication and Signaling* 2013 **11**:19.

VI. Determination of the biological function of the proteostasis regulator AIRAPL

Proteostasis maintenance is critical for tissue homeostasis. In this regard, aging and cancer are accompanied by alterations in the main regulatory systems controlling protein homeostasis. AIRAPL, encoded by *Zfand2b* gene, is a proteasome regulator previously associated with impaired proteostasis during aging in *Caenorhabditis elegans*. We have generated *Zfand2b*-deficient mice with the finding that AIRAPL absence causes alterations in the hematopoietic system that finally lead to the development of myeloid malignancies. We have also found that AIRAPL exerts its tumor suppressor function through the control of insulin-related growth factor receptor (IGF1R) levels. Finally, we have found alterations in this protein in human myeloid malignancies, further demonstrating the importance of AIRAPL in hematopoietic system homeostasis.

Article 8. Fernando G. Osorio, Clara Soria-Valles, Olaya Santiago-Fernández, Teresa Bernal, María Mittelbrunn, Enrique Colado, Francisco Rodríguez, Elena Bonzon-Kulichenko, Jesús Vázquez, Montserrat Porta-de-la-Riva, Julián Cerón, Antonio Fueyo, Juan Li, Anthony R. Green, José M.P. Freije and Carlos López-Otín.

Manuscript under revision

Personal contribution to this work

I have been responsible for most of the experiments shown in this work. I generated, managed, genotyped and characterized *Zfand2b*-deficient mice. Likewise, I performed subsequent *in vitro* and *in vivo* studies, including molecular, hematological and histological analyses, as well as the experiments with human samples. Finally, I analyzed the data, prepared the figures and wrote the manuscript under the supervision of Dr. José M.P. Freije and Dr. Carlos López-Otín.

Loss of the proteostasis modulator AIRAPL causes myeloid transformation by deregulating IGF-1 signaling

Fernando G. Osorio[1], Clara Soria-Valles[1], Olaya Santiago-Fernández[1], Teresa Bernal[1,2], María Mittelbrunn[1,3,4], Enrique Colado[2], Francisco Rodríguez[1], Elena Bonzon-Kulichenko[5], Jesús Vázquez[5], Montserrat Porta-de-la-Riva[6], Julián Cerón[6], Antonio Fueyo[7], Juan Li[8,9], Anthony R. Green[8,9,10], José M.P. Freije[1] & Carlos López-Otín[1]

[1]Departamento de Bioquímica y Biología Molecular, Facultad de Medicina, Instituto Universitario de Oncología (IUOPA), Universidad de Oviedo, 33006-Oviedo, Spain; [2]Servivio de Hematología, Hospital Universitario Central de Asturias, 33006-Oviedo, Spain; [3]Instituto de Investigación Sanitaria Hospital 12 de Octubre (i+12), 28041-Madrid, Spain; [4]Departamento de Bioquímica, Facultad de Medicina, Universidad Autónoma de Madrid (UAM), 28029-Madrid, Spain; [5]Laboratory of Cardiovascular Proteomics, Centro Nacional de Investigaciones Cardiovasculares, 28029-Madrid, Spain; [6]Cancer and Human Molecular Genetics, Bellvitge Biomedical Research Institute-IDIBELL, 08908- L'Hospitalet de Llobregat, Barcelona, Spain; [7]Área de Fisiología, Departamento de Biología Funcional, Facultad de Medicina, Universidad de Oviedo, 33006-Oviedo, Spain; [8]Cambridge Institute for Medical Research and Wellcome Trust/Medical Research Council Stem Cell Institute, University of Cambridge, Cambridge CB2 0XY, UK; [9]Department of Haematology, University of Cambridge, Cambridge CB2 0XY, UK; [10]Department of Haematology, Addenbrooke's Hospital, Cambridge CB2 0XY, UK

To whom correspondence should be addressed:

Carlos López-Otín (clo@uniovi.es) or José M.P. Freije (jmpf@uniovi.es)

Departamento de Bioquímica y Biología Molecular

Facultad de Medicina

Universidad de Oviedo, 33006-Oviedo, SPAIN

Tel. 34-985-104201; Fax: 34-985-103564

AIRAPL (arsenite-inducible regulatory particle-associated protein-like) is an evolutionarily conserved regulator of cellular proteostasis linked to longevity in nematodes, but whose biological function in mammals is unknown[1-3]. We show herein that AIRAPL-deficient mice develop a fully-penetrant myeloproliferative neoplastic process. Proteomic analysis of AIRAPL-deficient mice revealed that this protein exerts its antineoplastic function through the regulation of the insulin/IGF-1 signaling pathway. We demonstrate that AIRAPL interacts with newly synthesized insulin-related growth factor-1 receptor (IGF1R) polypeptides, promoting their ubiquitination and proteasome-mediated degradation. Accordingly, genetic and pharmacological IGF1R inhibitory strategies prevent the hematological disease found in AIRAPL-deficient mice as well as in mice carrying the JAK2-V617F mutation, which demonstrates the causal involvement of this pathway in the pathogenesis of myeloproliferative neoplasms[4-6]. Consistent with its proposed role as a tumor suppressor of myeloid transformation, AIRAPL expression is widely abrogated in human myeloproliferative disorders. Collectively, these findings support the oncogenic relevance of proteostasis deregulation in hematopoietic cells, and unveil novel therapeutic targets for these frequent hematological neoplasias.

Protein homeostasis is essential for a proper response to dynamic environments[7]. The existence of regulatory mechanisms of protein quality control preserves the stability and functionality of the cellular proteome, being the endoplasmic reticulum (ER) a critical organelle in this regulation[8-10]. Accordingly, different components of protein quality control machinery have been causally involved in cancer and aging[11,12], either affecting global regulation of protein degradation pathways or specifically controlling mediators of these processes. Among them, we focus herein on AIRAPL (encoded by *ZFAND2B* gene), a highly-conserved ER protein involved in proteostasis control. Inactivation of the AIRAPL orthologue in *Caenorhabditis elegans* (AIP-1) shortens lifespan due to proteostasis impairment[1]. Notably, AIRAPL is constitutively expressed in most mammalian tissues, but its biological function has remained largely unknown.

To investigate the biological role of AIRAPL, we have generated *Zfand2b*-deficient mice using a "knock-out first" strategy (**Supplementary Fig. 1a**)[13]. The initially modified allele (hereafter referred as *Zfand2b-KO*) generates a null-allele

through splicing to a trapping element contained in the targeting cassette (**Supplementary Fig. 1b-d**). Even though *Zfand2b*-deficient mice were born at a Mendelian ratio and showed normal postnatal development, we observed that most adult *Zfand2b*$^{-/-}$ mice presented a long period of illness starting from 6-month to one-year-old, and accompanied by a progressive weight loss, distended abdomen and wasting (**Fig. 1a**), which finally results in premature death. Thus, *Zfand2b*-deficient mice showed an average lifespan of 675 days, while that of controls was of 823 days (P<0.01) (**Fig. 1b**).

To gain insight into *Zfand2b*-deficient mice alterations, we performed necropsy analyses in wild-type and *Zfand2b*$^{-/-}$ mice of the same age, observing a remarkable splenomegaly in the knock-out animals (**Fig. 1c**), which prompted us to study their hematopoietic system. Histological and immunohistochemical analyses revealed that splenomegaly in *Zfand2b*-deficient mice resulted from extramedullary hematopoiesis and expansion of the myeloid lineage. Spleens from 1.5-month-old *Zfand2b*$^{-/-}$ mice were normal but they progressively showed an expansion of red pulp with signs of extramedullary hematopoiesis. In latter stages, red pulp outproliferated white pulp, which was almost completely absent (**Fig. 1d**; **Supplementary Fig. 2a**). In parallel to spleen abnormalities, we also observed central hematopoiesis alterations. Thus, bone marrow from *Zfand2b*-deficient mice started showing hypercellularity and trilineage hyperplasia but, at latter stages, it presented a remarkable reduction in cell number, trilineage dysplasia and myelofibrosis, as assessed by reticulin immunostaining (**Fig. 1d**).

Moreover, peripheral blood analyses in *Zfand2b*$^{-/-}$ and control mice revealed significant differences in blood cell populations. Thus, *Zfand2b*-deficient mice first showed an elevation in total leukocyte numbers as compared with controls (**Fig. 1e**). Then, a progressive myeloid skewing was observed in knock-out animals, characterize by an increase in myeloid cell numbers, as well as a left-shifted myeloid maturation pattern (**Supplementary Fig. 2b,c**). Hematological analyses from terminally-ill *Zfand2b*-deficient mice revealed a massive expansion of myeloid population in peripheral blood (up to 90% of total white blood cells). Notably, we did not detect evidence of hematological disease in *Zfand2b*$^{+/-}$ mice, but we observed a significant increase in myeloid cells (**Supplementary Fig. 2d**), further supporting the implication of AIRAPL in the control of myeloid hematopoiesis. Accompanying changes in white

blood cell populations, hematocrit and platelets were also increased in *Zfand2b*-deficient mice (**Fig. 1f**). Overall, the phenotypes described in AIRAPL-deficient mice strongly support the occurrence of myeloproliferative neoplasms (MPNs)[4-6,14].

To further characterize hematological alterations in *Zfand2b*-deficient mice, we next performed flow cytometry analysis of primitive ($Lin^-SCA\text{-}1^+c\text{-}KIT^+$; LSK positive cells) and committed progenitors ($Lin^-SCA\text{-}1^-c\text{-}KIT^+$; LSK negative cells) in bone marrow and spleen. Notably, knock-out animals showed a significant increase in the number of LSK^+ cells in both tissues (**Fig. 1g; Supplementary Fig. 2e**). Besides, we also observed a remarkable loss of SLAM-enriched long-term hematopoietic stem cells (HSCs)[15], as evidenced by the decrease in $LSK^+CD48^-CD150^+$ cells (**Fig. 1g; Supplementary Fig. 2e**), and a significant expansion of myeloid progenitors (**Supplementary Fig. 2f**), altogether pointing to hematopoietic intrinsic defects in myeloid maturation. To test the differentiation capacity of *Zfand2b*-deficient HSCs, we performed competitive repopulation assays in which we mixed mutant or wild-type Ly-5.2+ bone marrow cells with Ly-5.1+ wild-type cells, and transplanted them into chemically ablated recipient mice to test relative reconstitution potential. *Zfand2b*-deficient cells showed a significant competitive disadvantage over wild-type cells in peripheral blood and bone marrow (**Fig. 1h**), similarly to the situation described in other MPN mouse models[16]. Additionally, we found that the number of myeloid cells was significantly reduced in mutant bone marrows (**Supplementary Fig. 2g**). Finally, reciprocal bone marrow transplantation experiments showed that wild-type recipients of knock-out cells recapitulated MPN-related alterations, whereas wild-type bone marrow cells rescued hematological phenotypes in *Zfand2b*-deficient mice (**Supplementary Fig. 3**), supporting a primary HSC defect caused by AIRAPL deficiency.

Aimed to get further understanding on AIRAPL biological function, we first asked about the possibility that the latency of MPN phenotype in *Zfand2b*-deficient mice could involve the requirement of additional genetic events. To evaluate this question, we performed exome sequencing analysis of bone marrow polymorphonuclear cells from *Zfand2b*-deficient mice (**Supplementary Table 1**). However, we did not observe any common sequence variants or mutations in genes associated with MPN pathogenesis in mutant mice, supporting a driver role of AIRAPL deficiency in myeloid transformation in these animals. Then, we asked if AIRAPL deficiency could be challenging global ER stress response; in this regard, calreticulin mutations have been

recently described in a large number of myeloproliferative neoplasms[17,18]. However, no differences were observed in calreticulin **(Supplementary Fig. 4a,b)** or in unfolded protein response (UPR) **(Supplementary Fig. 4c,d)** between wild-type and mutant mice. Then, we analyzed JAK2 signaling in cells from *Zfand2b* mutant mice, as the activation of this pathway is a central feature of MPNs[19-21]. However, we did not find any differences in JAK2 or STAT5 activation in mutant cells when compared with the corresponding wild-type controls (**Supplementary Fig. 5a**). These results prompted us to extend the analysis to other tyrosine kinases. Accordingly, we compared the activity of an array of cellular kinases in *Zfand2b*-deficient and wild-type mice, observing a remarkable increase in IGF1R phosphorylation in knock-out animals (**Fig. 2a; Supplementary Fig. 5b**)[22-24]. Further examination of the IGF1R pathway revealed the subsequent activation of downstream effectors such as AKT/mTOR and ERK/MAPK (**Supplementary Fig. 5c**). Interestingly, we observed that total IGF1R levels were increased more than 10-fold in *Zfand2b*-deficient mice (**Fig. 2a,b**), which suggested that the augmented activity of this receptor was caused by the increase in its steady-state levels. Based on these results, we decided to delve deeper into the potential mechanistic link between IGF1R and AIRAPL.

To try to confirm the effect of AIRAPL on IGF1R levels, we first overexpressed AIRAPL in human HEK-293T cells, observing a dose-dependent reduction in IGF1R levels (**Fig. 2c**). This effect was reverted by the proteasome inhibitor MG-132 (**Fig. 2d**), suggesting the implication of an ubiquitin-proteasome-mediated mechanism. Accordingly, we found that AIRAPL overexpression was sufficient to induce a strong ubiquitination of this receptor (**Fig. 2e**). Moreover, AIRAPL immunoprecipitation experiments revealed a complex interaction network with multiple regulatory and catalytic proteasome subunits, as well as known members of endoplasmic reticulum associated degradation (ERAD) and pre-emptive quality-control (PQC) pathways such as BAG6, FAF2 or VCP[25,26] (**Supplementary Fig. 6**; **Supplementary Table 2**). To get functional validation of these putative molecular partners of AIRAPL, we used a genetic inhibitory strategy and evaluated the capacity of AIRAPL to promote IGF1R ubiquitination and degradation in the absence of these partners. These experiments led us to identify a set of ER proteins essential for AIRAPL function, including VCP, FAF2, DERL1, BAG6 and the E3-ligase HERC2, which had not been previously related with IGF-1 signaling regulation (**Fig. 2f**).

IGF1R is synthesized as a high-molecular-weight precursor (pro-IGF1R) that is then processed to yield both mature α- and β-IGF1R chains. Our first hypothesis about the regulatory function of AIRAPL on this receptor was that it would act on the mature form of IGF1R, but cycloheximide-chase assays did not show any significant differences in mature IGF1R degradation rates upon translation blockade (**Supplementary Fig. 5d**). We then analyzed the possibility of a regulatory role over nascent IGF1R peptides. Accordingly, IGF1R co-immunoprecipitation experiments showed the presence of AIRAPL in the immunoprecipitates (**Supplementary Fig. 5e**). Furthermore, AIRAPL co-immunoprecipitation revealed that, even though mature IGF1R was approximately five times more abundant than pro-IGF1R in total protein lysates, AIRAPL exclusively interacted with pro-IGF1R (**Fig. 2g; Supplementary Fig. 5f**).

We next performed pulse-chase experiments with [^{35}S] methionine-cysteine metabolic labeling to follow the fate of newly synthesized IGF1R. Accordingly, since pro-IGF1R conversion into mature IGF1R occurs mostly at the Golgi apparatus[27], the analysis of pro-IGF1R processing would provide a temporal measurement of pro-IGF1R translocation out of the ER. Pulse-chase analysis of HEK-293T cells overexpressing *ZFAND2B* revealed delayed translocation kinetics, as well as lower amounts of translocated IGF1R as compared with control cells (**Fig. 2h**; **Supplementary Fig. 5g**). To further investigate the effect of endogenous AIRAPL on pro-IGF1R processing in human cells, we used a CRISPR-Cas9 strategy to generate *ZFAND2B*-deficient HEK-293T cells (**Supplementary Fig. 7)**. We found that *ZFAND2B*-knock-out cells showed faster translocation kinetics as well as higher levels of mature IGF1R compared to control cells (**Fig. 2i**; **Supplementary Fig. 5h**). Altogether, these results demonstrate that AIRAPL controls nascent IGF1R translocation and degradation at ER, thus regulating the steady-state levels of this receptor.

To test the specific contribution of IGF1R to the alterations caused by AIRAPL deficiency, we first used a genetic strategy of *Igf1r* haploinsufficiency[28]. We generated *Zfand2b*$^{+/+}$*Igf1r*$^{+/+}$, *Zfand2b*$^{+/+}$*Igf1r*$^{+/-}$, *Zfand2b*$^{-/-}$*Igf1r*$^{+/+}$ and *Zfand2b*$^{-/-}$*Igf1r*$^{+/-}$ mice, and evaluated the effect of IGF1R levels on hematological alterations (**Supplementary Fig. 8a**). We observed that *Igf1r* haploinsufficiency prevented myeloid alterations in *Zfand2b*-deficient mice, as blood parameters from *Zfand2b*$^{-/-}$*Igf1r*$^{+/-}$ were

indistinguishable from wild-type littermates (**Fig. 3a; Supplementary Fig. 8b,c**). Furthermore, *Igf1r* haploinsufficiency also prevented histological abnormalities (**Fig. 3b,c**), and HSC alterations (**Fig. 3d; Supplementary Fig. 8d**) in *Zfand2b*-deficient mice. Next, we tested the effect of IGF1R kinase inhibitor NVP-AEW541 in *Zfand2b*-deficient mice[29], observing a remarkable reversion of MPN-related alterations (**Fig. 3e-g**; **Supplementary Fig. 8e-g**), which further demonstrated the implication of IGF1R in MPN pathogenesis caused by *Zfand2b* deficiency.

Given the complete penetrance of MPN in *Zfand2b*-deficient mice, we investigated the occurrence of AIRAPL alterations in human myeloproliferative disorders. To this end, we collected 70 samples from the three most frequent *BCR-ABL*-negative MPNs: essential thrombocythemia (ET) (n=34), polycythemia vera (PV) (n=22) and primary myelofibrosis (PMF) (n=14). Thirty samples from healthy age-matched controls were also collected. We first observed a remarkable down-regulation of *ZFAND2B* expression in white blood cells or CD34+ cells isolated from different MPN patients (**Fig. 4a and Supplementary Fig. 9a**). Protein analysis of these samples revealed a complete absence of AIRAPL in MPN samples, which correlated with a more than 3.5-fold increase in the corresponding IGF1R levels (**Fig. 4b**). Immunohistochemical analysis of bone marrow biopsies from MPN patients also revealed a complete absence of AIRAPL staining in myeloid cells, whereas a strong signal was observed in control bone marrow (**Fig. 4c**).

Aimed to explore the relevance of AIRAPL and IGF1R alterations in MPN pathogenesis, we focused on the study of a mouse model of essential thrombocythemia carrying the Jak2-V617F mutation[30]. Consistent with the results obtained in human MPN samples, we observed AIRAPL abrogation as well as IGF1R deregulation in Jak2-V617F-mutated mice ($Jak2^{R/+}$ mice) (**Fig. 4d-f**). Next, we administrated IGF1R inhibitor NVP-AEW541 to $Jak2^{R/+}$ mice, observing a significant amelioration of MPN-associated characteristics. Thus, we found a reduction in the number of white blood cells and platelets in peripheral blood (**Fig. 4g**), as well as a reversion of histological and HSCs alterations (**Fig. 4h**,**i**). To get further insights into the role of IGF-1 signaling deregulation in JAK2-associated myeloid transformation, we transduced bone marrow cells from *Igf1r*+/+ and *Igf1r*+/- mice with Jak2-V617F cDNA, and injected them into chemically ablated wild-type mice recipients. We observed that *Igf1r* haploinsufficiency prevented MPN characteristic alterations (**Supplementary Fig. 9b-e**), altogether

providing the first evidence about the role of IGF-1 signaling alterations in the initiation of myeloid transformation.

Next, we also analyzed the effect of IGF1R inhibition in two acute myeloid leukemia (AML) cell lines derived from patients carrying the JAK2-V617F mutation: SET2 and HEL. We found that both cell lines showed growth arrest upon IGF1R inhibition (**Fig. 4j; Supplementary Fig. 9f,g**), whereas IGF1R overexpression increased proliferation rates (**Supplementary Fig. 9h).** Transcriptional profiling of SET2 and HEL cell lines transduced with specific IGF1R shRNA revealed a significant down-regulation of gene sets associated with AML transformation, as well as a significant down-regulation of genetic programs associated with JAK2-STAT5 signaling (**Supplementary Fig. 10a)**. Conversely, JAK2 inhibition in SET2 and HEL cells with the JAK2 inhibitor ruxolotinib resulted in a significant up-regulation of AIRAPL as well as a reduction of IGF1R levels, further supporting a molecular crosstalk between these signaling pathways (**Supplementary Fig. 10b,c)**.

We also investigated the molecular mechanism responsible for *ZFAND2B* down-regulation in MPN. Thus, we first analyzed *ZFAND2B* gene alterations in human MPNs, but we did not observe mutations, structural alterations or methylation changes in this locus (**Supplementary Fig. 11a,b**)[17,18,31]. Accordingly, we evaluated the existence of putative microRNA-mediated changes in *ZFAND2B* levels. Computational search using TargetScan and miRanda programs identified miR-125a-3p as a potential regulator of *ZFAND2B* mRNA stability (**Supplementary Fig. 12a**), and this regulatory role was confirmed by luciferase experiments with *ZFAND2B* 3'-UTR (**Supplementary Fig. 12b**). Importantly, we found that this microRNA was significantly up-regulated in MPN samples (**Supplementary Fig. 12c,d**), and its expression levels negatively correlated with those of *ZFAND2B* (**Supplementary Fig. 12e,f)**. Moreover, we also found that miR-125a-3p was altered in mice carrying the Jak2-V617F mutation (**Supplementary Fig. 12g,h),** an effect that was specifically repressed upon JAK2 inhibition (**Supplementary Fig. 12i)**. Finally, we inhibited miR-125a-3p in SET2 and HEL cell lines using a miR-125a sponge, observing a complete reversion of AIRAPL-deficiency associated alterations (**Supplementary Fig. 13a-f**). Consistently, miR-125a-3p inhibition caused a remarkable reduction in SET2 and HEL proliferation rates (**Supplementary Fig. 13g,h**), supporting the causal implication of this regulatory pathway in the MPN mechanism proposed[32,33].

Although we mainly focused on the elucidation of AIRAPL alterations in myeloproliferative neoplasms, the reduced longevity observed in *aip-1*-deficient *C. elegans* made us to hypothesize about a possible evolutionary conserved function of this protein in insulin-IGF-1 signaling (IIS) control. In order to test this hypothesis, we generated *aip-1* deficient worms in a wild-type and *daf-2* mutant background (**Supplementary Fig. 14**). We observed that the characteristic reduced longevity of *aip-1* deficient nematodes was completely prevented by deficiency in the IGF1R orthologue *daf-2*, thereby demonstrating an evolutionary conserved role of AIRAPL in IIS regulation.

Collectively, the data shown herein demonstrate that AIRAPL acts as a potent suppressor of myeloid transformation through down-regulation of IGF1R levels, further assessing the involvement of insulin/IGF-1 signaling deregulation in myeloid malignancies. In this regard, it is remarkable that numerous clinical trials have evaluated IGF1R as a potential therapeutic target for solid tumors, but its clinical relevance in myeloproliferative syndromes has not been similarly addressed[23,34]. Accordingly, our *in vitro* and *in vivo* studies showing the efficacy of IGF1R inhibitory strategies in JAK2-driven myeloproliferative neoplasms constitute an important preclinical evidence of the use of IGF1R inhibitors for the treatment of these neoplasias, alone or in combination with JAK2 inhibitors[35]. Furthermore, we have also uncovered a novel mechanism of pathogenesis in human myeloproliferative disorders, which involves the complete abrogation of AIRAPL-tumor suppressor activity through overexpression of miR-125a-3p. Therefore, our study represents a clear demonstration of the oncogenic relevance of proteostasis deregulation in hematopoietic cells. Notably, most studies of the molecular mechanisms controlling HSC homeostasis have focused on the analysis of genetic and epigenetic alterations of key oncogenes and tumor suppressors, as well as on the evaluation of the signaling and transcriptional changes induced by these genomic damages. However, our finding that loss of AIRAPL contributes to the transformation of myeloid cells provides causal evidence about the crucial role of proteostatic processes in the regulation of quiescence, proliferation and differentiation of HSCs, which finally contribute to maintain normal adult hematopoiesis. Based on these findings, we propose that the identification of this novel pathway implicating AIRAPL, IGF1R and miR-125a-3p may offer new targets and opportunities for molecularly-directed therapies against human myeloproliferative neoplasias.

Acknowledgements: *We thank A.A. Ferrando, D.A. Puente, A.R. Folgueras, G.R. Ordoñez, I. Martín-Subero, A. Gutiérrez-Fernández, G. Mariño, E. Luño, S. Jeay, M. Holzenberger and G. Wulczyn for providing reagents, helpful comments and advice. We also thank A. Moyano and R. Feijoo for excellent technical assistance, and the Servicio de Histopatología (IUOPA) for histological studies. This work was supported by grants from Ministerio de Economía y Competitividad, Instituto de Salud Carlos III (RTICC), and Principado de Asturias, Spain. The Instituto Universitario de Oncología is supported by Fundación Bancaria Caja de Ahorros de Asturias. C.L-O. is an Investigator of the Botin Foundation supported by Banco Santander through its Santander Universities Global Division. Work in the Green lab is supported by Leukemia and Lymphoma Research, Cancer Research UK, the Wellcome Trust, the Kay Kendall Leukaemia Fund, the NIHR Cambridge Biomedical Research Centre, the Cambridge Experimental Cancer Medicine Centre, and the Leukemia & Lymphoma Society of America.*

METHODS

Mice. The gene-targeting vector for generation of *Zfand2b*-knock-out first allele was created through recombineering specific methodology as previously described[13,36]. Briefly, a 12.7 Kb fragment of mouse genomic DNA including *Zfand2b* entire sequence was cloned into pL253 vector, that contains the thymidine kinase gene for ESC negative selection. A loxP sequence was inserted into the intron 1-2 of this gene along with a trapping element consisting in a splice acceptor sequence followed by a neomycin resistance gene, used for positive selection of ESCs. The trapping element was flanked by FRT sites. Then, a second loxP site was inserted into the intron 8-9 of *Zfand2b* gene. Vector integrity was assessed by DNA sequencing and restriction mapping. The targeting vector was linearized and electroporated into the ES cell line AB2.2 from 129S5/SvEvBrd mice strain. ESCs clones were isolated after G418 and ganciclovir selection, and analyzed by Southern-blot for the identification of those clones that carried the targeted *Zfand2b-ko* first allele, using for this purpose XhoI-digested genomic DNA. The probes detected a 7.2-kb fragment in the recombinant allele. Two different clones of targeted AB2.2 ESCs were microinjected into C57BL/6 mouse blastocysts to produce chimeric mice that were then subsequently crossed with C57BL/6 mice to generate *Zfand2b*-heterozygous mice. Mouse genotyping was performed by PCR of genomic DNA with the following oligonucleotides: 5'-gtgagcactggagctggaaa-3'; 5'-gtgggaaagggttcgaagtt-3'; 5'-cgcaaagctgctactcaggt-3'; The PCR products consisted in fragments of 254 base pairs (bp) (ko-allele) and 150 bp (wild-type allele). Conditional Jak2-V617F mice generation was previously

described[30,37]. *Igf1r*-haploinsufficient mice were kindly provided by Dr. M. Holzenberger[28].

Mice experiments. All of the animal experiments were conducted in accordance with the guidelines of the Committee for Animal Experimentation of the Universidad de Oviedo. Both male and female mice, carrying a mixed background C57BL/6 x 129, were used in the experiments. For hematological determinations, blood was extracted directly from the mandibular sinus after anesthetizing mice with isoflurane. Blood samples were analyzed using Abacus junior vet equipment (Diatron Labs). For the experiments with Igf1r small molecule inhibitor, animals were administrated p.o. twice daily, 7 days/week with 50 mg/kg/day of NVP-AEW541, 10 mL/kg dissolved in 25 mM L(+)-tartaric acid. NVP-AEW541 was generously provided by Novartis. Tunicamycin (Sigma-Aldrich) was intraperitoneally injected into 8-week-old wild-type and *Zfand2b*-deficient mice at a dose of 1 μg/g body weight. Mice were euthanized 3 days after injection.

Human samples. Human MPN samples were collected from Hospital Universitario Central de Asturias (HUCA). The study was approved by the Ethical Committee of HUCA and all of the patients provided written informed consent. For *ZFAND2B* transcriptional analysis, 70 peripheral blood samples from MPN patients and 30 controls were analyzed. For AIRAPL immunohistochemistry analysis, 30 samples from MPN bone marrow biopsies and 10 controls were collected.

***Caenorhabditis elegans* experiments.** Standard nematode growth medium and conditions were used for *C. elegans* growth and maintenance. The CB1370 [daf-2(e1370)III] and DH26 [fer-15(b26)] strains were obtained from the Caenorhabditis Genetics Center. Temperature sensitive *fer-15* (fertility) mutation was used to prevent the production of offspring that would confound the evaluation of adult worms. The GM6 [fer-15(b26) II/ daf-2(e1370) II] strain was a kind gift of Dr. Manuel J. Muñoz Ruiz. All worm populations were synchronized with the alkaline hypochlorite treatment[38]. To perform RNA-mediated interference (RNAi) by feeding, nematode growth medium (NGM) plates were supplemented with 50 μg/ml ampicillin, 12.5 μg/ml

tetracycline, and 1 mM IPTG. Plates were seeded with the corresponding RNAi clone, validated by PCR and/or sequencing, and dsRNA synthesis induced o/n at 37 ºC. aip-1 RNAi clone was obtained from the ORFeome library[39], while daf-16 RNAi clone was from the Ahringer library[40]. Worms were grown on regular NGM plates and transferred to RNAi plates at L4 stage. For N2 and daf-2(e1370) strains, plates were supplemented with 0.1 mg/ml fluorodeoxyuridine (FUDR) to prevent progeny growth and lifespan assays were conducted at 20 ºC. For fer-15(b26) and fer-15(b26)/daf-2(e1370) strains, experiments were performed at 25 ºC to avoid self-fertilization. At least 100 worms were used in each of the three experimental replicates. Animals were considered dead when no movement or pharyngeal pumping was observed after gentle touch in the head.

Bone marrow transplantation. Recipient mice were treated with 25 mg/kg/day of busulfan (Sigma-Aldrich) for 4 days, followed by injection of 200 mg/kg of cyclophosphamide (Sigma-Aldrich). Twenty-four hours after last injection, bone marrow was collected from femurs and tibias of donor mice by flushing the cavity of freshly dissected bones with Hank's Balanced Salt Solution (HBSS). Cell suspension was filtered through 100 μm filters and counted. 2×10^6 cells were resuspended in HBSS and then injected in recipient animals via the jugular vein. Eight weeks later, the engraftment was evaluated by qRT-PCR and immunofluorescence analyses of peripheral blood from recipient mice. In competitive transplantation experiments, cell populations were distinguished through the Ly-5.1 marker. $2x10^6$ cells from mutant or wild-type littermates were mixed with $2x10^6$ cells from B6.SJL-PtprcaPepcb/BoyJ (Ly-5.1+) wild-type competitors and injected into mice recipients. Jak2-V617F transduction of bone marrow cells and subsequent transplantation of progenitors was performed as described previously[41]. Briefly, donor mice were treated for 5 days with 5-fluorouracil (150 mg/kg, intraperitoneal injection). Bone marrow cells were harvested and cultured for 24 h in transplant medium (RPMI 10% FBS, 6 ng/mL IL-3, 10 ng/mL IL-6, and 10 ng/mL stem cell factor). Then, cells were treated by spin infection with Jak2-V617F viral supernatants centrifuged at 1800x*g* for 30 min, 24 h before and on the day of transplantation. Whole BM cells ($1x\ 10^6$) were resuspended in HBSS and injected into the jugular vein of busulfan/cyclophosphamide-treated mice.

FACS analysis. All the antibodies used in the study were from Biolegend unless noted. The following monoclonal antibodies were used for HSC analysis: PE anti-mouse CD117 (105807), PerCP/Cy5.5 anti-mouse CD45 (103132), PE/Cy7 anti-mouse CD150 (115914), APC anti-mouse CD127 (135012), APC/Cy7 anti-mouse CD48 (103432), Brilliant Violet 421™ anti-mouse Ly-6A/E (Sca-1) (108127), FITC anti-mouse CD16/32 (101306), PE/Cy7 anti-mouse CD45.1 (110730), FITC anti-mouse CD45.2 (109806), Brilliant Violet 510™ anti-mouse/human CD45R/B220 (103247), Brilliant Violet 421™ anti-mouse CD3 (100227), anti-mouse CD34 (eBioscience, 11-0341-82), PE rat anti-mouse Ly-6G clone 1A8 (BD Pharmingen, 551461), APC rat anti-mouse Ly-6G and Ly-6C clone RB6-8C5 (BD Phamingen, 553129) and Lineage cocktail (BD PharMingen, 558074). FACS data were acquired using a FACScanto II flow cytometer (BD Biosciences) and analyzed using Infinicyt software (Cytognos, Santa Marta, Spain).

Cell culture, transient transfection and viral transduction. *Zfand2b* cDNA was amplified by PCR and either cloned into pcDNA3.1-HA, pEGFP-C1, or pCDH expression vectors. pBABE-bleo IGF1R was obtained from Addgene, and then an IGF1R insert was subcloned into pEGFP-N1 or pCDH expression vector. miR-125a locus was amplified by PCR from human genomic DNA and cloned into pCDH. HA-ubiquitin plasmid was obtained from Addgene. miR-125 sponge was kindly provided by Dr. G. Wulczyn[42], and then subcloned into pCDH lentiviral vector. IGF1R shRNA were obtained from GE Dharmacon. Wild-type and V617F Jak2 plasmids were previously described[43]. HEK-293T, SET2 and HEL cell lines were purchased from ATCC or DSMZ cell repositories and maintained in culture following the provider's specifications. Transient transfections were performed using Lipofectamine reagent (Life Technologies). For lentiviral transduction, HEK-293T cells were transfected with pCDH-based vectors along with second generation lentiviral packaging plasmids. Viral particles were collected from supernatants, filtered through 0.45 μm PES filters and concentrated using Lenti-X concentrator reagent (Clontech). MG-132 was purchased from Sigma-Aldrich and used at a 2 μM concentration for the indicated times. Control and specific siRNAs were purchased from Life Technologies and transduced in HEK-293T using Lipofectamine reagent, proteomic analyses were performed 48 h after transfection.

Western-blot analysis. Protein lysates were prepared in RIPA buffer; equal amounts of total proteins were loaded onto SDS-polyacrylamide gels. After electrophoresis, gels were electrotransferred onto nitrocellulose membranes and incubated overnight with the different primary antibodies used. Finally, blots were incubated for 1 h with secondary antibodies conjugated with horseradish peroxidase (HRP) to develop immunoreactive bands. The primary antibodies used in the study were: AIRAPL (Atlas Antibodies, HPA035160), phospho-IGF1R (Novus, NB100-92555), IGF1R (Cell Signaling, 9750), β-actin (Sigma, AC-40), HA (Roche, 3F10), GFP (Clontech, 632592), phospho-AKT (Cell Signaling, 9275), AKT (Cell Signaling, 9272), phospho-S6K (Cell Signaling, 9430), S6K (Cell Signaling, 2708), phospho-4EBP1 (Cell Signaling, 9451), 4EBP1 (Cell Signaling, 9452), phospho-ERK (Cell Signaling, 9101), ERK (Cell Signaling, 9102), phospho-JAK2 (Cell Signaling, 3771), JAK2 (Cell Signaling, 3229), phospho-STAT5 (Cell Signaling, 9351), STAT5 (Cell Signaling, 9310), phospho-PERK (Cell Signaling, 3179), PERK (Cell Signaling, 5683), IRE1α (Cell Signaling, 3294), ATF6 (Santa Cruz Biotechnology, sc-22799), BiP (Cell Signaling, 3177), calreticulin (Abcam, 22683) and VCP (Cell Signaling, 2648). Mouse phospho receptor tyrosine kinase (RTK) array was purchased from R&D systems and used following the manufacturer's indications.

Immunoprecipitation. AIRAPL co-immunoprecipitation experiments were performed in the HEK-293T cell line. To this end, cells were transfected with either pEGFP-*Zfand2b* plasmid or pEGFP empty vector and incubated with MG-132, 8 h prior to lysis. Cells were lysed with co-IP buffer (150 mM NaCl, 20 mM TrisHCl pH 7.4, 1% NP-40, 1 mM $MgCl_2$, 10% glycerol, and complete protease inhibitors 1x). Protein extracts were precleared for 2 h at 4 ºC with dynabeads (Life Technologies), and then incubated with anti-GFP-conjugated dynabeads for 1 h at 4 ºC. Beads were washed three times with lysis buffer, and bound proteins were released from beads by boiling in 2x Laemmli sample buffer. Immunoprecipitates and input samples were resolved by SDS-PAGE or subjected to protein digestion followed by nano-liquid chromatography coupled to mass spectrometry for protein identification and quantification by peptide counting[44]. For ubiquitination experiments, HEK-293T cells were transfected with HA-ubiquitin, pcDNA3.1-HA-*Zfand2b* and pEGFP-IGF1R plasmids, and total lysates were precipitated with anti-GFP antibody and immunostained with anti-HA antibody. For

cycloheximide chase, assayed cells were incubated with 100 μg/mL cycloheximide (Sigma-Aldrich) during the indicated times.

Pulse-chase metabolic labeling. Forty-eight hours after transfection with pEGFP-IGF1R construct, HEK-293T cells were incubated in cysteine- and methionine-free DMEM containing 10% dialyzed FBS for 12 h. Then, ^{35}S-label (0.1 mCi/mL; EasyTag™ express35S Protein Labeling Mix; Pelkin Elmer) was added to the cells for 1 h. After labeling, cells were washed with chase medium (DMEM with 15 mg/L cold-methionine) and incubated in chase medium for the times indicated. Cells were then lysed in RIPA buffer, immunoprecipitated with anti-GFP antibody and resolved by SDS-PAGE. Nitrocellulose filters were exposed overnight and scanned using a Phosphorimager.

RNA. For quantitative RT-PCR (qRT-PCR), total RNA was isolated with Trizol and cDNA was synthesized with the ThermoScript RT-PCR system (Invitrogen). PCR was carried out in triplicate for each sample with 20 ng of cDNA using power SYBR green PCR Master Mix (Applied Biosystems). Gene expression was normalized using Gapdh as endogenous control. The following oligonucleotides were used in the study; *Zfand2b*_fwd: 5'-AGGTCATCAGACCAGCAGGGCA-3', *Zfand2b*_rev: 5'-GGTGTA GCTCTGCTTGGGGAGGAT-3'. Human *ZFAND2B* mRNA and miR-125a-3p levels were quantified with Taqman assays (Life Technologies), using β-actin and RNU6b, respectively as Taqman endogenous controls. Xbp1 splicing was analyzed by RT-PCR with the following oligonucleotides: mXbp1.3S: 5'-AAACAGAGTAGCAGCGCAGA CTGC-3', mXBP1.12AS: 5'-TCCTTCTGGGTAGACCTCTGGGAG-3'. PCR products were then digested with PstI and run in agarose gels. For microarray hybridization, double-stranded cDNA was synthesized using the SuperScriptTM cDNA synthesis kit (Invitrogen) and *in vitro* transcription was carried out with the Bioarray high yield RNA transcript labeling kit (Enzo Diagnostics). The biotin-labeled cRNA was purified, fragmented and hybridized to Human Gene 2.0 ST (Affymetrix). Washing and scanning were performed using a Fluidics Station 400 and GeneChip Scanner (Affymetrix). After scanning, raw data were processed with Expression Console software (Affymetrix), using default settings.

Histological analysis. Tissues were fixed in 4% buffered paraformaldehyde solution. Paraffin sections were stained with hematoxylin and eosin (H&E) or reticulin stains as noted. For immunohistochemical analysis, the following antibodies were used: myeloperoxidase (DAKO, A0398), CD3 (Abcam, 5690), Mac2 (Cedarlane, CL8942AP), AIRAPL (Atlas Antibodies, HPA035160) and IGF1R (Santa Cruz Biotechnology; sc-713). Blood smears were stained using May-Grünwald-Giemsa staining procedure. Reticulin fibers were revealed by silver staining according to the Gordon Sweet method. Histological analyses were performed in a blinded fashion.

Immunofluorescence analysis. Cells were fixed with 4% paraformaldehyde, rinsed in PBS, and permeabilized with 0.5% Triton X-100. Cells were then incubated with primary antibodies diluted in 10% FBS in PBS from 2 h at room temperature to overnight at 4 ºC. After washing with PBS, cells were incubated with Alexa-488 (Life Technologies) conjugated secondary antibodies for 45 min at room temperature. Cells were counterstained with DAPI (Roche).

***In vitro* inhibitor assays.** To assess anti-proliferative effects of NVP-AEW541, SET2 and HEL cell lines were cultured at 10,000 cells/200 µL with increasing inhibitor concentrations in triplicate. Proliferation was assessed at 48 h using Cell Titer 96 Non-Radioactive proliferation kit (Promega), and normalized to cell growth in media with an equivalent volume of DMSO. The concentration inhibiting proliferation by 50% (IC50) was determined with Graph Pad Prism 5.0. Ruxolotinib was obtained from Selleckchem.

Luciferase experiments. *ZFAND2B* 3'-UTR sequence was amplified by PCR and cloned into psiCHECK2 vector downstream the *Renilla* luciferase sequence. Luminescence determinations were performed using the firefly luciferase values as an endogenous control. miR-125a-3p miRNA precursor and inhibitor were purchased from Life Technologies.

CRISPR-Cas9 experiments. Genome editing experiments were performed as described previously[45]. In brief, for the generation of *ZFAND2B*-deficient HEK-293T cells, two different plasmids encoding CRISPR-Cas9 and *ZFAND2B* guide RNA (gRNA) were obtained from Sigma-Aldrich (5544: 5'-GACCTCGGCGCTCACTGTT CGG-3'; 5545: 5'- CTCCGAACACTGAGCGCCGAGG). gRNAs were selected to target *ZFAND2B* exon 1 in order to generate frameshift mutations that would cause premature termination of the open reading frame in this gene. CRISPR-Cas9 plasmids were transiently transduced into HEK-293T cells and clones were isolated by serial dilution. To analyze the resulting genomic DNA modifications induced by CRISPR-Cas9 activity, we amplified by PCR the targeted DNA region using external oligonucleotides. The forward oligonucleotide was modified to include 6-FAM fluorophore in its 5' position, which allowed the fragment analysis of resulting PCR products by capillary electrophoresis. Indels were also confirmed by DNA sequencing. Three HEK-293T cell clones carrying deleterious modifications and three wild-type clones were selected for the experiments to rule out potential off-target effects of Cas9.

Exome sequencing and data analysis. Genomic DNA from bone marrow polymorphonuclear cells (200 ng) was sheared and used for the construction of a paired-end sequencing library as described in the protocol provided by Illumina. Enrichment of exonic sequences was then performed for each library using the SureSelectXT Mouse All Exon kit (Agilent) and following the manufacturer's instructions. Exon-enriched DNA was precipitated with magnetic beads coated with streptavidin (Invitrogen) and was washed and eluted. 18 additional cycles of amplification were then performed on the captured library. Enriched libraries were sequenced in two lanes of an Illumina Gene Analyzer II× sequencer, using the standard protocol. Data analysis and identification of sequence variants was performed using the Sidrón pipeline in a HD Genome One Research Edition station (DREAMgenics, Asturias, Spain)[46].

Gene set enrichment analysis. For data analysis, we used GSEA release 5 and MSigDB release 5 (http://www.broadinstitute.org/gsea/index.jsp). Weighted enrichment scores were calculated with gene expression lists ranked by signal to-noise ratio. The maximum gene set size was set to 500 genes; the minimum gene set size was set to 20 genes; the number of permutations was set to 1000. Selected enriched pathways had a

relaxed false discovery rate of <0.25 and $P< 0.05$. GSEA shown in Fig. 4f was performed with microarray datasets of a previous study[47]. Methylation and PMF cohorts analyses derived from datasets of previous studies[31,48].

Reproducibility of the experiments, statistical and bioinformatics analyses. For computational prediction of miRNAs targeting *ZFAND2B*, a combination of the following software was used: TargetScan (http://www.targetscan.org) and miRanda (http://www.microrna.org). All the experiments were performed at least in independent triplicates (unless noted otherwise) and statistical analyses were derived from these data. All comparisons between wild-type and knock-out animals were performed in animals from the same age. Experimental conditions were blinded randomized and no statistical method was used to predetermine sample size. Differences between groups were assayed using Microsoft Excel, SPSS and GraphPad Prism. In all cases, experimental data assumed t-test requirements (normal distribution and similar variance); in those cases where the assumption of the t-test was not valid, a non-parametric statistical method was used (for example, Wilcoxon signed-rank test). Significant differences were considered when $*P<0.05$ and $**P<0.01$. Error bars indicate the standard error of the mean, as indicated in figure legends.

Accession number. RNA expression data are available at the Gene Expression Omnibus repository (GSE71922). Reanalyzed microarray data sets are available at the Gene Expression Omnibus repository (GSE42042, ref. 31; GSE44961, ref. 47; GSE53482, ref. 48). Exome sequencing raw data are accessible at NCBI Sequence Read Archive (SRA) repository.

References

1. Yun, C., *et al.* Proteasomal adaptation to environmental stress links resistance to proteotoxicity with longevity in Caenorhabditis elegans. *Proc Natl Acad Sci U S A* **105**, 7094-7099 (2008).
2. Hassan, W.M., Merin, D.A., Fonte, V. & Link, C.D. AIP-1 ameliorates beta-amyloid peptide toxicity in a Caenorhabditis elegans Alzheimer's disease model. *Hum Mol Genet* **18**, 2739-2747 (2009).

3. Ferguson, A.A., Springer, M.G. & Fisher, A.L. skn-1-Dependent and -independent regulation of aip-1 expression following metabolic stress in Caenorhabditis elegans. *Mol Cell Biol* **30**, 2651-2667 (2010).

4. Levine, R.L. & Gilliland, D.G. Myeloproliferative disorders. *Blood* **112**, 2190-2198 (2008).

5. Campbell, P.J. & Green, A.R. The myeloproliferative disorders. *N Engl J Med* **355**, 2452-2466 (2006).

6. Tefferi, A. & Vainchenker, W. Myeloproliferative neoplasms: molecular pathophysiology, essential clinical understanding, and treatment strategies. *J Clin Oncol* **29**, 573-582 (2011).

7. Balch, W.E., Morimoto, R.I., Dillin, A. & Kelly, J.W. Adapting proteostasis for disease intervention. *Science* **319**, 916-919 (2008).

8. Hartl, F.U., Bracher, A. & Hayer-Hartl, M. Molecular chaperones in protein folding and proteostasis. *Nature* **475**, 324-332 (2011).

9. Vembar, S.S. & Brodsky, J.L. One step at a time: endoplasmic reticulum-associated degradation. *Nat Rev Mol Cell Biol* **9**, 944-957 (2008).

10. Walter, P. & Ron, D. The unfolded protein response: from stress pathway to homeostatic regulation. *Science* **334**, 1081-1086 (2011).

11. Lopez-Otin, C., Blasco, M.A., Partridge, L., Serrano, M. & Kroemer, G. The hallmarks of aging. *Cell* **153**, 1194-1217 (2013).

12. Hanahan, D. & Weinberg, R.A. Hallmarks of cancer: the next generation. *Cell* **144**, 646-674 (2011).

13. Skarnes, W.C.*, et al.* A conditional knockout resource for the genome-wide study of mouse gene function. *Nature* **474**, 337-342 (2011).

14. Zhou, T., Kinney, M.C., Scott, L.M., Zinkel, S.S. & Rebel, V.I. Revisiting the case for genetically engineered mouse models in human myelodysplastic syndrome research. *Blood* (2015).

15. Kiel, M.J., Yilmaz, O.H., Iwashita, T., Terhorst, C. & Morrison, S.J. SLAM family receptors distinguish hematopoietic stem and progenitor cells and reveal endothelial niches for stem cells. *Cell* **121**, 1109-1121 (2005).

16. Yildirim, E.*, et al.* Xist RNA is a potent suppressor of hematologic cancer in mice. *Cell* **152**, 727-742 (2013).

17. Nangalia, J.*, et al.* Somatic CALR mutations in myeloproliferative neoplasms with nonmutated JAK2. *N Engl J Med* **369**, 2391-2405 (2013).

18. Klampfl, T.*, et al.* Somatic mutations of calreticulin in myeloproliferative neoplasms. *N Engl J Med* **369**, 2379-2390 (2013).

19. Levine, R.L.*, et al.* Activating mutation in the tyrosine kinase JAK2 in polycythemia vera, essential thrombocythemia, and myeloid metaplasia with myelofibrosis. *Cancer Cell* **7**, 387-397 (2005).

20. James, C.*, et al.* A unique clonal JAK2 mutation leading to constitutive signalling causes polycythaemia vera. *Nature* **434**, 1144-1148 (2005).

21. Baxter, E.J., *et al.* Acquired mutation of the tyrosine kinase JAK2 in human myeloproliferative disorders. *Lancet* **365**, 1054-1061 (2005).

22. Renehan, A.G., *et al.* Insulin-like growth factor (IGF)-I, IGF binding protein-3, and cancer risk: systematic review and meta-regression analysis. *Lancet* **363**, 1346-1353 (2004).

23. Pollak, M. Insulin and insulin-like growth factor signalling in neoplasia. *Nat Rev Cancer* **8**, 915-928 (2008).

24. Gallagher, E.J. & LeRoith, D. Minireview: IGF, insulin, and cancer. *Endocrinology* **152**, 2546-2551 (2011).

25. Glinka, T., *et al.* Signal-peptide-mediated translocation is regulated by a p97-AIRAPL complex. *Biochem J* **457**, 253-261 (2014).

26. Kang, S.W., *et al.* Substrate-specific translocational attenuation during ER stress defines a pre-emptive quality control pathway. *Cell* **127**, 999-1013 (2006).

27. Khatib, A.M., *et al.* Inhibition of proprotein convertases is associated with loss of growth and tumorigenicity of HT-29 human colon carcinoma cells: importance of insulin-like growth factor-1 (IGF-1) receptor processing in IGF-1-mediated functions. *J Biol Chem* **276**, 30686-30693 (2001).

28. Holzenberger, M., *et al.* IGF-1 receptor regulates lifespan and resistance to oxidative stress in mice. *Nature* **421**, 182-187 (2003).

29. Garcia-Echeverria, C., *et al.* In vivo antitumor activity of NVP-AEW541-A novel, potent, and selective inhibitor of the IGF-IR kinase. *Cancer Cell* **5**, 231-239 (2004).

30. Li, J., *et al.* JAK2V617F homozygosity drives a phenotypic switch in myeloproliferative neoplasms, but is insufficient to sustain disease. *Blood* **123**, 3139-3151 (2014).

31. Perez, C., *et al.* Aberrant DNA methylation profile of chronic and transformed classic Philadelphia-negative myeloproliferative neoplasms. *Haematologica* **98**, 1414-1420 (2013).

32. Guo, S., *et al.* Complex oncogene dependence in microRNA-125a-induced myeloproliferative neoplasms. *Proc Natl Acad Sci U S A* **109**, 16636-16641 (2012).

33. Inoue, D., *et al.* Myelodysplastic syndromes are induced by histone methylation-altering ASXL1 mutations. *J Clin Invest* **123**, 4627-4640 (2013).

34. Lovly, C.M., *et al.* Rationale for co-targeting IGF-1R and ALK in ALK fusion-positive lung cancer. *Nat Med* **20**, 1027-1034 (2014).

35. Meyer, S.C., *et al.* CHZ868, a type II JAK2 inhibitor, reverses type I JAK inhibitor persistence and demonstrates efficacy in myeloproliferative neoplasms. *Cancer Cell* **28**, 15-28 (2015).

36. Liu, P., Jenkins, N.A. & Copeland, N.G. A highly efficient recombineering-based method for generating conditional knockout mutations. *Genome Res* **13**, 476-484 (2003).

37. Li, J., *et al.* JAK2 V617F impairs hematopoietic stem cell function in a conditional knock-in mouse model of JAK2 V617F-positive essential thrombocythemia. *Blood* **116**, 1528-1538 (2010).

38. Porta-de-la-Riva, M., Fontrodona, L., Villanueva, A. & Ceron, J. Basic Caenorhabditis elegans methods: synchronization and observation. *J Vis Exp*, e4019 (2012).

39. Rual, J.F., *et al.* Toward improving *Caenorhabditis elegans* phenome mapping with an ORFeome-based RNAi library. *Genome Res* **14**, 2162-2168 (2004).

40. Kamath, R.S. & Ahringer, J. Genome-wide RNAi screening in *Caenorhabditis elegans*. *Methods* **30**, 313-321 (2003).

41. Wernig, G., *et al.* Expression of Jak2V617F causes a polycythemia vera-like disease with associated myelofibrosis in a murine bone marrow transplant model. *Blood* **107**, 4274-4281 (2006).

42. Rybak, A., *et al.* A feedback loop comprising lin-28 and let-7 controls pre-let-7 maturation during neural stem-cell commitment. *Nat Cell Biol* **10**, 987-993 (2008).

43. Scott, L.M., *et al.* JAK2 exon 12 mutations in polycythemia vera and idiopathic erythrocytosis. *N Engl J Med* **356**, 459-468 (2007).

44. Villarroya-Beltri, C., *et al.* Sumoylated hnRNPA2B1 controls the sorting of miRNAs into exosomes through binding to specific motifs. *Nat Commun* **4**, 2980 (2013).

45. Soria-Valles, C., *et al.* NF-kappaB activation impairs somatic cell reprogramming in ageing. *Nat Cell Biol* **17**, 1004-1013 (2015).

46. Puente, X.S., *et al.* Non-coding recurrent mutations in chronic lymphocytic leukaemia. *Nature* (2015).

47. Mullally, A., *et al.* Depletion of Jak2V617F myeloproliferative neoplasm-propagating stem cells by interferon-alpha in a murine model of polycythemia vera. *Blood* **121**, 3692-3702 (2013).

48. Norfo, R., *et al.* miRNA-mRNA integrative analysis in primary myelofibrosis CD34+ cells: role of miR-155/JARID2 axis in abnormal megakaryopoiesis. *Blood* **124**, e21-32 (2014).

Figure legends

Figure 1. Myeloproliferative neoplasms in *Zfand2b*-deficient mice. (a) Representative picture of 18-month-old wild-type and *Zfand2b*-deficient mice. (b) Kaplan-Meier survival plot of *Zfand2b*$^{+/+}$ (n=20) and *Zfand2b*$^{-/-}$ (n=28) mice. $P<0.01$, log-rank/Mantel-Cox test. (c) Representative picture of spleens from wild-type, 9-month-old (KO1) and 18-month-old (KO2) *Zfand2b*-deficient mice. Mean spleen weights are represented. (d) Representative images from hematoxylin-eosin staining of spleen and bone-marrow sections from age-matched wild-type and knock-out animals. Scale bars,

500 μm and 25 μm, respectively. Black arrows indicate reticulin fibers. (e,f) Cell counts of peripheral blood from 1.5- and 18-month-old wild-type and knock-out animals (WBC: white blood cells; LYM: lymphocytes; GRA: granulocytes; HCT: hematocrit; PLT: platelets). (g) Representative FACS analysis of bone marrow cells from 6-month-old *Zfand2b*$^{+/+}$ (n=7) and *Zfand2b*$^{-/-}$ (n=7) mice. Percentage and absolute numbers of LSK+ and SLAM cells are represented. Values were normalized to total viable cellularity. (h) Competitive repopulation assay. Plots represent the percentage of wild-type or *Zfand2b*-deficient Ly-5.2 cells in peripheral blood or bone marrow from mice recipients. Error bars indicate SEM (*, $P<0.05$; **, $P<0.01$, two-tailed Student's t test).

Figure 2. AIRAPL regulates IGF1R steady-state levels. (a) Western-blot analyses of phospho-IGF1R and total IGF1R in bone marrow from wild-type and knock-out animals. (b) IGF1R immunohistochemistry in spleens from wild-type and knock-out mice. Bar, 50 μm. (c) Western-blot analysis of IGF1R and AIRAPL in HEK-293T cells transiently overexpressing AIRAPL. (d) IGF1R Western-blot analysis in control and AIRAPL-transfected HEK-293T cells either treated or not with the proteasome inhibitor MG-132 (2 μM). (e) Anti-HA Western-blot of GFP immunoprecipitates from HEK-293T cells transiently cotransfected with IGF1R-GFP, HA-ubiquitin and AIRAPL. Total IGF1R protein in the immunoprecipitates was detected by Western-blot. (f) Western-blot analyses of total and ubiquitinated IGF1R in HEK-293T, either transfected with pcDNA3.1 or AIRAPL, in the presence of specific siRNAs that target AIRAPL functional partners. (g) Western-blot analysis of IGF1R in total lysates and anti-HA immunoprecipitates from HEK-293T cells transfected with HA-AIRAPL. Cells were treated with 5 μM MG-1232 for 8 h prior to lysis. Mouse IgG was used as a negative control. (h,i) Metabolic labeling and anti-GFP immunoprecipitation of HEK-293T cells transiently transfected with IGF1R-GFP and either pcDNA3.1 or AIRAPL (h) or from *ZFAND2B*$^{+/+}$ and *ZFAND2B*$^{-/-}$ HEK-293T cells (i). Signal intensities of Western-blot analyses and metabolic labeling experiments were quantified and mean values from at least 3 independent experiments are represented or indicated. Error bars indicate SEM (**, $P<0.01$, two-tailed Student's t test).

Figure 3. IGF1R inhibition prevents myeloproliferative neoplasms. (a) Peripheral blood cell counts in 6- and 12-month-old wild-type, *Zfand2b*$^{+/+}$*Igf1r*$^{+/-}$, *Zfand2b*$^{-/-}$*Igf1r*$^{+/+}$ and *Zfand2b*$^{-/-}$*Igf1r*$^{+/-}$ mice (WBC: white blood cells; LYM: lymphocytes; GRA: granulocytes). (b) Representative photograph of spleens from 12-month-old mice of the indicated genotypes. Mean spleen weight values are shown. (c) Representative images from hematoxylin-eosin staining of spleen and bone marrow sections from 12-month-old wild-type, *Zfand2b*$^{+/+}$*Igf1r*$^{+/-}$, *Zfand2b*$^{-/-}$*Igf1r*$^{+/+}$ and *Zfand2b*$^{-/-}$*Igf1r*$^{+/-}$ mice. Scale bars, 100 μm. Black arrows indicate reticulin fibers. (d) FACS analysis of bone marrow from wild-type, *Zfand2b*$^{+/+}$*Igf1r*$^{+/-}$, *Zfand2b*$^{-/-}$*Igf1r*$^{+/+}$ and *Zfand2b*$^{-/-}$*Igf1r*$^{+/-}$ mice. Percentage and absolute number of LSK+ cells are represented. (e) Cell counts of knock-out animals before and after 1 or 2 months of daily NVP-AEW541 treatment (WBC: white blood cells; LYM: lymphocytes; GRA: granulocytes; HCT: hematocrit and PLT: platelets). (f) Mean spleen weight values of wild-type, untreated and 2-month-NVP-AEW541-treated *Zfand2b*-deficient mice. (g) FACS analysis of bone marrow from wild-type, untreated and NVP-AEW541-treated *Zfand2b*-deficient mice. Percentage and absolute number of LSK+ cells are represented. Error bars indicate SEM (*, $P<0.05$; **, $P<0.01$, two-tailed Student's t test).

Figure 4. AIRAPL and IGF1R alterations in JAK2-driven MPN. (a) Box-whiskers plot of *ZFAND2B* mRNA levels in human samples from controls, essential thrombocythemia (ET), polycythemia vera (PV) and primary myelofibrosis (PMF) ($P<0.01$, ANOVA). (b) Representative Western-blot analysis of AIRAPL and IGF1R in MPN samples and controls. β-actin was used as a loading control. (c) Representative images of AIRAPL and IGF1R immunohistochemical analysis in bone marrow biopsies from MPN and controls. Bar, 20 μm. (d) Western-blot analysis of AIRAPL and IGF1R in *Jak2*$^{+/+}$ and *Jak2*$^{R/+}$ mice. (e) *Zfand2b* mRNA relative levels in bone marrow from *Jak2*$^{+/+}$ and *Jak2*$^{R/+}$ mice. (f) GSEA plot comparing transcriptional profiles of hematopoietic stem cells (HSCs) from *Jak2*$^{R/+}$ and *Jak2*$^{+/+}$ mice. (g) Cell counts in peripheral blood from *Jak2*$^{R/+}$ before and after 1 or 2 months of daily NVP-AEW541 treatment (WBC: white blood cells; PLT: platelets). (h) Mean spleen weight values of *Jak2*$^{+/+}$, untreated and NVP-AEW541-treated *Jak2*$^{R/+}$ mice. (i) FACS analysis of bone marrow from *Jak2*$^{+/+}$, untreated and NVP-AEW541-treated *Jak2*$^{R/+}$ mice. (j) Relative proliferation with increasing concentrations of NVP-AEW541. IC50 values are

indicated in SET2 and HEL cell lines. Signal intensities of Western-blot analyses were quantified and mean values from at least 3 independent experiments are represented or indicated. Error bars indicate SEM (*, $P<0.05$; **, $P<0.01$, two-tailed Student's t test).

Supplementary Figure legends

Supplementary Figure 1. Generation of *Zfand2b*-deficient mice. (a) Schematic representation of the wild-type *Zfand2b* locus, targeting vector, and targeted allele. Positions of restriction enzyme cleavage sites and probes used for Southern-blot analysis are shown. (b) Southern-blot analysis of genomic DNA from two targeted *Zfand2b*-knock-out-first cell clones and wild-type ES cells. Probing of XhoI–digested DNA revealed fragments of 18.4 and 7.2 kb for wild-type (WT) and mutant alleles, respectively. (c) qRT-PCR of *Zfand2b* in liver, muscle and bone marrow from wild-type and *Zfand2b*-deficient mice. Mean relative mRNA levels are shown, error bars indicate SEM ($P<0.01$, two-tailed Student's t test). (d) Western-blot analysis of AIRAPL in wild-type and *Zfand2b*-deficient mice. β-actin was used as a loading control.

Supplementary Figure 2. Hematological alterations in *Zfand2b*-deficient mice. (a) Myeloperoxidase (MPO) and CD3 immunohistochemical analysis in spleens from wild-type and knock-out mice. Bar, 50 μm (b) Percentage of bands, metamyelocyte (meta) and blast cell populations in 18-month-old wild-type and *Zfand2b*-deficient mice. (c) Representative images of myeloid precursor cells in peripheral blood from *Zfand2b*-deficient mice. (d) Myeloid deviation in *Zfand2b*-haploinsufficient mice. Cell counts in $Zfand2b^{+/-}$ and wild-type animals. (WBC: white blood cells; LYM: lymphocytes; GRA: granulocytes; HCT: hematocrit; PLT: platelets). (e) Percentage and absolute numbers of LSK+ and SLAM cells in splenocytes from wild-type and *Zfand2b*-deficient mice. Values were normalized to total viable cellularity. (f) Myeloid progenitor analysis in bone marrow and spleen from wild-type and *Zfand2b*-deficient mice. (CMP: common myeloid progenitor; GMP: granulocyte-monocyte progenitor; MEP: megakaryocyte-erythrocyte progenitor). (g) FACS analysis of bone marrow and spleen from 6-month-old mutant and WT mice (n = 7 mice per group) (IM: immature myeloid; MM: mature myeloid; LYM: lymphocyte; NRC: nucleated red cells). Error bars indicate SEM (**, $P<0.01$, two-tailed Student's t test).

Supplementary Figure 3. Bone marrow transplantation in *Zfand2b*-deficient mice. (a,b,c) Cell counts in peripheral blood from 3- and 12-month-old wild-type and knock-out animals transplanted either with wild-type or knock-out bone marrow (WBC: white blood cells; LYM: lymphocytes; GRA: granulocytes; HCT: hematocrit; PLT: platelets; Rec: recipient). (d) Mean spleen weight values of wild-type and knock-out animals transplanted either with wild-type or knock-out bone marrow. (e,f) FACS analysis of bone marrow cells from wild-type and knock-out animals transplanted either with wild-type or knock-out bone marrow. (g) Representative FACS analysis of splenocytes from wild-type and knock-out animals transplanted either with wild-type or knock-out bone marrow. Values were normalized to total viable cellularity. Error bars indicate SEM (*, $P<0.05$; **, $P<0.01$, two-tailed Student's t test).

Supplementary Figure 4. Unfolded protein response (UPR) analysis in *Zfand2b*-deficient mice. (a) Calreticulin immunofluorescence analysis in wild-type and *ZFAND2B*-deficient HEK-293T cell line. (b) Western-blot analysis of calreticulin and VCP in wild-type and *Zfand2b*-deficient mice. (c) UPR challenge through tunicamycin injection in wild-type and *Zfand2b*-deficient mice. Representative images from hematoxylin-eosin staining of liver sections from liver of tunicamycin-exposed wild-type and knock-out animals. (d) Western-blot and RT-PCR analyses of UPR characteristic markers in untreated and tunicamycin-treated wild-type and *Zfand2b*-deficient mice. Signal intensities of Western-blot analyses were quantified and mean values from at least 3 independent experiments are represented or indicated. Error bars indicate SEM (**, $P<0.01$, two-tailed Student's t test).

Supplementary Figure 5. IGF1R deregulation in *Zfand2b*-deficient mice. (a) Western-blot analyses of phospho JAK2 and STAT5 proteins in $Zfand2b^{+/+}$ and $Zfand2b^{-/-}$ mice. β-actin was used as a loading control. (b) Proteome profiler of mouse receptor tyrosine kinase array. Mean signal intensities of 3 wild-type and *Zfand2b*-deficient mice are represented. (c) Western-blot analyses of activated AKT, S6K, 4EBP1 and ERK in $Zfand2b^{+/+}$ and $Zfand2b^{-/-}$ animals. (d) Cycloheximide (CHX) chase assay in HEK-293T cells transfected with either pcDNA3.1-empty vector or AIRAPL. Cells were

treated with 100 μg/mL of CHX during the indicated times. (e) Western-blot analysis of IGF1R and AIRAPL in total lysates and GFP immunoprecipitates from HEK-293T cells cotransfected with IGF1R-GFP and AIRAPL. MG-132 was used at 5 μM for 8 h. (f) GFP Western-blot analysis of anti-HA immunoprecipitates from HEK-293T cells transfected with either HA-AIRAPL and IGF1R-GFP or GFP. Cells were treated with 5 μM MG-1232 for 8 h prior lysis. (g,h) Western-blot analyses of IGF1R and AIRAPL in total lysates from metabolic labeling experiments in HEK-293T cells transiently transfected with IGF1R-GFP and either pcDNA3.1 or AIRAPL (g), or from *ZFAND2B*$^{+/+}$ and *ZFAND2B*$^{-/-}$ HEK-293T cells (h). β-actin was used as a loading control. Signal intensities of Western-blot analyses were quantified and mean values from at least 3 independent experiments are represented or indicated. Error bars indicate SEM (*, $P<0.05$; **, $P<0.01$, two-tailed Student's t test).

Supplementary Figure 6. AIRAPL pull-down experiments. Ingenuity Pathways Analysis of the data obtained from AIRAPL co-immunoprecipitation experiments in HEK-293T cells (Supplementary Table 2). The network includes different proteasome subunits and proteasome-associated proteins that physically interact with AIRAPL.

Supplementary Figure 7. CRISPR/Cas9-mediated generation of *ZFAND2B*-deficient HEK-293T cells. (a) Fragment length analysis of representative wild-type and *ZFAND2B*-deficient HEK-293T cell clones. (b) DNA sequencing of a representative clone of *ZFAND2B*-deficient cells. Note a 4-nucleotides insertion (red) in one of the alleles and a 23-nucleotide-deletion in the other (green). (c) *ZFAND2B* qRT-PCR in wild-type and knock-out cells demonstrated no significant changes in mRNA levels.

Supplementary Figure 8. Genetic and pharmacological IGF1R inhibitory strategies. (a) Western-blot analysis of IGF1R in wild-type, *Zfand2b*$^{+/+}$*Igf1r*$^{+/-}$, *Zfand2b*$^{-/-}$*Igf1r*$^{+/+}$ and *Zfand2b*$^{-/-}$*Igf1r*$^{+/-}$ mice. β-actin was used as a loading control. (b,c) Cell counts in peripheral blood from mice of the indicated genotypes (HCT: hematocrit; PLT: platelets). (d) FACS analysis in splenocytes from wild-type *Zfand2b*$^{+/+}$*Igf1r*$^{+/-}$, *Zfand2b*$^{-/-}$*Igf1r*$^{+/+}$ and *Zfand2b*$^{-/-}$*Igf1r*$^{+/-}$ mice. (e) FACS analysis of bone marrow cells (IM: immature myeloid; MM: mature myeloid; LYM: lymphocyte; NRC: nucleated red

cells). (f) Western-blot analyses of phospho-IGF1R and total IGF1R in untreated and NVP-AEW541-treated *Zfand2b*-deficient mice. (g) FACS analysis in splenocytes from wild-type, untreated and NVP-AEW541-treated *Zfand2b*-deficient mice. Signal intensities of Western-blot analyses were quantified and mean values from at least 3 independent experiments are represented or indicated. Error bars indicate SEM (*, $P<0.05$; **, $P<0.01$, two-tailed Student's t test).

Supplementary Figure 9. IGF1R inhibition in JAK2-driven MPN. (a) Box-whiskers plot of *ZFAND2B* expression in CD34+ cells from human primary myelofibrosis and controls. (b,c) Cell counts in peripheral blood from recipients of Jak2-V617F-transduced bone marrow cells derived from $Igf1^{+/+}$ and $Igf1r^{+/-}$ donors (WBC: white blood cells; LYM: lymphocytes; GRA: granulocytes; HCT: hematocrit; PLT: platelets). (d) Mean spleen weights of the same mice cohort. (e) Representative images from hematoxylin-eosin staining of spleen sections from Jak2-V617F transduced bone marrow. Scale bar, 100μm. (f) IGF1R Western-blot analysis in HEK-293T cells transduced with IGF1R-shRNA. β-actin was used as a loading control. (g) Relative proliferation values of SET2 and HEL lines transduced with IGF1R-shRNAs. (h) Increased proliferation values of SET2 and HEL cell lines overexpressing IGF1R. Signal intensities of Western-blot analyses were quantified and mean values from at least 3 independent experiments are represented or indicated. Error bars indicate SEM (*, $P<0.05$; **, $P<0.01$, two-tailed Student's t test).

Supplementary Figure 10. JAK2-mediated regulation of *ZFAND2B* levels. (a) GSEA comparing transcriptional profiles from SET2 and HEL cell lines either transduced with empty vector or IGF1R-shRNA. The enrichment score plot shown corresponds to AML-characteristic signature and STAT5 signaling pathway. (b) qRT-PCR analysis of *ZFAND2B* expression in untreated and ruxolotinib-treated SET2 and HEL cell lines (6 h, 0.5 μM (SET2), 2 μM (HEL)). (c) Western-blot analysis of AIRAPL and IGF1R in untreated and 24 h-ruxolotinib-treated SET2 and HEL cell lines (24 h). Signal intensities of Western-blot analyses were quantified and mean values from at least 3 independent experiments are represented or indicated. Error bars indicate SEM (*, $P<0.05$; **, $P<0.01$, two-tailed Student's t test).

Supplementary Figure 11. AIRAPL alterations in human cancer. (a) Percentage of genetic alterations in *ZFAND2B* gene in human tumors. adeno, adenocarcinoma; AML, acute myeloid leukemia; ccRCC, kidney renal clear cell carcinoma; CS, carcinosarcoma; GBM, glioblastoma; PCPG, pheochromocytoma and paraganglioma; pRCC, kidney renal papillary cell carcinoma; SC; small cell carcinoma; Squ, squamous cell carcinoma. Data were obtained from cBioPortal database. (b) Box-whiskers plot of methylation intensity values in two CpG islands included in *ZFAND2B* locus.

Supplementary Figure 12. miR-125a-3p regulation of *ZFAND2B* mRNA stability. (a) Pairwise alignment of miR-125a-3p and *ZFAND2B*. Base pair numbers on the *ZFAND2B* 3′-UTR region are indicated. (b) Luciferase assays in HEK-293T cells transfected with miR-125a-3p or a control miRNA, along with the 3′-UTR of *ZFAND2B* cloned downstream of *Renilla* luciferase. Data were normalized to the firefly luciferase and experiments were carried out in triplicate. (c) Box-whiskers plot of miR-125a-3p in human samples from controls, essential thrombocythemia (ET), polycythemia vera (PV) and primary myelofibrosis (PMF) (P<0.01, ANOVA). (d) Box-whiskers plot of *ZFAND2B* expression in CD34+ cells from human primary myelofibrosis and controls. (e,f) Scatter plots showing inverse correlation between miR-125a-3p and *ZFAND2B* levels in peripheral blood from MPN and control samples (e), and in CD34+ cells from human PMF (f). (g) miR-125a-3p qRT-PCR analysis in bone marrow from $Jak2^{+/+}$ and $Jak2^{R/+}$ mice. (h) miR-125a-3p qRT-PCR analysis in HEK-293T, SET2 and HEL cell lines. (i) miR-125a-3p qRT-PCR analysis in untreated and ruxolotinib-treated SET2 and HEL cell lines. Error bars indicate SEM (*, P<0.05; **, P<0.01, two-tailed Student's t test).

Supplementary Figure 13. miR-125a-3p inhibition in JAK2-mutated cell lines. (a,b) *ZFAND2B* and miR-125a-3p qRT-PCR analyses in SET2 and HEL cell lines, either transduced with miR-125 sponge or empty vector. (c) Western-blot analysis of AIRAPL and IGF1R in SET2 and HEL cell lines transduced with miR-125 sponge construct or empty vector. (d) GSEA comparing transcriptional profiles of SET2 and HEL cell lines transduced either with empty vector or miR-125 sponge. (e) Metabolic labeling and

anti-GFP immunoprecipitation of HEK-293T cells transiently transfected with IGF1R-GFP and either pCDH or pCDH-miR125a. (f) IGF1R and AIRAPL western-blot analyses in GFP immunoprecipitates from HEK-293T cells cotransfected with IGF1R-GFP and AIRAPL. MG-132 was used at 5 μM for 8 h. (g,h) Relative proliferation values of SET2 (g) and HEL (h) cell lines overexpressing AIRAPL or miR-125 sponge. Signal intensities of Western-blot analyses were quantified and mean values from at least 3 independent experiments are represented or indicated. Error bars indicate SEM (*, $P<0.05$; **, $P<0.01$, two-tailed Student's t test).

Supplementary Figure 14. *aip-1* deficiency shortens lifespan through deregulation of insulin/IGF-1 signaling pathway. Lifespan curves of wild-type (*N2*), *daf-2 (e1370)* and temperature-sensitive *fer-15(b26)/daf-2(e1370)* mutant animals subjected to the indicated RNAi. A representative experiment out of three is shown. Cumulative statistics on all three experiments are noted below the plots.

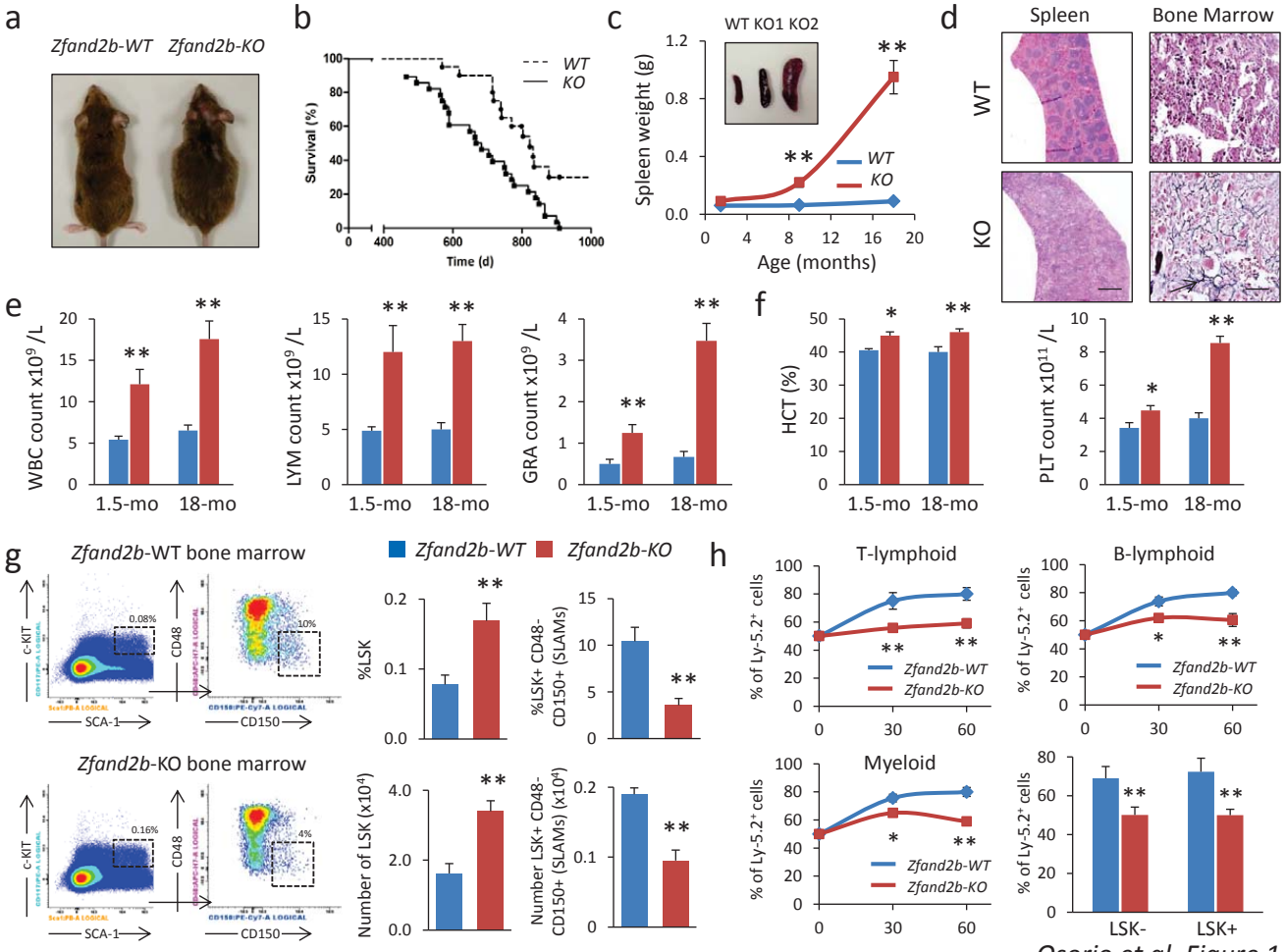

Osorio et al. Figure 1

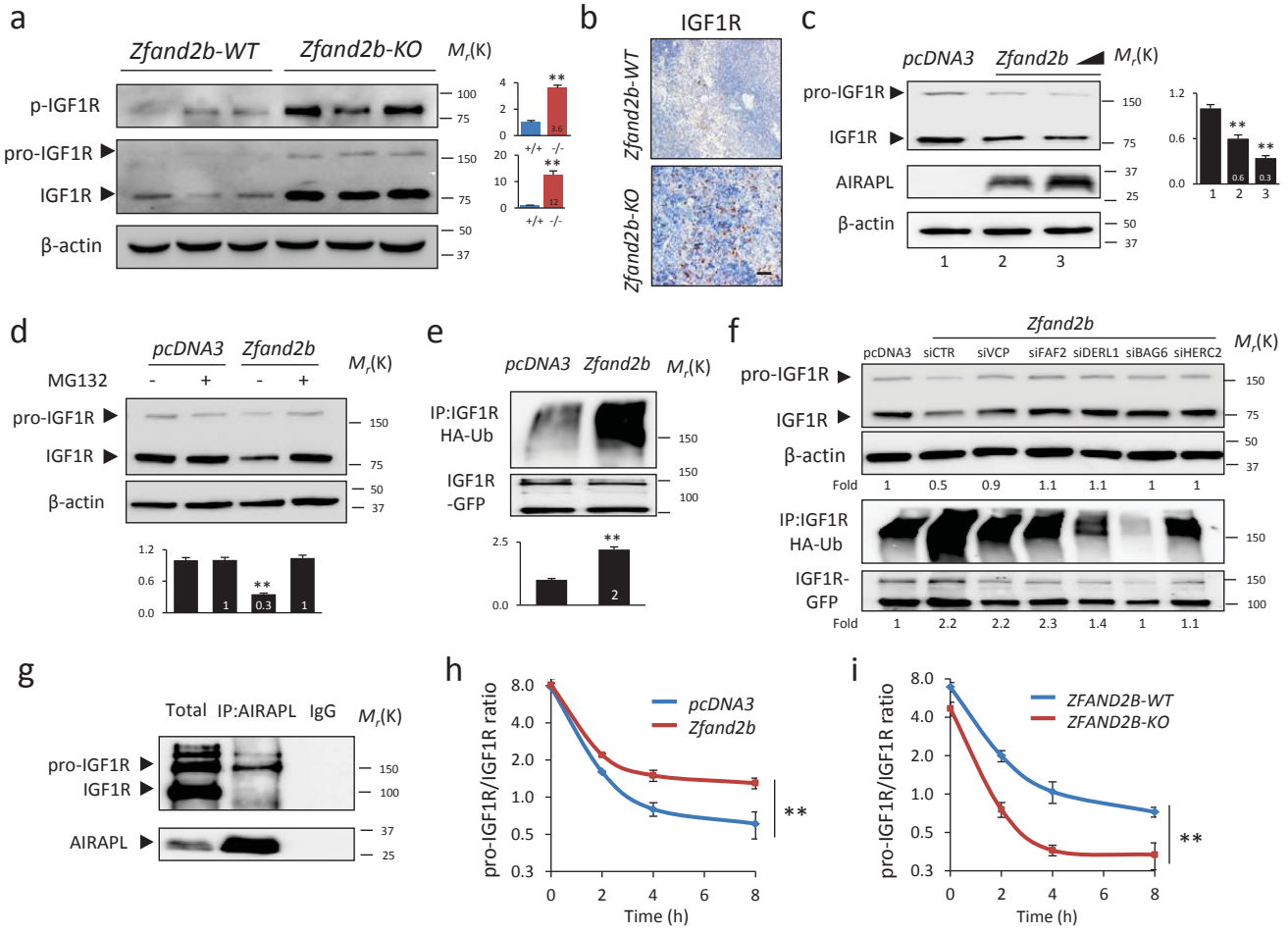

Osorio et al. Figure 2

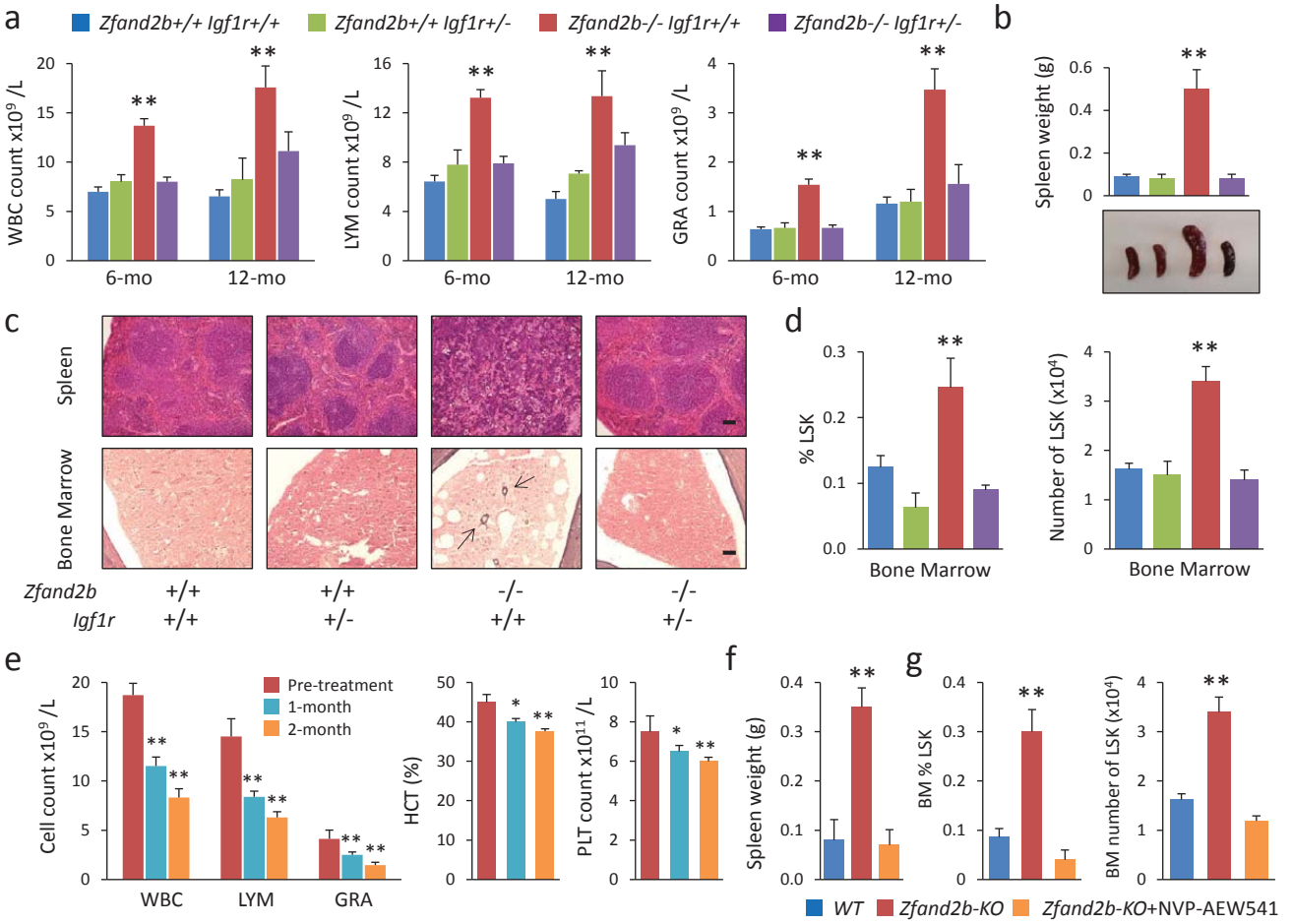

Osorio et al. Figure 3

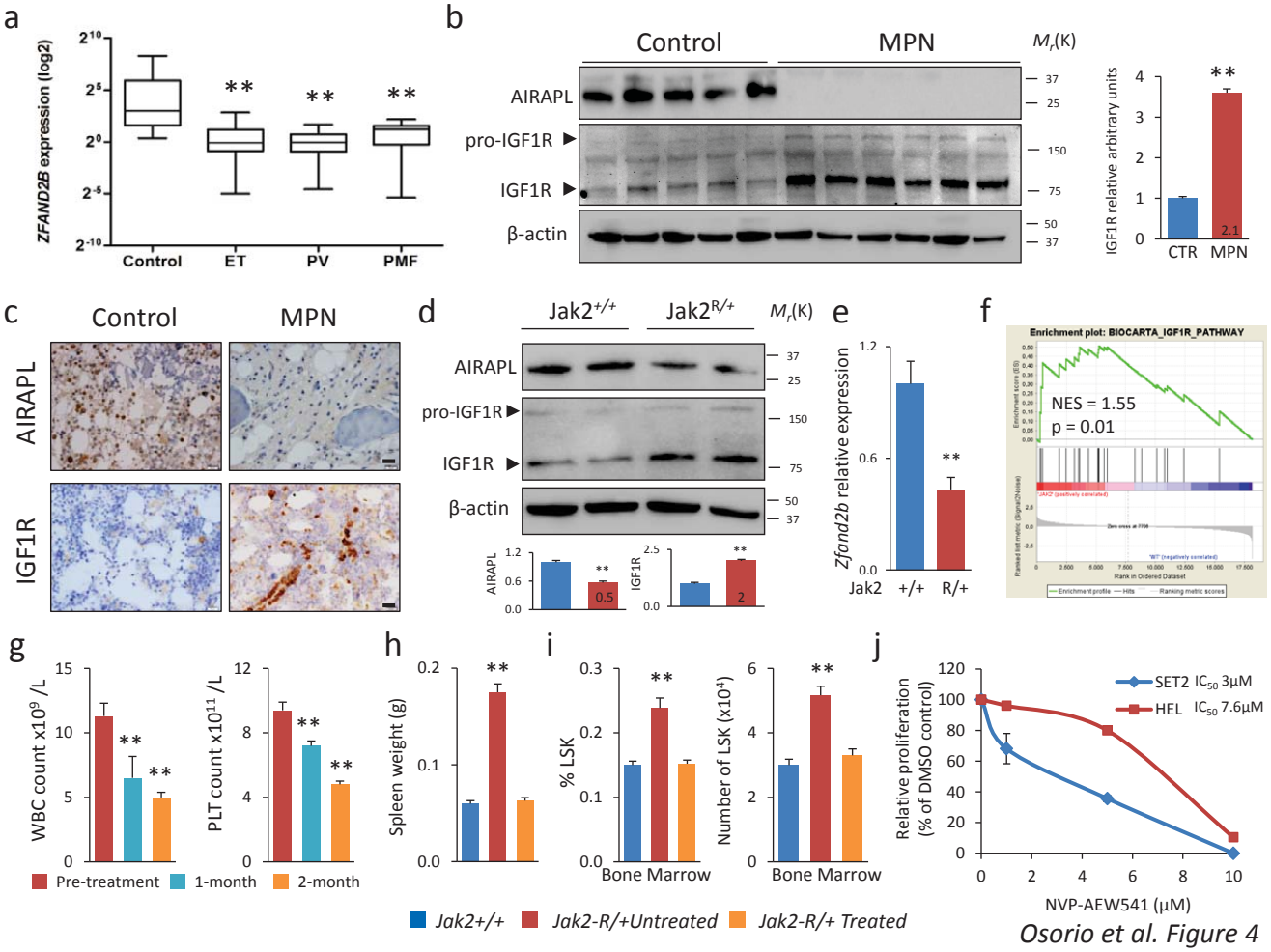

Osorio et al. Figure 4

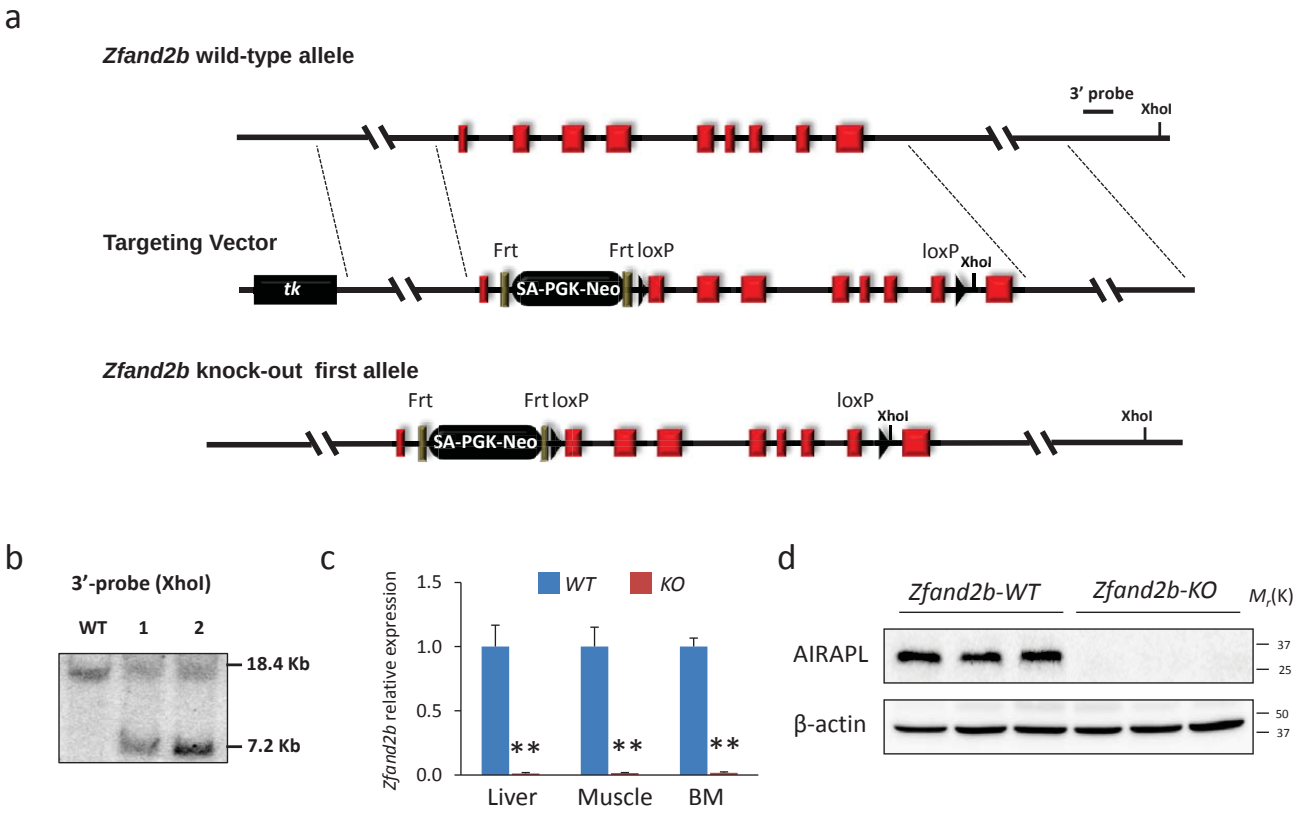

Osorio et al. Supplementary Figure 1

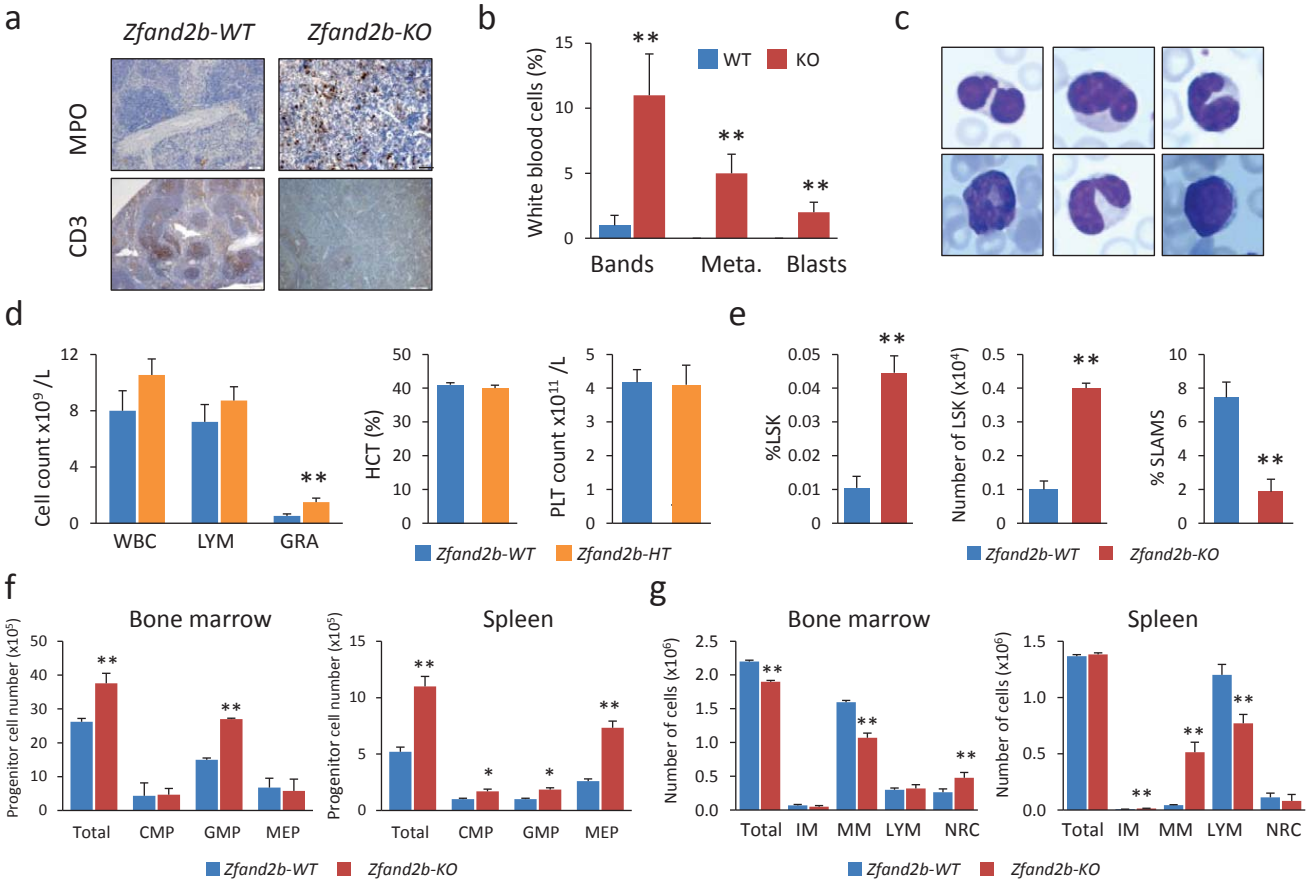

Osorio et al. Supplementary Figure 2

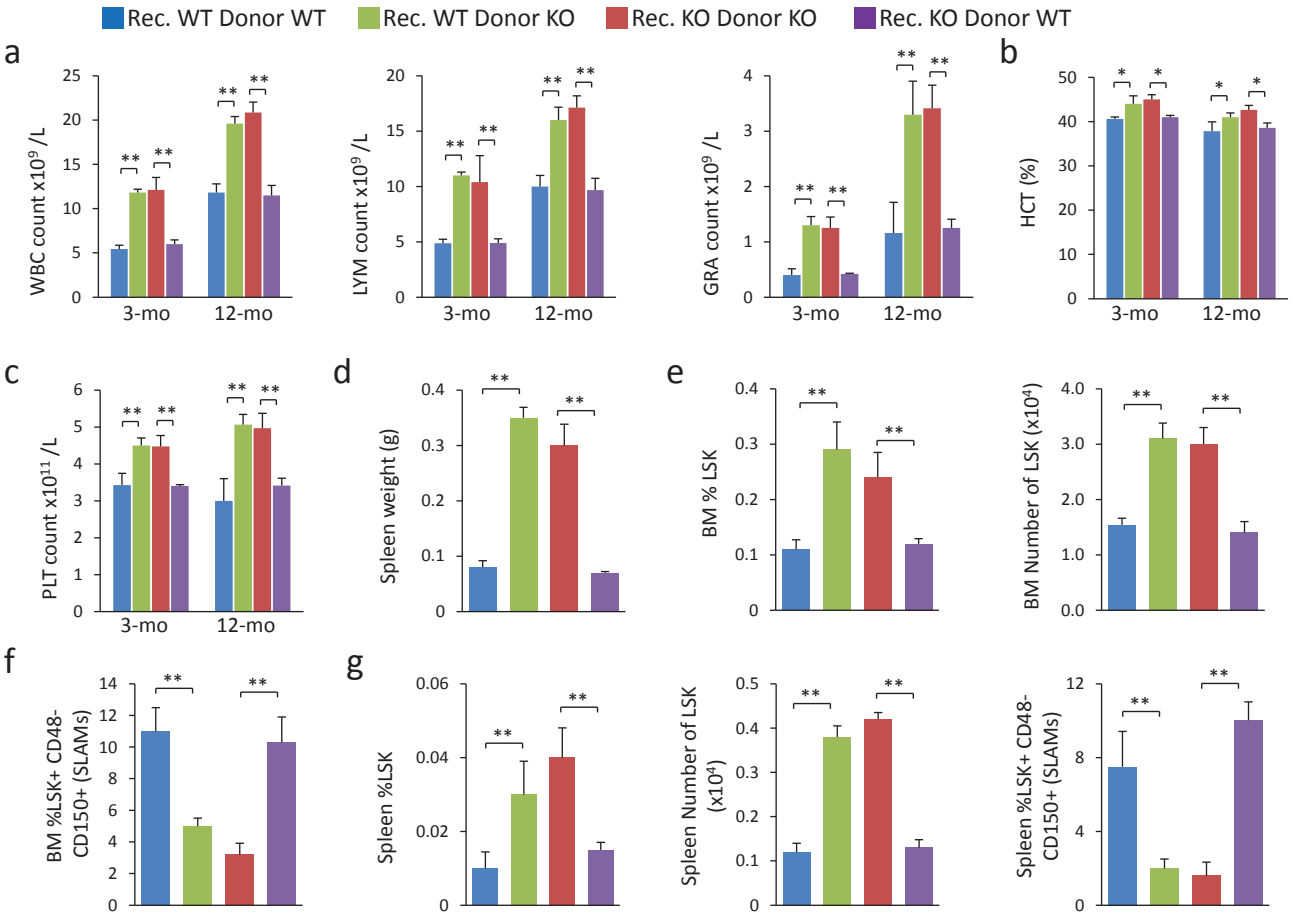

Osorio et al. Supplementary Figure 3

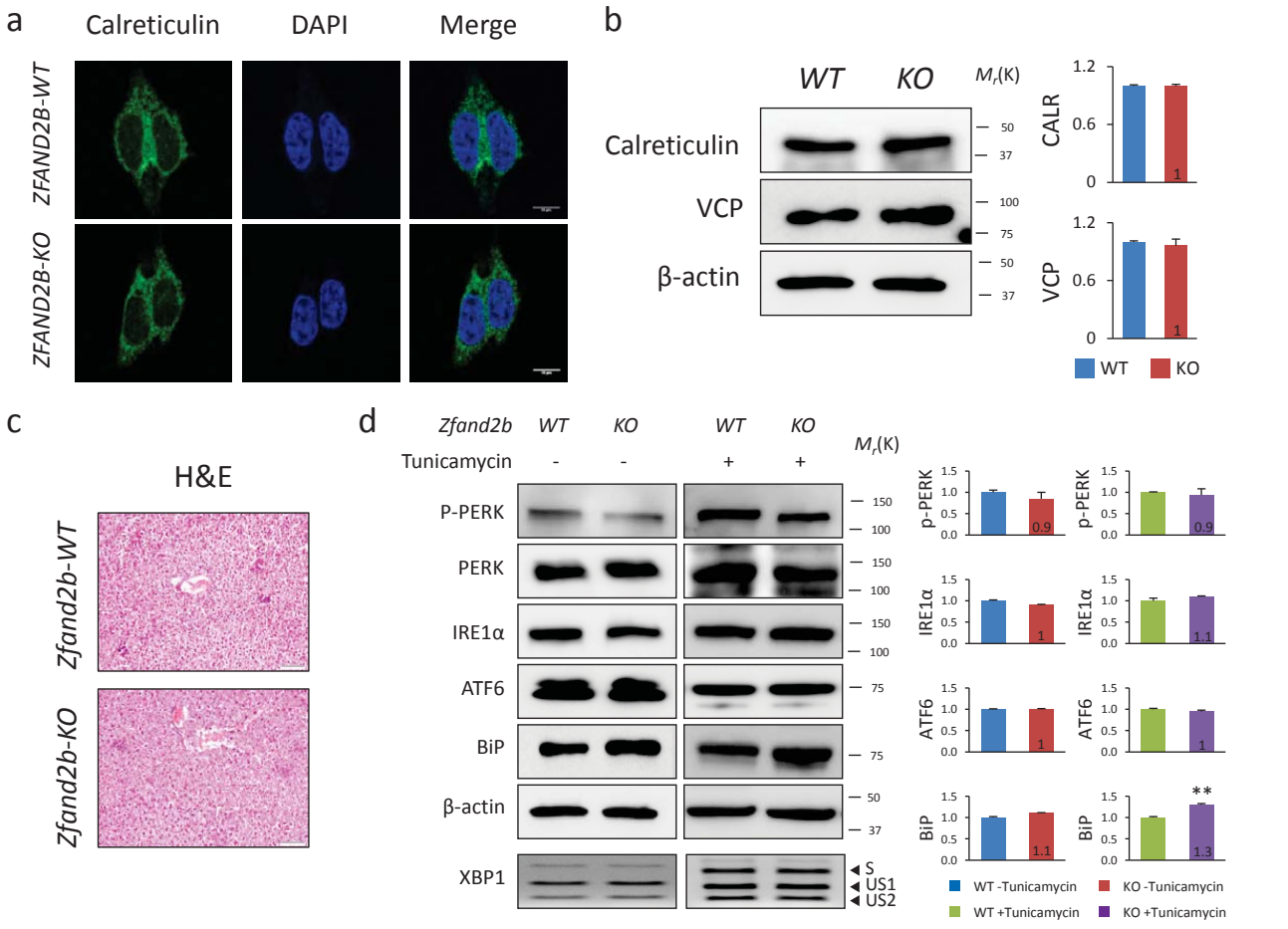

Osorio et al. Supplementary Figure 4

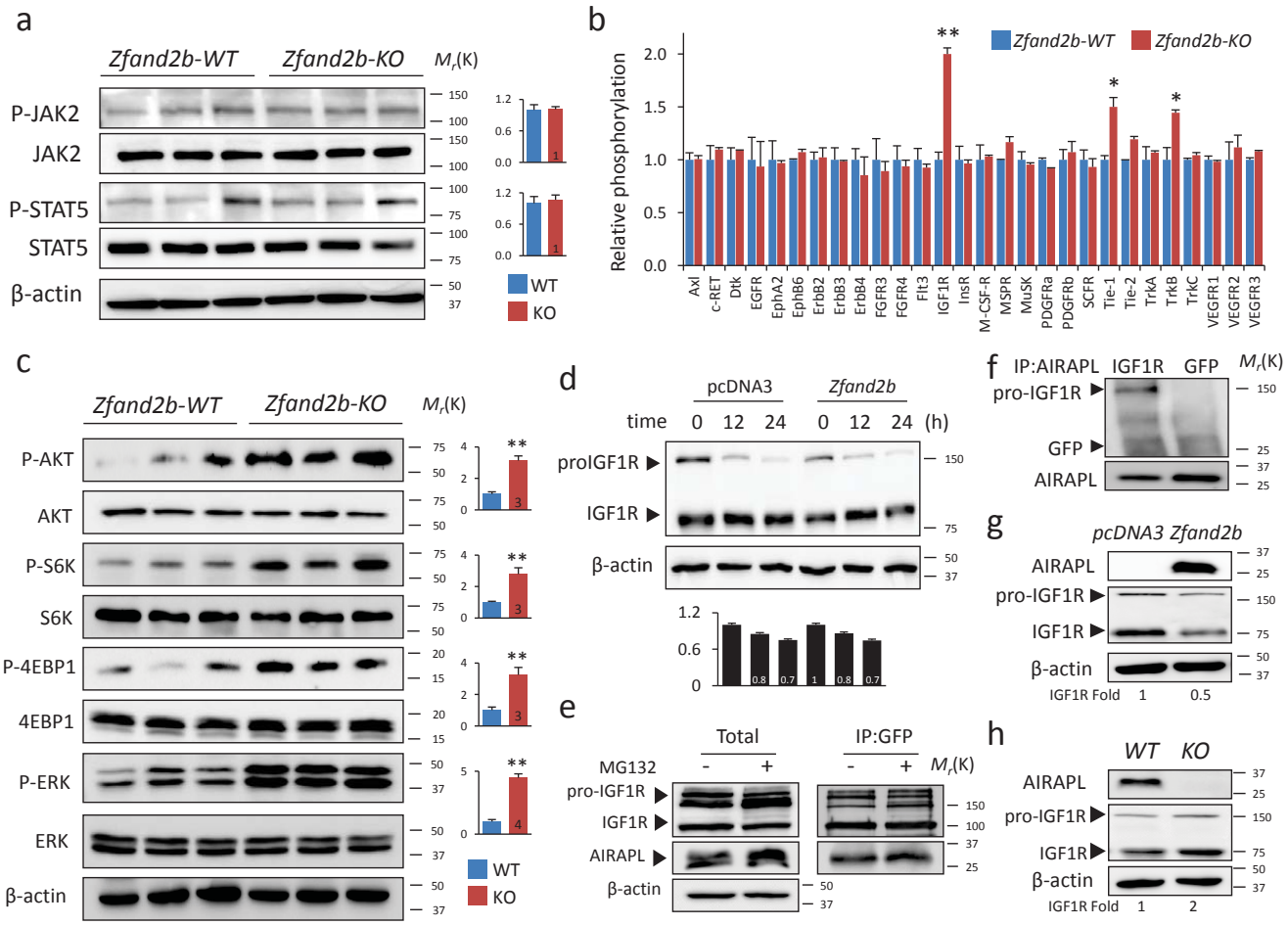

Osorio et al. Supplementary Figure 5

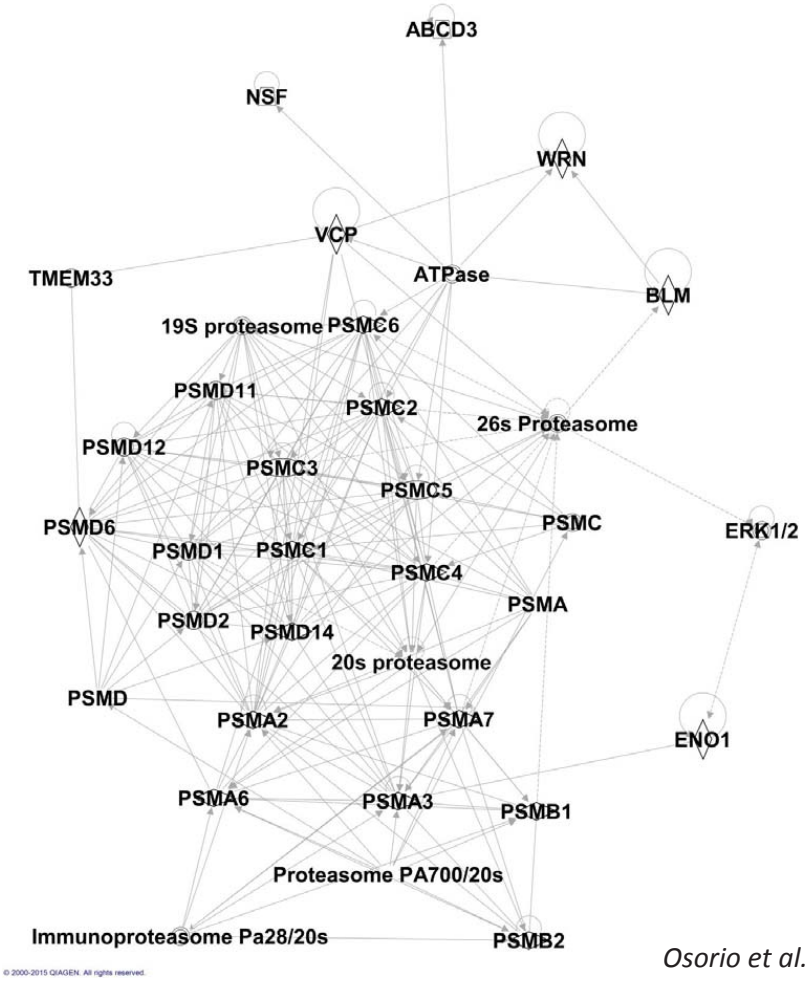

Osorio et al. Supplementary Figure 6

a

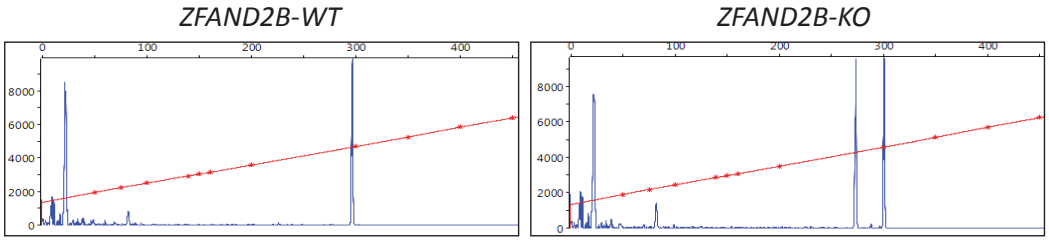

b

>clone 31

Allele 1

CACTCGTCGCTTCTCCTAGCagaccctgcccggcttggcgatggagtttccggacctc
ggACCTcgctcactgttcggagccgagctgtcagcgcttgggtgaggggcggagcgcgcgg
ggggcggggcccagcggacagggactttgaaccgcaggttgggagggaagggtgggctccc
aggctggcaatgccgggggggcggggcttgaagctgggggggggtggtcagcggcagaggg
ggcgtggccaaggaggtaatgggcttgggaaggggcggtgtgtcgaAAATAGGGTGGC
GTTTTCCT

Allele 2

CACTCGTCGCTTCTCCTAGCagaccctgcccggcttggcgatggagtttccggacctc
ggcgctcactgttcggagccgagctgtcagcgcttgggtgaggggcggagcgcgcgggggggc
ggggcccagcggacagggactttgaaccgcaggttgggagggaagggtgggctcccaggct
ggcaatgccgggggggcggggcttgaagctgggggggggtggtcagcggcagaggggcgt
ggccaaggaggtaatgggcttgggaaggggcggtgtgtcgaAAATAGGGTGGCGTTT
TCCT

c

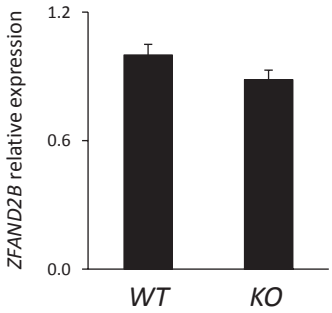

Osorio et al. Supplementary Figure 7

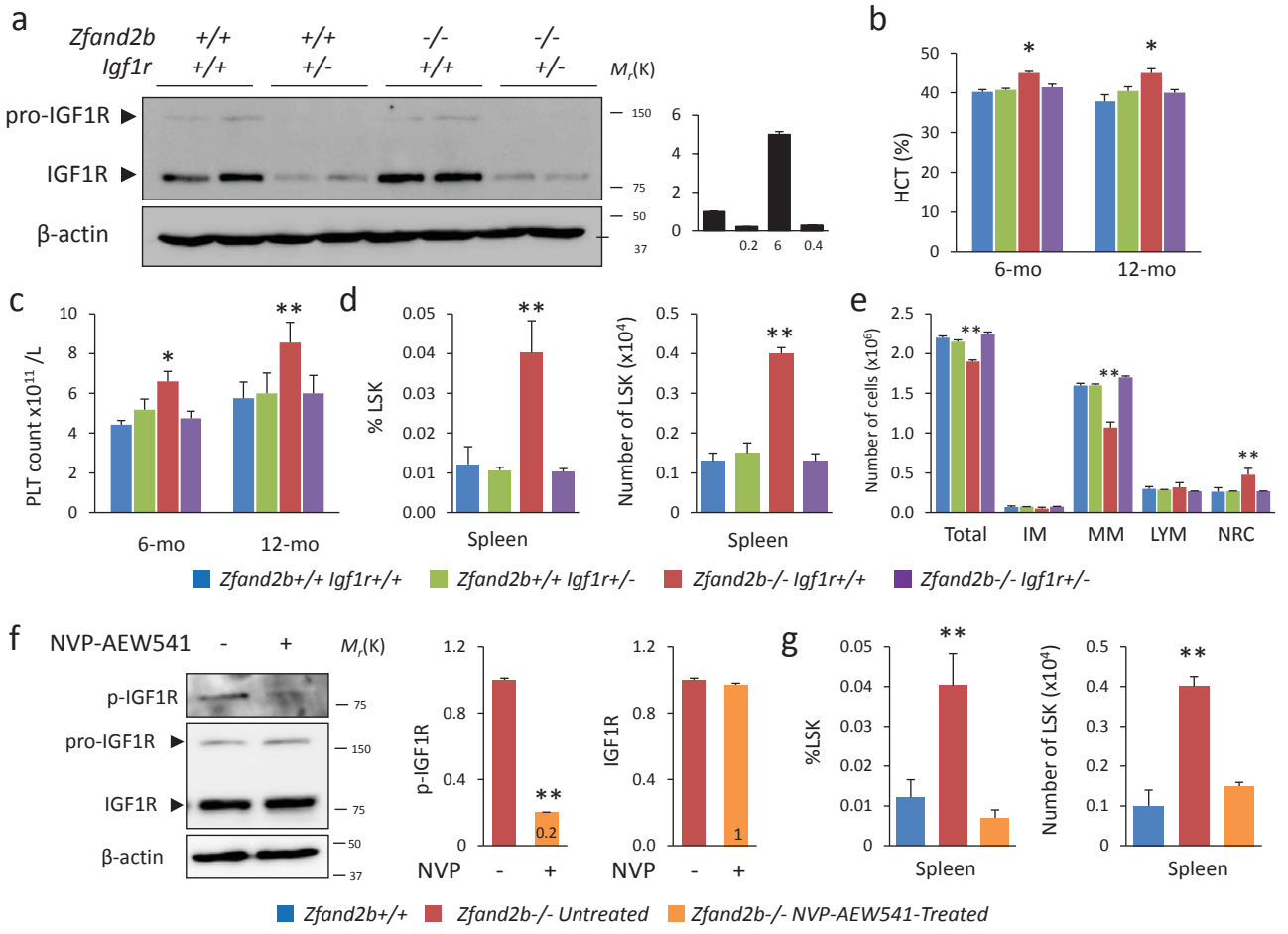

Osorio et al. Supplementary Figure 8

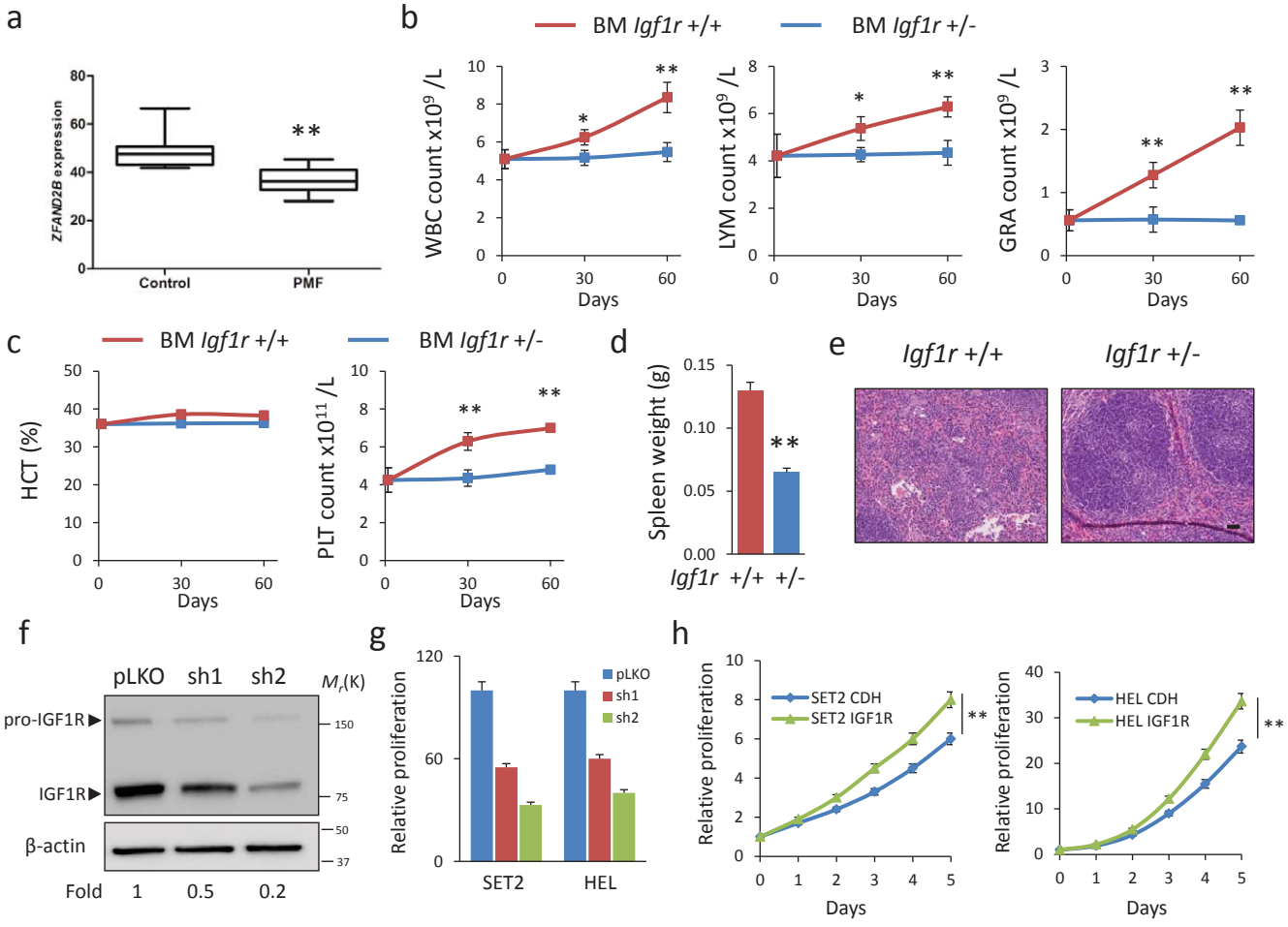

Osorio et al. Supplementary Figure 9

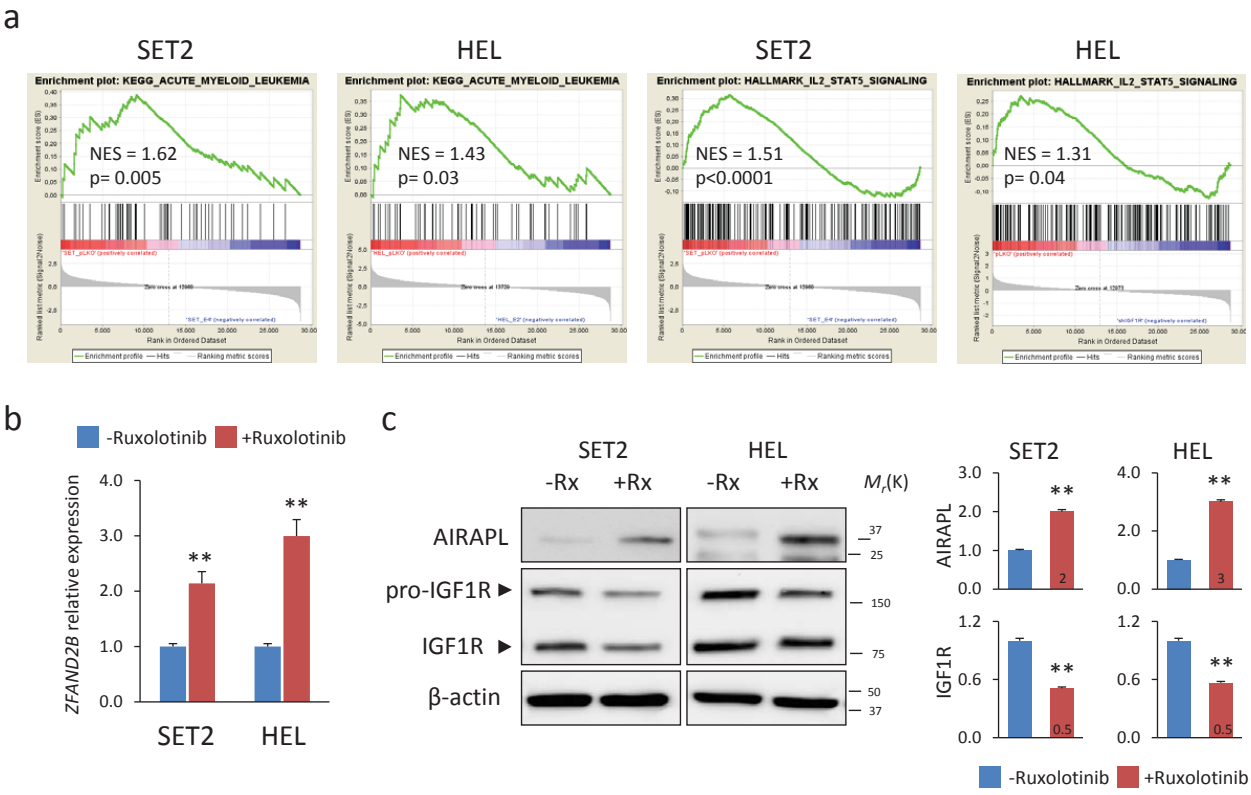

Osorio et al. Supplementary Figure 10

a

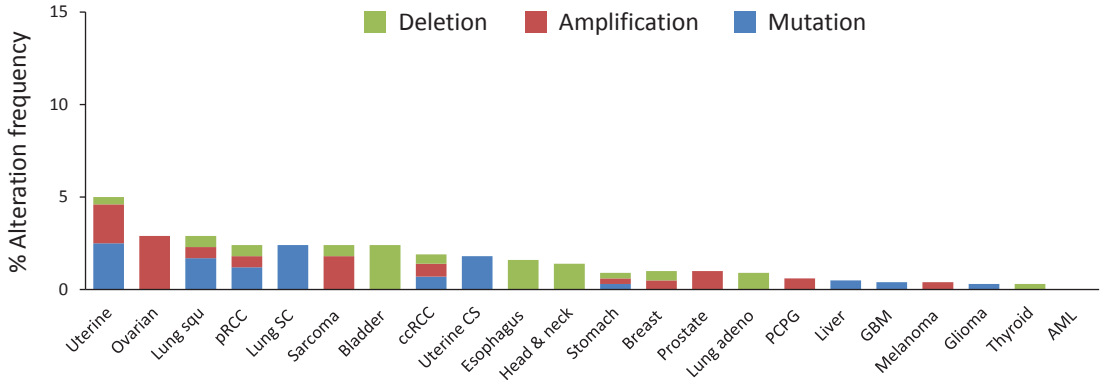

b

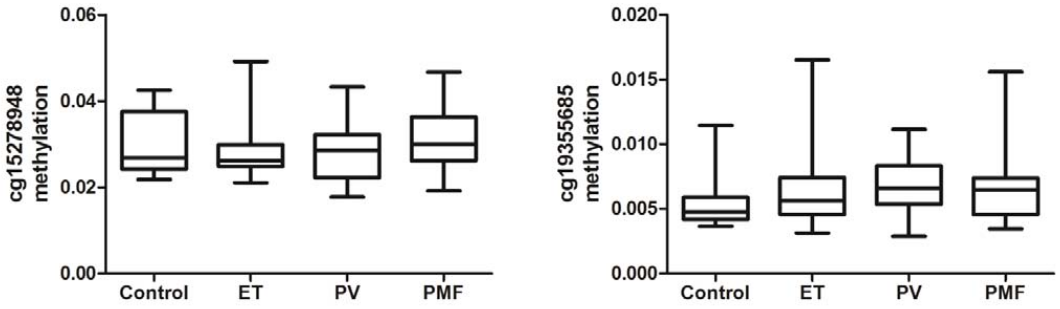

Osorio et al. Supplementary Figure 11

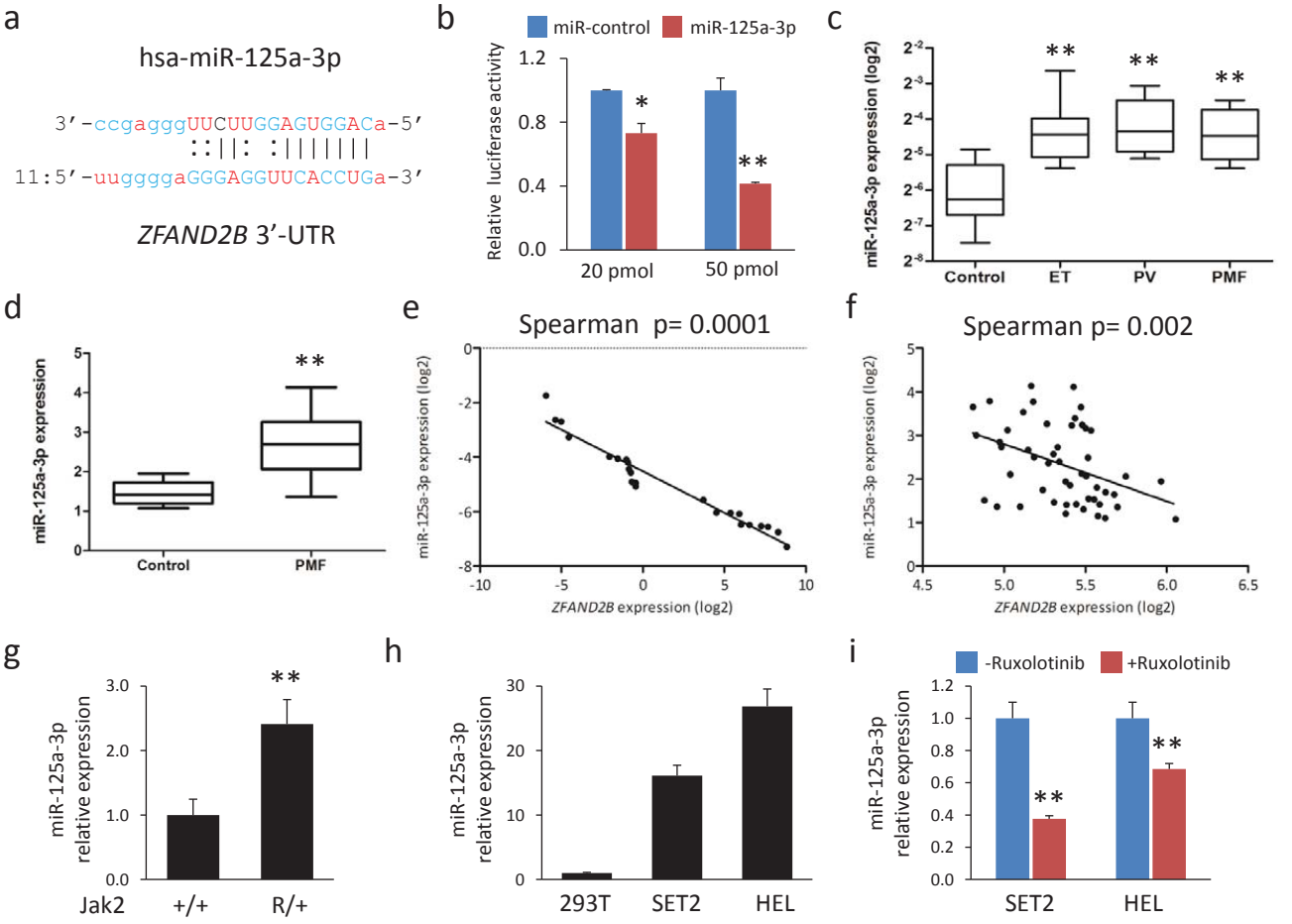

Osorio et al. Supplementary Figure 12

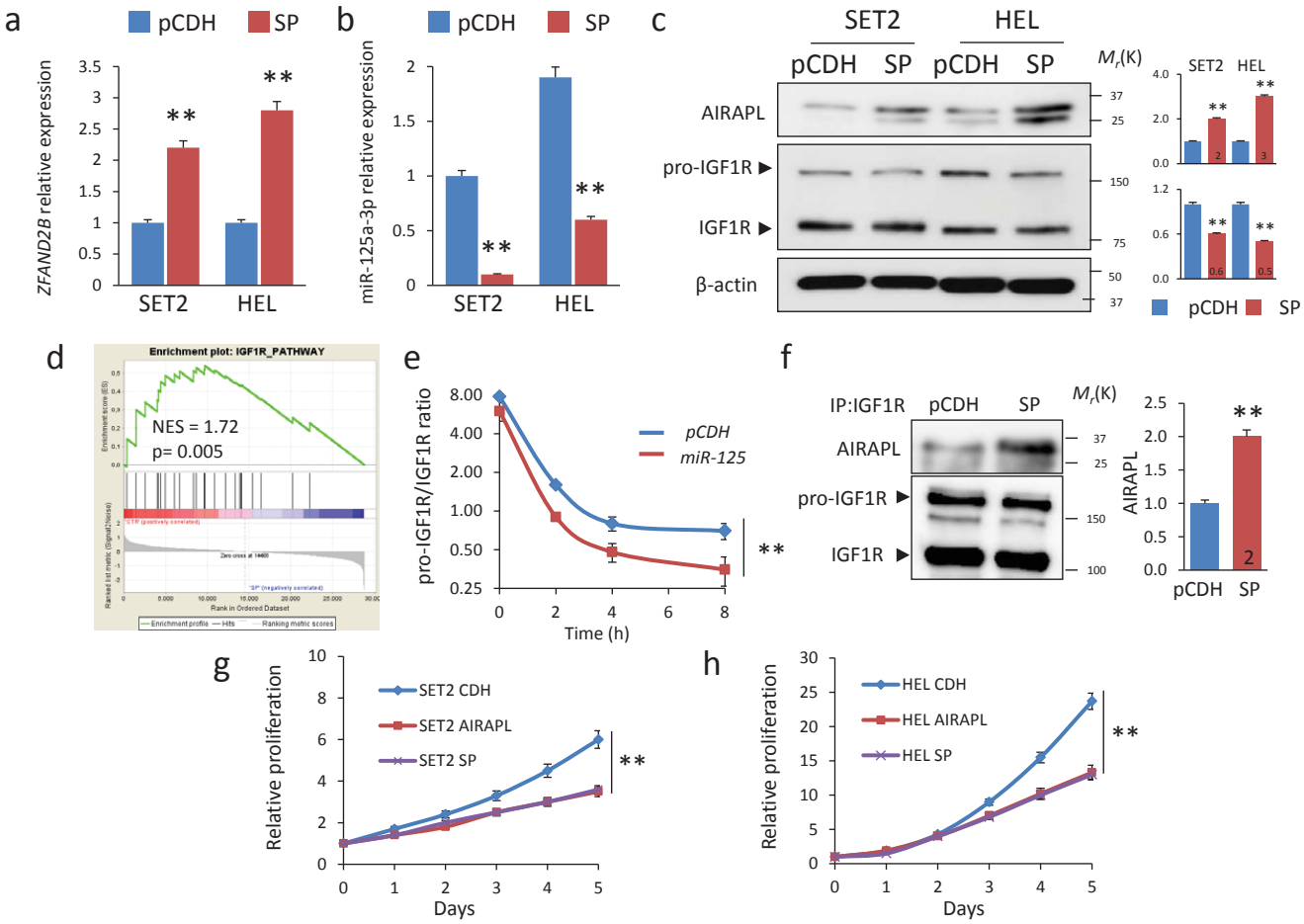

Osorio et al. Supplementary Figure 13

a

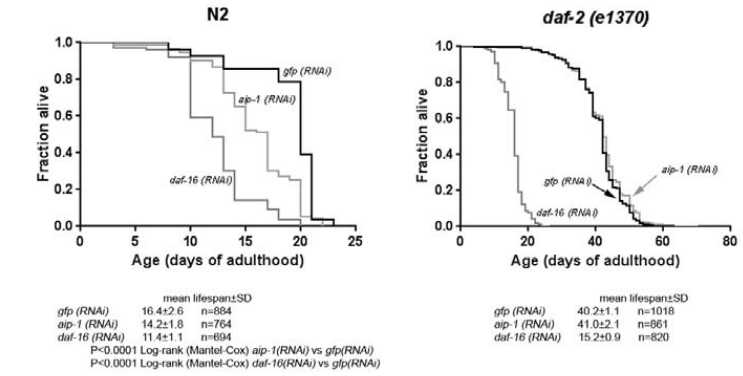

b

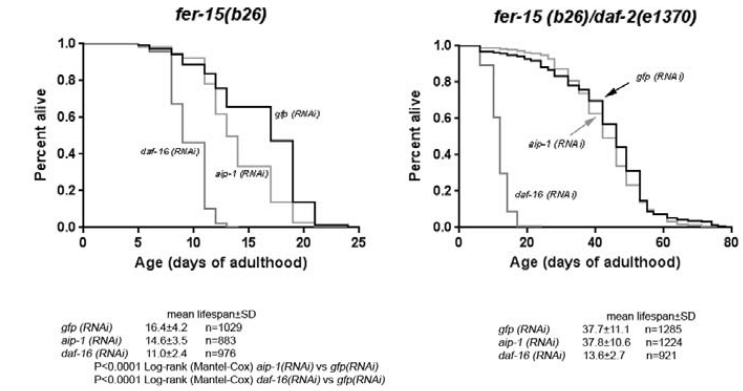

Osorio et al. Supplementary Figure 14

VII. Other works related to this Doctoral Thesis period

Article 9. Ignacio Varela, Sandrine Pereira, Alejandro P. Ugalde, Claire L. Navarro, María F. Suárez, Pierre Cau, Juan Cadiñanos, **Fernando G. Osorio**, Nicolas Foray, Juan Cobo, Félix de Carlos, Nicolas Lévy, José M. P. Freije and Carlos López-Otín. "Combined treatment with statins and aminobisphosphonates extends longevity in a mouse model of human premature aging". Nature Medicine. 2008 Jul; 14(7):767-72.

Article 10. Guillermo Mariño, Alejandro P. Ugalde, Álvaro F. Fernández, **Fernando G. Osorio**, Antonio Fueyo, José M.P. Freije and Carlos López-Otín. "IGF-1 treatment extends longevity in a mouse model of human premature aging by restoring somatotroph axis function". PNAS. 2010 Sep 14; 107(37):16268-73.

Article 11. Xose S. Puente, Victor Quesada, **Fernando G. Osorio**, Rubén Cabanillas, Juan Cadiñanos, Julia M. Fraile, Gonzalo R. Ordóñez, Diana A. Puente, Ana Gutiérrez-Fernández, Miriam Fanjul-Fernández, Nicolas Lévy, José M.P. Freije and Carlos López-Otín. "Exome sequencing and functional analysis identifies BANF1 mutation as the cause of a hereditary progeroid syndrome". American Journal of Human Genetics. 2011 May 13; 88(5):650-6.

Article 12. Irene Centeno, Pilar Blay, Iñigo Santamaría, Aurora Astudillo, Ana S. Pitiot, **Fernando G. Osorio**, Patricia González-Arriaga, Fernando Iglesias, Primitiva Menéndez, Adonina Tardón, Jose M.P. Freije and Milagros Balbín. "Germ-line mutations in epidermal growth factor receptor (EGFR) are rare but may contribute to oncogenesis: A novel germ-line mutation in EGFR detected in a patient with lung adenocarcinoma". BMC Cancer. 2011 May 16; 11:172.

Article 13. Isabel C. Lopez-Mejia, Valentin Vautrot, Marion de Toledo, Isabelle Behm-Ansmant, Cyril F. Bourgeois, Claire L. Navarro, **Fernando G. Osorio**, José M.P.Freije, James Stevenin, Annachiara de Sandre-Giovannoli, Carlos López-Otín, Nicolas Lévy, Christiane Branlant and Jamal Tazi. "A conserved splicing mechanism of the LMNA gene controls premature aging". Human Molecular Genetics. 2011 Dec 1; 20(23):4540-55.

Article 14. Clea Bárcena, **Fernando G. Osorio** and José M.P. Freije. "Detection of nuclear envelope alterations in senescence". Methods Molecular Biology. 2013; 965:243-51.

Article 15. Ricardo Villa-Bellosta, José Rivera-Torres, **Fernando G. Osorio**, Rebeca Acín-Pérez, José A. Enriquez, Carlos López-Otín and Vicente Andrés. "Defective extracellular pyrophosphate metabolism promotes vascular calcification in a mouse model of Hutchinson-Gilford progeria syndrome that is ameliorated on pyrophosphate treatment clinical perspective". Circulation. 2013 Jun 18; 127(24):2442-51.

Article 16. Jorge de la Rosa, José M.P. Freije, Rubén Cabanillas, **Fernando G. Osorio**, Mario F. Fraga, M. Soledad Fernández-García, Roland Rad, Víctor Fanjul, Alejandro P. Ugalde, Qi Liang, Haydn M. Prosser, Allan Bradley, Juan Cadiñanos and Carlos López-Otín. "Prelamin A causes progeria through cell-extrinsic mechanisms and prevents cancer invasion". Nature Communications. 2013; 4:2268.

Article 17. José Rivera-Torres, Rebeca Acín-Perez, Pablo Cabezas-Sánchez, **Fernando G. Osorio**, Cristina Gonzalez-Gómeza, Diego Megias, Carmen Cámara, Carlos López-Otín, José Antonio Enríquez, José L. Luque-García and Vicente Andrés. "Identification of mitochondrial dysfunction in Hutchinson–Gilford progeria syndrome through use of stable isotope labeling with amino acids in cell culture". Journal of Proteomics. 2013 Oct 8; 91:466-77.

Article 18. José M. González-Granado, Carlos Silvestre-Roig, Vera Rocha-Perugini, Laia Trigueros-Motos, Danay Cibrián, Giulia Morlino, Marta Blanco-Berrocal, **Fernando G. Osorio**, José M. P. Freije, Carlos López-Otín, Francisco Sánchez-Madrid and Vicente Andrés. "Nuclear envelope lamin-A couples actin dynamics with immunological synapse architecture and T cell activation". Science Signaling. 2014 Apr 22; 7(322):ra37.

Article 19. Pablo Garrido, **Fernando G. Osorio**, Javier Morán, Estefanía Cabello, Ana Alonso, José M.P. Freije and Celestino González. "Loss of GLUT4 induces metabolic reprogramming and impairs viability of breast cancer cells". Journal Cell Physiology. 2015 Jan; 230(1):191-8.

Article 20. Ana Gutiérrez-Fernández, Clara Soria-Valles, **Fernando G. Osorio**, Jesús Gutiérrez-Abril, Cecilia Garabaya, Alina Aguirre, Antonio Fueyo, M. Soledad Fernández-García, Xose S. Puente and Carlos López-Otín. "Loss of MT1-MMP causes cell senescence and nuclear defects which can be reversed by retinoic acid". EMBO Journal. 2015 Jul 14; 34(14):1875-88.

Article 21. Clara Soria-Valles*, **Fernando G. Osorio***, Ana Gutiérrez-Fernández, Alejandro De Los Angeles, Clara Bueno, Pablo Menéndez, José I. Martín-Subero, George Q. Daley, José M. P. Freije and Carlos López-Otín. "NF-κB activation impairs somatic cell reprogramming in ageing". Nature Cell Biology. 2015 Aug; 17(8):1004-13.

* Contributed equally to this work.

Article 22. Clara Soria-Valles, **Fernando G. Osorio** and Carlos López-Otín. "Reprogramming aging through DOT1L inhibition". Cell Cycle. 2015 Sep; 16.

Note

All the articles and manuscripts that have been included in this Thesis Work, together with their supplementary material, have been incorporated to the electronic version of the Thesis.

Discussion

Although aging research has been primarily focused on non-vertebrate short-lived model organisms, such as yeast (*Saccharomyces cerevisae*), worm (*Caenorhabditis elegans*), and fly (*Drosophila melanogaster*) [9], some important aspects of human aging and associated diseases cannot be faithfully recapitulated in invertebrate models as they lack specific organs and systems. Vertebrate model systems, as mouse (*Mus musculus*) and zebrafish (*Danio rerio*), have also been largely exploited to study genes involved in aging and age-related diseases. However, experimental studies have been hampered by the relative long lifespan of mice and zebrafish (maximal lifespan of 3-4 years and 5 years, respectively) and high costs of maintenance, especially for mice. Remarkably, the use of mouse models of accelerated aging has mostly addressed this issue. Overall, progeroid mouse models extensively resemble primary and secondary alterations involved in aging development, providing an experimental platform for genotype-to-phenotype analysis in a compressed timescale. Therefore, these progeroid mice offer a promising avenue for modeling human aging (**I**).

The generation and characterization of progeroid laminopathy mouse models represents a paradigm of the utility of these experimental models, and has been essential for a deeper understanding of the molecular basis of both accelerated aging syndromes and normal aging (**I**). In the case of HGPS, a rapid progress has been made in the last decade, since the identification of *LMNA* mutations in 2003 to the first clinical trial in HGPS patients [62]. Despite the utility of *Zmpste24*-deficient mice for HGPS studies, it has not been possible until now, with the generation of $Lmna^{G609G}$ mice, to recapitulate both genetic and phenotypic HGPS characteristic alterations, therefore allowing the development of *in vivo* approaches directed to the correction of *LMNA* aberrant splicing (**II**).

$Lmna^{G609G}$ knock-in mice recapitulate most of the alterations associated with HGPS, such as shortened lifespan, reduced body weight, and bone and cardiovascular abnormalities (**II**). Moreover, the cardiovascular phenotype shown by $Lmna^{G609G}$ mice resembles that of HGPS patients, as assessed by the loss of VSMCs and the alterations in ECG parameters. These similarities are a unique feature of this animal model when compared with previously available models of HGPS and may facilitate further studies on the role of A-type lamins in cardiovascular pathophysiology during normal and pathological aging. Additionally, $Lmna^{G609G}$ knock-in mice have also helped to clarify the relevance of systemic factors as

regulators of aging, as *Lmna*$^{G609G/G609G}$ animals exhibited severe alterations in nutrient-sensing pathways (**II**).

Splicing-directed therapies developed in this animal model focused on lowering the intracellular quantities of progerin itself, which represents an advantage as compared with the first generation of HGPS therapies, aimed at reducing progerin toxicity by pharmacologically inhibiting its prenylation. In this regard, the preclinical *in vivo* success of this approach in the *Lmna*^{G609G} knock-in mouse model represents a fundamental proof-of-concept in the field of progeria therapeutics. Thus, we demonstrated that the combined administration of two antisense oligonucleotides that block the aberrant splicing in *Lmna* caused by the p.Gly609Gly mutation reduces progerin amounts in vivo, prevents age-associated alterations and extends lifespan. Together, these findings provide an *in vivo* demonstration of the feasibility of ameliorating the characteristic alterations caused by progerin-linked premature aging through splicing modulation. The clinical development of this splicing-directed protocol for HGPS treatment may be facilitated by antisense oligonucleotide–based therapies that have already displayed preclinical efficacy in several other diseases and are being currently tested in clinical trials for Duchenne muscular dystrophy [140, 141].

The characterization of murine models of accelerated aging has also provided important clues about the regulatory signals that contribute to the establishment of aged state. In this regard, the study of epigenetic alterations in aging is critical as they are primary aging contributors and could constitute potential therapeutic targets [1]. Thus, we have reported the presence of epigenetic alterations in *Zmpste24*-deficient mice which are closely related to those observed in physiologically aging **(III)**. We have also proposed that these epigenetic abnormalities may be implicated in the development of the progeroid phenotype (**III**). Thus, we have found a direct correlation between the loss of acetylated forms of histone H2B and transcriptional down-regulation of several genes involved in the control of proliferation, metabolism and senescence such as *Bcl6*, *Apcs*, and *Htatip2* (**III**). The functional involvement of histone acetylation loss in progeria development has been further confirmed in *Zmpste24*-deficient mice [20]. Moreover, and in contrast to the absence of alterations in global methylation, we observed a marked hypermethylation of the rDNA loci in *Zmpste24*$^{-/-}$ progeroid mice, an alteration that may be functionally involved in the development of age-associated phenotypes and consequently it could provide a potential target for anti-progeroid

therapies. Accordingly, the treatment with 5-azacytidine prevented this alteration, further illustrating the possibility of reverting age-related epigenetic alterations *in vivo*.

Understanding organismal aging might rely on the identification of molecular pathways that integrate cells-autonomous and systemic alterations during aging. Thus, nuclear envelope defects causative of progeroid laminopathies lead to perturbations in cellular pathways, including p53-dependent cell senescence, deregulation of the somatotroph axis, and changes in metabolic master regulators [80, 84]. However, little is still known about intercellular communication signals involved in this regulation. Aging signals are mediated by a combination of structural and diffusible factors. In this regard, parabiosis experiments, in which the circulatory systems of young and old mice are artificially connected, have already shown the potential of systemic factors to prevent certain characteristics of natural aging [53, 54]. Conversely, soluble factors have also demonstrated pro-aging effect [142] and the secretion of signaling molecules by affected cells could be a major contributor to progeria development, as secreted molecules can act on distant organs, leading to an amplifying cascade of aged signals.

In this work, we have identified an ATM-dependent NF-κB activation pathway that links nuclear lamina defects to systemic inflammation (**IV**), demonstrating the causal role for this pathway in the appearance of age-associated pathologies and illustrating the feasibility of targeting this signaling cascade for the treatment of premature aging symptoms. Thus, we showed that accumulation of prelamin A/progerin at the nuclear lamina activates the NF-κB pathway in an ATM- and NEMO-dependent manner, illustrating that alterations in the nuclear architecture generate stress signals that activate important DNA damage sensors. In this context, ATM and NEMO act coordinately to activate NF-κB, as demonstrated by the finding that their respective inhibition prevents prelamin A-induced NF-κB activation. Consistent with the observed activation of NF-κB signaling in *Zmpste24*$^{-/-}$ and *Lmna*$^{G609G/G609G}$ progeroid mice, several cytokines and adhesion molecules are strongly up-regulated in cells and tissues from these mice, likely contributing to the initiation and maintenance of an inflammatory response (Figure 6).

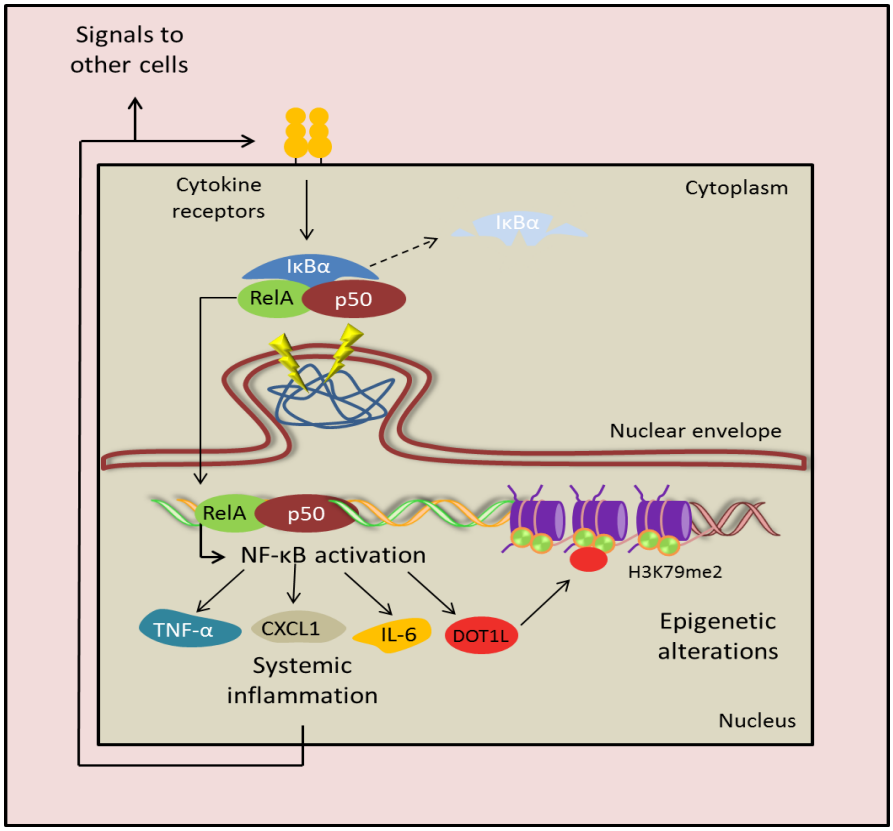

Figure 6. NF-κB hyperactivation in aging.

Among the plethora of proinflammatory cytokines secreted by senescent cells, we propose that IL-6, CXCL1, and TNF-α may have essential roles in progeria development by non-autonomous stimulation of surrounding cells, through the activation of their cognate cell surface receptors and signal transduction pathways [143, 144]. Thus, systemically increased levels of cytokines amplify the inflammatory stimuli and are implicated in the establishment of a feed-forward signaling process [145]. Since senescent cells are potentially time-persisting, the continued production of cytokines and the subsequent NF-κB activation lead to an increased inflammation in progeroid mice that contributes to age-related wasting and dramatically shortens organismal lifespan. According to our results, NF-κB could be regarded as a major regulator of accelerated aging, as demonstrated by the fact that NF-κB blockade significantly increases lifespan in both *Zmpste24*$^{-/-}$ and *Lmna*$^{G609G/G609G}$ progeroid mice.

Furthermore, the NF-κB blockade strategies used in this study have allowed us to provide new molecular insights into the involvement of NF-κB in dermal and immunological homeostasis. The primary manifestations of accelerated aging in skin affect cell proliferation,

hair follicles, and the subcutaneous fat layer [146]. NF-κB blockade was able to prevent these alterations, demonstrating a causal role of NF-κB deregulation in age-associated defects in skin homeostasis. A similar situation has been shown in lymphoid organs, which is of special interest, as thymic involution is considered one of the leading regulators of aging [147]. The reduction in tissue mass and cellularity and the loss of tissue structure leads to a decline in naive T-cell output as well as to the occurrence of changes in the peripheral T-cell compartment that contribute to the clinical signs of immunosenescence [148]. Consistent with these observations, we demonstrated that NF-κB hyperactivation and the systemic inflammation derived thereof drive thymus and spleen involution, and that NF-κB inhibition is able to prevent these age-related alterations.

Although the biological significance of NF-κB activation during aging is not completely clear, the findings reported, together with the fact that other models of normal and accelerated aging show increased levels of NF-κB activity [149, 150], support the idea that inflammation is a major regulator of the aging process as it accomplishes the three hallmark-defining characteristics: NF-κB signaling is active during normal aging [48], its hyperactivation is associated with the development of accelerated aging, and its amelioration retards the aging process [47, 149, 151, 152]. The mechanism by which NF-κB signaling is activated with age also remained largely unexplored, but our data indicate that the nuclear envelope abnormalities occurring in both normal and premature aging may contribute, at least in part, to the activation of this inflammatory pathway. The primary function of NF-κB activation in response to nuclear envelope defects could be to protect damaged cells against apoptosis [153], as well as induce immune system-mediated clearance of damaged and senescence cells. Since a proper clearance of senescent cells by the immune system is crucial for homeostasis maintenance in aging and cancer [41, 154], both NF-κB hyperactivation and the subsequent age-related immunological decline could be threatening an appropriate response against age-accumulated senescent cells.

Apart from systemic inflammation control, we have also recently demonstrated the involvement of NF-κB signaling in the control of cell differentiation and reprogramming through active regulation of the epigenetic landscape [21]. This work has also led us to identify new effectors involved in NF-κB signaling in aging. Thus, we have demonstrated that NF-B modulation of chromatin-modifying factor DOT1L has a direct impact in aging through the regulation of the methylation of Lys79 in histone H3, which represents a molecular

crosstalk between aging and differentiation control. DOT1L has thus emerged as a prominent effector of NF-B activity in aging **(IV)**.

The results of our work also suggest that the use of NF-κB or DOT1L inhibitors, alone or in combination with statins and aminobisphosphonates, could be useful for the treatment of age-associated alterations occurring during the course of progeroid laminopathies (**IV**). Moreover, pharmacological modulation of the NF-κB pathway also could be of interest for slowing down the progression of physiological aging. The identification of NF-κB signaling activation in accelerated and normal aging provides further support for the proposal that the maintenance of the aged state requires an active signaling program and that age-linked phenotypes can be substantially reversed by intervention on the activity of individual genes. Globally, our data support the use of strategies aimed at controlling NF-κB related inflammation as putative rejuvenation strategies during both normal and pathological aging, suggesting that the rational design of new interventions aimed at slowing down aging should act in a coordinate way, targeting pro-aging signals as well as altered cellular communication pathways for the effective prevention of aging-related disorders.

The main conclusions of our study derived from the characterization of subtle changes in NF-κB signaling over time. However, monitoring biological processes *in vivo* is still experimentally challenging. Thus, the visualization of biochemical perturbations in whole organisms requires highly sensitive methods that allow detection in a quantitative and reproducible manner [155]. Reporter gene approaches are based on the use of specific regulatory sequences attached to genes that confer organisms a property that could be easily detected and quantified, typically light or fluorescence emission. The method developed in this work, based on the use of a luciferase reporter gene has been successfully used for studying constitutive and acute-induced NF-κB signaling in mouse tissues (**V**). The use of this approach allowed us to monitor chronic activation of NF-κB and the specific response in these models to NF-κB inhibitory drugs. These results support the utility of this approach to study both chronic conditions as well as acute inflammatory responses. The possibility of using viral vectors with different tissue tropisms for the reporter delivery potentially allows monitoring NF-κB in virtually any tissue. Additionally, the same strategy may be applied for studying different signaling pathways, replacing the NF-κB response element with other regulatory sequences in the luciferase reporter system.

The relationship between aging and cancer processes is complex and difficult to interpret in part due to the lack of proper experimental models. Thus, it has been largely anticipated that the incidence of hematological malignancies in the elderly can be traced back to age-associated alterations in both the hematopoietic system and the hematopoietic stem cell compartment. [105-107]. Although damage accumulation drives the functional decline of organisms, several conserved signaling pathways influence how rapidly damage accumulates and how organisms respond to it. Among them, the insulin/IGF-1 signaling pathway (IIS) is one of the most important determinants of organism lifespan [9, 156]. Prolonged suppression of the IIS pathway promotes longevity, whereas persistent activation shortens lifespan and increases cancer incidence [84, 120, 133, 157-162].

In this work, we provide experimental support for an unanticipated tumor suppressor activity of AIRAPL in myeloid malignancies, connecting alterations in the IIS pathway with myeloproliferative neoplasms (MPN) ethiopathogenesis. AIRAPL is an endoplasmic reticulum (ER) protein that contains a CAAX motif, similar to that observed in lamin A. Until now, functional data of this protein was obtained from *C. elegans* ortologue aip-1 [26], which demonstrated its involvement in proteostasis control during aging. However, we found that the inactivation of *Zfand2b* gene in mice was sufficient to cause cell-autonomous defects in HSC compartment, giving rise to a myeloproliferative neoplasm that faithfully resemble most of the alterations shown by MPN patients and MPN animal models [163-166] (**VI**). Furthermore, we demonstrate that dose changes in *Zfand2b* levels remarkably affect myeloid hematopoiesis, suggesting a prominent role of this protein in the control of white blood cell formation.

AIRAPL then emerges as a central regulator of IGF1R steady-state levels at the ER (**VI**). The proposed mechanism agrees with evidences that demonstrate the implication of AIRAPL in pre-emptive quality control (PQC) pathway [167]. Accordingly, AIRAPL-dependent PQC activity would regulate translocation of IGF1R nascent polypeptides in the ER and their proteasome-mediated degradation. Although AIRAPL is unlikely to display E3-ligase activity, we demonstrate that its overexpression is able to promote IGF1R ubiquitination similarly to other proteins sharing related ubiquitin-interacting motifs (UIMs) [168, 169]. The degradation of IGF1R polypeptides prior to their arrival to the cell surface would eventually suppress aberrant signaling in a similar way to that recently reported for other tyrosine kinase receptors (Figure 7) [170-172].

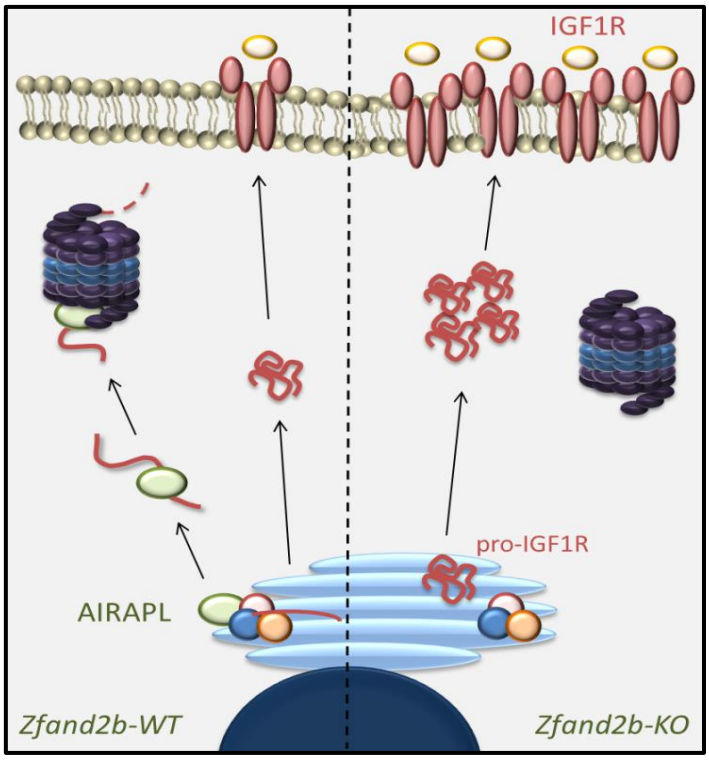

Figure 7. Model depicting AIRAPL biological function. AIRAPL interacts with newly synthesized IGF1R polypeptides at ER, inducing its ubiquitination and proteasome-mediated degradation. In the absence of AIRAPL, the lack of this regulatory mechanism increases IGF1R steady-state levels.

It is remarkable that numerous clinical trials have evaluated IGF1R as a potential therapeutic target for solid tumors, but its clinical relevance in myeloproliferative syndromes has not been similarly addressed [160, 173]. Accordingly, our *in vitro* and *in vivo* studies showing the efficacy of IGF1R inhibitory strategies in JAK2-driven myeloproliferative neoplasms constitute an important preclinical evidence of the use of IGF1R inhibitors for the treatment of these neoplasias, alone or in combination with JAK2 inhibitors [174]. Furthermore, our study represents a clear demonstration of the oncogenic relevance of proteostasis deregulation in hematopoietic cells. Notably, most studies of the molecular mechanisms controlling HSC homeostasis have focused on the analysis of genetic and epigenetic alterations of key oncogenes and tumor suppressors, as well as on the evaluation of the signaling and transcriptional changes induced by these genomic damages. However, our finding that loss of AIRAPL contributes to the transformation of myeloid cells provides causal evidence about the crucial role of proteostatic processes in the regulation of

quiescence, proliferation and differentiation of HSCs, which finally contribute to maintain normal adult hematopoiesis.

Globally, our work uncovers AIRAPL biological function as a novel regulator of the somatotropic axis involved in the control of myeloid hematopoiesis. Although further work should address the precise nature of the signals that regulate AIRAPL function, it is tempting to speculate that its location at ER would allow it to act as a sensor of different extrinsic and intrinsic stress signals. *Zfand2b*-deficient mice then provide a valuable experimental system for studying myeloproliferative neoplasms and also for assessing the implication of AIRAPL in other pathological conditions associated with cancer and aging processes through IGF1R-dependent and independent mechanisms.

In summary, we have focused on this Doctoral Thesis work in the development and characterization of new experimental models for the study of aging and cancer, which has allowed us to develop different intervention strategies aimed at correcting functional alterations in these two complex biological processes. Besides, our work has highlighted the importance of systemic alterations in aging, evidencing new regulatory mechanisms that integrate organismal age signals. Finally, we have provided new insights between the molecular relationships of aging and cancer in the hematological system, illustrating that alterations in evolutionarily conserved regulatory pathways are common hallmarks of both processes, which may result in the identification of new prognostic and therapeutic markers for myeloid malignancies. Future work in aging may benefit from the possibility of inducing complex alterations through genome-editing technology, and applying the increasing mechanistic understanding of the aging process derived from genetic, epigenetic and transcriptional analyses. The ability to program and reprogram cellular age on demand will represent a critical step forward on the road to capture and sequence the multiple steps involved in aging development.

Conclusions

1- *Lmna*^{G609G} knock-in mice show an accelerated aging phenotype characterized by shortened lifespan, reduced body weight, and bone and cardiovascular alterations.

2- Administration of specific antisense oligonucleotides corrects *Lmna* splicing alterations in *Lmna*$^{G609G/G609G}$ mice, extending lifespan and preventing age-associated alterations.

3- *Zmpste24*-deficient mice show age-related epigenetic alterations, including changes in H2B histone acetylation and ribosomal DNA methylation levels.

4- ATM-mediated NF-κB hyperactivation in aging causes systemic inflammation, compromising tissue homeostasis.

5- NF-κB *in vivo* inhibition ameliorates age-associated alterations and extends longevity of *Zmpste24*-deficient and *Lmna*^{G609G} mice.

6- The proteostasis regulator AIRAPL suppresses myeloid transformation through the regulation of steady state levels of IGF1R at endoplasmic reticulum.

7- AIRAPL expression is ablated in human myeloproliferative neoplasms by the up-regulation of the microRNA miR-125-3p.

8- IGF1R inhibition in myeloid malignancies reverts hematopoietic alterations caused by AIRAPL deficiency.

Bibliography

1. Lopez-Otin, C., et al., *The hallmarks of aging.* Cell, 2013. **153**(6): p. 1194-217.
2. Kirkwood, T.B., *Understanding the odd science of aging.* Cell, 2005. **120**(4): p. 437-47.
3. Hayflick, L., *Biological aging is no longer an unsolved problem.* Ann N Y Acad Sci, 2007. **1100**: p. 1-13.
4. Kirkwood, T.B. and S. Melov, *On the programmed/non-programmed nature of ageing within the life history.* Curr Biol, 2011. **21**(18): p. R701-7.
5. Bredesen, D.E., *The non-existent aging program: how does it work?* Aging Cell, 2004. **3**(5): p. 255-9.
6. Jones, O.R., et al., *Diversity of ageing across the tree of life.* Nature, 2014. **505**(7482): p. 169-73.
7. Rando, T.A. and H.Y. Chang, *Aging, rejuvenation, and epigenetic reprogramming: resetting the aging clock.* Cell, 2012. **148**(1-2): p. 46-57.
8. Guarente, L. and C. Kenyon, *Genetic pathways that regulate ageing in model organisms.* Nature, 2000. **408**(6809): p. 255-62.
9. Kenyon, C.J., *The genetics of ageing.* Nature, 2010. **464**(7288): p. 504-12.
10. Hoeijmakers, J.H., *DNA damage, aging, and cancer.* N Engl J Med, 2009. **361**(15): p. 1475-85.
11. Worman, H.J., *Nuclear lamins and laminopathies.* J Pathol, 2012. **226**(2): p. 316-25.
12. Baker, D.J., et al., *Increased expression of BubR1 protects against aneuploidy and cancer and extends healthy lifespan.* Nat Cell Biol, 2013. **15**(1): p. 96-102.
13. Vaidya, A., et al., *Knock-in reporter mice demonstrate that DNA repair by non-homologous end joining declines with age.* PLoS Genet, 2014. **10**(7): p. e1004511.
14. Blackburn, E.H., C.W. Greider, and J.W. Szostak, *Telomeres and telomerase: the path from maize, Tetrahymena and yeast to human cancer and aging.* Nat Med, 2006. **12**(10): p. 1133-8.
15. Armanios, M. and E.H. Blackburn, *The telomere syndromes.* Nat Rev Genet, 2012. **13**(10): p. 693-704.
16. Blasco, M.A., et al., *Telomere shortening and tumor formation by mouse cells lacking telomerase RNA.* Cell, 1997. **91**(1): p. 25-34.
17. Jaskelioff, M., et al., *Telomerase reactivation reverses tissue degeneration in aged telomerase-deficient mice.* Nature, 2011. **469**(7328): p. 102-6.
18. Talens, R.P., et al., *Epigenetic variation during the adult lifespan: cross-sectional and longitudinal data on monozygotic twin pairs.* Aging Cell, 2012. **11**(4): p. 694-703.
19. Mostoslavsky, R., et al., *Genomic instability and aging-like phenotype in the absence of mammalian SIRT6.* Cell, 2006. **124**(2): p. 315-29.
20. Krishnan, V., et al., *Histone H4 lysine 16 hypoacetylation is associated with defective DNA repair and premature senescence in Zmpste24-deficient mice.* Proc Natl Acad Sci U S A, 2011. **108**(30): p. 12325-30.

21. Soria-Valles, C., et al., *NF-kappaB activation impairs somatic cell reprogramming in ageing.* Nat Cell Biol, 2015. **17**(8): p. 1004-13.

22. Houtkooper, R.H., E. Pirinen, and J. Auwerx, *Sirtuins as regulators of metabolism and healthspan.* Nat Rev Mol Cell Biol, 2012. **13**(4): p. 225-38.

23. Powers, E.T., et al., *Biological and chemical approaches to diseases of proteostasis deficiency.* Annu Rev Biochem, 2009. **78**: p. 959-91.

24. Hartl, F.U., A. Bracher, and M. Hayer-Hartl, *Molecular chaperones in protein folding and proteostasis.* Nature, 2011. **475**(7356): p. 324-32.

25. Koga, H., S. Kaushik, and A.M. Cuervo, *Protein homeostasis and aging: The importance of exquisite quality control.* Ageing Res Rev, 2011. **10**(2): p. 205-15.

26. Yun, C., et al., *Proteasomal adaptation to environmental stress links resistance to proteotoxicity with longevity in Caenorhabditis elegans.* Proc Natl Acad Sci U S A, 2008. **105**(19): p. 7094-9.

27. Morrow, G., et al., *Overexpression of the small mitochondrial Hsp22 extends Drosophila life span and increases resistance to oxidative stress.* FASEB J, 2004. **18**(3): p. 598-9.

28. Walker, G.A. and G.J. Lithgow, *Lifespan extension in C. elegans by a molecular chaperone dependent upon insulin-like signals.* Aging Cell, 2003. **2**(2): p. 131-9.

29. Zhang, C. and A.M. Cuervo, *Restoration of chaperone-mediated autophagy in aging liver improves cellular maintenance and hepatic function.* Nat Med, 2008. **14**(9): p. 959-65.

30. Eisenberg, T., et al., *Induction of autophagy by spermidine promotes longevity.* Nat Cell Biol, 2009. **11**(11): p. 1305-14.

31. Fontana, L., L. Partridge, and V.D. Longo, *Extending healthy life span--from yeast to humans.* Science, 2010. **328**(5976): p. 321-6.

32. Martin-Montalvo, A., et al., *Metformin improves healthspan and lifespan in mice.* Nat Commun, 2013. **4**: p. 2192.

33. Harrison, D.E., et al., *Rapamycin fed late in life extends lifespan in genetically heterogeneous mice.* Nature, 2009. **460**(7253): p. 392-5.

34. Green, D.R., L. Galluzzi, and G. Kroemer, *Mitochondria and the autophagy-inflammation-cell death axis in organismal aging.* Science, 2011. **333**(6046): p. 1109-12.

35. Hekimi, S., J. Lapointe, and Y. Wen, *Taking a "good" look at free radicals in the aging process.* Trends Cell Biol, 2011. **21**(10): p. 569-76.

36. Edgar, D., et al., *Random point mutations with major effects on protein-coding genes are the driving force behind premature aging in mtDNA mutator mice.* Cell Metab, 2009. **10**(2): p. 131-8.

37. Campisi, J. and F. d'Adda di Fagagna, *Cellular senescence: when bad things happen to good cells.* Nat Rev Mol Cell Biol, 2007. **8**(9): p. 729-40.

38. Collado, M., M.A. Blasco, and M. Serrano, *Cellular senescence in cancer and aging.* Cell, 2007. **130**(2): p. 223-33.

39. van Deursen, J.M., *The role of senescent cells in ageing.* Nature, 2014. **509**(7501): p. 439-46.

40. Demaria, M., et al., *An essential role for senescent cells in optimal wound healing through secretion of PDGF-AA.* Dev Cell, 2014. **31**(6): p. 722-33.

41. Baker, D.J., et al., *Clearance of p16Ink4a-positive senescent cells delays ageing-associated disorders.* Nature, 2011. **479**(7372): p. 232-6.

42. Molofsky, A.V., et al., *Increasing p16INK4a expression decreases forebrain progenitors and neurogenesis during ageing.* Nature, 2006. **443**(7110): p. 448-52.

43. Conboy, I.M. and T.A. Rando, *Heterochronic parabiosis for the study of the effects of aging on stem cells and their niches.* Cell Cycle, 2012. **11**(12): p. 2260-7.

44. Sousa-Victor, P., et al., *Muscle stem cell aging: regulation and rejuvenation.* Trends Endocrinol Metab, 2015. **26**(6): p. 287-96.

45. Sousa-Victor, P., et al., *Geriatric muscle stem cells switch reversible quiescence into senescence.* Nature, 2014. **506**(7488): p. 316-21.

46. Russell, S.J. and C.R. Kahn, *Endocrine regulation of ageing.* Nat Rev Mol Cell Biol, 2007. **8**(9): p. 681-91.

47. Zhang, G., et al., *Hypothalamic programming of systemic ageing involving IKK-beta, NF-kappaB and GnRH.* Nature, 2013. **497**(7448): p. 211-6.

48. Adler, A.S., et al., *Motif module map reveals enforcement of aging by continual NF-kappaB activity.* Genes Dev, 2007. **21**(24): p. 3244-57.

49. Vafaie, F., et al., *Collagenase-resistant collagen promotes mouse aging and vascular cell senescence.* Aging Cell, 2014. **13**(1): p. 121-30.

50. Gutierrez-Fernandez, A., et al., *Loss of MT1-MMP causes cell senescence and nuclear defects which can be reversed by retinoic acid.* EMBO J, 2015. **34**(14): p. 1875-88.

51. Baker, D.J., R.L. Weaver, and J.M. van Deursen, *p21 both attenuates and drives senescence and aging in BubR1 progeroid mice.* Cell Rep, 2013. **3**(4): p. 1164-74.

52. Freije, J.M. and C. Lopez-Otin, *Reprogramming aging and progeria.* Curr Opin Cell Biol, 2012. **24**(6): p. 757-64.

53. Conboy, I.M., et al., *Rejuvenation of aged progenitor cells by exposure to a young systemic environment.* Nature, 2005. **433**(7027): p. 760-4.

54. Loffredo, F.S., et al., *Growth differentiation factor 11 is a circulating factor that reverses age-related cardiac hypertrophy.* Cell, 2013. **153**(4): p. 828-39.

55. Villeda, S.A., et al., *The ageing systemic milieu negatively regulates neurogenesis and cognitive function.* Nature, 2011. **477**(7362): p. 90-4.

56. Gurdon, J.B., *Adult frogs derived from the nuclei of single somatic cells.* Dev Biol, 1962. **4**: p. 256-73.

57. Takahashi, K. and S. Yamanaka, *Induction of pluripotent stem cells from mouse embryonic and adult fibroblast cultures by defined factors.* Cell, 2006. **126**(4): p. 663-76.

58. Lapasset, L., et al., *Rejuvenating senescent and centenarian human cells by reprogramming through the pluripotent state.* Genes Dev, 2011. **25**(21): p. 2248-53.

59. de Cabo, R., et al., *The search for antiaging interventions: from elixirs to fasting regimens.* Cell, 2014. **157**(7): p. 1515-26.

60. Merino, M.M., et al., *Elimination of unfit cells maintains tissue health and prolongs lifespan.* Cell, 2015. **160**(3): p. 461-76.

61. Chen, C., Y. Liu, and P. Zheng, *mTOR regulation and therapeutic rejuvenation of aging hematopoietic stem cells.* Sci Signal, 2009. **2**(98): p. ra75.

62. Gordon, L.B., et al., *Progeria: a paradigm for translational medicine.* Cell, 2014. **156**(3): p. 400-7.

63. Ramirez, C.L., et al., *Human progeroid syndromes, aging and cancer: new genetic and epigenetic insights into old questions.* Cell Mol Life Sci, 2007. **64**(2): p. 155-70.

64. Burtner, C.R. and B.K. Kennedy, *Progeria syndromes and ageing: what is the connection?* Nat Rev Mol Cell Biol, 2010. **11**(8): p. 567-78.

65. Hennekam, R.C., *Hutchinson-Gilford progeria syndrome: review of the phenotype.* Am J Med Genet A, 2006. **140**(23): p. 2603-24.

66. Merideth, M.A., et al., *Phenotype and course of Hutchinson-Gilford progeria syndrome.* N Engl J Med, 2008. **358**(6): p. 592-604.

67. Kudlow, B.A., B.K. Kennedy, and R.J. Monnat, Jr., *Werner and Hutchinson-Gilford progeria syndromes: mechanistic basis of human progeroid diseases.* Nat Rev Mol Cell Biol, 2007. **8**(5): p. 394-404.

68. Puente, X.S., et al., *Exome sequencing and functional analysis identifies BANF1 mutation as the cause of a hereditary progeroid syndrome.* Am J Hum Genet, 2011. **88**(5): p. 650-6.

69. Cabanillas, R., et al., *Nestor-Guillermo progeria syndrome: a novel premature aging condition with early onset and chronic development caused by BANF1 mutations.* Am J Med Genet A, 2011. **155A**(11): p. 2617-25.

70. Pereira, S., et al., *HGPS and related premature aging disorders: from genomic identification to the first therapeutic approaches.* Mech Ageing Dev, 2008. **129**(7-8): p. 449-59.

71. Gruenbaum, Y., et al., *The nuclear lamina comes of age.* Nat Rev Mol Cell Biol, 2005. **6**(1): p. 21-31.

72. De Sandre-Giovannoli, A., et al., *Lamin a truncation in Hutchinson-Gilford progeria.* Science, 2003. **300**(5628): p. 2055.

73. Eriksson, M., et al., *Recurrent de novo point mutations in lamin A cause Hutchinson-Gilford progeria syndrome.* Nature, 2003. **423**(6937): p. 293-8.

74. Pendas, A.M., et al., *Defective prelamin A processing and muscular and adipocyte alterations in Zmpste24 metalloproteinase-deficient mice.* Nat Genet, 2002. **31**(1): p. 94-9.

75. Scaffidi, P. and T. Misteli, *Lamin A-dependent nuclear defects in human aging.* Science, 2006. **312**(5776): p. 1059-63.

76. Bergo, M.O., et al., *Zmpste24 deficiency in mice causes spontaneous bone fractures, muscle weakness, and a prelamin A processing defect.* Proc Natl Acad Sci U S A, 2002. **99**(20): p. 13049-54.

77. Yang, S.H., et al., *Blocking protein farnesyltransferase improves nuclear blebbing in mouse fibroblasts with a targeted Hutchinson-Gilford progeria syndrome mutation.* Proc Natl Acad Sci U S A, 2005. **102**(29): p. 10291-6.

78. Varga, R., et al., *Progressive vascular smooth muscle cell defects in a mouse model of Hutchinson-Gilford progeria syndrome.* Proc Natl Acad Sci U S A, 2006. **103**(9): p. 3250-5.

79. Liu, B., et al., *Genomic instability in laminopathy-based premature aging.* Nat Med, 2005. **11**(7): p. 780-5.

80. Varela, I., et al., *Accelerated ageing in mice deficient in Zmpste24 protease is linked to p53 signalling activation.* Nature, 2005. **437**(7058): p. 564-8.

81. Marino, G., et al., *Premature aging in mice activates a systemic metabolic response involving autophagy induction.* Hum Mol Genet, 2008. **17**(14): p. 2196-211.

82. Espada, J., et al., *Nuclear envelope defects cause stem cell dysfunction in premature-aging mice.* J Cell Biol, 2008. **181**(1): p. 27-35.

83. Ugalde, A.P., et al., *Aging and chronic DNA damage response activate a regulatory pathway involving miR-29 and p53.* EMBO J, 2011. **30**(11): p. 2219-32.

84. Marino, G., et al., *Insulin-like growth factor 1 treatment extends longevity in a mouse model of human premature aging by restoring somatotroph axis function.* Proc Natl Acad Sci U S A, 2010. **107**(37): p. 16268-73.

85. Fong, L.G., et al., *A protein farnesyltransferase inhibitor ameliorates disease in a mouse model of progeria.* Science, 2006. **311**(5767): p. 1621-3.

86. Varela, I., et al., *Combined treatment with statins and aminobisphosphonates extends longevity in a mouse model of human premature aging.* Nat Med, 2008. **14**(7): p. 767-72.

87. Scaffidi, P. and T. Misteli, *Reversal of the cellular phenotype in the premature aging disease Hutchinson-Gilford progeria syndrome.* Nat Med, 2005. **11**(4): p. 440-5.

88. Hsu, P.D., E.S. Lander, and F. Zhang, *Development and applications of CRISPR-Cas9 for genome engineering.* Cell, 2014. **157**(6): p. 1262-78.

89. Liu, G.H., et al., *Targeted gene correction of laminopathy-associated LMNA mutations in patient-specific iPSCs.* Cell Stem Cell, 2011. **8**(6): p. 688-94.

90. Liu, G.H., et al., *Recapitulation of premature ageing with iPSCs from Hutchinson-Gilford progeria syndrome.* Nature, 2011. **472**(7342): p. 221-5.

91. Zhang, J., et al., *A human iPSC model of Hutchinson Gilford Progeria reveals vascular smooth muscle and mesenchymal stem cell defects.* Cell Stem Cell, 2011. **8**(1): p. 31-45.

92. Hanahan, D. and R.A. Weinberg, *Hallmarks of cancer: the next generation.* Cell, 2011. **144**(5): p. 646-74.

93. Hofmann, J.W., et al., *Reduced expression of MYC increases longevity and enhances healthspan.* Cell, 2015. **160**(3): p. 477-88.

94. Slack, C., et al., *The Ras-Erk-ETS-Signaling Pathway Is a Drug Target for Longevity.* Cell, 2015. **162**(1): p. 72-83.

95. Herranz, D., et al., *A NOTCH1-driven MYC enhancer promotes T cell development, transformation and acute lymphoblastic leukemia.* Nat Med, 2014. **20**(10): p. 1130-7.

96. Hoeijmakers, J.H., *Genome maintenance mechanisms for preventing cancer.* Nature, 2001. **411**(6835): p. 366-74.

97. de la Rosa, J., et al., *Prelamin A causes progeria through cell-extrinsic mechanisms and prevents cancer invasion.* Nat Commun, 2013. **4**: p. 2268.

98. Flach, J., et al., *Replication stress is a potent driver of functional decline in ageing haematopoietic stem cells.* Nature, 2014. **512**(7513): p. 198-202.

99. Geiger, H., M. Denkinger, and R. Schirmbeck, *Hematopoietic stem cell aging.* Curr Opin Immunol, 2014. **29**: p. 86-92.

100. Snoeck, H.W., *Aging of the hematopoietic system.* Curr Opin Hematol, 2013. **20**(4): p. 355-61.

101. Lichtman, M.A. and J.M. Rowe, *The relationship of patient age to the pathobiology of the clonal myeloid diseases.* Semin Oncol, 2004. **31**(2): p. 185-97.

102. Campbell, P.J. and A.R. Green, *The myeloproliferative disorders.* N Engl J Med, 2006. **355**(23): p. 2452-66.

103. Levine, R.L. and D.G. Gilliland, *Myeloproliferative disorders.* Blood, 2008. **112**(6): p. 2190-8.

104. Titmarsh, G.J., et al., *How common are myeloproliferative neoplasms? A systematic review and meta-analysis.* Am J Hematol, 2014. **89**(6): p. 581-7.

105. Dykstra, B., et al., *Clonal analysis reveals multiple functional defects of aged murine hematopoietic stem cells.* J Exp Med, 2011. **208**(13): p. 2691-703.

106. Morrison, S.J., et al., *The aging of hematopoietic stem cells.* Nat Med, 1996. **2**(9): p. 1011-6.

107. Pang, W.W., et al., *Human bone marrow hematopoietic stem cells are increased in frequency and myeloid-biased with age.* Proc Natl Acad Sci U S A, 2011. **108**(50): p. 20012-7.

108. Chen, B., et al., *Cellular strategies of protein quality control.* Cold Spring Harb Perspect Biol, 2011. **3**(8): p. a004374.

109. Chavous, D.A., F.R. Jackson, and C.M. O'Connor, *Extension of the Drosophila lifespan by overexpression of a protein repair methyltransferase.* Proc Natl Acad Sci U S A, 2001. **98**(26): p. 14814-8.

110. Min, J.N., et al., *CHIP deficiency decreases longevity, with accelerated aging phenotypes accompanied by altered protein quality control.* Mol Cell Biol, 2008. **28**(12): p. 4018-25.

111. Vembar, S.S. and J.L. Brodsky, *One step at a time: endoplasmic reticulum-associated degradation.* Nat Rev Mol Cell Biol, 2008. **9**(12): p. 944-57.

112. Walter, P. and D. Ron, *The unfolded protein response: from stress pathway to homeostatic regulation.* Science, 2011. **334**(6059): p. 1081-6.

113. Gidalevitz, T., V. Prahlad, and R.I. Morimoto, *The stress of protein misfolding: from single cells to multicellular organisms.* Cold Spring Harb Perspect Biol, 2011. **3**(6).

114. Ghazi, A., S. Henis-Korenblit, and C. Kenyon, *Regulation of Caenorhabditis elegans lifespan by a proteasomal E3 ligase complex.* Proc Natl Acad Sci U S A, 2007. **104**(14): p. 5947-52.

115. Carrano, A.C., et al., *A conserved ubiquitination pathway determines longevity in response to diet restriction.* Nature, 2009. **460**(7253): p. 396-9.

116. Mehta, R., et al., *Proteasomal regulation of the hypoxic response modulates aging in C. elegans.* Science, 2009. **324**(5931): p. 1196-8.

117. Kuhlbrodt, K., et al., *The Machado-Joseph disease deubiquitylase ATX-3 couples longevity and proteostasis.* Nat Cell Biol, 2011. **13**(3): p. 273-81.

118. Cuervo, A.M., et al., *Autophagy and aging: the importance of maintaining "clean" cells.* Autophagy, 2005. **1**(3): p. 131-40.

119. Cuervo, A.M., *Chaperone-mediated autophagy: selectivity pays off.* Trends Endocrinol Metab, 2010. **21**(3): p. 142-50.

120. Cohen, E., et al., *Reduced IGF-1 signaling delays age-associated proteotoxicity in mice.* Cell, 2009. **139**(6): p. 1157-69.

121. Rybak, A., et al., *A feedback loop comprising lin-28 and let-7 controls pre-let-7 maturation during neural stem-cell commitment.* Nat Cell Biol, 2008. **10**(8): p. 987-93.

122. Scott, L.M., et al., *JAK2 exon 12 mutations in polycythemia vera and idiopathic erythrocytosis.* N Engl J Med, 2007. **356**(5): p. 459-68.

123. Puente, X.S., et al., *Non-coding recurrent mutations in chronic lymphocytic leukaemia.* Nature, 2015.

124. Fraga, M.F., et al., *Loss of acetylation at Lys16 and trimethylation at Lys20 of histone H4 is a common hallmark of human cancer.* Nat Genet, 2005. **37**(4): p. 391-400.

125. Fraga, M.F., et al., *High-performance capillary electrophoretic method for the quantification of 5-methyl 2'-deoxycytidine in genomic DNA: application to plant, animal and human cancer tissues.* Electrophoresis, 2002. **23**(11): p. 1677-81.

126. Schreiber, E., et al., *Rapid detection of octamer binding proteins with 'mini-extracts', prepared from a small number of cells.* Nucleic Acids Res, 1989. **17**(15): p. 6419.

127. Villarroya-Beltri, C., et al., *Sumoylated hnRNPA2B1 controls the sorting of miRNAs into exosomes through binding to specific motifs.* Nat Commun, 2013. **4**: p. 2980.

128. Turner, B.M. and G. Fellows, *Specific antibodies reveal ordered and cell-cycle-related use of histone-H4 acetylation sites in mammalian cells.* Eur J Biochem, 1989. **179**(1): p. 131-9.

129. Skarnes, W.C., et al., *A conditional knockout resource for the genome-wide study of mouse gene function.* Nature, 2011. **474**(7351): p. 337-42.

130. Liu, P., N.A. Jenkins, and N.G. Copeland, *A highly efficient recombineering-based method for generating conditional knockout mutations.* Genome Res, 2003. **13**(3): p. 476-84.

131. Li, J., et al., *JAK2V617F homozygosity drives a phenotypic switch in myeloproliferative neoplasms, but is insufficient to sustain disease.* Blood, 2014. **123**(20): p. 3139-51.

132. Li, J., et al., *JAK2 V617F impairs hematopoietic stem cell function in a conditional knock-in mouse model of JAK2 V617F-positive essential thrombocythemia.* Blood, 2010. **116**(9): p. 1528-38.

133. Holzenberger, M., et al., *IGF-1 receptor regulates lifespan and resistance to oxidative stress in mice.* Nature, 2003. **421**(6919): p. 182-7.

134. Wernig, G., et al., *Expression of Jak2V617F causes a polycythemia vera-like disease with associated myelofibrosis in a murine bone marrow transplant model.* Blood, 2006. **107**(11): p. 4274-81.

135. Herweijer, H. and J.A. Wolff, *Gene therapy progress and prospects: hydrodynamic gene delivery.* Gene Ther, 2007. **14**(2): p. 99-107.

136. Porta-de-la-Riva, M., et al., *Basic Caenorhabditis elegans methods: synchronization and observation.* J Vis Exp, 2012(64): p. e4019.

137. Rual, J.F., et al., *Toward improving Caenorhabditis elegans phenome mapping with an ORFeome-based RNAi library.* Genome Res, 2004. **14**(10B): p. 2162-8.

138. Kamath, R.S. and J. Ahringer, *Genome-wide RNAi screening in Caenorhabditis elegans.* Methods, 2003. **30**(4): p. 313-21.

139. Subramanian, A., et al., *Gene set enrichment analysis: a knowledge-based approach for interpreting genome-wide expression profiles.* Proc Natl Acad Sci U S A, 2005. **102**(43): p. 15545-50.

140. Hammond, S.M. and M.J. Wood, *Genetic therapies for RNA mis-splicing diseases.* Trends Genet, 2011. **27**(5): p. 196-205.

141. Cirak, S., et al., *Exon skipping and dystrophin restoration in patients with Duchenne muscular dystrophy after systemic phosphorodiamidate morpholino oligomer treatment: an open-label, phase 2, dose-escalation study.* Lancet, 2011. **378**(9791): p. 595-605.

142. Smith, L.K., et al., *beta2-microglobulin is a systemic pro-aging factor that impairs cognitive function and neurogenesis.* Nat Med, 2015. **21**(8): p. 932-7.

143. Coppe, J.P., et al., *The senescence-associated secretory phenotype: the dark side of tumor suppression.* Annu Rev Pathol, 2010. **5**: p. 99-118.

144. Freund, A., et al., *Inflammatory networks during cellular senescence: causes and consequences.* Trends Mol Med, 2010. **16**(5): p. 238-46.

145. Biton, S. and A. Ashkenazi, *NEMO and RIP1 control cell fate in response to extensive DNA damage via TNF-alpha feedforward signaling.* Cell, 2011. **145**(1): p. 92-103.

146. Sur, I., M. Ulvmar, and R. Toftgard, *The two-faced NF-kappaB in the skin.* Int Rev Immunol, 2008. **27**(4): p. 205-23.

147. Aw, D. and D.B. Palmer, *The origin and implication of thymic involution.* Aging Dis, 2011. **2**(5): p. 437-43.

148. Hale, J.S., et al., *Cell-extrinsic defective lymphocyte development in Lmna(-/-) mice.* PLoS One, 2010. **5**(4): p. e10127.

149. Kawahara, T.L., et al., *SIRT6 links histone H3 lysine 9 deacetylation to NF-kappaB-dependent gene expression and organismal life span.* Cell, 2009. **136**(1): p. 62-74.

150. Rodier, F., et al., *Persistent DNA damage signalling triggers senescence-associated inflammatory cytokine secretion.* Nat Cell Biol, 2009. **11**(8): p. 973-9.

151. Tilstra, J.S., et al., *NF-kappaB inhibition delays DNA damage-induced senescence and aging in mice.* J Clin Invest, 2012. **122**(7): p. 2601-12.

152. Jurk, D., et al., *Chronic inflammation induces telomere dysfunction and accelerates ageing in mice.* Nat Commun, 2014. **2**: p. 4172.

153. Salminen, A., J. Ojala, and K. Kaarniranta, *Apoptosis and aging: increased resistance to apoptosis enhances the aging process.* Cell Mol Life Sci, 2011. **68**(6): p. 1021-31.

154. Kang, T.W., et al., *Senescence surveillance of pre-malignant hepatocytes limits liver cancer development.* Nature, 2011. **479**(7374): p. 547-51.

155. Badr, C.E. and B.A. Tannous, *Bioluminescence imaging: progress and applications.* Trends Biotechnol, 2011. **29**(12): p. 624-33.

156. Barzilai, N., et al., *The critical role of metabolic pathways in aging.* Diabetes, 2012. **61**(6): p. 1315-22.

157. Niedernhofer, L.J., et al., *A new progeroid syndrome reveals that genotoxic stress suppresses the somatotroph axis.* Nature, 2006. **444**(7122): p. 1038-43.

158. Steuerman, R., O. Shevah, and Z. Laron, *Congenital IGF1 deficiency tends to confer protection against post-natal development of malignancies.* Eur J Endocrinol, 2011. **164**(4): p. 485-9.

159. Guevara-Aguirre, J., et al., *Growth hormone receptor deficiency is associated with a major reduction in pro-aging signaling, cancer, and diabetes in humans.* Sci Transl Med, 2011. **3**(70): p. 70ra13.

160. Pollak, M., *Insulin and insulin-like growth factor signalling in neoplasia.* Nat Rev Cancer, 2008. **8**(12): p. 915-28.

161. Pollak, M., *The insulin and insulin-like growth factor receptor family in neoplasia: an update.* Nat Rev Cancer, 2012. **12**(3): p. 159-69.

162. Garinis, G.A., et al., *Persistent transcription-blocking DNA lesions trigger somatic growth attenuation associated with longevity.* Nat Cell Biol, 2009. **11**(5): p. 604-15.

163. Akada, H., et al., *Conditional expression of heterozygous or homozygous Jak2V617F from its endogenous promoter induces a polycythemia vera-like disease.* Blood, 2010. **115**(17): p. 3589-97.

164. Marty, C., et al., *Myeloproliferative neoplasm induced by constitutive expression of JAK2V617F in knock-in mice.* Blood, 2010. **116**(5): p. 783-7.

165. Mullally, A., et al., *Physiological Jak2V617F expression causes a lethal myeloproliferative neoplasm with differential effects on hematopoietic stem and progenitor cells.* Cancer Cell, 2010. **17**(6): p. 584-96.

166. Yildirim, E., et al., *Xist RNA is a potent suppressor of hematologic cancer in mice.* Cell, 2013. **152**(4): p. 727-42.

167. Glinka, T., et al., *Signal-peptide-mediated translocation is regulated by a p97-AIRAPL complex.* Biochem J, 2014. **457**(2): p. 253-61.

168. Fan, J., et al., *Hrs promotes ubiquitination and mediates endosomal trafficking of smoothened in Drosophila hedgehog signaling.* PLoS One, 2013. **8**(11): p. e79021.

169. Harper, J.W. and B.A. Schulman, *Structural complexity in ubiquitin recognition.* Cell, 2006. **124**(6): p. 1133-6.

170. Fry, W.H., et al., *Quantity control of the ErbB3 receptor tyrosine kinase at the endoplasmic reticulum.* Mol Cell Biol, 2011. **31**(14): p. 3009-18.

171. Kang, S.W., et al., *Substrate-specific translocational attenuation during ER stress defines a pre-emptive quality control pathway.* Cell, 2006. **127**(5): p. 999-1013.

172. Rane, N.S., et al., *Reduced translocation of nascent prion protein during ER stress contributes to neurodegeneration.* Dev Cell, 2008. **15**(3): p. 359-70.

173. Lovly, C.M., et al., *Rationale for co-targeting IGF-1R and ALK in ALK fusion-positive lung cancer.* Nat Med, 2014. **20**(9): p. 1027-34.

174. Meyer, S.C., et al., *CHZ868, a type II JAK2 inhibitor, reverses type I JAK inhibitor persistence and demonstrates efficacy in myeloproliferative neoplasms.* Cancer Cell, 2015. **28**(1): p. 15-28.